SOURCE LOCATION OF SUBSONIC AND SUPERSONIC JETS OF VARIOUS GEOMETRIES VIA ACOUSTIC BEAMFORMING

A Dissertation
Presented to
The Academic Faculty

By

Nicholas Breen

In Partial Fulfillment
of the Requirements for the Degree
Doctor of Philosophy in the
School of Aerospace Engineering

Georgia Institute of Technology

May 2019

SOURCE LOCATION OF SUBSONIC AND SUPERSONIC JETS OF VARIOUS GEOMETRIES VIA ACOUSTIC BEAMFORMING

Approved by:

Dr. K. K. Ahuja, Advisor
School of Aerospace Engineering
Georgia Institute of Technology

Dr. L. N. Sankar
School of Aerospace Engineering
Georgia Institute of Technology

Dr. M. Ruzzene
School of Aerospace Engineering
Georgia Institute of Technology

Dr. K. Sabra
School of Mechanical Engineering
Georgia Institute of Technology

Dr. J. Gavin
Gulfstream Aerospace
Savannah, Georgia

Dr. J. Bridges
NASA Glenn Research Center
Cleveland, Ohio

Date Approved: November 15, 2018

It is well known that a vital ingredient of success is not knowing that what you're attempting can't be done.

Terry Pratchett

For my grandparents who have passed on and for the one who continues to support me.

ACKNOWLEDGEMENTS

The author of this work would like to thank his advisor Dr. Krish Ahuja for all the time and guidance he has given over the course of this work. The author would also like to thank the other members of his committee, Dr. Lakshmi Sankar, Dr. Massimo Ruzzene, Dr. Karim Sabra, Dr. Joe Gavin, and Dr. James Bridges for their support and guidance throughout the doctoral process.

Many thanks to the engineers at Georgia Tech Research Institute, Dr. Robert Funk, Darryl Dickey, Dr. Aharon Karon, Michael Mayo, and Dr. Alessio Medda, for help acquiring data and for general advice for issues that arose during the data collection process. An additional thanks to Michael Mayo for acquiring the PIV measurements used in this work. Thank you to the fellow students at GTRI, Dr. Shane Lymphany, Jonathan Carroll, and Markus Lorenzo, for the support and encouragement during difficult periods of this work and for the help that they provided to overcome them.

The author would also like to thank Dr. Robert Dougherty for his support on the Beamform Interactive software package and his willingness to add features to the program to help with the processing performed in this work.

Finally, the author would like to thank his family, his lovely wife, Nicole Breen, and his dog Rupee for their support during his time as a graduate student and beyond. Additional thanks to Nicole for her editing support.

TABLE OF CONTENTS

LIST OF TABLES

LIST OF FIGURES

NOMENCLATURE

Latin Symbols

A	Amplitude of harmonic point source
Az	Azimuth angle with respect to the array center
B_F	Bias limit of value F
$B_f(f)$	Microphone freefield correction
$B_i(f, \psi)$	Microphone incidence correction
$B_s(f)$	Microphone screen (foam ball) correction
$B_\alpha(f)$	Microphone humidity correction
C	Offset, in x/D, of jet noise source distribution
c	Speed of sound
d, D	Nozzle diameter
D_j	Fully-expanded diameter
d_z	Normal distance between measurement plane and the beamformer
F	Arbitrary calculated or measured value
f	Frequency
f_o	Center frequency
f_s	Sampling frequency
g_k	Steering vector for the kth frequency bin
K	Number for frequency bins after FFT
M_d	Design Mach number of a nozzle
M_j	Jet Mach number

N	Number of microphones in an array
p_a	Ambient pressure
P_F	Precision limit of value F
P_k	Array power response for the kth frequency bin
p_n	Pressure signal at the nth microphone in the array
p_t	Stagnation/total pressure
R	Specific gas constant for dry air
R'	Distance between the source and a reference location in the array
R_k	Cross spectral matrix for the kth frequency bin
R'_n	Distance between the source and the nth microphone in the array
r_o	Distance from center of polar arc to microphone
r_{corr}	Corrected distance
r_{mic}	Distance from farfield microphone to nozzle exit
$R_{n,m}$	Cross-correlation matrix between the nth and mth microphones
s	Separation distance between twin jets
$s(\tau)$	Shift operator
s_o	Signal received at the array center
St	Strouhal number, fD/U
t	Time
T_a	Ambient temperature
T_t	Stagnation/total temperature
U, U_j	Jet velocity
U_F	Total uncertainty of value F
W	Beam pattern of an array
w_n	Scaling function for the nth microphone in the array
$X', \vec{X}$	Location of the sound source, from the center of the array
x, X	Distance downstream of the nozzle exit

x_i Measured variables used to calculate F, if applicable

$X_n, \vec{X_n}$ Location of nth microphone in the array, from the center of the array

x_o X position of noise source with respect to the image center

y Distance normal to the jet axis

Y_n Frequency domain signal received at the nth microphone in the array

y_n Time signal received at the nth microphone in the array

Z Beamforming response in frequency domain

z Beamforming response in time domain

Greek Symbols

α Azimuth angle

α_f Azimuth angle corresponding to array focus location

δ Delta operator

Δ_n Time delay for the nth microphone in the array

δ_{99} Distance between 99% of jet velocity and 0% jet velocity at a downstream location

γ Ratio of specific heats

λ Acoustic wavelength

μ Mean value of a distribution

ω Angular frequency

ψ Microphone incidence angle

σ Standard deviation of a distribution

$\tau_{n,l}$ Time it takes sound to propagate from the lth grid point to the nth microphone

θ Microphone polar angle with respect to the downstream axis

Superscripts

$'$ Complex conjugate transpose

Subscripts

a Ambient condition

j	Jet property
k	kth frequency bin of the K-point FFT
l	lth grid point in the region of interest
m	mth microphone in the array
n	nth microphone in the array
t	Total flow condition

Acronyms

BBSAN	Broadband Shock Associated Noise
FFT	Fast Fourier Transform
NPR	Nozzle Pressure Ratio, $\frac{p_t}{p_a}$
PIV	Particle Image Velocimetry
SAN	Shock Associated Noise
SPL	Sound Pressure Level

SUMMARY

Over the years, the need to understand and reduce aircraft noise emissions has led numerous researchers to apply various source location techniques to jet noise. Prior to 1985, several methods for determining jet-noise source locations were explored: acoustic mirrors, microphone arrays, two-microphone methods, causality correlation and coherence techniques, nearfield contour surveys, and automated source breakdown. More recently there have been developments in the microphone array, notably acoustic beamforming, and two-microphone method techniques. Many of the older techniques require significant amount of time to acquire data at each jet condition; this requirement is often caused by the necessity to move microphones in order to obtain source locations at all frequencies. The acoustic beamformer does not need to be moved during the acquisition of data, resulting in very rapid tests compared to other source-location methods.

Upon examination of prior studies containing jet noise source location measurements, it is clear that there are a few areas in the field that need additional work: (1) no study has compared the results of the acoustic beamforming method with another method using the same nozzles and facilities, (2) no study has been performed that analyzes the effects of differing nozzle geometry, and hence the nozzle exit boundary layer, on the jet noise source location, (3) no study has performed a detailed analysis of the noise source distributions of supersonic jets, and (4) no study has examined the noise source distribution of twin jets and the effect of separation distance on the said distribution. The goal of this current work is to systematically address these areas with the use of source location measurements, schlieren flow visualization, farfield spectra, and jet velocity measurements. The source location measurements are primarily acquired using an acoustic beamformer. Jet velocity measurements include both nozzle exit boundary layer profiles and downstream velocity profiles and are obtained with the use of boundary layer probes and particle imaging velocimetry.

While acoustic beamforming has been used in the past by researchers to locate the

sources of jet noise, no one has sufficiently validated this method against other well-established methods. In this work, the jet noise source location obtained with an acoustic beamformer is compared against other source location methods from previous studies, yielding agreement within one diameter at most frequencies. This level of agreement is acceptable, as the data from these previous studies only agree within two diameters among themselves. The source location data from the beamformer is further compared to that generated from nearfield noise contours. These contours are generated using the same nozzles in very similar facilities, resulting in a more accurate comparison between two source location methods. The acoustic beamformer similarly falls within one diameter of the nearfield contours. It is shown in this work that source location error on the order of one diameter has little impact on applications of source location such as nearfield corrections or nearfield to farfield extrapolation of jet noise. Due to these comparisons, the beamformer has been validated for measuring the noise source locations of jet-mixing noise, and as a result the remainder of this work uses the beamformer to acquire the jet noise source distributions. While not verified in this work, this should also apply to jet-mixing noise due to small-scale turbulent structures in supersonic jets.

Subsonic noise source distributions in jets are generated by turbulence in the mixing layer of the jet. These distributions are typically plotted as Strouhal number (fD/U) versus normalized downstream distance (x/D), corresponding to the locations of sources of normalized frequencies. Internal geometry of the nozzles, and thus the nozzle exit boundary layer, do have an effect on the noise source distributions. The thinner boundary layers of ASME nozzles cause the turbulent structures in the mixing layer to, at least initially, grow faster than conical nozzles of similar diameters. This results in noise source distributions that are shifted upstream at all frequencies with respect to those of nozzles with larger exit boundary layers.

Supersonic noise source distributions are more complex than those of subsonic jets. The source distributions for supersonic jets can be divided into three different Strouhal regions.

At the lowest Strouhal numbers measured in this work, the noise source distributions appear very similar to those of a subsonic jet. This Strouhal region is dominated by jet-mixing noise. At the highest Strouhal numbers, the noise source distributions are comprised of several repetitive sources at various discrete downstream jet locations that produce noise at all frequencies. The locations of these sources roughly correspond to the shock cells in the jet, and thus vary with jet Mach number. The final region exists at Strouhal numbers between these two, and has a shape that is due to resolution limits of the source location tool measuring it. This region roughly corresponds to the frequencies of noise where jet-mixing noise and shock noise are of similar levels. The shock sources in this region have spacings between them that are smaller than the beam width of the array measuring them. Their locations no longer can be separately recorded at these frequencies, and instead they are averaged together and their centroid location is plotted.

The noise source distributions of the subsonic twin jets examined in this work are strongly affected by the resolution of the beamformer used to measure them. These distributions do not differ much from single jets when plotted as Strouhal number versus normalized downstream distance. However, when plotted as a function of distance normal to the jet axis (y/D) between the two nozzles, the effects of array resolution on source location become apparent. The beamformer's resolution is a function of the size of its beam width. Smaller beam widths correspond to better source location resolution; however, the beam width increases in size as source frequency of the source is decreased. At higher frequencies, where the beam width of the beamformer is rather small, separate noise source distributions appear for each nozzle, centered on the axis of each nozzle. At some point as source frequency is decreased, the spacing between the jets becomes smaller than the beam width of the array, and the noise source distributions of each nozzle erroneously appear to move inwards towards the plane of symmetry between the nozzles. At the lowest frequencies measured, the two sources from the two jets at each frequency cannot be separated and the large beam width displays one distribution that is centered on the central axis between

the two nozzles. When the twin nozzles are placed further apart, the noise sources from the two jets can be separated at lower frequencies than when they are close together.

CHAPTER 1
INTRODUCTION

1.1 Motivation

This work deals with locating sources of noise in subsonic and supersonic jets of various geometries using beamforming. In the context of aeroacoustics, source location refers to a methodology that allows the identification of locations of noise sources of a given frequency in the noise-producing region of the flow. The need to understand and reduce aircraft noise emissions has led numerous researchers to apply various source location techniques to jet noise as discussed in great detail in the next chapter [1]. Acoustic beamforming is, however, a relatively new methodology for locating noise sources that are aeroacoustic in nature. The beamformer does not need to be moved during the acquisition of data, resulting in very rapid tests compared to other source-location methods. It has been successfully used to locate sources of noise on aircraft, such as flap-edge noise and landing gear noise [2, 3]. This technique has also been used by a few researchers to locate the sources of jet noise [4–6], but no one has sufficiently validated this method against other well-established methods. The data that has been compared has been from different nozzles tested in different facilities, which can result in vastly different nozzle exit boundary layers. Karon [7] has shown that changes in the nozzle exit boundary layer affect the jet noise; thus these slightly different jets result in added uncertainty in any comparison of source location that was obtained. The present study is primarily motivated by the need to validate the beamforming technique against existing techniques using the exact same nozzles in the same facilities.

There are a number of applications where the knowledge of the location of sources of various frequencies along the length of the jet is required. For example, as shown below,

an accurate knowledge of the source location distributions for model-scale jets, (1) helps researchers apply the effect of flight on jet noise tested in flight simulation facilities, (2) helps design ejectors for proper noise shielding, and (3) helps render measured nearfield data into lossless data.

Due to the high costs that come with full-scale testing, model-scale jets are often used when testing jet noise. As a result, flight effects need to be simulated during these tests. The model jet is often fixed in place and the forward motion of the jet is simulated by having the jet immersed in flow that is either generated by a wind tunnel or a larger secondary nozzle (the later of which is called a free-jet facility). In 1977, Tanna and Morris [8] examined how scaling laws change due to simulated flight effects, and in 1978, Ahuja et al. [9] throughly examined the differences caused by simulated forward motion and developed methods to convert simulated data to flight data.

For experiments conducted in free-jet facilities, the measurement microphones are located outside of the secondary air stream, which results in any sound coming from the model jet having to pass through the secondary nozzle's mixing layer before it can reach the microphones. The secondary air stream refracts the sound as it passes through the mixing layer, resulting in a different acoustic path as illustrated in Figure 1.1. It is known that the sources of different frequencies are located at different locations along the length of the jet. Thus the spectrum measured at the microphone shown in Figure 1.1 is made up of different frequencies, each emanating from a source at a different downstream location. Thus, as shown for a single source in this figure, the data measured at the microphone has been affected by shear layer refraction, which would not have been there if the microphone were inside the jet. This refraction effect needs to be removed from the microphone data that has been acquired outside the free jet-mixing layer to determine the true effect of flight on jet noise. This correction is referred to as the "shear layer correction" as described in Ahuja et al. [9]. For a fixed microphone, the actual noise path changes depending upon where the noise source of a given frequency is, so different corrections need to be applied

for each source location (or frequency).

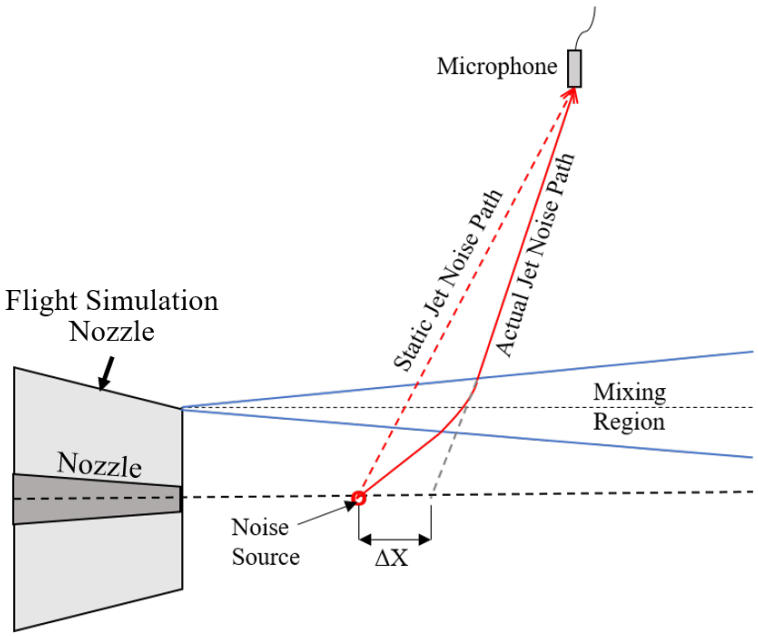

Figure 1.1: An example of how a jet's noise source's path changes due to the presence of flight effects.

Ejectors are used to entrain outside air with the primary jet in order to modify the thrust of an engine. An ejector has a shroud that extends past the primary jet's exit; as a result, it can be used to shield some of the noise from the jet. A study performed by Lord et al. [10] demonstrated that a mixer-ejector could cause a significant decrease in a conical nozzle's shock noise. Knowledge of a jet's noise source distribution would allow for the proper design of an ejector for noise shielding; the length of the ejector can be changed to shield certain frequencies and the proper acoustic lining can be chosen to absorb those frequencies. It is also possible to change the jet's source distribution through methods such as mixing. Moving the noise sources closer to the nozzle exit would allow the ejectors to be of a shorter length.

The knowledge of a particular jet's noise source distribution is often very important when acquiring nearfield data. When sound is considered to be measured in the nearfield of a jet, different noise sources can be perceived of as coming from different locations in space. In contrast, farfield measurements for jet noise are recorded far enough away that all

sources can be assumed to emanate from the nozzle exit. This difference between nearfield and farfield measurements makes data acquired in these two regions very difficult to compare with one another. One reason for this is that it is impossible to calibrate microphones in the nearfield, for angle of incidence as well has humidity corrections, without an accurate description of the source distribution. Accounting for effects such as humidity and microphone directionality requires the distance and the direction to the noise source with respect to the nearfield microphone. Once nearfield data is corrected, it can be compared to farfield data through a method developed by Ahuja et al. [11] to extrapolate data between the two regions. This method uses the geometry between the measurement locations and the source locations to extrapolate the nearfield sound measurements to the farfield and vice versa.

Applications like those listed above have led researchers over the years to develop numerous methods for the determination of jet noise source location. Prior to 1985, several methods for determining jet noise source locations were explored, which included acoustic mirrors, microphone arrays, two microphone methods, causality correlation and coherence techniques, nearfield contour surveys, and automated source breakdown. More recently, there have been developments in the microphone array, notably acoustic beamforming [6, 12–14], and in two microphone method techniques [15]. Most of the older techniques, while they would successfully produce source location results, require significant amount of time to acquire data at each jet condition; this requirement is often caused by the necessity to move microphones, while the jet is running on condition, to obtain source locations at all frequencies.

One of the newer methods, beamforming, was first developed for detecting electromagnetic sources via RADAR, but has since been adapted to locate sound sources with an array of microphones. The acoustic beamformer, also referred to as an acoustic phased array, uses an array of microphones to locate the origin of a sound source. The sound from a noise source reaches each microphone at slightly different times based on the location of the microphone and the source; thus, there is a time lag dependence on each microphone's

relative distance from the source. As mentioned before, acoustic beamforming is still a relatively new method for locating sources of jet noise and, as a result, the validation of this technique for jet noise source location is one of the main drivers of this work.

While performing the literature review detailed in chapter 2 of this work, it became clear that there are a few gaps in the field of jet noise source location that still need to be filled in. For example, there has been no study that examines how a noise source distribution of a subsonic jet is affected by the size of the nozzle exit boundary layer. Likewise there is an absence of fundamental studies that examine the noise source distributions of shock-containing supersonic jets and twin jets. Thus, the additional motivations of this work are to address these gaps.

1.2 Objectives

The primary objective of this thesis is to determine how well the acoustic beamforming technique compares with existing methods when measuring the locations of sources of various frequencies in a jet. To accomplish this, the source location data acquired by beamforming is compared with the data acquired with other jet noise source location methods.

The secondary objectives of this work are to examine and understand the noise source distributions of jets under various conditions:

- as a function of Mach number and diameter for subsonic round jets,
- as a function of nozzle boundary layer thickness for subsonic round jets using ASME and conical nozzles,
- as a function of fully-expanded Mach number and diameter for supersonic round jets,
- and as a function of separation distance for subsonic twin round jets.

1.3 Expected Contributions to the State-of-the-Art

This work contributes to the state-of-the-art of jet noise source research in several ways, the first being:

- the first study to compare the acoustic beamforming technique with another well-established technique, nearfield noise contours, for jet noise source location using the exact same nozzles and using facilities that have similar upstream piping.

As mentioned previously, using the same nozzles and same facilities for jet noise research removes any uncertainty in a comparison of data that may result from factors outside of the source location methods themselves. While the facilities in this work are different for each method, both facilities have plenum chambers and downstream piping that are exactly the same as the other.

The next contribution to the state of the art is as follows:

- the first study to analyze changes in the subsonic noise source distribution due to changes in the nozzle exit boundary layer.

Because different nozzle geometries, namely conical and ASME converging nozzles, can have vastly different exit boundary layers, it is important to categorize how such changes affect the jet's source location.

The final two contributions are for more complex jet conditions and configurations: subsonic twin jets and shock-containing supersonic jets.

- the first study to examine the noise source distributions of subsonic twin jets and examine how they are impacted by source location resolution

- the first study to examine the noise source distributions of shock-containing supersonic jets

Both of these cases have noise source distributions that are very different from that of a single subsonic jet. The examination of these different conditions and geometry will be beneficial to future researchers for when they attempt to design quieter aircraft engines. Additionally, examining how the noise source distributions of these more complex cases of jet noise are affected by measuring resolution is a good reference for future studies performing the same type of experiments.

1.4 Thesis Outline

This thesis is divided into nine separate chapters. The next (second) chapter contains a detailed overview of the state-of-the-art for jet noise research, with specific emphasis placed on jet noise source location. This is followed by a detailed description of the facilities and testing procedures used for this thesis in Chapter three. Chapter four contains the backbone of this thesis; it presents a comparison between the acoustic beamformer and other techniques for jet noise source location as well as an analysis of how source location uncertainty affects jet noise applications. Chapters five through seven detail three different jet-noise source location cases: nozzle geometry effects on subsonic jet-noise source location, subsonic twin jet noise source distributions, and supersonic noise source distributions, respectively. Following these three chapters, which make up the essence of the contribution of the present work, chapter eight contains the uncertainty analysis of this work. Finally, chapter nine summarizes the findings and contributions of the present work. It also provides a list of suggestions for future work.

CHAPTER 2
LITERATURE SURVEY

Jet noise source location has been obtained in one form or another since at least the 1950's. This chapter summarizes much of the work that has been accomplished since then. The chapter is split into four parts: a very brief summary of jet noise theory, an overview of published jet noise source location methods, a summary of the results of these jet noise source location studies, and some concluding remarks by way of identifying the missing gaps in the literature. The main focus of this chapter is placed on the different source location techniques and the results therefrom. Some nomenclature used by the various studies described in this chapter differs from the nomenclature used in this work. When this is the case, the additional symbols are not listed in the nomenclature section of this work but are instead described in text.

2.1 Summary of Jet Noise Theory

One could spend hundreds of pages summarizing the various incarnations of published jet noise research. Only a very brief summary is provided below, as to connect them with the distributions of noise sources of different frequencies that are located along the length of a typical jet.

Since the 1950s, Lighthills Acoustic Analogy [16–18] and its many variants have been the basis of dominant jet noise theories. Simply put, the Acoustic Analogy states that aerodynamic sound sources can be divided into three different types of sources: the monopole, due to fluctuating mass; the dipole, due to fluctuating force; and the quadrupole, due to fluctuating stress.

The main outcome of Lighthill's theory for subsonic jet noise can be summarized as

follows: (1) the acoustic power of the jet varies approximately by jet velocity to the eighth, (2) the jet noise spectra is very broad (covered a wide range of frequencies) and has a peak value around $\frac{U}{2D}$, (3) most of the sound radiates downstream of the jet, (4) high frequency sources seem to emanate from near the nozzle exit and propagate at most 45 degrees from the nozzle axis, and (5) low frequency sources seem to emanate from five to twenty diameters downstream from the nozzle exit and have a much smaller maximum propagation angle. It is well accepted that the mixing layer of a jet is comprised of turbulent structures that form near the nozzle exit, and grow in size as they propagate downstream at some convection Mach number. Lighthill hypothesized that the sound that propagates from these structures can be modeled as lateral quadrupoles. These quadrupoles are oriented such that they are aligned with the principal axis of the mean rate of strain (this is 45 degrees to the direction of motion of the structure); however, the sound field of these quadrupoles are distorted due to the structures convecting along the jet, resulting in more sound propagation downstream than upstream. These structures also generate noise of different frequencies depending on their size; smaller structures produce higher frequency noise and vice versa. This results in a source location distribution in which the highest frequency sources are generated near the nozzle exit and the lowest frequency sources are generated downstream.

Laufer et al. [19] and Schlinker [20] proposed a model for supersonic jets based on experimental evidence that consists of two different sources of jet noise. They noted that the noise radiated downstream of the jet and in the sideline were distinctly different. After examining supersonic and subsonic jet data, in 1996 Tam et al. [21] proposed that these separate sources of noise were made up of (1) the fine scale turbulence and (2) the large turbulent structures. They accomplished this by developing two separate similarity spectra, one for fine scale turbulence and one for large turbulent structures, and comparing them with measured spectra from a large number of experiments in the field. A good example of one of these comparisons is shown in Figure 2.1, noting that the figure comes from a 2006 paper by Tam et al. [22]. Figure 2.1(a) shows that the data Schlinker acquired in the max-

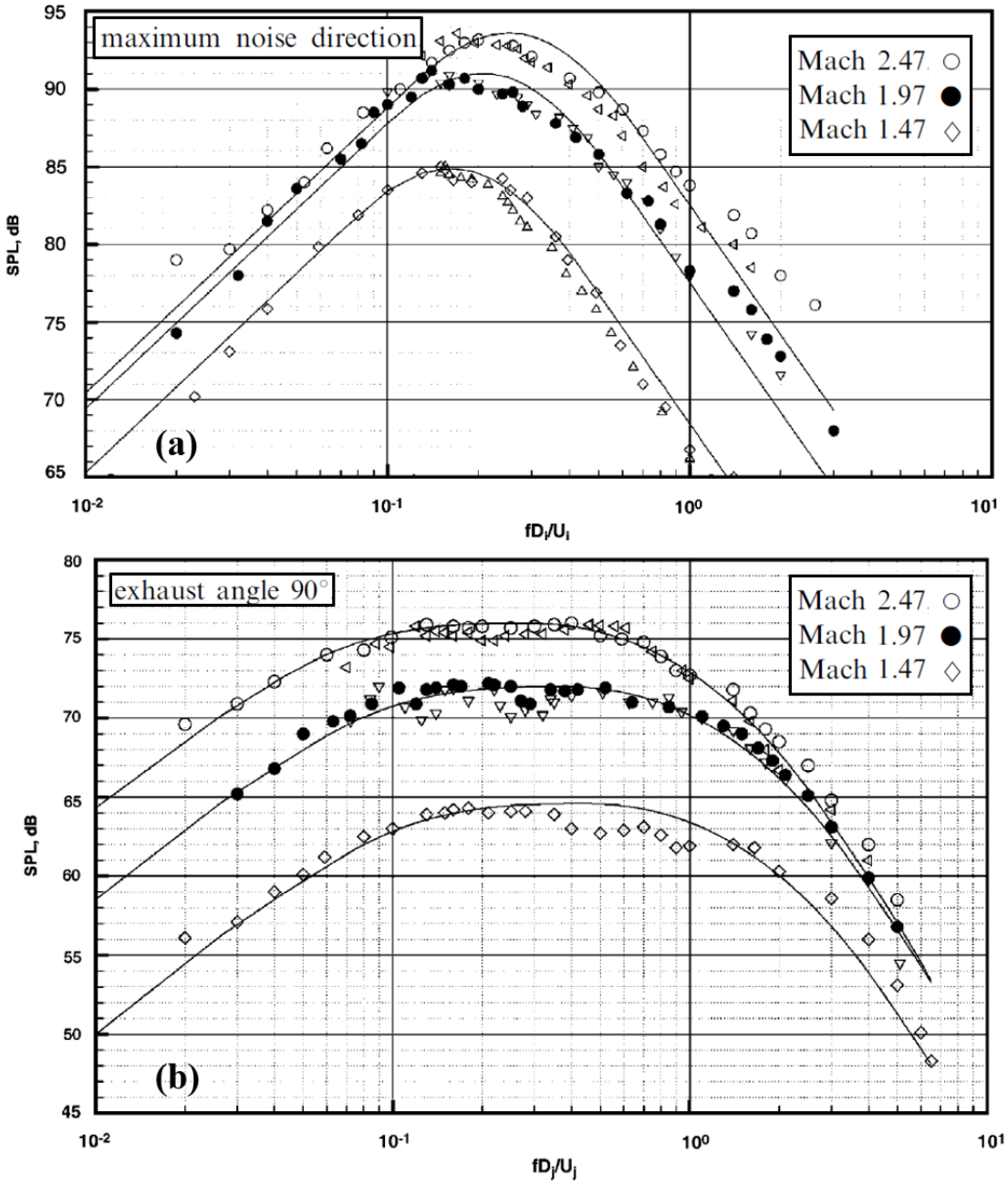

Figure 2.1: A comparison of similarity spectra for three supersonic jet conditions: Mach 2.47, Mach 1.97, and Mach 1.47. (a) Data from the maximum noise direction (45.0°, 37.5°, and 32.5°, respectively) compared with similarity spectra of large turbulence structures. (b) Data from the 90 degree direction compared with similarity spectra of fine scale turbulence. Data points are from supersonic tests performed by Schlinker [20], the plot and similarity spectra are from Tam el al. [22].

imum downstream direction matches the similarity spectra of large turbulent structures. Similarly, Figure 2.1(b) shows that the data acquired in the sideline of the jet matches the similarity spectra of fine scale turbulence. Similar comparisons were made for subsonic jet noise and excellent agreement was found. In 2008 Tam et al. [23] performed a detailed study that used single microphone farfield measurements, two-microphone farfield correlation measurements, correlations of jet noise fluctuations, and noise source distribution data to further confirm that this is indeed the case.

2.2 Jet Noise Source Location Methods

2.2.1 Nearfield Contour Surveys

Nearfield contours are one of the earliest methods used for jet noise source location. Nearfield contour surveys require sound to be recorded at several measurement points in space in a plane that contains the jet axis. This can potentially be achieved quickly by using many stationary microphones; however, the presence of many microphones adjacent to one another disturbs the very noise the microphones are supposed to measure. As such, typically a single microphone is traversed in space instead while maintaining the jet operating condition as steady as possible. Once recorded, contours of constant sound pressure level are generated throughout the measurement space for each individual frequency bin. Jet noise source location can be obtained by tracing a line through the contour peaks and finding the intersection with the jet axis as shown in a typical near field contour obtained by Westley and Lilley [24] in 1952 (Figure 2.2).

Westley and Lilley [24] traversed a single microphone along the length of a jet axis, with the microphone pointing normal towards the jet axis, to generate noise contours for a small jet. They examined the noise contours for a one-inch jet at pressure ratios of 0.9 and 1.33 for octave bands at frequencies below 12,800 Hz. Using their contours, Westley and Lilley noted that, for a given octave band, the noise source seems to be distributed

along the jet axis. These distributions would be longer and extend further downstream for lower frequencies and their lengths seemed to be proportional to the jet velocity. They concluded that the maximum strength of these distributions were located near the end of the distribution. These results can be seen illustrated for the 6,400 Hz to 12,800 Hz octave band in Figure 2.2 and for the 3,200 Hz to 6,400 Hz octave band in Figure 2.3; the lower frequency noise as shown in Figure 2.3 appears to be located further downstream than that in Figure 2.2. Westley and Lilley concluded that the noise sources appear to behave as

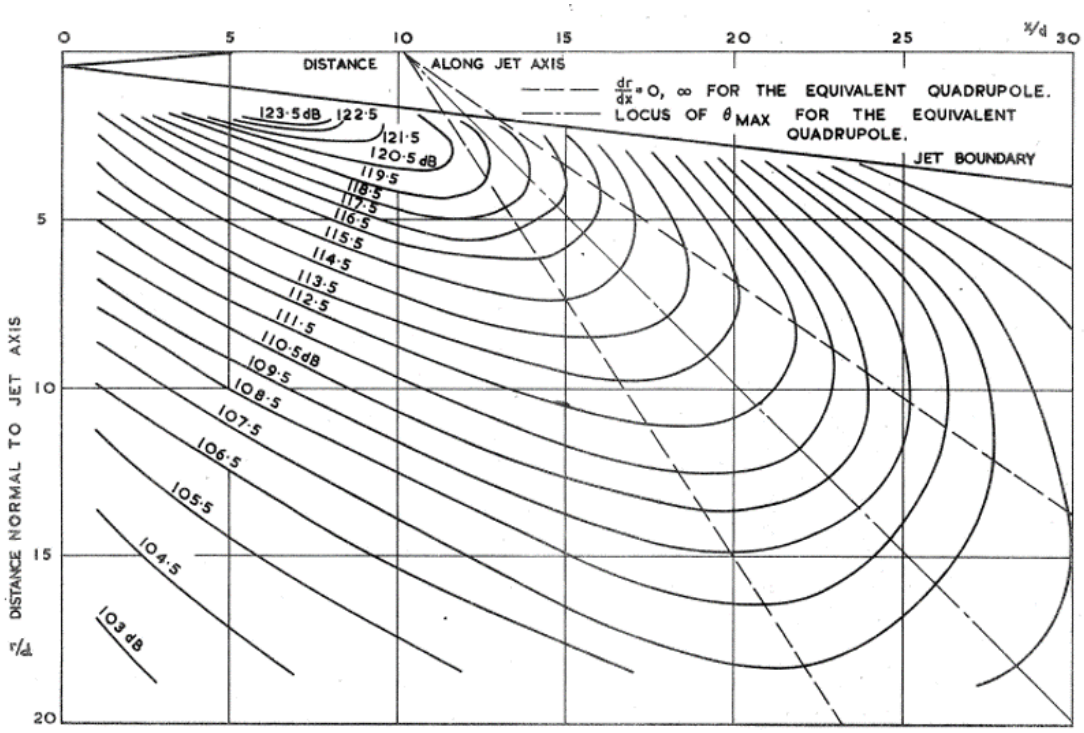

Figure 2.2: 6400-12800 Hz octave band nearfield contours for a one-inch jet with an operating pressure ratio of 0.9 [24].

lateral quadrupoles from Lighthill's theory, noting that the conclusion was difficult to make for the lowest frequency sources due to their long extent making seeing any directionality in their contours difficult.

In 1971, Yu and Dosanjh [25] used nearfield contours to examine the noise field of a jet produced by a converging-diverging nozzle of design Mach number 1.5 at both shock-free and underexpanded conditions. Yu and Dosanjh examined both the noise contours for the

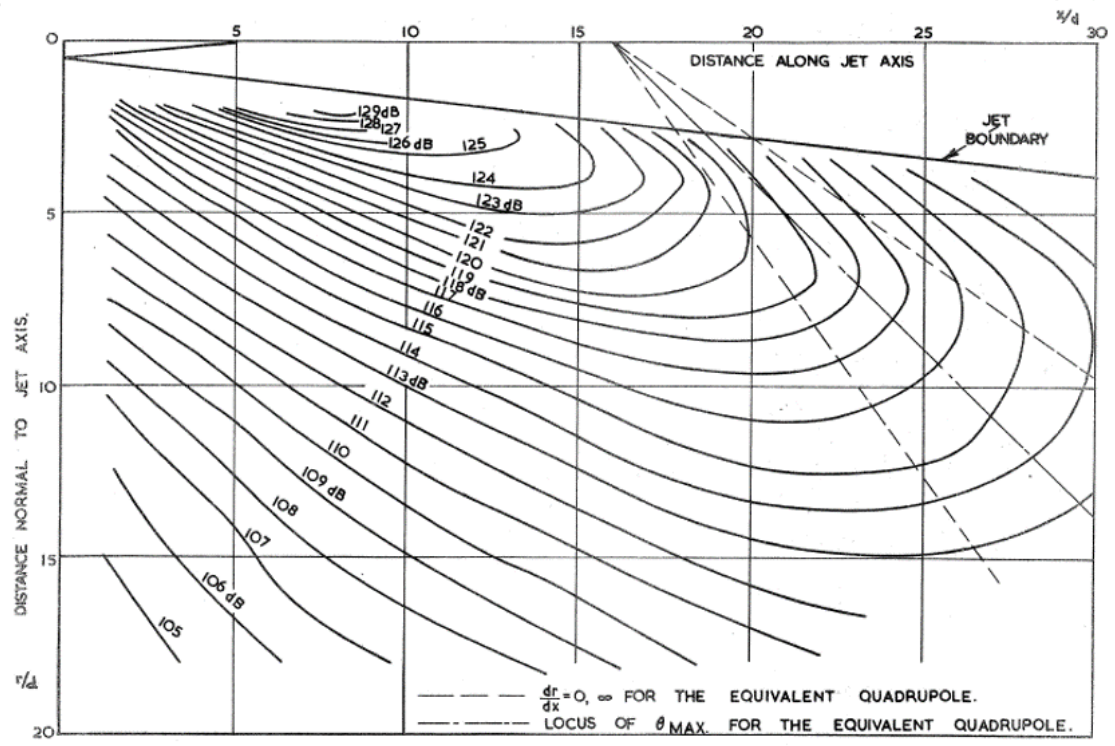

Figure 2.3: 3200-6400 Hz octave band nearfield contours for a one-inch jet with an operating pressure ratio of 0.9 [24].

OASPL of the jet, as shown in Figure 2.4, and for 1/3 octave frequencies, as shown in Figure 2.5. They saw that at both jet conditions there appeared to be two distinct lobe

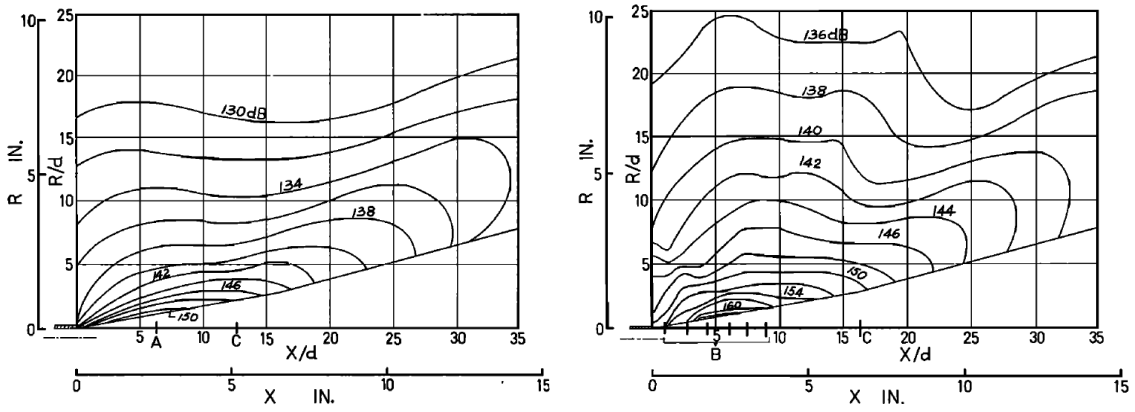

(a) Shock-free jet (b) Underexpanded jet

Figure 2.4: Nearfield OASPL noise contours. (a) shock-free. (b) underexpanded. A: location of laminar core tip. B: approximate location of shock cells. C: location of supersonic core tip [25].

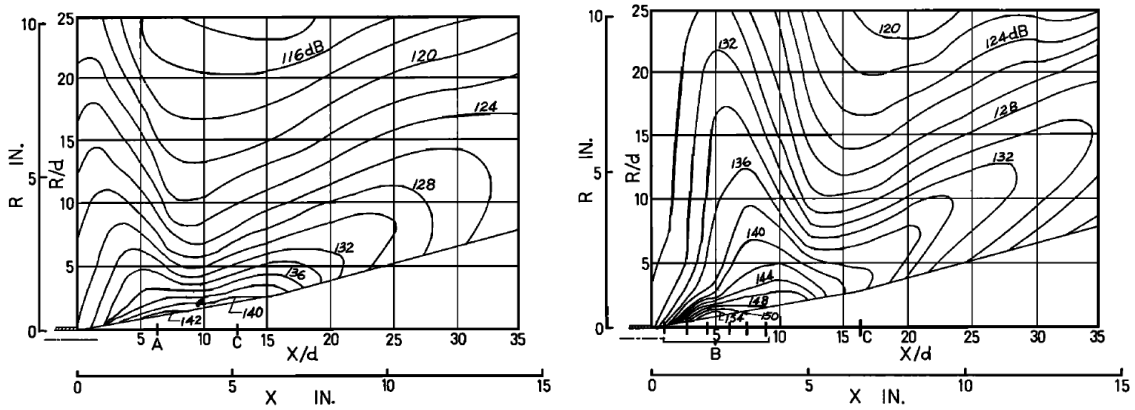

(a) Shock-free jet (b) Underexpanded jet

Figure 2.5: Nearfield 1/3-octave-band noise contours. (a) shock-free, f_o = 20kHz. (b) underexpanded, f_o = 20kHz. A: location of laminar core tip. B: approximate location of shock cells. C: location of supersonic core tip [25].

patterns: one in the 30 degree direction and one normal to the jet axis. The sources of these patterns appeared to be located between the laminar core tip and the supersonic core tip of the jet, which are marked as “A” and “C” on the plots, respectively. The locations of shocks are indicated with vertical lines and are marked by the letter “B”. From the OASPL

contours, the contour levels in these directions were much lower at a given location for the shock-free jet condition (shown in Figure 2.4a) than for the underexpanded condition (shown in Figure 2.4b). Yu and Dosanjh state that, for the underexpanded jet, the increase in noise in the normal direction is due to shock noise and the increase in the 30 degree direction is due to the enhanced mixing from the shocks. The 1/3 octave contours are very similar between these two jet conditions for frequencies below 5 kHz and above 100 kHz. However between these two frequency values, the 1/3 octave contours show similar differences between the two jet conditions as the OASPL contours. This can be seen in Figure 2.5, both conditions have contour lobes normal to the jet axis and in the 30 degree direction; the underexpanded jet condition has larger contour values in these lobes. Yu and Dosanjh plotted the source location distributions for the two jet conditions (where ξ is the nozzle pressure ratio) as shown in Figure 2.6. They found that the underexpanded jet had

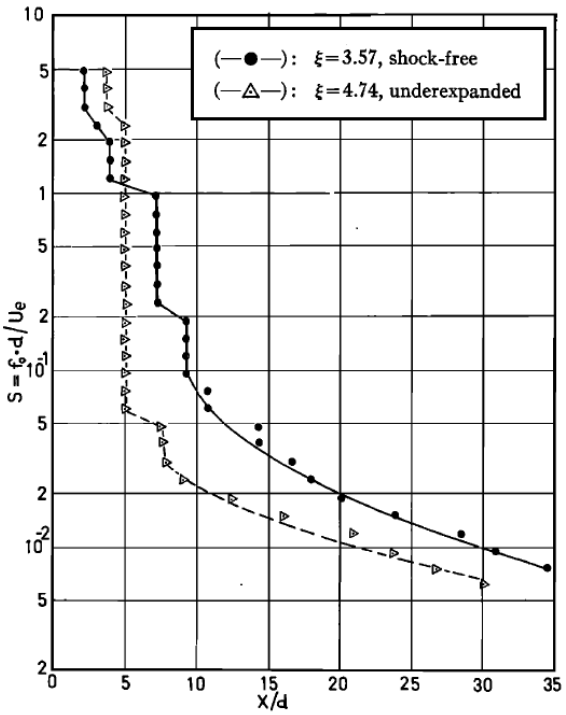

Figure 2.6: Location of the 1/3-octave-band noise sources of a supersonic jet [25].

noise sources further upstream than the shock-free jet, which they proposed was due to enhanced mixing caused by the presence of shocks in the underexpanded jet.

2.2.2 Acoustic Mirror Methods

In 1972 Chu et al. [26] presented a method of jet noise source location that used a spherical concave reflector and noted that other source location methods at the time were either too qualitative or too involved. This method places an acoustic reflector, also called an acoustic mirror, some distance, R, from the jet axis with a microphone at the reflectors focus. Based on the size and geometry of the reflector, only sound from a small section of the jet is reflected by the reflector and focused into the microphone; this allows the researcher to scan specific points of the jet for its sound sources. Chu et al. used a three foot diameter spherical reflector located 82 inches from the jet axis to measure the source distributions of one-inch and two-inch diameter nozzles operated at Mach 1. This method often requires moving the reflector to measure different parts of the jet; Chu et al. partially overcame this limitation by only placing their reflector at two fixed positions downstream of the nozzle (four and nine diameters) and then rotating it to achieve a finer resolution.

For given frequency bands, Chu et al. plotted how the noise strength ($W'/4\pi R^2$) is distributed along the jet axis as shown in Figure 2.7. As they expected and as shown in Figure 2.7, their method showed that the higher frequency noise sources are located closer to the nozzle exit for subsonic jets.

2.2.3 Causality Correlation and Coherence Techniques

Fisher et al. [27] developed a jet noise source location method known as the Polar Correlation Technique. To describe this method in the simplest terms, imagine two microphones located in the far field, on a polar arc of radius r_o and centered on a jet nozzle exit as seen in Figure 2.8. The separation angle between the two microphones, one of which is aligned 90 degrees with respect to the jet axis and is always fixed at that location (called the "fixed microphone"), is denoted by α shown in Figure 2.8. The second microphone (called the "traversable microphone") can be traversed along the polar arc. In practice, traversing a single microphone is very time consuming and often several microphones evenly spaced

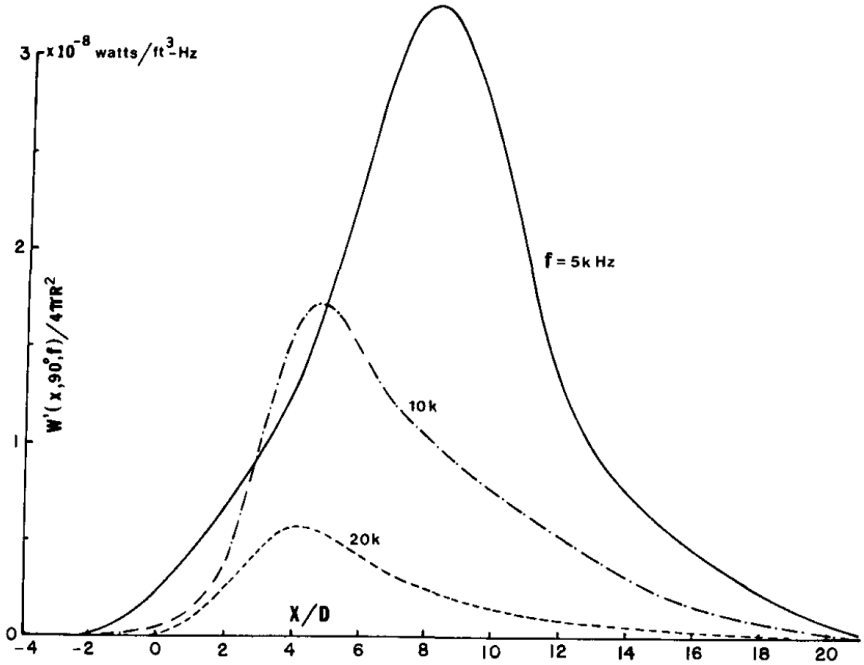

Figure 2.7: Noise source strength distributions for a one-inch jet operated at Mach one [26].

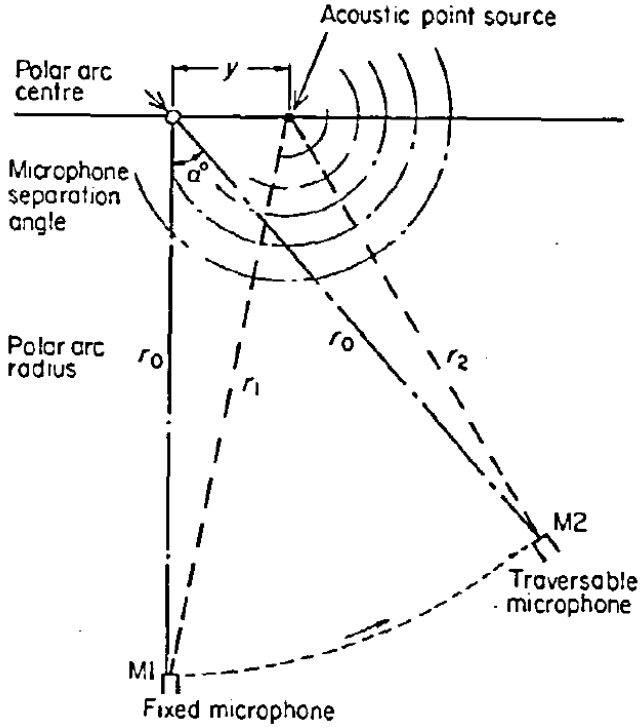

Figure 2.8: Simplified geometry for the Polar Correlation Technique where $r_o >> y$ [27].

along the arc are used instead. The two microphones record the sound generated by a harmonic point source located a distance y from the nozzle exit along the jet axis.

The cross correlation between the two microphones is taken for every measurement location of the traversable microphone. For zero time delay ($\tau = 0$), the cross-correlation between the two microphones is shown in Equation 2.1 below.

$$C(\alpha, \omega, \tau = 0) = \frac{A^2}{2r_o^2} \cos\left(\frac{\omega y}{c} \sin\alpha\right) \tag{2.1}$$

In the above equation, all variables refer to the ones depicted in Figure 2.8. With this equation, Fisher et al. show that the cross-correlation between these two microphones vary sinusoidally as a function of $\sin\alpha$, and the frequency ($\frac{\omega y}{c}$) of this relationship is a function of the location of the noise source with respect to the center of the polar arc.

Multiple uncorrelated noise sources operating simultaneously, but at different locations, result in a cross-correlation function that is a sum of the cross-correlation functions of the sources if they were operated individually. As each of these sources contribute a different frequency based on their location, Fourier analysis can be applied to the total cross-correlation function to obtain each source's amplitude and position. For a given frequency, the source strength ($S(y, \omega)$) can be calculated as a function of position as seen in Equation 2.2 below, where $k = \frac{\omega}{c} \sin\alpha$, $k_m = \frac{\omega}{c} \sin\alpha_m$, and τ_p is the time delay between the two microphones for a given frequency.

$$S(y, \omega) = \frac{1}{2\pi} \int_{-k_m}^{k_m} C(\alpha, \omega, \tau_p) \cos\left(\omega\tau_p - ky\right) dk \tag{2.2}$$

These source strength distributions can then be used to determine the source location of a particular frequency; this is usually accomplished by taking the centroid of the distribution to be the source location.

This method is very simple if the jet is assumed to be comprised of uncorrelated omni-directional sources; however because this is rarely the case in jet noise, the method becomes

much more complex as more general source models are used to derive the cross correlation relationships. For the noise sources in a jet, Fisher et al. used an equation similar to Equation 2.2, but instead the equation is more tailored to the noise sources that occur in a jet; this relation can be seen in Equation 2.3.

$$S(y,\omega) = \frac{p_1(\omega)}{\pi} \int_0^{k_m} R(\alpha,\omega,\tau_p)\cos(\omega\tau_p - ky)dk \tag{2.3}$$

In the above equation, p_1 is the power spectral density of the reference microphone and $R(\alpha,\omega,\tau_p)$ is the cross-correlation coefficient amplitude function of the two microphones. It is these two terms that account for the directivity of jet noise sources and no longer treat them as monopoles, as was shown in Equation 2.2.

Applying Equation 2.3 to data acquired from a one-inch jet operating at Mach 0.8, Fisher et al. obtained the source strength distributions for four different Strouhal numbers as seen in Figure 2.9. Similar to the acoustic mirror method by Chu et al. [26], the Polar Correlation Technique shows that noise sources of a given frequency are not point sources, but have a finite extent downstream. The lowest Strouhal number source was not resolved

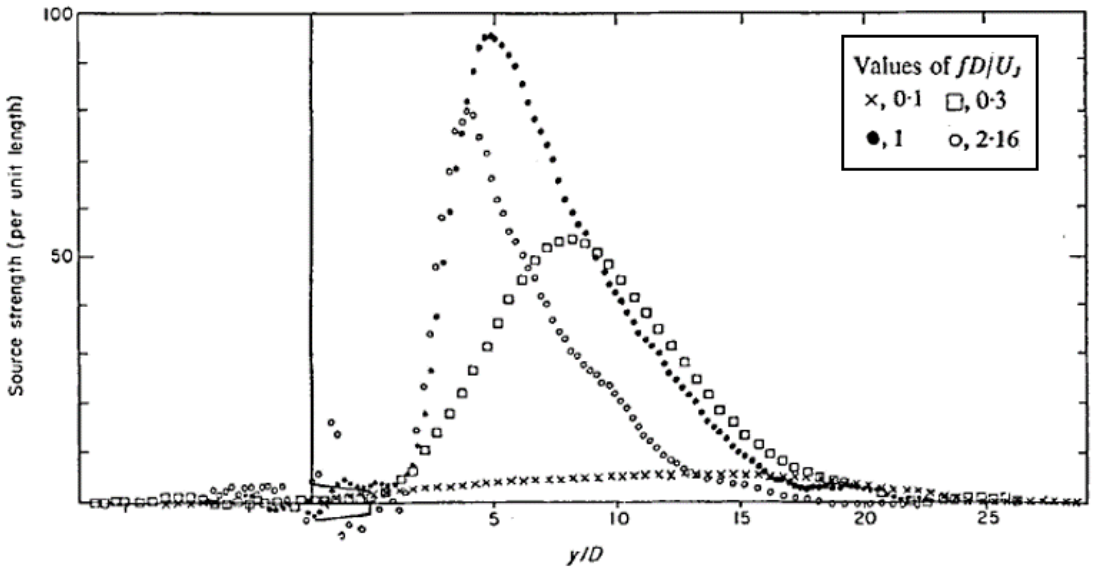

Figure 2.9: Acoustic source strength at different jet locations for various Strouhal numbers, calculated using the Polar Correlation Technique [27]. ($D = 1$ in, $M_j = 0.8$)

well by the method, as the acoustic wavelength was very large. The noise source distributions for the two highest Strouhal number sources, on the other hand, were well resolved and did not display symmetry around their peak values. This lack of symmetry, where the source strength increases sharply near the nozzle exit and gradually tapers off downstream, results in the centroid of the distributions to be further downstream than their peak value.

For a given acoustic wavelength, the resolution of the Polar Correlation Technique for source location is limited by the maximum angle obtained with the second microphone on the polar arc. The best resolution is obtained when the secondary microphone can be shifted between ± 90 degrees with respect to the reference microphone; this results in a resolution of one acoustic wavelength (λ). In reality, the maximum possible angle, $\pm\alpha_m$, is usually less than 90 degrees, which results in a more coarse resolution of $\frac{\lambda}{\sin \alpha_m}$. The resolution limits how close two similar noise sources can be and still have the method detect them as individual sources.

2.2.4 Automated Source Breakdown Techniques

The accuracy of the Polar Correlation Technique is limited by the design of the microphone arc used in testing. Tester and Fisher [28] note that due to the finite region of measurement, multiple sources at a single frequency start to blend together at lower frequencies, and due to only measuring discrete numbers of locations in the arc, aliasing becomes an issue at higher frequencies. Figure 2.10 illustrates, through the use of simulated sources, how the resolution of this technique decreases with frequency. Tester and Fisher noted that, in the case of the 600 Hz sources in Figure 2.10b, each source can be located; however the sources' images have begun to overlap, making determining each sources' individual contribution difficult to determine. The images of the lowest frequency sources, shown in Figures 2.10c and 2.10d, have completely merged, rendering the individual locations and contributions of each source impossible to determine from the given figure. Tester and Fisher state that, for the Polar Correlation Technique, the lowest frequency, f_l,

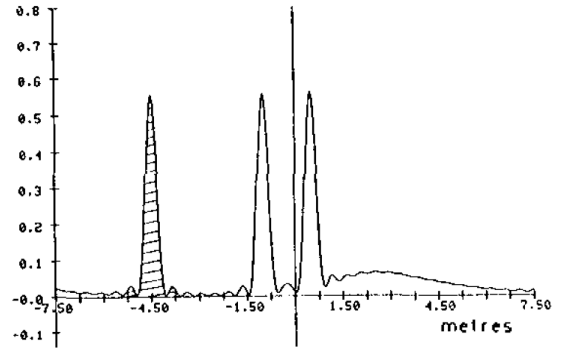

(a) Source image at 1500 Hz

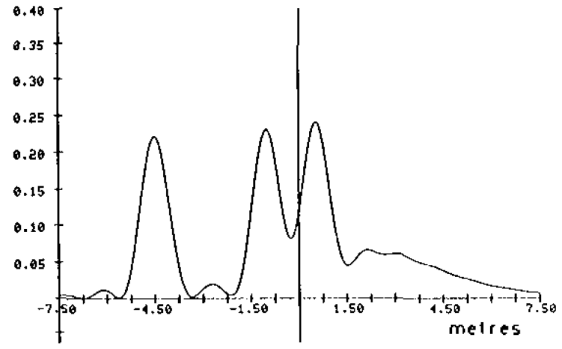

(b) Source image at 600 Hz

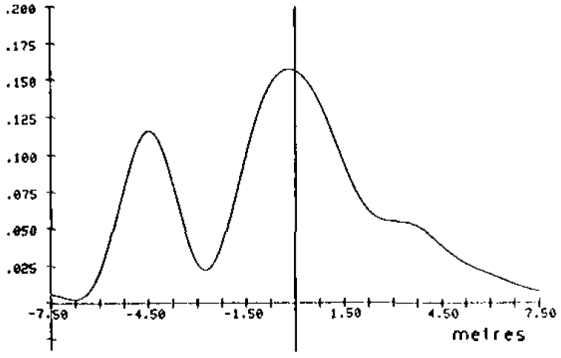

(c) Source image at 300 Hz

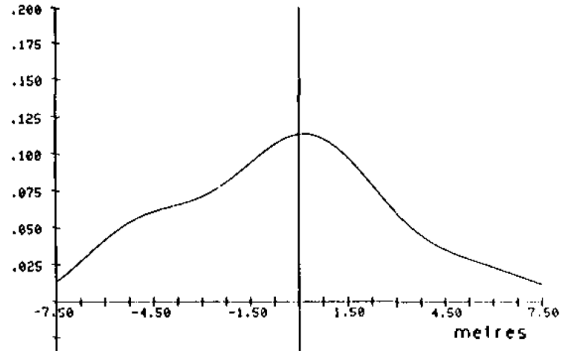

(d) Source image at 150 Hz

Figure 2.10: Source images generated from simulated sources of different frequencies by Tester and Fisher [28]. Low frequency sources that are in close proximity with each other cannot be resolved.

that can be resolved when the sources are a distance, l, apart is a function of the maximum aperture, α_m as shown in Equation 2.4.

$$f_l \sim \frac{c}{l \sin \alpha_m} \tag{2.4}$$

The upper frequency limit of the Polar Correlation Technique is due to aliasing and is a function of microphone angular spacing, $\Delta\alpha$, as shown in Equation 2.5,

$$f \leq \frac{c}{L \sin \Delta\alpha}, \tag{2.5}$$

where f is the highest frequency that can be measured and L is the length of the region of interest.

To combat these issues, Tester and Fisher modified the method to automatically separate out the different sources of noise. They argue that the principal application of "source location" techniques is not locating the noise sources in space, but determining how different noise sources contribute to the farfield noise. The modification is achieved by assuming that the measured cross spectra are generated by a fixed number, n, of mutually incoherent point sources; taking n measurements of cross spectra allows for n equations that can be solved for the individual source strengths. Their method was not fully automated however, the locations of the different sources must be provided in order to solve for the strengths. They found that errors in these locations had little effect on the source contributions of mid-to-low frequencies. At higher frequencies where source location errors have a larger effect, Tester and Fisher coded the method to optimize the source position with respect to the measured source image.

Battaner [29] similarly modified the Polar Correlation Technique by using a process known as Matched Field Processing to automatically compare advanced jet noise models to test measurements, completely removing any human subjective element from the method. For single jets, Battaner modeled the source locations as a single distributed source that

originates at the nozzle exit (somewhere near the center of the polar arc). These models were validated by using a Barlett processor on the acquired data; essentially turning the polar arc into a beamformer to obtain source location information and comparing it with the model. The validated models are then used in the Polar Correlation Technique to determine the different source contributions of the jet.

Battaner applied this method on both coannular and single jets. For conannular jets, Battaner used the Four Sources Model that was developed by Fisher and Preston for the jet noise model. This model breaks the contributions of a conannular jet into four different "single" jet components and sums them together: the secondary/ambient shear layer, the primary/secondary shear layer, the primary ambient shear layer, and the mixed/ambient shear layer. Battaner ignores the contributions of the primary/secondary shear layer as its relative contribution to the overall noise is minor.

2.2.5 Two Microphone Methods

Ahuja et al. [15] developed the Phase Minimum technique to measure source locations in subsonic jets, most notably in jets with simulated forward motion. The Phase Minimum technique uses the cross correlation between a microphone pair that can be traversed parallel to the axis of the jet as depicted in Figure 2.11. The microphones are traversed beneath the jet, one microphone under the other, until the minimum phase for a given frequency is found between the two microphones; this location is directly under the source. The minimum phase occurs at this location due to the difference in the sound propagation path between the two microphones being at a maximum at this point. Phase data between the two microphones for a 128 Hz source from a one inch jet operated at Mach 0.89 is shown in Figure 2.12. From this plot, the source location of the 128 Hz frequency can be said to emanate from about six inched from the nozzle exit. It is worth noting, that the phase is minimum at this location because Ahuja et al. used the furtherest microphone as the reference microphone; switching which microphone is the reference would result in a phase

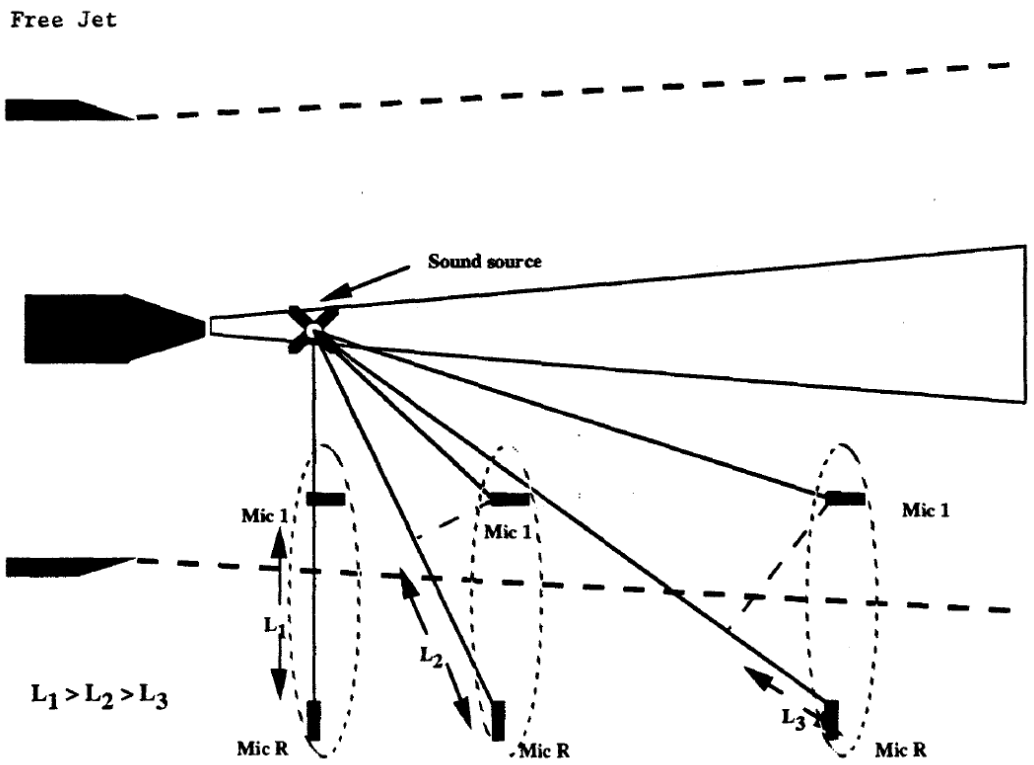

Figure 2.11: Methodology behind the microphone spacing in the Phase Minimum Technique. The maximum distance between the two microphones occurs when the pair is right underneath the noise source, resulting in a minimum phase difference between the two microphones [15].

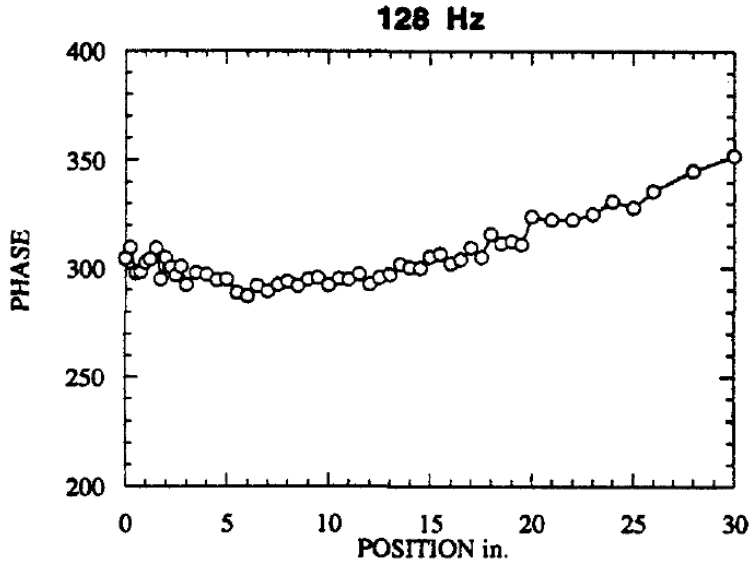

Figure 2.12: Phase difference between the two microphones as a function of downstream position [15]. ($M_j = 0.89, D = 1in$)

maximum at this point. It then can be said that the Phase Minimum Technique, contrary to its name, uses the location of maximum phase difference between the two microphones to determine jet noise source location. Ideally this technique should be referred to as the "Phase Extrema Technique." Ahuja et al. also developed this method to work with jets under flight simulation effects; as illustrated in Figure 2.11, one microphone is placed in the free jet and the other outside of the free jet for these types of tests. Because the microphones are oriented 90 degrees with respect to the flow direction, their measurements are not affected by refraction of sounds rays through the flight simulation jet shear layer.

Ahuja et al. applied the Phase Minimum Technique to a one-inch conical jet operated at Mach 0.89 and examined the effects of tabs and flight simulation on the noise source distributions of the jet. Figure 2.13 contains plots of Strouhal number vs. normalized axial location for the jet with and without tabs. The presence of tabs enhance the mixing of the

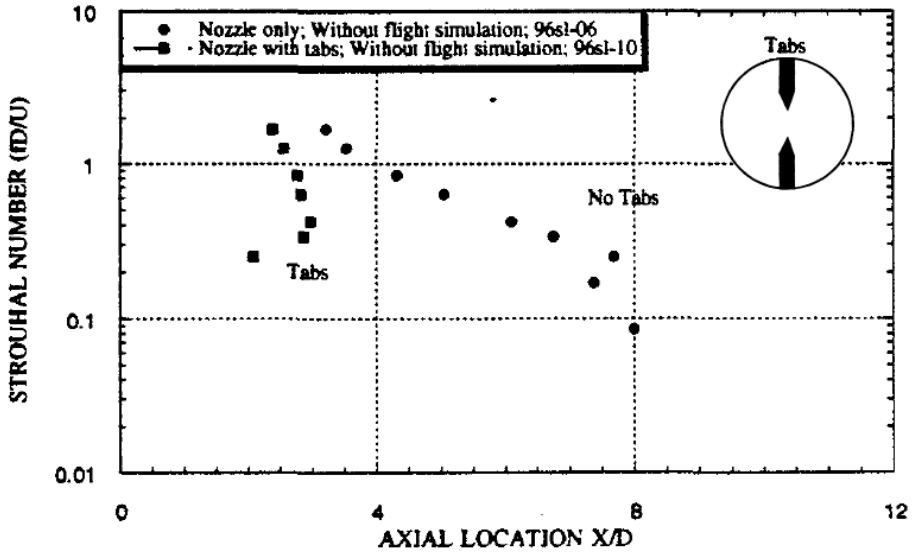

Figure 2.13: Effect of tabs on source location [15]. ($M_j = 0.89$, $D = 1$ in)

jet and reduce the length of the potential core. The reduction of the potential core shifts the noise sources closer to the nozzle exit. Ahuja et al. demonstrated this effect as well as showed that the lowest frequency noise sources shift more than the highest frequency sources due to the tabs. Figure 2.14 contains plots of Strouhal number vs. normalized axial

location for the jet with simulated flight effects of 115 ft/s, 175 ft/s, and 225 ft/s. Ahuja et al. show that, especially at the lowest frequencies, flight effects shift the noise sources of a jet further downstream. Higher velocity outer flows result in larger shifts in source location.

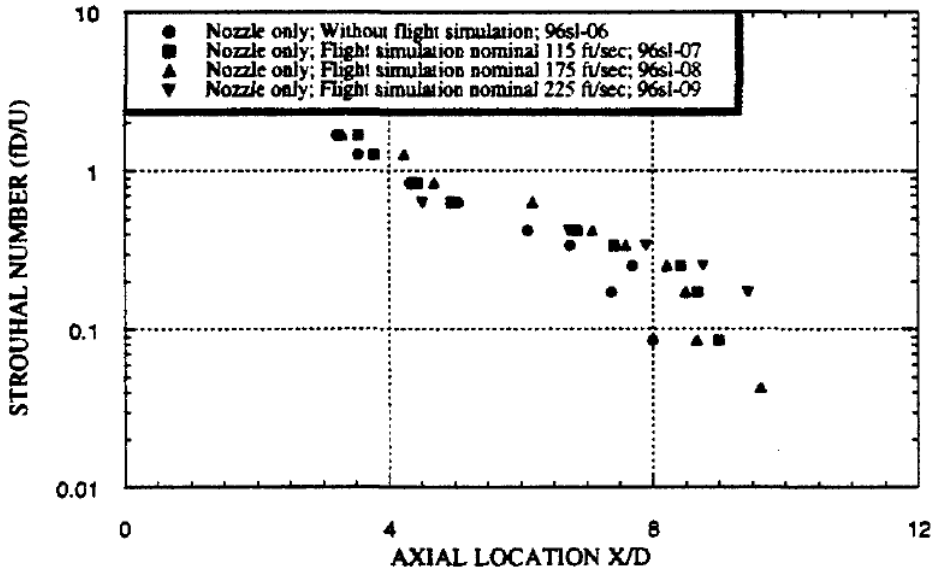

Figure 2.14: Effect of flight simulation on source location [15]. ($M_j = 0.89$, $D = 1$ in)

2.2.6 Phased Arrays

Acoustic phased arrays, or acoustic beamformers, have been used in wind tunnels as early as the mid 1970s [1, 30]. Around this time a phased array method, using a device called an acoustic telescope by Billingsley and Kinns [31], was developed for the use of jet noise. Since then, many advances have been made in acoustic beamforming technology, which is now routinely used in many aerospace applications such as estimating aircraft frame noise and engine noise [6, 12–14]. As mentioned in Chapter 1, an acoustic beamformer uses an array of microphones to locate the origin of a sound source. The sound from a noise source reaches each microphone in the array at slightly different times based on the location of the microphone and the source; thus, there is a measured phase difference for each microphone based on its relative distance from the source. By adjusting the

time lag for each microphone to correspond to a specific location in space, one can then scan through space to find the where the adjusted phase of the signal perfectly matches and cancels with the actual phase, thus locating the sound source. This description of the beamforming methodology is very much simplified; a detailed description can be found in Chapter 3 of this work.

Narayanan et al. [32] and Lee and Bridges [5] have both used linear phased arrays to examine the noise source locations of round jets. The linear phased array used by Narayanan et al. was composed of 36 microphones, had an aperture of 32.6 nozzle diameters, and was located 19.9 diameters from the jet centerline. The 18 microphones that were aligned closest to the nozzle exit were spaced 0.084 diameters apart, to better capture the high frequency noise sources, and the 18 microphones located more downstream were spaced 1.72 diameters apart, to better capture the low frequency noise sources. This array geometry resulted in a beam width at most five degrees for frequencies below 33 kHz with a sidelobe rejection of about 20 dB. Small values of beam width are critical for the accurate determination of source magnitude and location, whereas larger values of sidelobe rejection reduces the chances that sidelobes (artificial sources) mask the actual noise source. Narayanan et al. determined that with this array geometry, and only acquiring two seconds of data at each condition, the source location measurements of their jet were reliable within ± 1 diameters.

Narayanan et al. obtained the source locations for a 3.25 inch diameter jet operated at Mach numbers from 0.6 to 0.9. The source strength distributions of several Strouhal numbers (Sr) for the jet operated at Mach 0.6 are displayed in Figure 2.15. As illustrated in Figure 2.15, Narayanan et al. observed that the main contributions from low frequencies occur in the downstream region (five to ten diameters) and the main contributions from high frequencies occur close to the nozzle exit (zero to two diameters). They also observed that low frequency sources seem to be distributed over a large extent of the jet axis and have slow drop off in intensity.

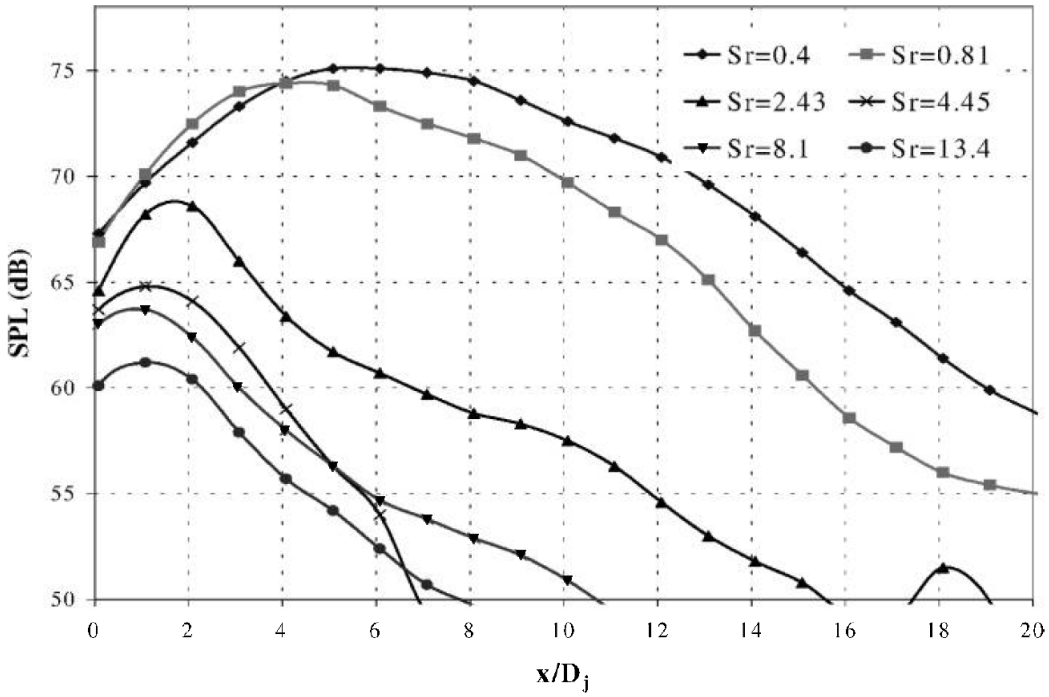

Figure 2.15: Noise source strength distributions for a $M_j = 0.60$, $D = 3.25$ in jet obtained with a linear phased array by Narayanen et al. [32].

The linear phased array used by Lee and Bridges [5] was comprised of 16 microphones, was placed about 25 nozzle diameters from the jet axis, and had an array aperture of 60 diameters. The microphones were unevenly spaced throughout the array, with closer spacing at the center of the array than the fringes. They used this system with conventional beamforming techniques to examine the source locations of a two-inch diameter jet operated at a range of subsonic and supersonic Mach numbers for both heated and unheated jets. For the unheated jets, Lee and Bridges observed that high frequency source location seemed to be independent of jet velocity and low frequency (Strouhal numbers less than 1.5) source location seemed to shift further downstream as the jet velocity was increased. This effect is illustrated by the two source location curves, one for a Mach 0.343 jet and the other for a Mach 0.891 jet, in Figure 2.16. The source locations measured with this method are the locations of the peak sound pressure level, not the centroid location as has been used by other methods such as the Polar Correlation Technique. This difference is important as, for many frequencies, the centroid is located one-to-two diameters further downstream than the

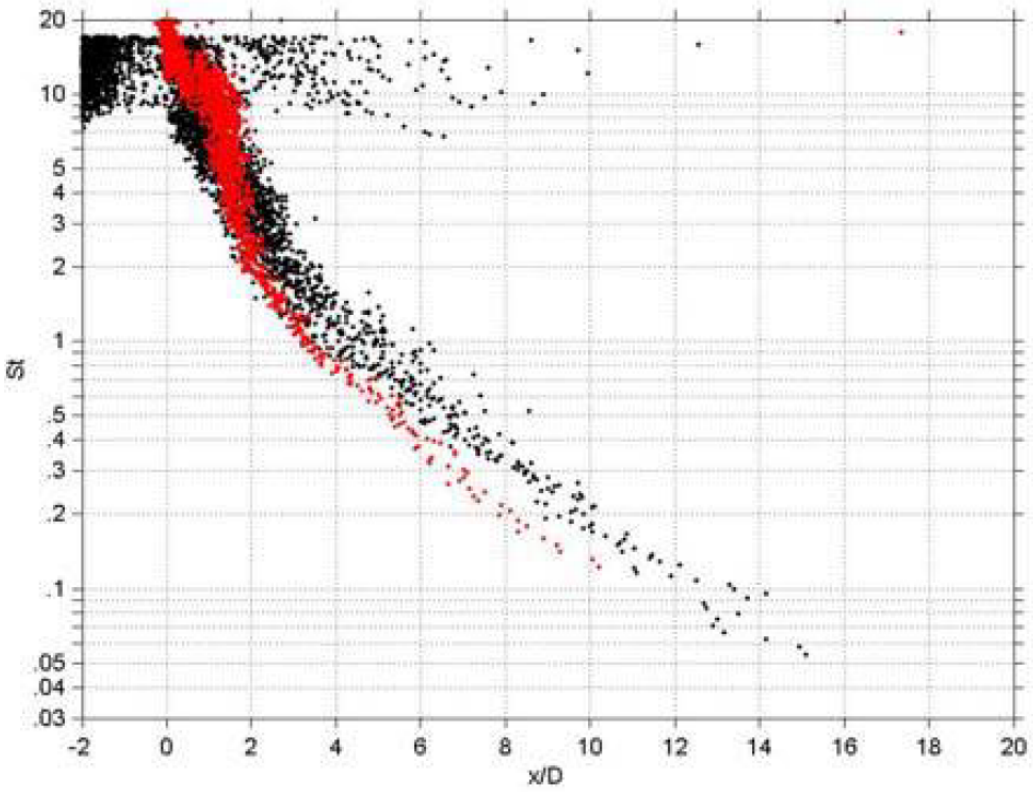

Figure 2.16: Source location curves as a function of Mach number for cold jets using a linear phased array by Lee and Bridges [5]. Red data: $M_j = 0.394$, $D = 2$ in, black data: $M_j = 0.891$, $D = 2$ in.

peak location. For the heated jets, Lee and Bridges observed that higher jet temperatures would shift the lower frequency noise sources upstream, without affecting the location of the highest frequency noise sources. This effect can be seen for a Mach 0.9 jet in Figure 2.17. The noise sources in both Figures 2.16 and 2.17, at Strouhal numbers above 10 and at

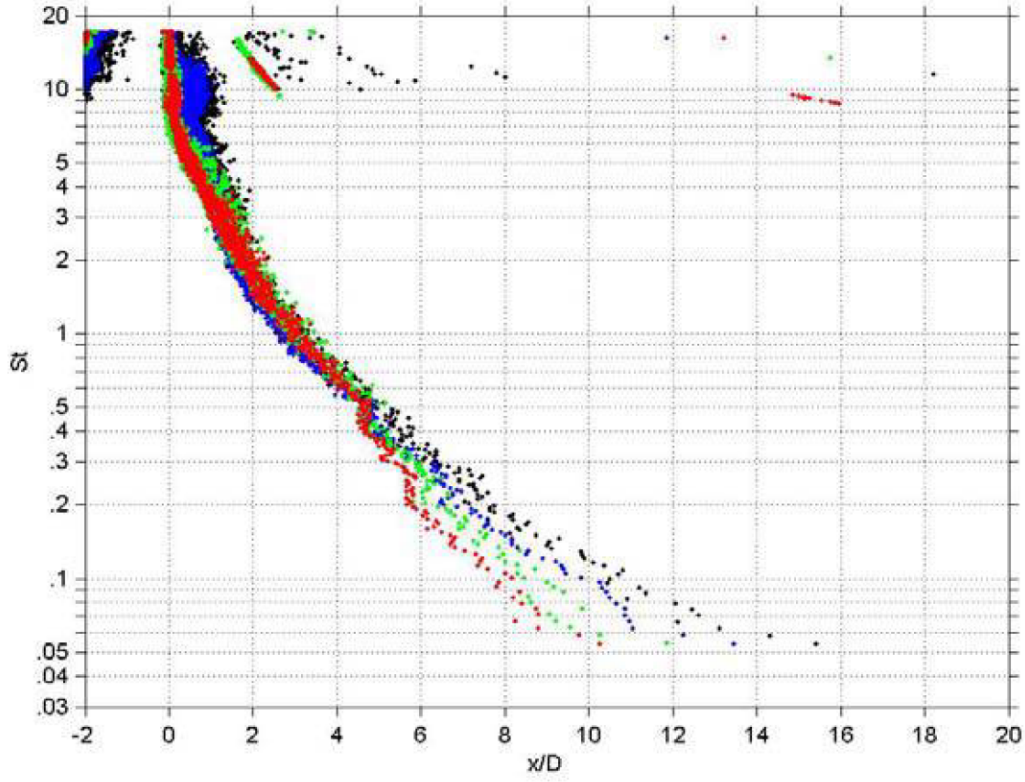

Figure 2.17: Source location curves as a function of static temperature ratio for a Mach 0.9 jet using a linear phased array by Lee and Bridges [5]. Black data: $\frac{T_{SJ}}{T_a} = 1.431$, blue data: $\frac{T_{SJ}}{T_a} = 1.764$, green data: $\frac{T_{SJ}}{T_a} = 2.271$, red data: $\frac{T_{SJ}}{T_a} = 2.699$.

x/D locations less than zero or greater than 2, are most likely the result of side lobes in the array's beam pattern. Side lobes are false noise sources that are functions of the measuring array's geometry and the frequency of noise being measured.

To reinforce their results, Lee and Bridges compared their cold-jet source location results with results from Narayanan et al. [32] and from other source location methods. They found that their linear phased array produces source location results that are within two diameters of the results from other source location techniques. While Lee and Bridges did

show reasonable agreement between an acoustic beamformer and older well-established methods, the data for the comparison was not from the same facility, or for that matter, from the same physical nozzle. As shown by Karon [7], upstream conditions and boundary layer thickness affects the jet noise. In addition, as shown by Breen and Ahuja [33], the jet noise source location distribution also depends upon the boundary layer at the nozzle exit. So even though it has been common practice to compare source location results acquired in different facilities, often from different nozzles, the most accurate comparisons should be performed with data acquired in the same facility with the exact same nozzle. This is accomplished in this work.

Robert Dougherty has spent the last two decades working on improving acoustic beamforming methods [34–38] with no particular emphasis on jet noise. His company, Optinav, produced the beamforming array and software that is used in this thesis. Dougherty [37] has used a two dimensional beamformer to visualize source locations of both round and rectangular supersonic jets in an attempt to improve the source location for jet noise. The problem with the beamforming technique is that it is designed to locate point sources; large coherent sources can be either missed or incorrectly located when applying this technique. In his paper, Dougherty outlines methods of improving the accuracy of the beamformer for these types of sources. Using generalized inverse processing (GINV), Dougherty was able to more accurately locate and visualize these large coherent sources with the microphone array in the nearfield.

Dougherty and Podboy [39] use the 48 microphone array developed by Optinav (similar to the one used in this thesis) to examine how the phased array method improves on past methods for obtaining the sound source images of both subsonic and supersonic jets. Figure 2.18 shows the source location at 90 degrees for a converging round jet operated at Mach 0.95. The data shown in this figure covers frequency bands from 22,627-45,254 Hz to 707-1,414 Hz. As has also been shown by other methods, Figure 2.18 shows that high frequency sources are generated near the nozzle exit, and lower frequency sources

are generated further downstream. For the supersonic jets, Dougherty and Podboy show results that differ from the two source model for supersonic jet noise described by Tam et al. [21]. They show that the high frequency component of the fine scale turbulence seems to originate in the shear layer when theory states is should start downstream of the potential core. Using wideband frequencies, they were also able to use the beamformer to somewhat visualize the shock structure in the supersonic jets.

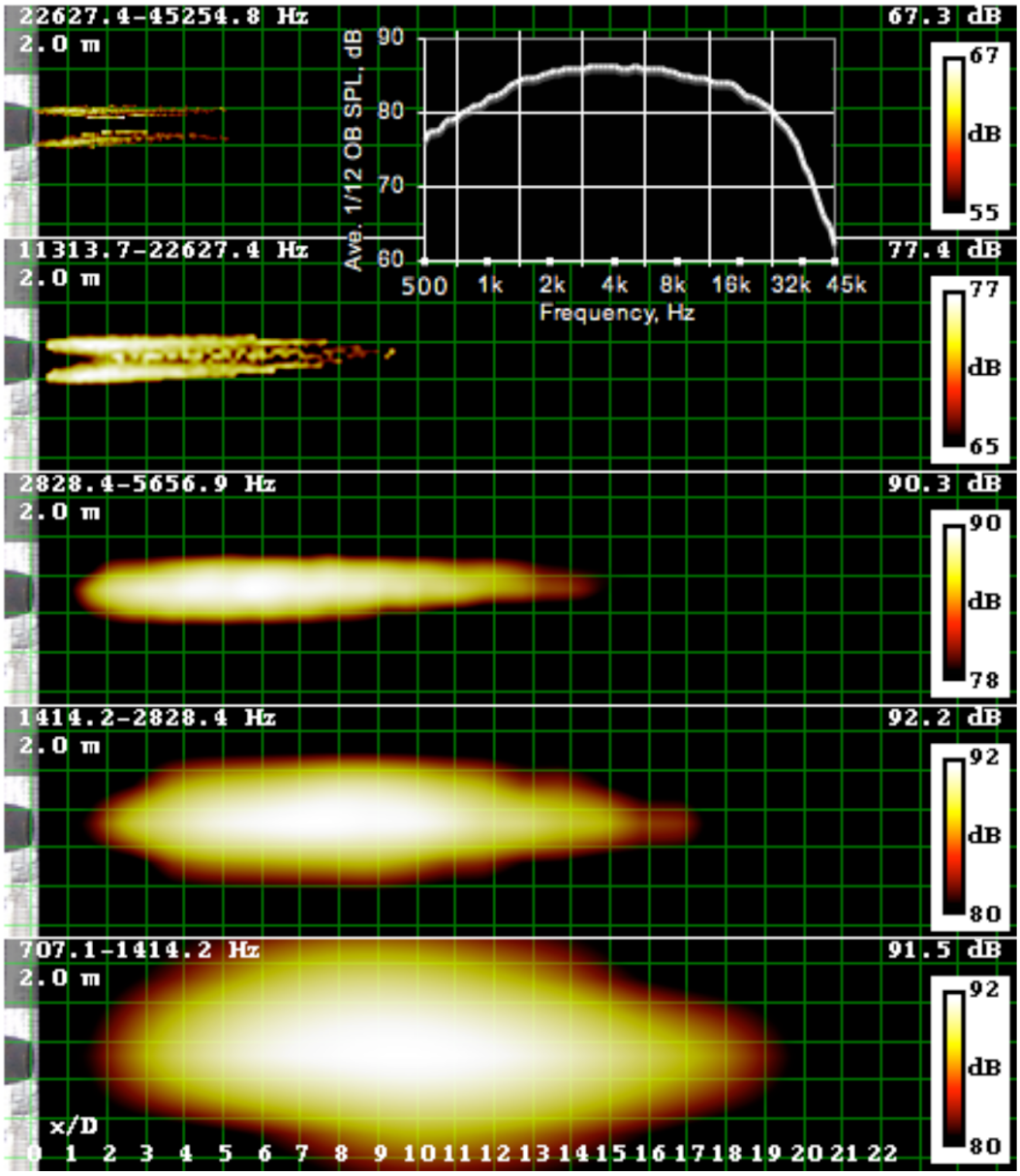

Figure 2.18: Sound source images at 90 degrees for a round converging jet operated at Mach 0.95 obtained by Dougherty and Podboy [39].

2.3 Comparison of Various Jet Noise Source Location Studies

2.3.1 Subsonic Jets

All of the methods listed in the previous section have been applied to subsonic jets. Westley and Lilley [24] noted that the nearfield contours point closer to the nozzle exit for higher frequencies. Many other studies [5, 6, 13, 15, 26, 27, 32] have corroborated this finding that higher frequency sources are generated near the nozzle exit and lower frequency sources are generated downstream. Westley and Lilley [24] also observed that the sound field of the jet, for a given frequency band, appeared as if it was generated by distributed lateral quadrupole sources. Some of the other source location methods, notably the Polar Correlation Technique [27] and acoustic mirror methods [26], illustrate how a frequency source's strength changes over the extent of the jet. They show that low frequency sources are distributed over a large extent of the jet, with no well defined peak strength. High frequency sources, on the other hand, have a much smaller extent but very well defined peaks. A good example of these distributions can be seen in Figure 2.9. Fisher et al. [27] observed that at the highest frequencies the source strength distributions are not symmetric, but instead increase sharply after the nozzle exit and gradually downstream after the peak. This asymmetry results in the centroid for the distributed noise source to be located further downstream (can be as much as 1-2 diameters) than the peak source strength. As a result, several studies plot the source centroid location instead of the source peak location.

Figure 2.19 contains the data from a few of these studies plotted as Strouhal number (fD/U) vs normalized distance downstream from the nozzle exit (x/D). The source location data from these three studies agree within 2 diameters, noting some of this difference may be due to the difference between plotting source peak location and source centroid location. The source distribution of subsonic jet is not fixed for all jet operating conditions; it can be modified by changing conditions of the jet. Fisher et al. [27] observed that the sources of jet noise tended to move closer to the nozzle exit as jet velocity was decreased;

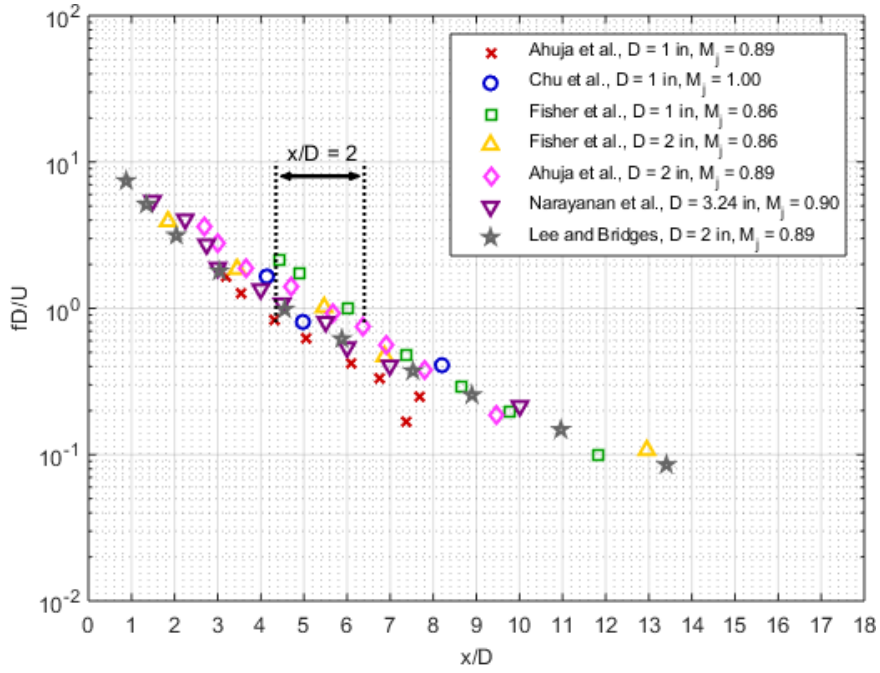

Figure 2.19: Subsonic jet noise source data acquired from four different source location methods: the Acoustic Mirror technique by Chu et al. [26], the Polar Correlation technique by Fisher et al. [27], the Phase Minimum technique by Ahuja et al. [15], and with a linear phased array by Narayanan et al. [32] and Lee and Bridges [5].

this effect was more prominent at lower frequencies. Lee and Bridges [5] also confirmed this effect, as well as showing that heating the jet resulted in the lowest frequency noise sources moving closer to the nozzle exit. The effect of jet velocity and temperature on low frequency noise sources can be seen in Figures 2.16 and 2.17, respectively. Ahuja et al. [15] examined how the source location of subsonic jets would change due to tabs, an ejector, and flight simulation. They found that, due to the enhanced mixing caused by the tabs [40], the jet source locations were shifted upstream. Flight simulation moved the noise sources further downstream. Both of these effects were stronger for the lower frequency sources than the higher frequency sources.

2.3.2 Supersonic Jets

Schlinker [20] used a spherical reflector to examine the noise sources of perfectly expanded supersonic jets. He observed that there were two independent sources of mixing

noise for supersonic jets, one that radiates downstream direction and another that radiates at 90 degrees. Tam et al. [21–23] have since linked these two sources to large turbulent structures and fine scale turbulence, respectively.

Yu and Dosanjh [25] have shown the noise contours in the nearfield of a jet produced by a converging-diverging nozzle of design Mach number 1.5 at both shock-free and underexpanded conditions. In a similar fashion to what was seen by Schlinker [20], Yu and Dosanjh observed two distinct lobe patterns in their contours that seemed to emanate from a point between the laminar core tip and the supersonic core tip of the jet: one normal to the jet axis and one in a downstream direction. They also found that the presence of shocks shifted low frequency noise sources upstream, an effect they attributed to enhanced mixing cause by the shocks.

2.3.3 Recent Studies

While working on this thesis, there have been several additional studies released pertaining to jet noise source location. Currently, one of the largest topics has been the modeling of jet noise through the use of wavepackets. Wavepacket models, as described in depth by Papamoschou [41], are in essence an amplitude-modulated traveling pressure wave that exists on a nearfield cylinder right outside of the jet. These models have been used in conjunction with beamforming to improve measurements. For instance, Harker et al. [42] have used a hybrid approach, with wavepackets and beamforming, to examine the noise field from the jets of a F-22. Further studies on the jet noise of the F-22 include one performed by Stout et al. [43] in which they use intensity ray tracing to roughly measure the noise source distributions of the jet at both nominal and afterburner conditions. They show similar trends in noise source distributions as those shown in Figure 2.19, as well as show that afterburner effects shift the noise source distributions downstream.

There also has been many studies examining the full-scale jet noise of a F-35, notably the study by Wall et al. [44] in which they use nearfield acoustical holography to image

the noise field behind the F-35. The results of this study show multiple lobes in the noise field of the supersonic jet and also show how the directionality of the lobes tend to "shift" downstream and decrease in amplitude as frequency is increased.

While not exactly a study dedicated to jet noise source location, the author would be remiss to not mention the excellent literature review by Merino-Martinez et al. [45] on different acoustic imaging techniques with respect to aircraft applications. This paper has a concise description of the theory behind conventional beamforming as well as the more advanced beamforming techniques and deconvolution methods.

2.4 Concluding Remarks

As an area of study, jet noise source location has been examined by numerous researchers, using several different methods, since at least the 1950's. These methods of source location all have different strengths and weaknesses that affect the practicality of their use and the reliability of their results. Source location via acoustic phased array, which is the main method of source location used in this thesis, is convenient in that it allows for rapid acquisition of jet noise data at condition without requiring the researcher to move any of the sensors. Other methods, such as the Phase Minimum Technique, nearfield contours, acoustic mirror methods, and the Polar Correlation Technique (depending on the implementation), require at least one microphone to be moved through space while the jet remains on condition. This can lead to long periods of time where the jet needs to be held on condition, which can be difficult or costly and labor intensive.

In general, studies have shown that subsonic jets have noise sources distributions of which the sources of the highest frequencies are located close to the nozzle exit and of which the sources of the lowest frequencies are located further downstream. For a given frequency, these sources seem distributed along the length of the jet axis, with low frequency sources being longer with less well defined peak strengths. Studies on supersonic jets have shown two different sources of jet noise: one that radiates 90 degrees to the jet and

one that radiates in the downstream direction. These sources are produced by fine scale turbulence and large turbulence structures, respectively and seem to increase in strength due to the presence of shocks.

Upon performing this literature overview, it became clear that there are a few areas in the field of jet noise source location that need additional work, as listed below.

1. No study has compared the results of the acoustic beamforming method with another method using the same nozzles and facilities (which can make a difference in resulting source location).

2. It is a common trend for published studies in jet noise to provide almost no details about the nozzle exit boundary layer, which can be markedly different from one facility to another, making it difficult to compare the source location of various studies. When comparing the results from these studies, it is not clear whether or not any nozzle geometry effects may result in any differences seen. A study needs to be completed analyzing the effects of differing nozzle geometry, and hence the nozzle exit boundary layer, on the jet noise source location.

3. There has never been a dedicated study examining the noise source distribution of twin jets and the effect of separation distance on the said distribution.

4. There is no detailed analysis of the noise source distributions of supersonic jets. While there have been many studies that examine the sources of noise in specific supersonic jets, to the author's best knowledge no one has attempted to track how the distribution of noise sources change with various parameters such as nozzle pressure ratio or diameter.

The goal of this work is to fill in the holes in these four areas.

CHAPTER 3
TECHNICAL APPROACH

This chapter details the technical approach used for experiments outlined in this effort. The first half of this chapter covers the nozzles used for source location as well as the facilities they were tested in. The second half of the chapter contains a detailed explanation of the methods used to obtain the data for the remainder of this effort and the analysis performed on that data.

3.1 Facilities and Instrumentation

3.1.1 Test Articles: Nozzles

Many related existing works either do not detail their nozzle geometry beyond descriptions such as "axisymmetric" or they use a simple geometry description (i.e. "conical" nozzles). In order to maintain a point of comparison to existing studies, a majority of which use converging conical nozzles, most of the nozzles that are used in this work are conical. The conical nozzles used in this work have exit diameters ranging from 1.0 inches in diameter to 2.44 inches. That being said, nozzle geometry, both size and internal contours, does have a distinct effect on the noise produced by a jet. In order to examine the effects of nozzle geometry on jet noise source distributions, several different contoured nozzles were also used for this effort, which include ASME nozzles ranging from 0.5 inches in diameter to 2.0 inches in diameter and 0.75-inch hybrid conical-ASME twin jets. Key dimensions for these nozzles are listed in Table 3.1 and corresponding sketches are shown in Figure 3.1. Pictures of each nozzle are shown in Figure 3.2. The length dimensions listed in Table 3.1 correspond to the total length of the ASME nozzles and just the nozzle part of the conical nozzles (does not include the mounting section). The contraction ratio is the ratio of the

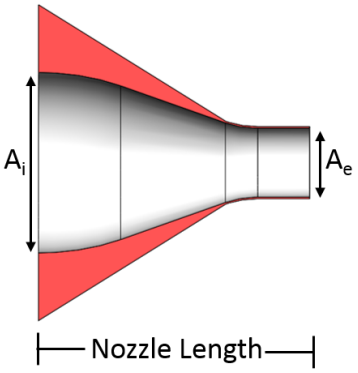

(a) ASME

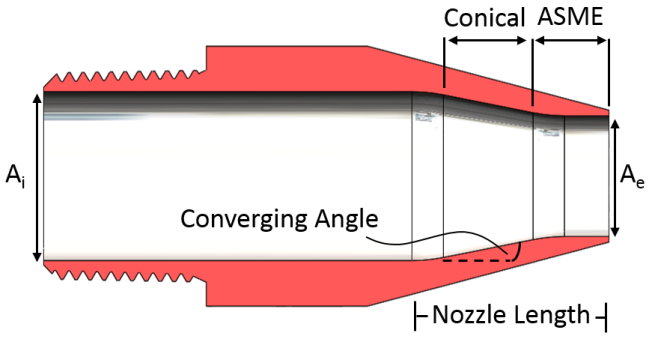

(b) Twin

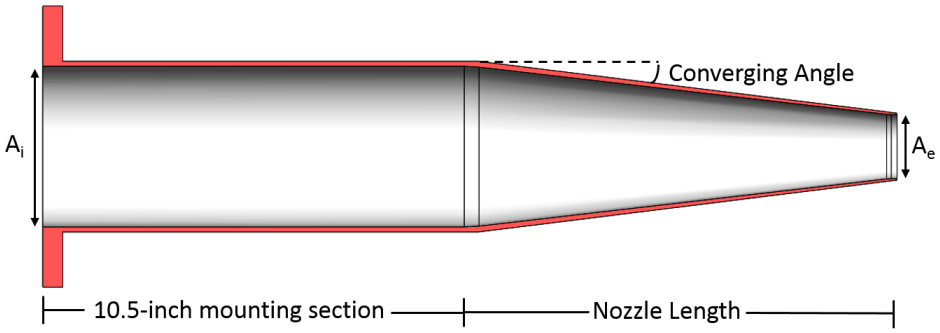

(c) Conical

Figure 3.1: Cross-section views of different nozzle types. Conical nozzles are attached to a 10.5-inch mounting section. See nozzle lengths and converging angles in Table 3.1.

Table 3.1: Dimensions for nozzles. Note: The 0.75 inch twin nozzle is a hybrid conical and ASME nozzle. Basic drawings for these nozzle types are supplied in Figure 3.1.

Nozzle Type	**Diameter (in)**	**Length (in)**	**Converging Angle**	**Contraction Ratio ($\frac{A_e}{A_i}$)**
ASME	0.50	11.25	-	0.0156
ASME	1.10	6.13	-	0.0721
ASME	1.53	6.13	-	0.1406
ASME	2.00	6.13	-	0.2500
Twin	0.75	1.22	11.3°	0.5625
Conical	1.00	15.25	5.6°	0.0625
Conical	1.597	10.81	6.4°	0.1526
Conical	2.44	10.44	4.3°	0.3713

(a) ASME (0.5 in)

(b) ASME (1.10 in, 1.53 in, and 2.00 in)

(c) Conical (1.00 in, 1.597 in, and 2.44 in)

(d) Twin Conical (0.75 in)

Figure 3.2: Pictures of nozzles. The 1.597-inch conical nozzle is attached to the 10.5-inch mounting section for conical nozzles.

exit area of each nozzle with respect to the inlet, which for most nozzles is the area of a four-inch diameter supply duct. The ASME nozzles are designed to the standard described by Benedict and Wyler [46] and, for a given diameter, have a more laminar exit boundary layer than a conical counterpart. Each conical nozzle has a small straight section at the exit to encourage parallel flow.

These nozzles have all, with the exception of the twin jets, been designed to be mounted directly to a four-inch diameter pipe. The conical nozzles require an additional 10.5-inch long pipe to interface with this piping. Because these nozzles can all be mounted to the same four-inch duct exit, different upstream geometry can be eliminated as a factor that causes changes in the jet noise examined. The four-inch duct used in this work is attached to a plenum chamber with a contraction ratio of 36. This large plenum chamber reduces upstream turbulence and is used to measure the stagnation properties of the jets. The discussion of the measurement of these properties can be found later on in this Chapter.

While the majority of the nozzle configurations tested in this effort have unmodified circular exits, tabs are used in a few select cases to enhance the mixing of the jets and thus change the source location distributions of those jets. The nozzle exit geometries that have tabs equipped are henceforth referred to as having a "tabbed exit." The tabbed nozzle geometry, as depicted on a conical nozzle in Figure 3.3, consists of two 5/16-inch, triangular, aluminum tabs that are attached 180 degrees from each other in the nozzle exit plane. These configurations are primarily used to show the beamforming methodology's ability

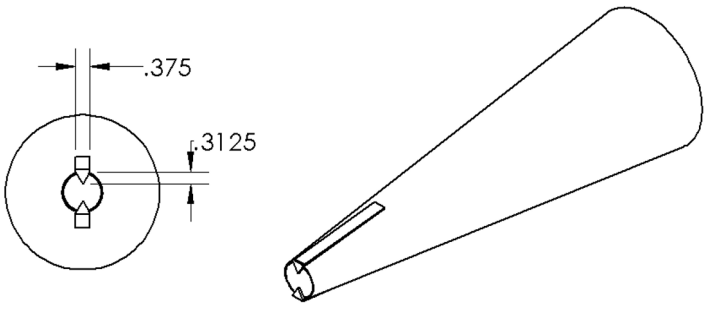

Figure 3.3: Tab dimensions and attachment points.

to detect changes in jet noise source location that results from the mixing enhancement brought about by tabs at the nozzle exit.

The twin jets are mounted to the same four-inch supply duct in a different manner than the other nozzles, as illustrated in Figure 3.4. This configuration consists of two 0.75-inch

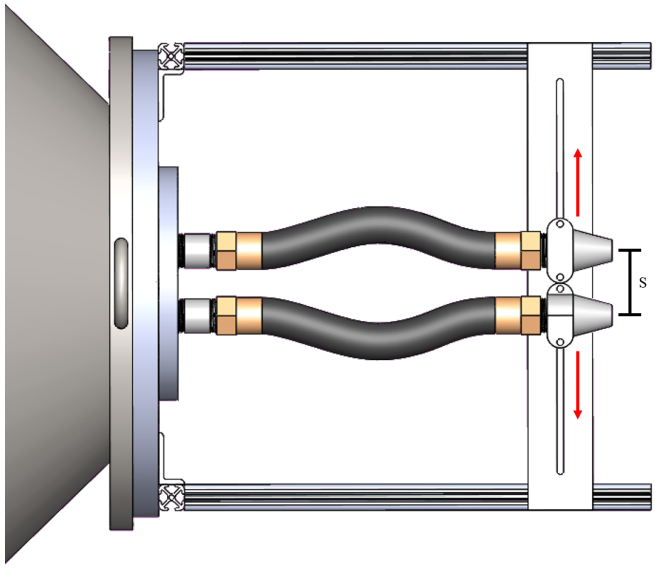

Figure 3.4: Nozzle configuration of twin jets.

3D-printed nozzles attached to the plenum with one-inch rubber hoses. The two nozzles are depicted in Figure 3.2d. The nozzles are held in place by a sheet of aluminum with a slot drilled along its length. The flexibility of the rubber hoses combined with the grooves in the mounting frame allows the nozzles to be locked into place at fixed separation distances. The dimension marked as s in Figure 3.4 is the distance between the nozzle centerlines and is what this work defines as the separation distance of the nozzles. This distance is varied between 3 and 10 diameters for this work.

As shown in Figure 3.1c, the internal geometry of these nozzles are not purely one type of nozzle. The last 0.472 inches of the nozzle are designed to ASME standards and has a small 0.25-inch straight section just prior to the nozzle exit. The 0.556 inches of nozzle prior to the ASME section is purely conical. As a result these twin nozzles are said to have a geometry that is a hybrid of the ASME and conical geometries.

3.1.2 Test Facilities

The data obtained for this effort is acquired in two main facilities: the flow diagnostics lab and the static anechoic chamber. The following subsections outline the capabilities of these facilities.

Flow Diagnostics Lab

The primary laboratory where the beamforming experiments were performed for this effort was the flow diagnostics lab located at the Cobb County Complex of the Georgia Tech Research Institute (GTRI). This lab, as depicted in Figure 3.5, contains an acoustic beamformer and schlieren flow visualization system and is not anechoic. A traversable boundary layer probe and a particle imaging velocimetry (PIV) system are also available in this facility for jet velocity measurements as needed.

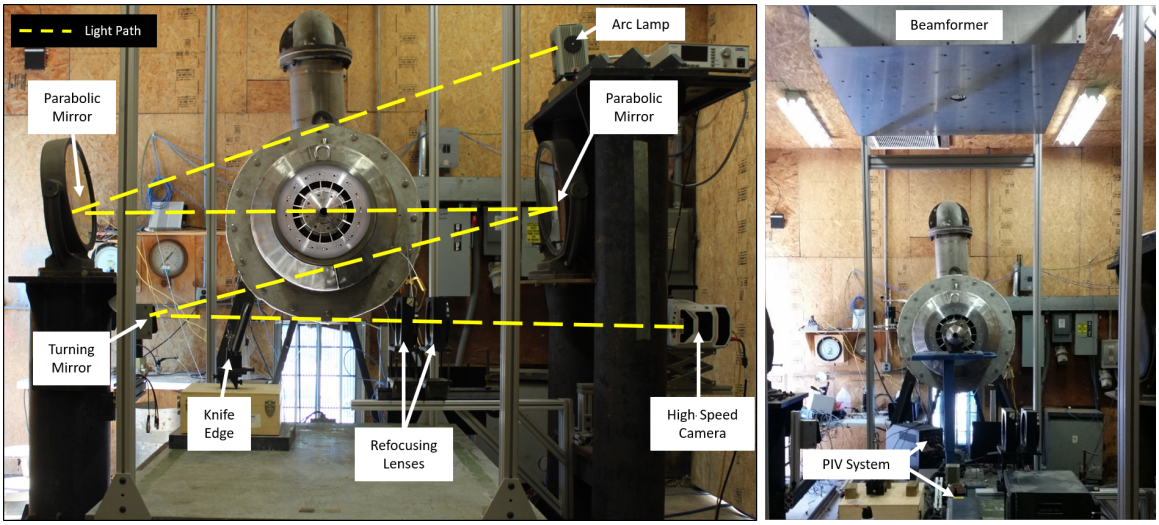

Figure 3.5: Flow diagnostics lab with beamforming and schlieren flow visualization capabilities.

The acoustic beamformer used for this work was developed by Optinav for use at GTRI. This beamformer, shown in Figure 3.5, is comprised of 48 Earthworks M30 microphones set in a spiral pattern emanating from the center of the beamformer. The spiral pattern results in an array that is approximately three feet across. The Earthworks M30s are one-

quarter-inch omnidirectional microphones that have a flat free-field response from 5 Hz to 30 kHz and a peak acoustic input sound pressure level of 142 dB. An iCubie usb camera is mounted in the center of the beamformer pointing in the direction of measurement. The camera has a resolution of 1.49 miliradians per pixel. This camera allows one to visually tie the noise sources to a photograph of the nozzle geometry. As explained later in Section 3.2.2 (Beamforming Data Processing), the image from this camera is not directly used in this effort, but the resolution of the camera is used to determine the actual location of the noise sources.

The beamformer is mounted on an 80/20 structure that allows the device to be raised and lowered above the nozzle. The face of the beamformer is aligned such that it is parallel to the ground and the axis of the jet. For all nozzle configurations, the beamformer was 46 inches above the jet plane. The 80/20 structure is attached to a table that can be shifted along the jet axis, allowing for different length nozzles to be easily tested. The beamformer was aligned such that the center of the array was approximately 90 degrees with respect to the exit of each nozzle.

When recording, the signals from the 48 microphones are passed through preamplifiers that are inside a nearby lab. The preamplifiers are eight-channel Avid PRE preamplifiers. The signals can be adjusted in 3 dB increments and are mainly used to balance the signals between the different channels. Zero amplification was often used for larger nozzle exit diameters at high Mach numbers.

From the amplifiers, the microphone outputs are sampled at 96 kHz and read into the computer. The 48 channels of microphone data are recorded simultaneously along with video from the iCubie camera using the "Camera Capture" function of the Beamform Interactive software. This software package allows the user to use several different beamforming methods to examine the source locations as well as to examine the source location of specific frequency bands at different planes in space and at different times. A more detailed description of the processing of the beamforming data is given later in Section

3.2.2.

The schlieren flow visualization system consists of a light source, two parabolic mirrors, a flat turning mirror, two focusing lenses, a knife edge, and a high speed camera. Most of the system is mounted on two vibration-damped metal pylons that can roll on tracks parallel to the jet axis. The light path, as indicated by yellow dashed lines in Figure 3.5, starts from a light source located at the focus of one of the two parabolic mirrors. Light travels from the sources and reflects off the first parabolic mirror into the second parabolic mirror; the jet is located in the light path between these two mirrors. The light from the second mirror is re-directed with a turning mirror such that it focuses onto a knife edge. Afterwards, the light is focused through a series of lenses and into a high speed video camera for recording.

The light source that is used in this effort is an Oriel DC arc lamp fitted with a 100 W mercury bulb. This source is very bright ($1700cd/mm^2$) and very small ($0.25mm$ by $0.25mm$), making it a good approximation of a point source. The parabolic mirrors are 16.25 inches in diameter and have a focal length of 80 inches. The large size of the mirrors allow for a larger region of the jets to be examined without needing to move the whole system.

The camera used to record the schlieren flow visualization is a Vision Research Phantom V2512 monochrome ultrahigh speed camera. This camera is capable of recording at 25,600 frames per second at full resolution, but is set at 31,000 frames per second (at a slightly lower resolution) for this current work. The camera's minimum exposure is one microsecond, requiring the use of the powerful light source mentioned above, which results in crisp images of fast moving flow features.

The nozzle exit boundary layers and jet-mixing layers are measured with a traversable boundary layer probe as shown in Figure 3.6a. The probe is mounted to a one-dimensional traverse that allows measurement normal to the jet axis. The one-dimensional traverse is attached to the same movable table that the beamformer frame is mounted to, allowing for measurements parallel to the jet axis as well. It is not shown in Figure 3.6a, but the probe

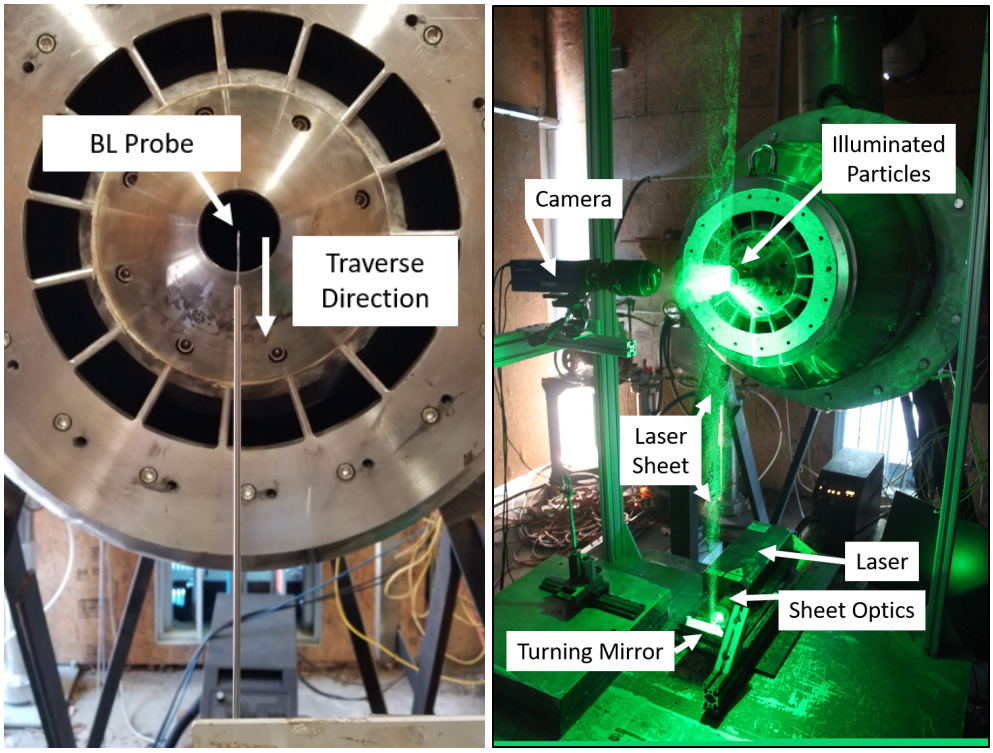

(a) Boundary layer probe (b) PIV system

Figure 3.6: Boundary layer probe and PIV system used for jet velocity measurements.

has a one-inch wide, 1/10th-inch thick piece of aluminum running along the thick part of the probe. This stiffens the probe and prevents it from vibrating when in the jet.

A particle imaging velocimetry (PIV) system is used for velocity measurements in select cases and can be seen depicted in Figure 3.6b. Particles that are seeded into the flow upstream of the plenum are illuminated in the jet by two separate laser sheets. The laser sheets highlight the same regions of the jet, but are illuminate the jet separately at intervals of 0.2-0.5 μs. A LaVision Intense camera is used to capture the movement of the particles between the flashes of the two laser sheets. A LaVisison Davis software package is then used to analyze these images and obtain the velocity field of the jets.

Static Anechoic Chamber

The facility at GTRI where nearfield contour and other acoustics experiments are performed for this work is known as the "static anechoic chamber". The static anechoic chamber is a 22-foot by 20-foot room that is 28 feet tall and is completely lined with 18-inch melamine wedges. This facility is anechoic above 175 Hz. Figure 3.7 illustrates the layout of the facility.

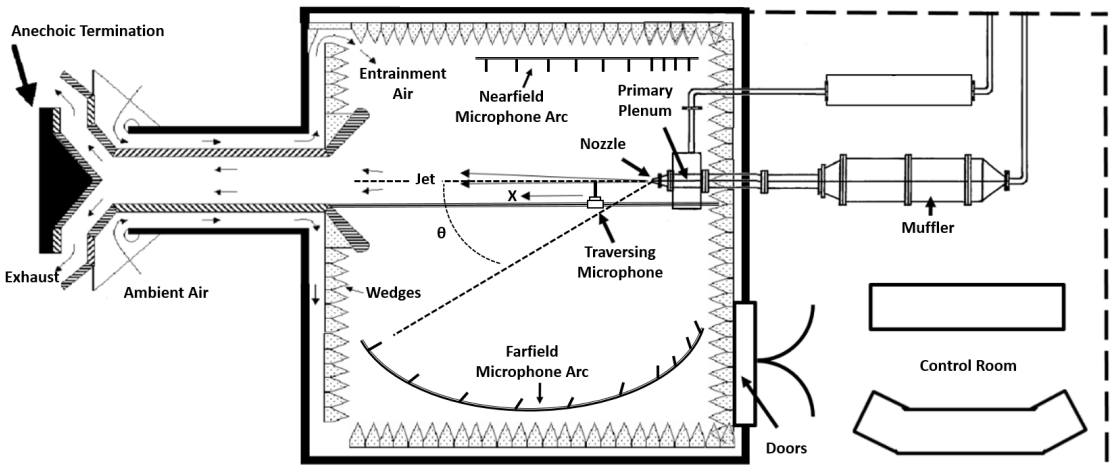

Figure 3.7: A drawing of the Static Anechoic Chamber at GTRI. Only one of the three polar farfield arcs are depicted in this drawing. θ is the polar angle defined from the jet axis.

The plenum chamber of this facility and the piping downstream of it are identical to those in the flow diagnostics lab; as a result, the source location data taken in the flow diagnostics lab and the static anechoic chamber can be treated as if they were acquired in almost the same facility.

The static anechoic chamber contains four microphone arcs: three located in the acoustic farfield and one in the nearfield. A two-dimensional traverse is mounted on the ceiling and runs along the jet axis. The microphone arcs and the traversable microphone are depicted in Figure 3.8. The same type of 1/4-inch PCB microphones are used in this facility

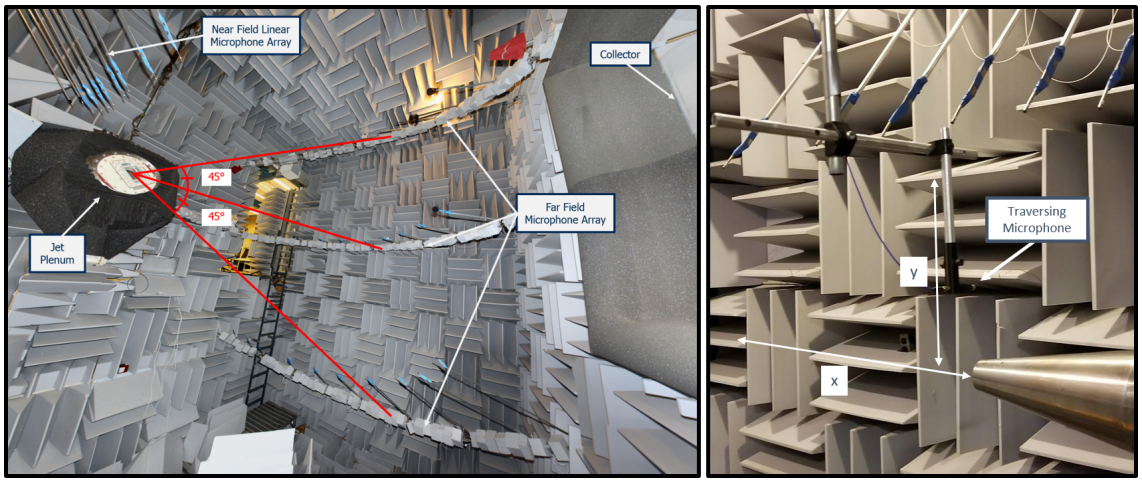

Figure 3.8: Microphone orientations in the Static Anechoic Chamber.

on the traverse. The microphone is attached to the traverse with a custom 3D printed fitting that orients the microphone such that the incidence of recording (ψ) is always 90 degrees for every point along the jet axis. This effect is illustrated by the drawing shown in Figure 3.9. While the side view shows multiple hypothetical noise sources at different points along the jet axis, from the front all of these noise sources are located at the same angle of incidence with respect to the microphone face. Because the traversing microphone only moves in a plane that is coincident with the jet axis, the angle of incidence for sources along the jet axis never changes.

For select conditions, farfield data is acquired using the upper most farfield polar arc shown in Figure 3.8 along with nearfield data from the linear nearfield array. The upper

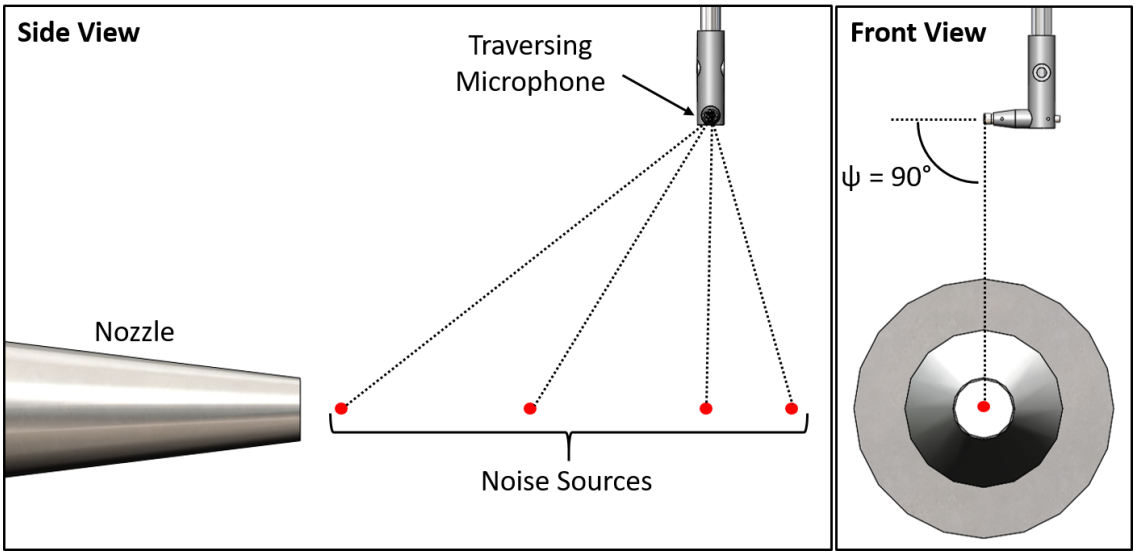

Figure 3.9: Front and side views of the 90 degree microphone mount for the traversable microphone in the static anechoic chamber. Microphone incidence angle, ψ, is defined in the side view.

farfield microphone arc is comprised ten 1/4-inch Brüel and Kjær free-field microphones spaced at polar angles from 30 degrees to 120 degrees. The 1/4-inch PCB free-field microphones in the linear nearfield arc are spaced at the same polar angles (the 110 and 120 degree microphones were not used) at a sideline distance of 20 inches with respect to the jet axis. Polar angles and distance to the nozzle exit can be found for each microphone in Table 3.2. Specifications for each type of microphone used in this effort are listed in Table 3.3. All the microphones in this facility, including the one on the traverse, are sampled at 204.8 kHz with National Instruments PXIe-4499 data acquisition cards.

Table 3.2: Locations of microphones in the polar arcs. The farfield microphones are pointed at the nozzle exit and the nearfield microphones are pointed at the jet centerline. The nearfield arc is at a sideline distance of 20 inches. The angle θ is measured from the jet centerline as shown in Figure 3.7.

Polar Angle (θ)	**Distance to nozzle exit (inches)**	**FF or NF**
30°	113.9	Farfield
40°	113.5	Farfield
50°	115.0	Farfield
60°	115.2	Farfield
70°	118.6	Farfield
80°	119.3	Farfield
90°	121.1	Farfield
100°	118.8	Farfield
110°	113.5	Farfield
120°	106.4	Farfield
30°	51.4	Nearfield
40°	38.9	Nearfield
50°	31.1	Nearfield
60°	25.5	Nearfield
70°	22.5	Nearfield
80°	20.4	Nearfield
90°	20.0	Nearfield
100°	21.0	Nearfield

Table 3.3: Specifications of microphones used, including the beamforming Earthworks microphones. Nominal sensitivities that have "unamplified" are for microphones that are amplified when measured.

	Brüel and Kjær 4939	**PCB 378C01**	**Earthworks M30**
Nominal Sensitivity (mV/Pa)	4 (unamplified)	2	34 (unamplified)
Frequency Range (Hz)	4 - 100,000	4 - 100,000	3 - 30,000
Dynamic Range (Hz)	28 - 164	42 - 165	140 max

3.2 Data Acquisition and Analysis

This section first details the methodologies behind the source location methods that are used in the current work: beamforming and nearfield contours. A brief description of the methodologies behind the jet velocity measurements and farfield acoustic measurements performed for this work is the presented. As beamforming is the key methodology used in this work, this section begins with a brief description of the theory behind its use.

3.2.1 Acoustic Beamforming Theory

A directional phased array makes use of the phase and amplitude differences of signals received by a series of microphones at known locations. By adjusting these differences, the beamformer can be steered to focus in on a specific area in space. On a basic level, beamforming can be broken up into two different forms: time domain beamforming and frequency domain beamforming. These methods lay the foundation for the understanding of the more advanced algorithms. David Arnold [47] describes these techniques in great detail in his thesis. The next two subsections briefly summarize the descriptions laid out by Arnold of these basic beamforming techniques.

Time Domain Beamforming

Imagine an array of N microphones, as depicted in Figure 3.10, each located X_n from the center of an array. Also consider a spherically propagating point noise source located at X' (propagates outward following the equation below).

$$f(r,t) = \frac{s(t - \frac{r}{c})}{r} \tag{3.1}$$

The distance between the n^{th} microphone and the source is $R'_n = |X' - X_n|$. Since this distance is often unique for each microphone and because sound from the source travels at the speed of sound, c, each microphone receives the same sound at a different time,

as given by $(t_n = \frac{R'_n}{c})$. This time difference accounts for the phase differences between each microphone. Additionally, the difference in distance also causes each microphone to receive slightly different amplitudes of sound (proportional to the inverse of the distance between the microphone and the source). The amplitude of the pressure signal, $y_n(t)$, received by the n^{th} microphone can thus be expressed as:

$$y_n(t) = f(R'_n, t) = \frac{s(t - \frac{R'_n}{c})}{R'_n}. \tag{3.2}$$

Hence the time delay, $t - \frac{R'_n}{c}$, results in a phase delay between the sound generated at time t and the reception of the sound at a microphone located at a distance of R'_n.

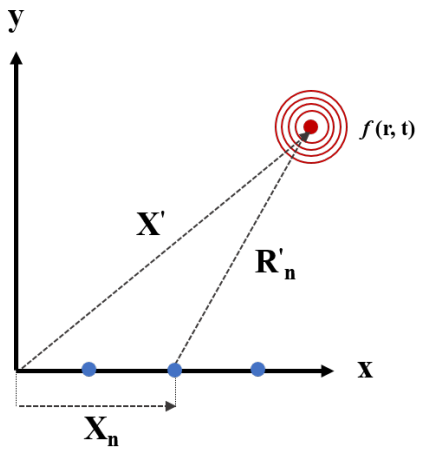

Figure 3.10: A linear phased array, where the microphones are on the x-axis and the source is located above the array.

From Equation 3.2, the classical equation for continuous time, delay-and-sum beamforming can be formed,

$$z(t) \equiv \sum_{n=1}^{N} w_n y_n(t - \Delta_n). \tag{3.3}$$

In the beamforming algorithm, as the signals are read, they are delayed by Δ_n seconds and scaled by w_n before being summed together. The time delays and scaling factors are to account for the difference in time traveled from the point source to each microphone and the difference in amplitudes produced by the inverse square law, respectively. These

scaling values are calculated based off some reference location, often the array center, as shown in Equations 3.4 and 3.5.

$$\Delta_n = \frac{R' - R'_n}{c} \tag{3.4}$$

$$w_n = \frac{R'_n}{R'} \tag{3.5}$$

The value R' is the distance between the noise source and the reference location, which in the case of the current example shown in Figure 3.10 would have a value of X'. If the scaling values are chosen correctly for each microphone, it will appear as if all of the microphones are in phase and at the same distance from the source and the summation in Equation 3.3 will reduce to,

$$z(t) = N s_o(t), \tag{3.6}$$

where $s_o(t)$ is the signal received at the reference location. If the time delays and scaling factors are chosen for a point in space that does not contain the noise source, the signals will not add up coherently.

This method is used to find noise sources by changing the delay and scaling values in order to scan through space. The location that has the maximum output in the summation is the location of the source.

Frequency Domain Beamforming

Frequency domain beamforming follows the same premise as the time domain beamforming; however, as the name suggests, the equations and relations are all in the frequency domain. Instead of time shifting the signals, they are now phase shifted. The Fourier Trans-

form of the beamformer output, Equation 3.3, is shown below:

$$Z(\omega) \equiv \sum_{n=1}^{N} w_n Y_n(\omega) e^{-j\omega\Delta_n}. \tag{3.7}$$

Equation 3.7 only works assuming continuous sampling of data; however in reality, each channel samples at some frequency, f_s, and thus a Fast Fourier Transform (FFT) must be used to obtain a discrete representation of the data. Equation 3.7 can be rewritten as Equation 3.8 where Z_k is the array response of the k^{th} frequency bin.

$$Z_k(\omega) = \sum_{n=1}^{N} w_n Y_{n,k}(\omega) e^{-j\frac{2\pi k f_s}{K}\Delta_n}, (k = 0, 1, ..., K-1). \tag{3.8}$$

Equation 3.8 can be represented in matrix form (as seen below in Equations 3.9-3.11), where $(\cdot)'$ represents a complex conjugate transpose of a matrix.

$$\mathbf{Z_k} = \mathbf{g_k}'\mathbf{Y_k} \tag{3.9}$$

$$\mathbf{g_k} = \begin{bmatrix} w_1 e^{-j\frac{2\pi k f_s}{K}\Delta_1} \\ \vdots \\ w_N e^{-j\frac{2\pi k f_s}{K}\Delta_N} \end{bmatrix} \tag{3.10}$$

$$\mathbf{Y_k} = \begin{bmatrix} Y_{1,k} \\ \vdots \\ Y_{N,k} \end{bmatrix} \tag{3.11}$$

The value $\mathbf{g_k}$, as seen in Equation 3.10, is known as the steering vector; it contains the information about the phase shifts and amplitude scaling that needs to be applied to each microphone. $\mathbf{Y_k}$ represents the signal received for the k^{th} FFT coefficient for each of the N microphones.

Instead of $\mathbf{Z_k}$, the array power response, given by the equation below, is used more

commonly,

$$\mathbf{P_k} = \mathbf{g_k}' E[\mathbf{Y_k}\mathbf{Y_k}'] \mathbf{g_k} \tag{3.12}$$

where $E[\cdot]$ is the expected value. The array power response is defined as the average power in the k^{th} bin of the beamformers output spectrum due to the steering vector $\mathbf{g_k}$. The term between the steering vectors,

$$\mathbf{R_k} \equiv E[\mathbf{Y_k}\mathbf{Y_k}'] \tag{3.13}$$

is known as the cross spectral matrix. This matrix contains information relating the phase and magnitude between each microphone pair in the array.

Similar to the method used in time domain beamforming, the values of the steering vectors are changed to scan through space. The location that corresponds with the maximum array power response for each k^{th} frequency bin (Equation 3.12) is considered to be the location of the noise source for that frequency bin.

3.2.2 Acoustic Beamforming Methodology

Beamformer Array Response

A plot of array response, also called the beam pattern, of an acoustic beamformer is a tool that can be used to determine the accuracy of the device over a range of frequencies and measurement angles. The array response is a measurement of how well the beamformer receives a signal in a given direction and is often plotted as a function of an angle of measurement (the beam pattern). These angles of measurement, azimuth and elevation, are defined from the center of the array geometry. In this work, maximum array response is defined as 0 dB, or no loss of measured acoustic signal in the given direction. Logically, all other values of array response are less than this maximum value, resulting in a reduction of the acoustic signal for those directions. The reduction of the acoustic signal for a given direction is directly related to how low (or how negative) the array response is in that direction.

For a given frequency, the beamformer has a specific beam pattern, which usually consists of one main lobe and sometimes several side lobes. The main lobe of the array response, which has no loss of signal (0 dB) at its center, is what one "steers" through space to search for source locations. At low frequencies, this main lobe is very wide (the array response slowly drops off from the maximum value) and as a result the array detects sound in areas around the measurement location. Side lobes, which are similar to the main lobe but do not receive signals as well, exist for higher frequencies and can result in detecting sound from regions nowhere near the measurement location. An ideal beam pattern has a very narrow main lobe with side lobes that are either nonexistent or are much weaker than the main lobe. If the beam pattern of an array is too poor, the resulting source location suffers. For instance, a wide main lobe prevents the beamformer from differentiating multiple noise sources that are close together.

The array response of a beamformer is highly dependent on the geometry of the array. As mentioned previously, the beamformer used for this work is made up of a spiral array of 48 Earthworks M30 microphones, this results in an array response as shown in Figure 3.11. This figure contains a waterfall plot which is, in essence, a compilation of all of the beam patterns for this beamformer configuration at all of the frequencies measured in this work. This plot is for when the array is focused at an azimuth angle of zero degrees. A more detailed analysis of array response and its effect on the source location can be found in Section 6.2.2 of Chapter 6. In summary, the 3 dB beam width is smaller than 1.25 degrees (or one inch at a distance of 46 inches) for frequencies greater than 14 kHz. Frequencies above 7.5 kHz result in a beam width of less than 2.5 degrees (or two inches at a distance of 46 inches).

Beamform Interactive

As mentioned earlier, a commercial beamforming system built by OptiNav is used for this present work. Beamforming analysis is conducted using the Beamform Interactive

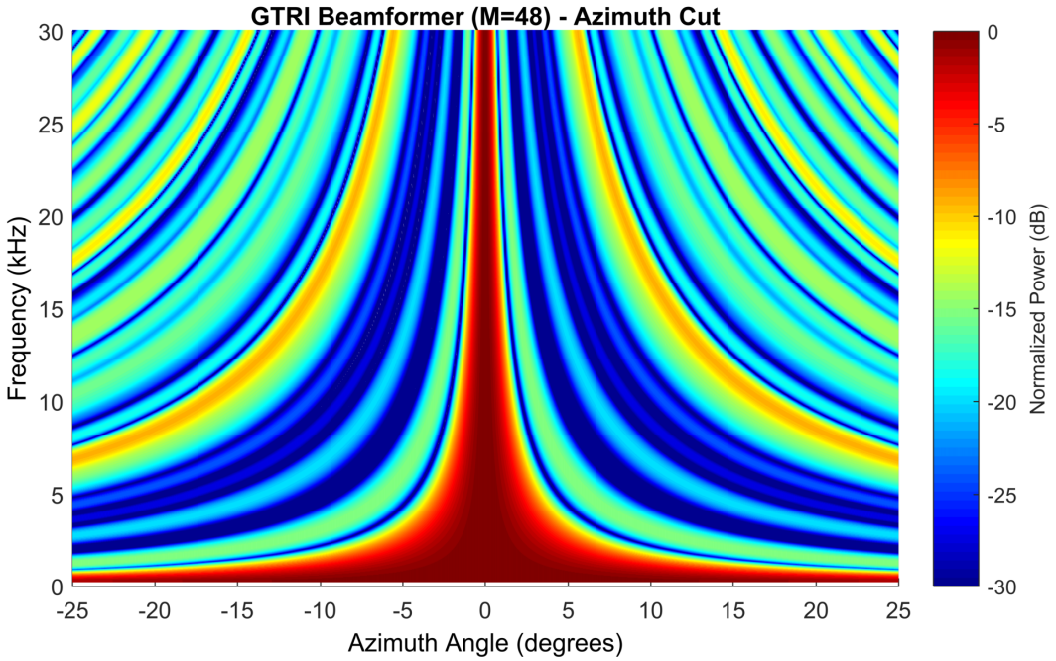

Figure 3.11: Waterfall plot of beamformer array response with the array focused at an azimuth angle of zero degrees.

software package, which is a post-processing package designed to give the user many different options when performing beamforming analysis and is, in essence, based upon the fundamentals outlined in Section 3.2.1. The primary feature that is used from this program is called "frequency sweep.". The frequency sweep function beamforms each band of the recorded 1/12th Octave spectra individually and records the resulting location for each frequency band. This process was run from the 250.12 Hz to 30,084.82 Hz bands for each test condition. The source location of 1/12th octave bands was chosen as a balance between having so many data points that it was too hard to compare conditions (narrowband) and not having enough points to adequately see trends in the data, which appeared to be the case for 1/3rd octave band data. The 1/12th octave source location acts as a "best-fit" of sorts for the narrowband data.

Beamform Interactive offers many different advanced beamforming options to chose from when processing data; this work mainly uses the program's default beamforming option that is described by Dougherty [35]. This method is an advanced version of time

domain beamforming.

In order to manipulate a cross spectral matrix for time domain beamforming, Dougherty rewrites Equation 3.3 in terms of microphone pressures as indicated below:

$$z(x_l) = \sum_{n=0}^{N-1} \sum_{m=0}^{N-1} \langle p_n(t - \tau_{n,l}) p_m(t - \tau_{m,l}) \rangle. \tag{3.14}$$

x_l is one of the grid points in space that the beamformer is "steered" towards and $\tau_{n,l}$ is the time it takes sound to propagate from x_l to the nth microphone in the array. Using the relation for a cross-correlation matrix in Equation 3.15 and the definition for the shift operator in Equation 3.16, Equation 3.14 can be reduced to Equation 3.17, in a form that resembles the frequency domain beamforming Equation 3.12. The shift operator acts as a steering vector by performing a convolution with the delta operator on a given time signal, shifting the signal in time.

$$R_{n,m}(\tau) \equiv \langle p_n(t) p_m(t - \tau) \rangle \tag{3.15}$$

$$s(\tau) f(t) \equiv \delta(t - \tau) * f(t) = f(t - \tau) \tag{3.16}$$

$$z(x_l) = \sum_{n=0}^{N-1} \sum_{m=0}^{N-1} s(\tau_{n,l}) R_{n,m}(t) s(-\tau_{m,l}) \Bigg|_{t=0} \tag{3.17}$$

Equation 3.17 is the basis for the beamforming that was performed in this work. This equation is still, in essence, time domain beamforming as shown in Equation 3.3.

Beamforming Data Processing

After performing a frequency sweep, Beamform Interactive outputs a file that lists the x and y coordinates, in pixels with respect to the image captured by the beamformer's iCubie camera, of the peak value of each 1/12th octave band in the sweep. In order to convert

the units of these locations into something useful, for example inches, the resolution of the camera is used in conjunction with the distance to the measurement plane (d_z) as shown in Equation 3.18.

$$x(inches) = d_z(inches)x_o(pixels)\frac{1.49}{1000}(radians/pixel) \tag{3.18}$$

The variable x_o is the x-coordinate with respect to the image center and is calculated as shown in Equation 3.19,

$$x_o(pixels) = x(pixels) - 640/2 \tag{3.19}$$

where 640/2 is half the width of the recorded image in pixels. The y-coordinate of the source location is calculated in a similar manner, with the only difference being that half of the image height (480/2) is used in Equation 3.19 instead of half of the image width. The end result of these calculations is a list of x and y coordinates, in inches, that are in reference to the center of the acquired image. For this work, the actual image is not used, and thus no calibration is needed to align the image with the source location. Beamform Interactive thus treats the center of the image as the center of the array, making the array center a true distance reference for the calculated coordinates. By measuring the downstream distance between the array center and the nozzle exit, these coordinates can then be shifted such that (0,0) is located at the nozzle exit. No measurement is required to align the y-coordinate, as the nozzles are aligned with the array centerline for most test cases.

At this point, noise sources that are obviously erroneous are thrown out. This mainly includes noise sources that are on the perimeter of the image grid, as there is no way to tell if these points are actually points of maximum array output. When plotting this data, points that are likely the result of side-lobes are also eliminated: points with y-coordinates that are greater than 1.5 nozzle diameters from the jet centerline and points that have x-coordinates less than zero. True jet noise sources should be downstream of the nozzle exit

and relatively near the nozzle centerline, thus these ranges were chosen based this fact as to not eliminate any real data. Special care was taken for the twin jet data, as the nozzles are no longer at y/D = 0 and the actual jet noise sources no longer follow the jet centerlines after a certain point downstream. The data for these conditions has to be examined on a case by case basis and side lobes need to me manually removed.

The source location data is plotted as Strouhal number (fD/U) versus normalized downstream distance (x/D), as is the norm in jet noise source location literature. Normalizing the source location allows for easier comparison of the data between different nozzle types and jet conditions. For the majority of this work, these plots all have the same axes: x/D from 0 to 18 and fD/U from 0.01 to 100.

3.2.3 Nearfield Noise Contours

A classical method of locating sources of various frequencies of jet noise is to measure nearfield noise contours as a function of frequency. For jet noise, these contours have directionality. Generally this directionality appears somewhat elliptical in shape, where the points roughly corresponding to the major axis are called the contour peaks. Conventionally, when the peaks of noise contours are joined by a line that connects to the jet center axis, the intersection location with the jet axis is considered to be the source of noise for that frequency. This well-established methodology is used as a reference to validate the acoustic beamforming technique discussed above. As mentioned previously, the plenum chamber and the subsequent downstream ducting in the static anechoic chamber where the nearfield contours are acquired is identical to that of the flow diagnostics lab where the beamforming data is acquired. This allows for a more accurate comparison of the two source location methods. In this section, the steps used to acquire a noise contour for a Mach 0.8 jet and to obtain the resulting source location are outlined.

To acquire noise contour data, a microphone is traversed through 859 grid points above the jet, as depicted in Figure 3.12, and records the jet noise for one second at each point.

The grid spacing is approximately 0.4 diameters in the x-direction and 0.6 diameters in the y-direction.

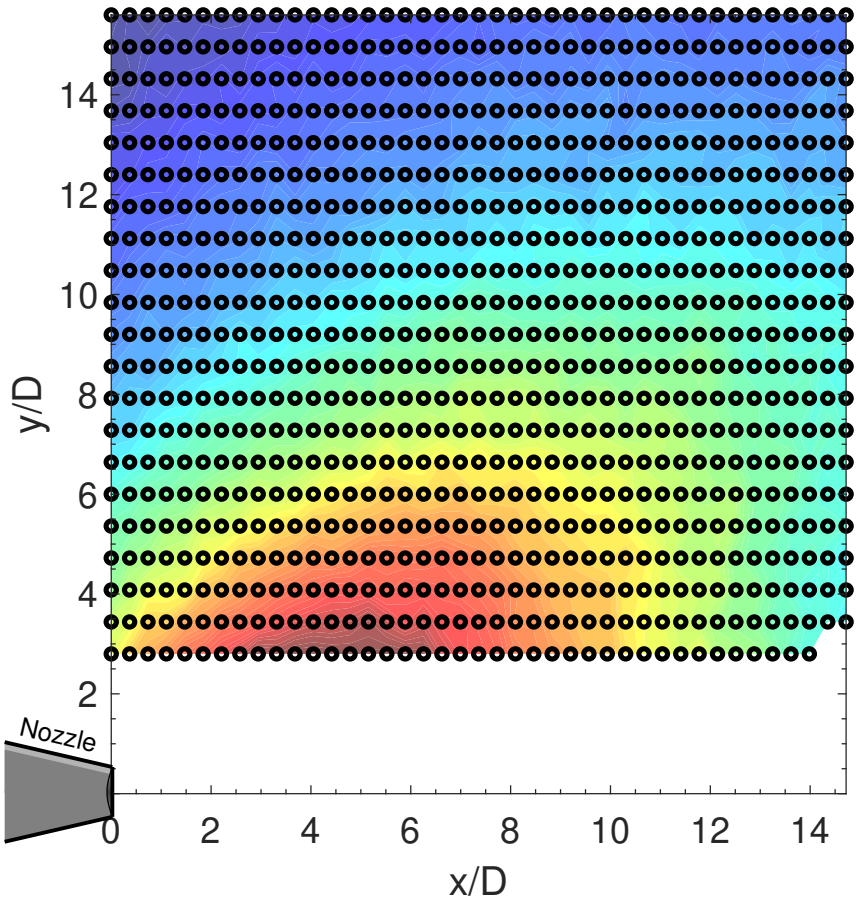

Figure 3.12: Locations under the jet where spectra were acquired.

Narrowband spectra is then generated for each measurement point in the recording gird. For a given frequency, the sound pressure level is plotted at each point to create nearfield contours. A 11.5 kHz contour map with prominent peaks can be seen in Figure 3.13. A line is drawn joining the jet centerline and the peaks of the contours; the intersection with the jet axis is assumed to be roughly the location of the source of noise for the given frequency.

The lines used to determine the source location with contours are drawn by hand using the "ginput" and "polyfit" functions in MATLAB, as described below. The "ginput" function allows the user to click points on a graph and use the resulting coordinates for

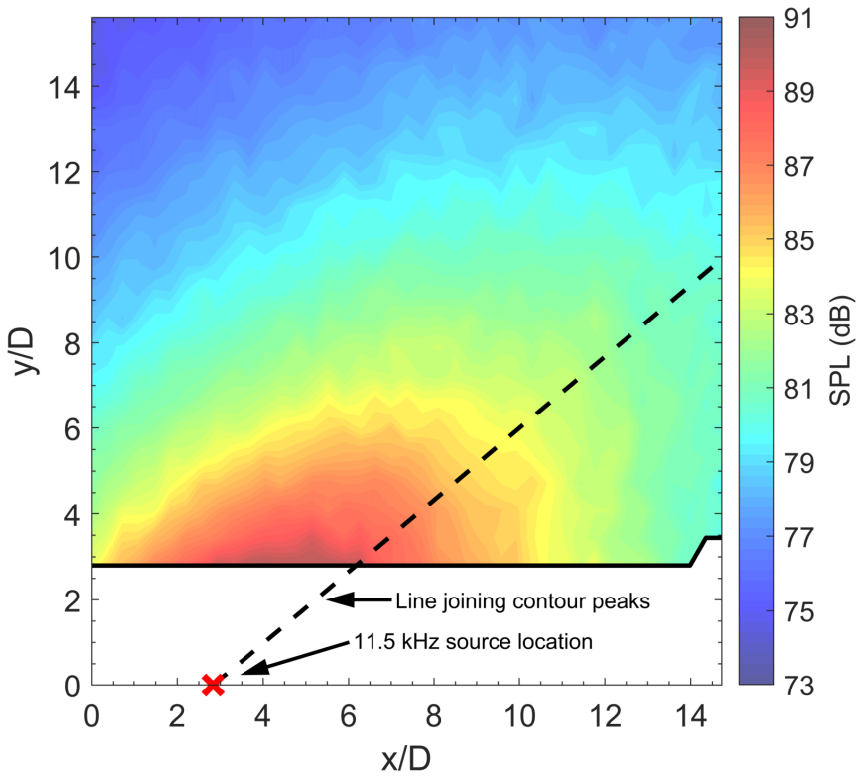

Figure 3.13: Example 11.5 kHz noise contour for a conical jet operating at Mach 0.8.

calculations. To draw the line, the user clicks several points along the apparent contour peaks which are then fitted with a first-order polynomial using the "polyfit" function. The value of this polynomial at $y/D = 0$, the location at which the polynomial intersects the jet axis, is used as the source location. Because there is a human element to obtaining these noise sources, measures are taken to remove bias. First, as shown in Figure 3.13, the axes are made such that the spacing is equal in both the y and x direction. This ensures that the image is not warped by unequal spacing. Then, any information about frequency is removed from the plot and the plots are processed in a random order (i.e. not in order of increasing frequency), so that the user does not accidentally change how they select point based on their preexisting knowledge of jet noise source location trends. Even with these measures taken, there is still an impact on the results due to inherent subjectivity that is built into the method. This uncertainty is outlined in Section 8.4 of Chapter 8.

Only incidence microphone corrections are applied to the traverse microphone data ob-

tained for the noise contours. The microphone is mounted such that the angle of incidence is always 90 degrees, making the correction value constant at all points in the grid for a given frequency. Humidity corrections are not applied to the data, as each contour is only for a given frequency and thus humidity should not have an impact on the shape of the contours. A more detailed description of the microphone corrections used can be found in Section 3.2.5 (Farfield and Nearfield Acoustic Measurements).

Even when recording the acoustic data for one second at each point, a full sweep of the traverse takes over two hours to complete. During this time, it is impossible to keep the jet at a rock-steady condition with no oscillations. To account for this, logic is placed in the acquisition code to only record at a given point when the jet is within ± 0.005 of the desired Mach number. Furthermore, data from a stationary reference microphone is used to correct the SPL of the traverse microphone for any changes due to changes in jet condition. This is accomplished by calculating the difference in reference level of a specific frequency at a given grid point from the initial level recorded (the first grid point) and subtracting that from the traverse microphone's level for the given frequency.

3.2.4 Jet Condition Measurements

Every facility used in this work has the capability to record atmospheric conditions (pressure, temperature, and humidity) as well as plenum conditions (pressure and temperature). For the nozzles used in this work, the air in the plenum chamber is nearly stagnant; as a result, the plenum conditions can be used as the stagnation conditions for the jets. The jet can be thought to be expanding from the stagnation/total pressure (p_t) to ambient pressure (p_a), which gives a pressure ratio that can be used to calculate the jet Mach number using isentropic flow relations as shown in Equation 3.20 (the specific heat ratio, gamma, is assumed to be 1.4 for this work).

$$M_j = \sqrt{5\left[\left(\frac{p_a}{p_t}\right)^{-0.2857} - 1\right]} \tag{3.20}$$

This Mach number is known as the "fully expanded" Mach number and it loses some of its usefulness for supersonic conditions of converging nozzles, which are all underexpanded. As a result, nozzle pressure ratio (NPR) is also included at these conditions. The NPR of a jet is defined as the ratio of total pressure to ambient pressure ($\frac{p_t}{p_a}$) for this work.

Calculation of the jet velocity requires knowledge of the jet static temperature (T_j) in order to be calculated. Similar to the Mach number, an isentropic flow relation can be used to calculate the jet temperature, as shown in Equation 3.21.

$$T_j = T_t \left(\frac{p_a}{p_t} \right)^{0.2857} \tag{3.21}$$

The local static temperature (T_j) allows the local speed of sound to be calculated, which with the Mach number can be used to calculate the jet velocity (Equation 3.22).

$$U_j = M_j \sqrt{\gamma R T_j} \tag{3.22}$$

Jet exit boundary layer and jet-mixing layer velocity measurements are acquired in the Flow Diagnostics Lab, mainly with the use of a boundary layer probe. The boundary layer probe measures total pressure, which is used in tandem with atmospheric conditions and Equations 3.20 through 3.22 to calculate the Mach number and jet velocity at the measurement location. The probe is small enough and the traverse it is attached to has fine enough movement to measure these conditions at intervals of 0.01 inches.

3.2.5 Farfield and Nearfield Acoustic Measurements

All acoustic data measured in the static anechoic chamber is saved as time histories and averaged narrowband SPL spectra. The time histories are processed into averaged SPL spectra with the use of a 6400 sample Hanning window with 50% overlap. This results in a narrowband spectra with a bandwidth (Δf) of 32 Hz. While the nearfield data (and traverse data) are saved as is, the farfield measurements have additional corrections applied on top

of this averaging to render them into lossless SPL.

The farfield data is rendered to lossless through four different corrections: microphone incidence, microphone screen, humidity, and distance. The corrections applied in the GTRI facility are outlined in detail by Ahuja [48] and Karon [7], but is described briefly in this section. The equation used to apply these corrections is shown in Equation 3.23.

$$SPL_{lossless} = SPL_{uncorrected} - \underbrace{B_f(f)}_{\text{freefield}} - \underbrace{B_i(f,\psi)}_{\text{incidence}} + \underbrace{B_s(f)}_{\text{screen}} + \underbrace{B_\alpha(f) r_{mic}}_{\text{humidity}} + \underbrace{20\log_{10}\left(\frac{r_{mic}}{r_{corr}}\right)}_{\text{distance}} \tag{3.23}$$

Microphones do not have flat response at all frequencies. In other words, while microphones are usually designed to measure the sound at most frequencies equally, there are ranges of frequencies, usually frequencies above a certain threshold, at which the microphone cannot measure as well. To account for this, microphone manufacturers often provide tables listing freefield corrections which allow the user to account for the reduction at these frequencies. The term $B_f(f)$ in Equation 3.23 represents this correction and is only a function of frequency for each given microphone.

While the microphones used in this work are listed as "freefield" (i.e. can measure at any incidence without losses), it is actually impossible to make perfectly freefield measurements due to the physical presence of the microphone body in the path of the sound; thus a correction is required to account for this. The $B_i(f,\psi)$ term in Equation 3.23 represents the microphone incidence correction and it is supplied by the manufacturer of the microphone. It is both a function of measured frequency and angle (ψ) of the source with respect to normal incidence of the microphone.

The microphones at lower polar angles are close enough to the jet that hydrodynamic noise may become an issue, so these microphones have a foam ball installed to remove this effect. These foam balls also affect the measured noise, and thus need to be accounted for with microphone corrections. The $B_s(f)$ term in Equation 3.23 represents the microphone screen (foam ball) correction and was determined experimentally by Karon [7]. It is only a

function of measured frequency.

The $B_\alpha(f)$ term in Equation 3.23 represents the humidity correction. Sound is attenuated differently at different frequencies as it propagates through the atmosphere. To put it simply, higher frequency noise is attenuated much quicker than lower frequency noise. The amount of attenuation is a function of atmospheric conditions such as humidity, temperature, and pressure. For a given frequency at measured atmospheric conditions, the attenuation is calculated using the method listed in ANSI S1.26-1995 [49]. This method gives a value that has units of dB/ft and requires the distance between the microphone and the noise source (r_{mic}) to be applied.

The final term in Equation 3.23 is the distance correction. Because the microphones are in the farfield, the sound levels can be shown to follow the inverse square law. This correction is used so that the farfield measurements are all shown at the same distance (r_{corr}) and eliminates discrepancies due to differences in microphone positioning, the actual positions of which are listed in Table 3.2. The farfield data is corrected to twelve feet through this method.

Only the farfield data is corrected in this manner because it is the only data that can use farfield approximations. When in the farfield, all noise sources from the jet can be assumed to emanate from the nozzle exit. This assumption allows the above corrections to be made, as it gives a position to calculate distances and angles. This assumption cannot be made for nearfield data, and would require an accurate knowledge of the jet's source location to perform. This is further elaborated on in Chapter 4 with the help of data acquired for subsonic conditions.

3.3 Concluding Remarks

This work examines data from several nozzles of various sizes and geometry using several different methodologies: source location via beamforming, source location via nearfield contours, schlieren flow visualization, velocity profile measurements, and farfield

acoustic measurements. In the end, this results in more data than can be succinctly discussed in this work. As a result, only certain conditions are focused on in each chapter and the additional conditions are placed in the Appendix. The emphasis of this work is placed on new results, and the data not shown in a given chapter but included in the appendices often displays the same trends as the included data.

CHAPTER 4
VALIDATION OF ACOUSTIC BEAMFORMING AS A VIABLE TECHNIQUE FOR JET-MIXING NOISE SOURCE LOCATION

4.1 Introduction

The acoustic beamformer is a relatively new jet-noise source-location tool. As mentioned in Chapter 2, several studies [4–6] have used this method and have compared their results to other methods of locating jet noise sources. However, to the author's best knowledge, there has never been a study that has compared beamforming data to other methods using data that has been acquired in the same facility with the same nozzles. Such a comparison forms the backbone of this chapter. This chapter is split into four main sections: (1) an explanation of how the beamformer results used in this work are interpreted, (2) a comparison of the current beamforming results with those of existing studies using source location methods other than beamforming, (3) a validation of the beamformer as a jet-noise source-location tool with nearfield contour data, and (4) illustrating the effects of source location error on applications of source location.

4.2 A Note on Terminology and Interpreting Beamforming Results

Terminologies like "array response," "beam pattern," "source strength distribution," "peak source location," and "centroid source location," are used in this chapter. Their definitions and how they are measured are central to the understanding of the results presented here. Also, the understanding of how the source location is chosen for each frequency is especially important when comparing the beamformer to other methods of source location. This section defines these terminologies in two parts: (1) Array Response and Source Strength Distributions and (2) Peak and Centroid Source Locations.

4.2.1 Array Response and Source Strength Distributions

Array Response and Beam Patterns

The array response of a beamformer is a measure of how well the array receives a signal, of a given frequency, from a given direction when the array is focused in a specific direction. A plot of the array response for a given frequency as a function of direction is called the beam pattern at that frequency. Figure 4.1 provides an example of a 20 kHz beam pattern for the beamformer used in this work with the x-axis normalized by the size of the diameter of the 1.60-inch conical nozzle and with the array focused in the direction of $x/D = 0$. The

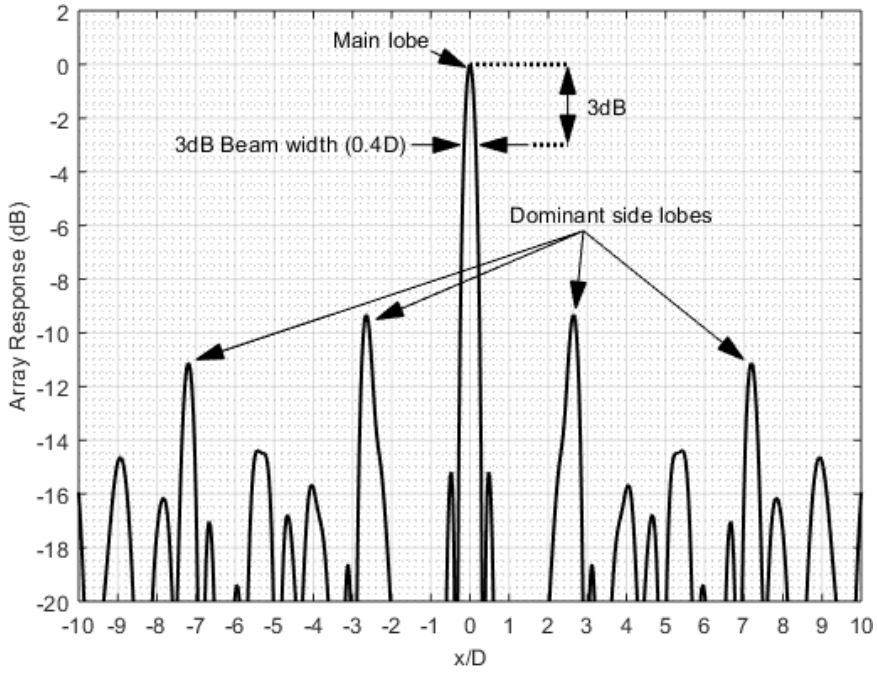

Figure 4.1: Beamformer beam pattern at z = 45.5 inches for 20 kHz. The x-coordinate is normalized by the diameter of the 1.60-inch nozzle. In this plot, $x/D = 0$ is referenced from the array center.

focus location is represented by the location of the main lobe. The shape of an array's beam pattern has a sizable effect on the accuracy of any source location performed by the array. For example, in Figure 4.1 the 3 dB "beam width" of the main lobe for a frequency of 20 kHz is about 0.4 diameters. This means that at this frequency, the beamformer has trouble differentiating noise sources that are within 0.4 nozzle diameters of each other. The beam

width of the main lobe increases as measurement frequency decreases, resulting in lower resolution measurements for low frequency noise sources.

Separate from the main lobe, there are several "side lobes" at different x/D locations. In the case of Figure 4.1, the most dominant side lobes are located at $x/D = \pm 2.75$ and $x/D = \pm 7.25$. These side lobes have much lower array response (less than -9 dB) than the main lobe; however, if a loud enough noise source happens to be located in the same position as a side lobe, it will affect the resulting measured source strength at the measuring location (in this case $x/D = 0$). The number and level of these side lobes are a function of the measurement frequency, becoming more numerous for higher frequencies. Additionally, the term "side lobe" is also used for any "false positive" in the source location that may arise from the presence of side lobes in the beam pattern.

As a side note, the usual convention in beamforming literature is to plot the beam pattern as a function of measurement angle, like elevation or azimuth. It is similarly the convention to display the actual source location as a function of measurement angle. For jet noise source location, however, it is useful to know the locations of the noise sources within a Cartesian plane that contains the jet axis, as is done in this work. The noise sources are reported at (x, y) coordinates within this plane, with x being along the jet axis and y being normal to the jet axis. As a result, angle measurements are not as useful and thus are converted into Cartesian coordinates in the measurement plane, which is parallel to and 46 inches below the array, for this work.

An additional description of the array response is found in Section 3.2.2 of Chapter 3 and a more detailed analysis of the beam pattern's affect on source location is found in Section 6.2.2 of Chapter 6.

Source Strength Distributions

Figure 4.2 contains the measured source strength distributions, along the jet centerline ($y/D = 0$, see Figure 3.12 for jet-axis terminology), at four different frequencies for the

1.60-inch conical jet operated at a Mach number of 0.8. In this work, "source strength dis-

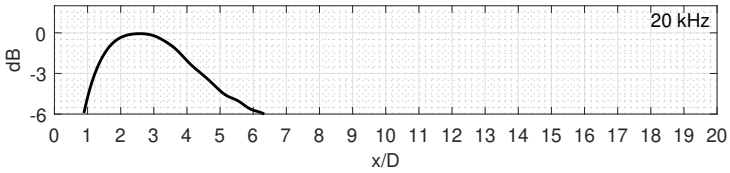

(a) 20 kHz source strength distribution

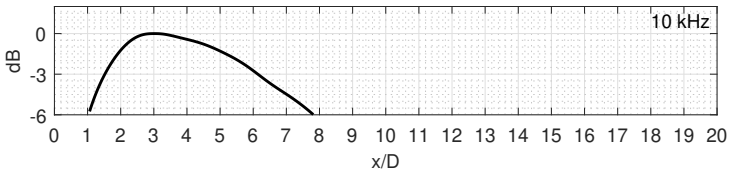

(b) 10 kHz source strength distribution

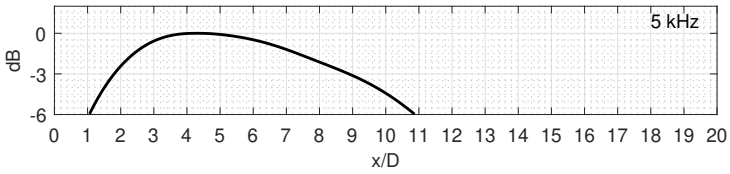

(c) 5 kHz source strength distribution

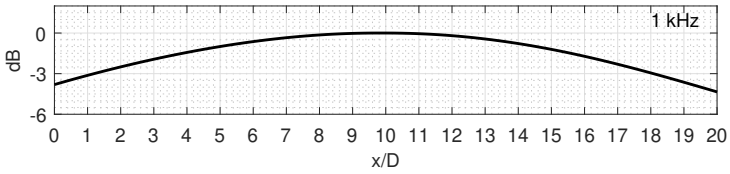

(d) 1 kHz source strength distribution

Figure 4.2: Noise source strength distributions along the nozzle centerline at four different frequencies for the 1.60-inch conical jet operated at Mach 0.8: (a) 20 kHz, (b) 10 kHz, (c) 5 kHz, and (d) 1 kHz.

tribution" is defined as the output from the beamformer, showing measured sound pressure level as a function of position, that is used to determine the locations of noise sources of a given frequency. Very similar to that of the beam patterns shown earlier, the source strength distributions are plotted such that the location of the loudest "point" of a given frequency has a value of 0 dB and all other locations have some negative decibel strength with respect to the loudest "point." From these source strength distributions, two observations can be made: (1) each frequency is not emanating from just one downstream locations and (2) as frequency decreases the extent of the array response grows along the jet centerline.

It has been common practice in the past to model the jet noise sources of a subsonic jet as single point sources for each frequency. These point sources would be aligned such that the highest frequency sources are located near the nozzle exit and the lower frequency sources are located further downstream. This model is based on the thinking that the turbulent mixing layer of the jet grows along the extent of the jet, and the turbulent structures in the mixing layer produce noise with wavelengths that are proportional to the size of the mixing layer at the given downstream location. The results shown in Figure 4.2 appear contrary to this model however, noise of a given frequency appears to emanate from several locations along the jet centerline. For instance, as shown in Figure 4.2a, there is 20 kHz sound, that is within six decibels of the loudest location, coming from one diameter downstream to six diameters downstream. This may very well show that sound of a given frequency is produced at many downstream locations and not just at one point.

There is a caveat, however, with using the measured source strength distributions similar to those shown in Figure 4.2 as the actual source strength distributions for the jet; the source strength distributions shown are a function of the beam pattern of the beamformer array. As mentioned previously, the beamforming array has a specific "array response" to given frequencies that is a result of the array geometry. As a result, the measured source strength distributions are strongly influenced by the shape of the beam pattern for each given frequency. The beamformer used in this work is essentially an antenna of microphones that is electronically scanned through space to locate noise sources. The size of the main lobe of the beam pattern for each frequency determines how small a region of space the beamformer can focus on without noise sources from other regions of space interfering.

The narrow beam width size in the 20 kHz beam pattern (see Figure 4.1) is the reason why the source strength distribution for 20 kHz in Figure 4.2a is so well defined but the source strength distribution for 1 kHz in Figure 4.2d is not. Figures 4.3 and 4.4 help illustrate how the size of the beam width affects the source strength distributions of the 20 kHz sources and 1 kHz sources, respectively. The array responses from the 20 kHz and 1

kHz sources are modeled as point sources (the black, red, and green dots on the x axis), as shown in Figures 4.3a and 4.4a, respectively, where the size of each dot is roughly proportional to the strength of the theoretical point source. For the sake of this explanation, it is assumed these dots are the only sources of noise for their given frequency.

The beam patterns for 20 kHz are plotted in Figure 4.3a with the main lobes focused at $x/D = 2.5$ and $x/D = 4.5$. The 6 db beam width of the main lobe (at a distance of 29

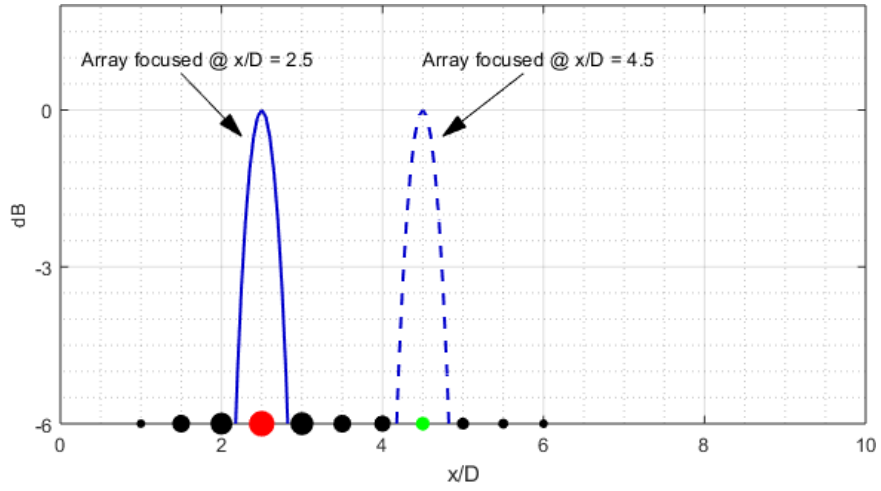

(a) 20 kHz beam batterns

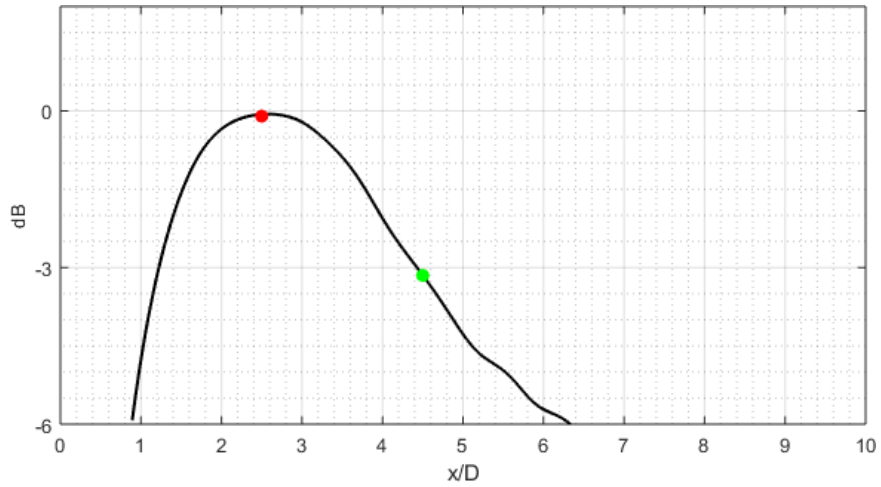

(b) 20 kHz source strength distribtuion of a jet operated at Mach 0.8

Figure 4.3: Example of the width of the main lobe's effect on the measuring of the source location for the 20 kHz source in a jet: (a) 20 kHz beam patterns with noise sources simulated as points and (b) the measured 20 kHz source strength distribution with the points of measurement highlighted.

nozzle diameters from the array) is a little under a diameter. When focused at $x/D = 2.5$,

the main lobe only encompasses the noise source at that location, which has been plotted in red. This noise source is detected with no losses (0 dB), whereas the other noise sources, plotted in black or green, barely contribute to the measured source strength at that location. Due to the beam pattern of the array, the measured strengths of these other sources are reduced by more than 6 dB and have little impact on the measured source strength. The plot in Figure 4.3b shows the measured 20 kHz noise source strength distribution, with a red point at $x/D = 2.5$ showing the result of the interaction of the beam pattern and noise sources presented in Figure 4.3a. Note that the noise source strength distribution in Figure 4.3b is the actual measured distribution from the jet and not the result of the point sources shown in Figure 4.3a. The actual distribution of noise sources in a jet is most likely the result of a continuous string of sources and not a few discrete ones as shown in this example. This means that, while the premise of this example show here still holds true, there is most likely more than one source encapsulated by the main lobe.

As the array is focused on other locations in space, the beam pattern, and thus the main lobe, can be pictured as being shifted to these other locations. This thought process is an oversimplification of what actually happens; the shape of the beam pattern of an array changes as a function of focus location. For the frequencies and angles used in this example, however, the change in shape of the beam pattern is minimal, so the "shifting" explanation is reasonable. To illustrate this, the beam pattern of the array focused at $x/D = 4.5$ is shown, represented by a dashed line, in Figure 4.3a as well. At this new location, the beam pattern similarly filters out most noise sources except for the green one located at $x/D = 4.5$. The sources encapsulated by the main lobe at this location contribute significantly to the measured value at $x/D = 4.5$ in Figure 4.3b. Because there are many more 20 kHz sources than the ones shown in this example in an actual jet, it is very unlikely that only one source is measured at each location when measuring jet noise. In general, it can be said that thinner main lobes result in more accurate source strength distributions.

The beam pattern for 1 kHz is plotted in Figure 4.4a with the main lobe focused at

$x/D = 10$. In contrast to the 20 kHz beam pattern, the 6 db beam width of the main

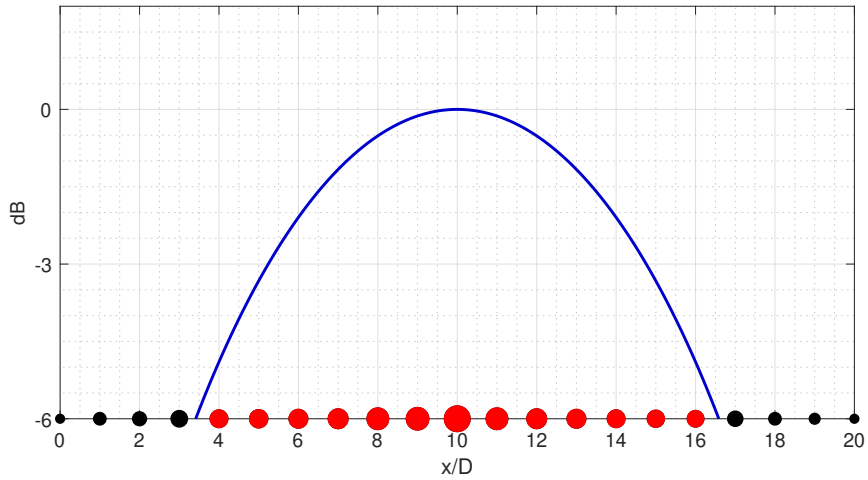

(a) 1 kHz beam battern

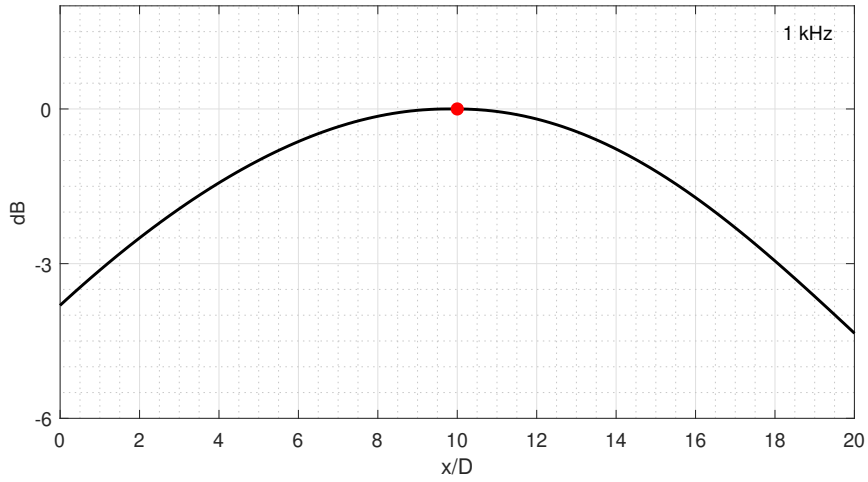

(b) 1 kHz source strength distribtuion with the array focused at $x/D = 10$

Figure 4.4: Example of the beam pattern's main lobe's beam width effect on the measuring of the source location for the 1 kHz source in a jet: (a) 1 kHz beam pattern with noise sources simulated as points and (b) the measured 1 kHz source strength distribution with the point of measurement highlighted.

lobe for 1 kHz beam pattern is approximately 13 diameters. Because the beam width is so large, the point sources from $x/D = 4$ to $x/D = 16$ (plotted in red) are encapsulated by the main lobe when it is focused at $x/D = 10$. Unlike the 20 kHz case, there are now multiple noise sources that have a significant effect on the source strength shown by the point in Figure 4.4b. Because more noise sources affect the measured source strength at each measurement location, the resulting noise source strength distribution appears wider

than it should. While the distribution of noise sources for low frequency cannot be trusted, the peak location of said distributions should still have some merit. In essence, the wide main lobe can be thought to spatially average the contributions of many noise sources of the same frequency in a region, while more heavily weighting the contributions of those nearest to the measurement location. This is because the center of the main lobe is the only location at which there are no losses of signal. This results in the location "peak value" of the noise source source distribution being in the same location as the centroid of all of the noise sources. The meaning behind "peak locations" and "centroid locations" is discussed in the next section.

The next logical questions are "Is there any precedent for this?" and "How will this data be used?" To answer the first question, as discussed in Chapter 2, Chu et al. [26] and Fisher et al. [27] have both shown similar distributions of noise sources for a given frequency as those shown in Figure 4.2. In fact Fisher et al. [27], who use the Polar Correlation technique, specifically mention that the lowest frequencies are difficult to resolve and as a result appear as very symmetric, very distributed source strength distributions. Next, to answer the second question, a discussion on the differences between peak and centroid values is performed.

4.2.2 Peak and Centroid Source Locations

Even though knowledge of the source strength distribution is useful, it is not very easy to display when one is trying to show the source location for hundreds of frequencies at a time. In this case, it is much simpler to represent the distribution as a point that allows for the data to be compared more easily. For each distribution there is a case to be made to use one of two different points for this purpose: the location of the peak value or the location of the centroid of the distribution. The location of the centroid is calculated very similarly to that of a mass centroid, but using sound pressure level instead of mass.

For the majority of this work, the location of the peak value of the source strength

distribution, as first shown in Figure 4.2, is the location that is used for the noise source of the given frequency. This is mainly for two reasons: (1) the software used for processing the beamforming data does not generate centroid locations by default and the method available cannot be automated and (2) identifying centroids locations is impractical for complex jet sources like those in shock containing jets due to multiple noise sources at a given frequency. However, for selected subsonic conditions, centroid locations are shown. This allows a comparison can be made between the present results and those obtained by Fisher et al. [27], who used only the centroid location to plot noise source location curves.

Before showing how the centroid locations are calculated in this work, first a demonstration on how peak and centroid locations differ is shown in Figure 4.5. This figure contains the same source strength distribution shown earlier in Figure 4.2; however, the location of the peak sound power and the location of the centroid of the source strength distribution are plotted as well. The 20 kHz, 10 kHz, and 5 kHz source strength distributions, shown in Figures 4.5a through 4.5c, respectively, are very asymmetrical around their peak value. This results in the centroid location being somewhat downstream of the peak location. In contrast, the 1 kHz source strength distribution, shown in Figure 4.5d, is very wide and symmetrical. As a result, the location of the source peak and centroid is practically the same for this frequency. These are the same trends observed by Fisher et al. [27]. Fisher et al. also mentioned that as measuring resolution decreases, the peak of the source strength distribution aligns with the centroid location of the sources. This enforces the claim made in the previous section, that while the source strength distribution for low frequency noise sources cannot be assumed to be accurate, its peak value can reliably be used to determine the centroid location of noise sources for the given frequency. Because the measured peak source location starts representing the centroid location of a given frequency at lower frequencies, plots of peak source location likewise transition from showing peak source location at higher frequencies to centroid source locations at lower frequencies. This is not a large issue, however, as the difference between peak and centroid locations at the upper

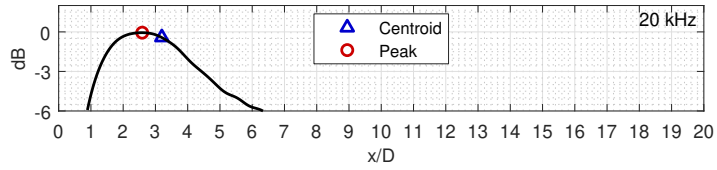

(a) 20 kHz source strength distribution

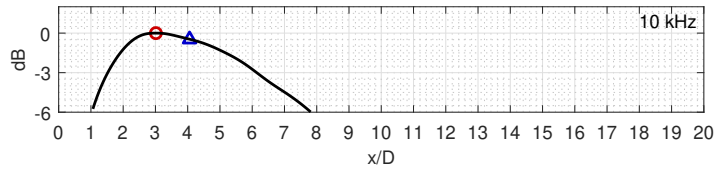

(b) 10 kHz source strength distribution

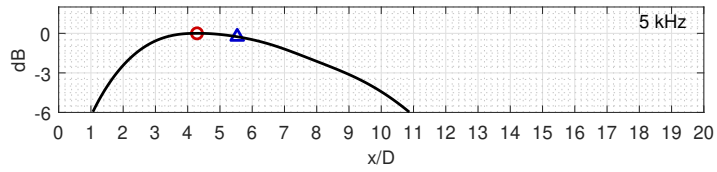

(c) 5 kHz source strength distribution

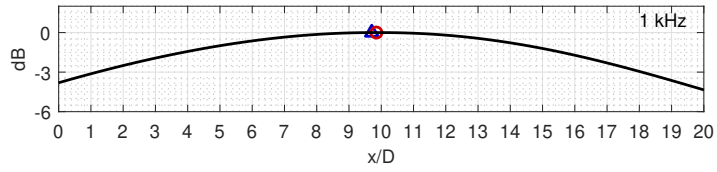

(d) 1 kHz source strength distribution

Figure 4.5: Noise source strength distributions along the nozzle centerline at four different frequencies for the 1.60-inch conical jet operated at Mach 0.8: (a) 20 kHz, (b) 10 kHz, (c) 5 kHz, and (d) 1 kHz. The locations of peak source strength and the centroid of the source strength distribution are plotted as well.

frequencies measured in this work is less than a diameter. Furthermore, since all the source location measurements performed in this work are only plotted using "peak" values, they are all equally impacted by the lowered source location resolution, and thus they can be compared with each other without resolution impacting the differences between the plots (i.e. peak locations are compared with peak locations and centroid locations are compared with centroid locations).

In this work, the source centroid location is calculated the same way as a mass centroid, with the sound pressure level (SPL, first converted from dB back to pressure squared) at each location instead of mass. The equation used for this calculation is Equation 4.1.

$$\frac{x_{cent}}{D} = \frac{\sum_{x=x_1}^{x_2} \frac{x}{D} 10^{SPL_x/10}}{\sum_{x=x_1}^{x_2} 10^{SPL_x/10}} \tag{4.1}$$

Ideally, x_1 and x_2 in this equation would be 0 and ∞, respectively; however, due to measuring region limitations and side lobes at higher frequencies, this region is limited to only the area around the peak that is within six decibels of the peak value. Increasing the range of this region does not have much effect on the centroid location unless the increased region intersects a side lobe, resulting in a discontinuity in the centroid source location.

4.2.3 Summary of Terminology and Interpreting Beamforming Results

The ability for the beamformer to accurately determine the locations of noise sources is highly dependent on the array response. For a given frequency, the beamformer has a specific beam pattern, which affects both the resolution of measurement and whether "false positives" (side lobes) show up. With respect to the effects of the beam pattern on jet noise source location, at high frequencies the beamformer can accurately provide the source strength distribution, and at low frequencies the beamformer outputs a source strength distribution that can only be used for its peak location. As having a distribution of sound power for each frequency is very difficult to show when hundreds of frequencies are

measured, the peak location of each distribution is used in this work as the indication of the source location of that frequency.

4.3 Comparison of Beamforming Results with Existing Studies

There have been a number of studies that have examined the source location of one-to-two inch diameter nozzles operating at Mach numbers around 0.8, each using a different method of source location to obtain their results. These studies were described in detail in Chapter 2. In this section, the results of these studies are compared with those obtained in the current study for a one-inch and a 2.44-inch conical nozzle operated at Mach 0.8 using an acoustic beamforming as the source location method.

Data from selected past studies is presented in Figure 4.6. When plotted together as

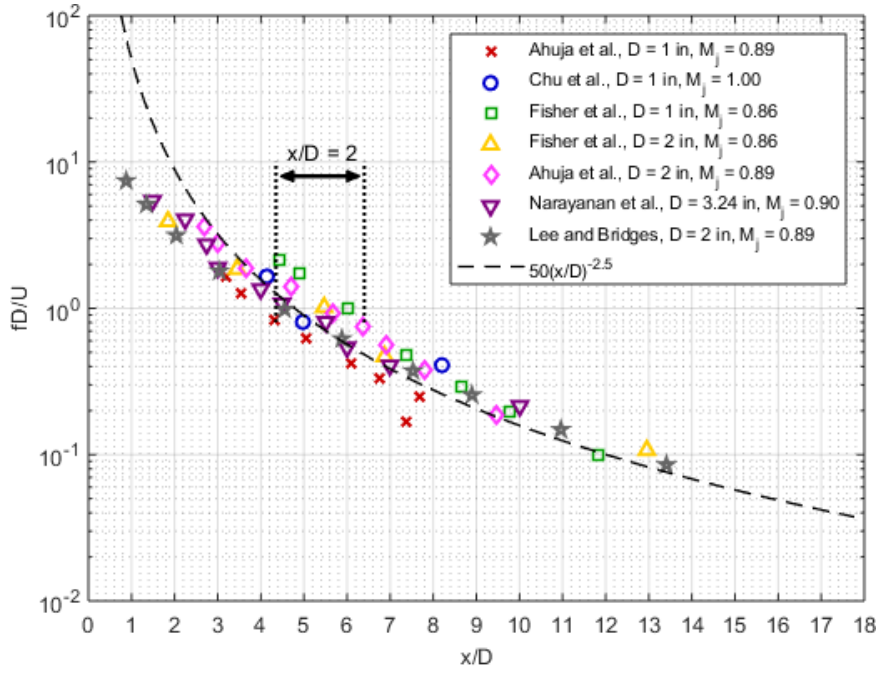

Figure 4.6: Subsonic jet noise source data acquired from four different source location methods: the Acoustic Mirror technique by Chu et al. [26], the Polar Correlation technique by Fisher et al. [27], the Phase Minimum technique by Ahuja et al. [15], and with a linear phased array by Narayanan et al. [32] and Lee and Bridges [5].

Strouhal number versus x/D, it is clear that there is a spread of about two nozzle diameters between the studies for a given Strouhal number. A disagreement on the order of

two diameters in results may be due to slightly different jet conditions, nozzle geometry, and test facilities; however, at least part of the source location discrepancy is attributed to differences in what each method defines to be the source. A best fit curve is drawn through these studies, given by Equation 4.2, and is used as a reference in later plots.

$$\frac{fD}{U} = 50\left(\frac{x}{D}\right)^{-2.5} \tag{4.2}$$

As shown in Section 4.2, for a given frequency there is not a single point in space downstream of a subsonic jet exit that solely produces the noise for that given frequency. Instead, subsonic jet noise sources appears to be distributed along the jet axis such that their strength increases until some downstream distance and then falls off. Westley and Lilley [24] noted that these distributions became longer at lower frequencies. Fisher et al. [27], using the Polar Correlation Technique, noted that the high frequency distributions were not symmetric around their peak value. The source strength would rise quickly before the peak and taper off slowly downstream; this results in the centroid of the source being located further downstream than the peak value. As shown in the previous section, the difference between the peak value and the centroid value decreases with frequency, because the distributions become more symmetric at lower frequencies (often due to measurement limitations). Of the studies shown in Figure 4.6, the data acquired by Chu et al. [26], Narayanan et al. [32] and Lee and Bridges [5] uses the source peak locations and the data acquired by Fisher et al. [27] uses the source centroid locations. The source location data from Ahuja et al. [15] was obtained using phase information, making it difficult to determine which of these two categories it falls under.

This section is divided into two parts: (1) an overview of the source location results obtained in this present study and (2) a comparison of these results with those from other studies using different source location techniques.

4.3.1 Source Location Results of the Present Study

In section 4.2, it was shown how the peak locations and centroid locations of the measured source strength distribution differ as a function of frequency. When these locations are plotted with respect to their frequency (or their Strouhal number), the resulting plot is called a "noise source distribution." Figures 4.7 through 4.9 contain the noise source distributions obtained for this current work for 1.00-inch, 1.60-inch, and 2.44-inch jets operated at Mach 0.8, respectively. As is the convention in jet noise literature, these distributions are plotted as Strouhal number (fD/U) versus normalized downstream distance (x/D). For the convenience of the reader, the dotted lines in these plots point out the Strouhal numbers associated with 1 kHz, 5 kHz, 10 kHz, and 20 kHz. Both the peak locations and centroid locations of the source strength distributions are plotted for each Strouhal number. The curve from Equation 4.2 is plotted as for a point of reference.

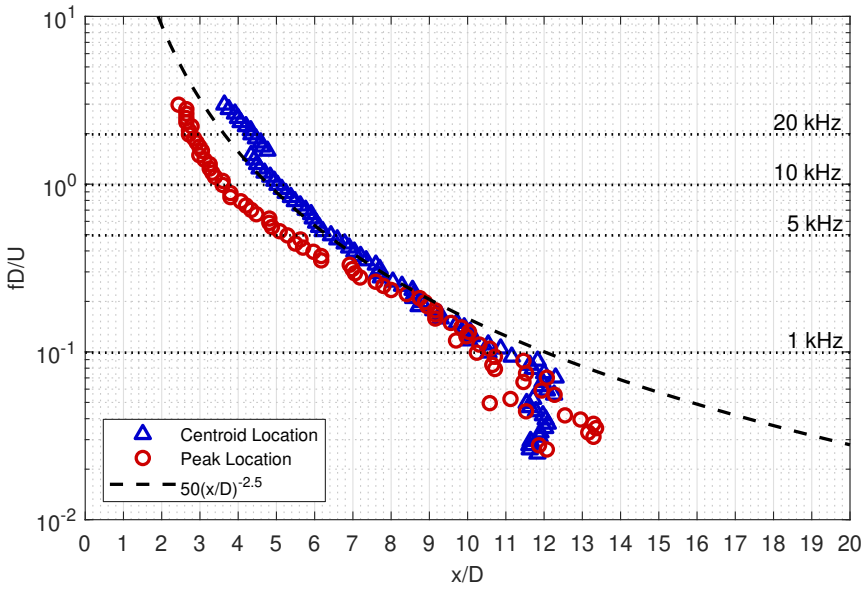

Figure 4.7: Noise source distribution for a 1.00-inch conical jet at Mach 0.8. Both peak locations and centroid locations are shown.

The noise source distributions shown in Figures 4.7 through 4.9 all exhibit the same trends as expected for subsonic jet noise. The highest frequency noise sources appear to come from near the nozzle exit and as frequency is decreased the noise sources appear to

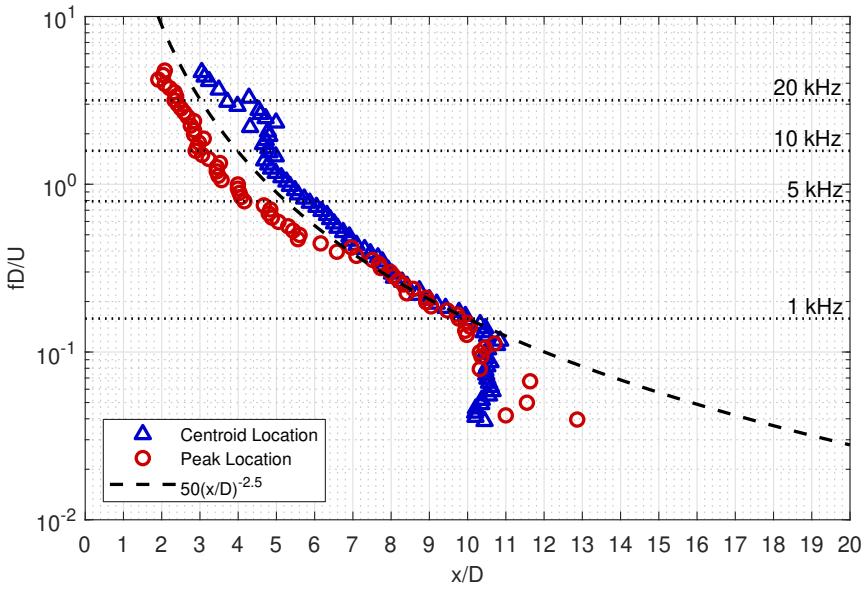

Figure 4.8: Noise source distribution for a 1.60-inch conical jet at Mach 0.8. Both peak locations and centroid locations are shown.

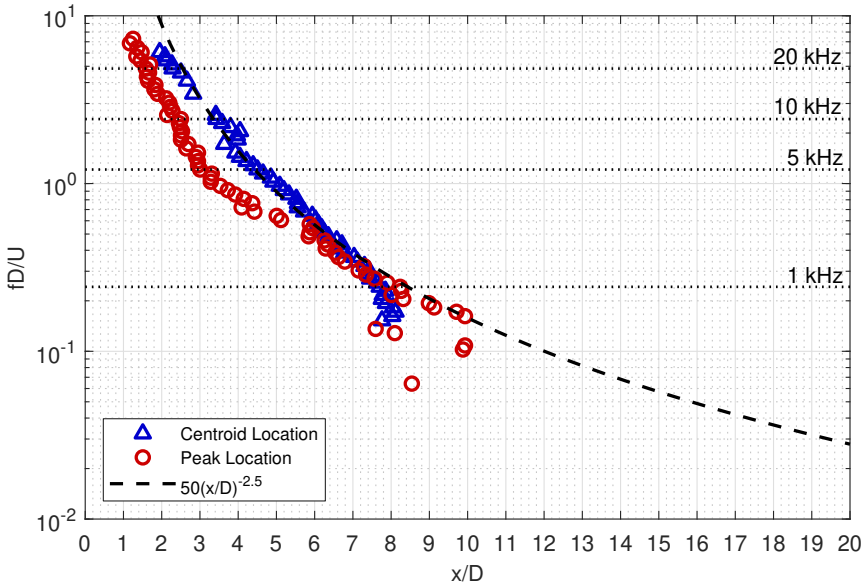

Figure 4.9: Noise source distribution for a 2.44-inch conical jet at Mach 0.8. Both peak locations and centroid locations are shown.

come from further downstream. For the 1.00-inch and 1.60-inch nozzles, it appears as if the peak and centroid locations are mostly the same for frequencies below about 2000 Hz. At frequencies above this value, the peak location is always upstream of the centroid location. The noise source distributions for the 2.44-inch nozzle in Figure 4.9 does not quite follow these rules; the data appears to cross at around 1 kHz, below which the centroid location appears to be upstream of the peak location. The discrepancy at this condition is mostly likely due to difficulties in calculating the centroid location for the 2.44-inch nozzle. At a measuring distance of 45.5 inches, the beamformer can easily measure the whole extent of the source strength distributions of low frequency sources for the smaller nozzles. The large 2.44-inch nozzle, however, has low frequency source strength distributions that extend well past the measuring window of the beamformer. As a result, part of this distribution is cut off at lower frequencies, skewing centroid calculations.

The noise source distributions shown in Figure 4.8 correspond to the source strength distributions shown in Figure 4.5 from the previous section. As mentioned in that section, as the resolution of the beamformer becomes poor at lower frequencies, the peak value of the source strength distributions begins to approach the centroid location for the given frequency. In Figure 4.8 it can be seen that about a Strouhal number of about 1.0, the beamformer's resolution is good enough to accurately measure the source strength distribution and the peak location can be trusted as the true peak location. Below this value but above a Strouhal number of about 0.4, the peak location appears to be approaching that of the centroid. In this range, the measured peak location is probably somewhere between the true peak location and the centroid location. Finally, at Strouhal numbers below 0.4 the measured peak location is the same as the centroid location of the noise sources, due to the poor resolution of the beamformer. In order to better capture the source locations at these lower Strouhal numbers, a larger array would need to be designed and built that has a narrower beam pattern at low frequencies. As doing so would be costly and is beyond the scope of this work, these measuring oddities are thusly tolerated.

4.3.2 Comparisons of Current Source Location Results with those of Prior Studies

The comparisons of the current work with those of past studies in this section are limited to studies that use nozzles with diameters of one and two inches and have data at Mach numbers that are close to 0.8. The past studies that meet both these criteria are the ones by Fisher et al. [27] and Ahuja et al. [9], both shown previously in Figure 4.6. The data from these studies are compared against source location data from a one-inch conical nozzle and a 2.44-inch conical nozzle operated at Mach 0.8. Using a 2.44-inch nozzle to compare with the source location of two-inch nozzles at Mach 0.8 is acceptable because, at Mach 0.8, the noise source distributions for conical nozzles are independent of diameter when plotted as Strouhal number vs x/D. Evidence of this independence is shown in Chapter 5. Furthermore, small differences in Mach number are acceptable for these comparisons as well, as the subsonic noise source distributions for conical nozzles are also independent of Mach number (for the range of Mach numbers used in this chapter) when plotted this way.

This subsection is divided into two parts: (1) a comparison of the beamformer's peak source location with data from Ahuja et al. [9] and (2) a comparison of the beamformer's centroid source location with data from Fisher et al. [27]. As discussed earlier, the data from Fisher et al. uses the centroid locations of the source strength distributions as the source locations of the jet, requiring the data to be compared to the centroid locations obtained in this present work. For the data from Ahuja et al., on the other hand, it is not clear from the methodology behind the Phase Minimum Technique whether the measured source location is the peak location, centroid location, or somewhere in between. As a result, the data from this study is compared with the peak location data from this present study. These comparisons are also plotted along with the best fit curve first shown in Figure 4.6 for another point of reference.

Source location derived from the peaks of the source strength distributions, obtained with acoustic beamforming, is plotted as "Current Work" in Figure 4.10. This data is for

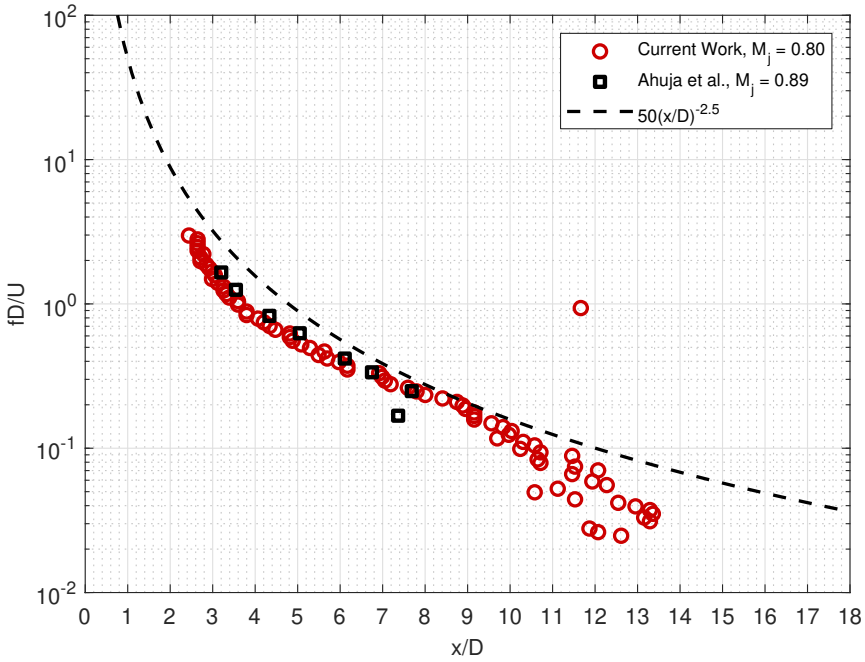

Figure 4.10: Comparison of beamforming peak source location for a 1.00-inch conical jet operated at Mach 0.8 from the current work with similar jet data acquired with the Phase Minimum Technique by Ahuja et al. [15].

the one-inch conical nozzle operated at Mach 0.8. The source location data for a one-inch jet ran at Mach 0.89 from Ahuja et al. [15] is plotted as well. The one-inch nozzle used by Ahuja et al. [15] is the exact same nozzle used in this present work. These two sets of data lie practically on top of each other. This helps illustrate the importance of comparing source location using the same nozzle geometry, as the noise source distribution is repeatable even when using two totally different source location methods. When compared to the best fit curve of all the other studies, the present data is within one diameter for all noise sources above a Strouhal number of about 0.1.

The beamforming data shown in Figure 4.11 are the peak noise sources for the 2.44-inch nozzle operated at Mach 0.8. Likewise, data for a two-inch jet operated at Mach 0.89

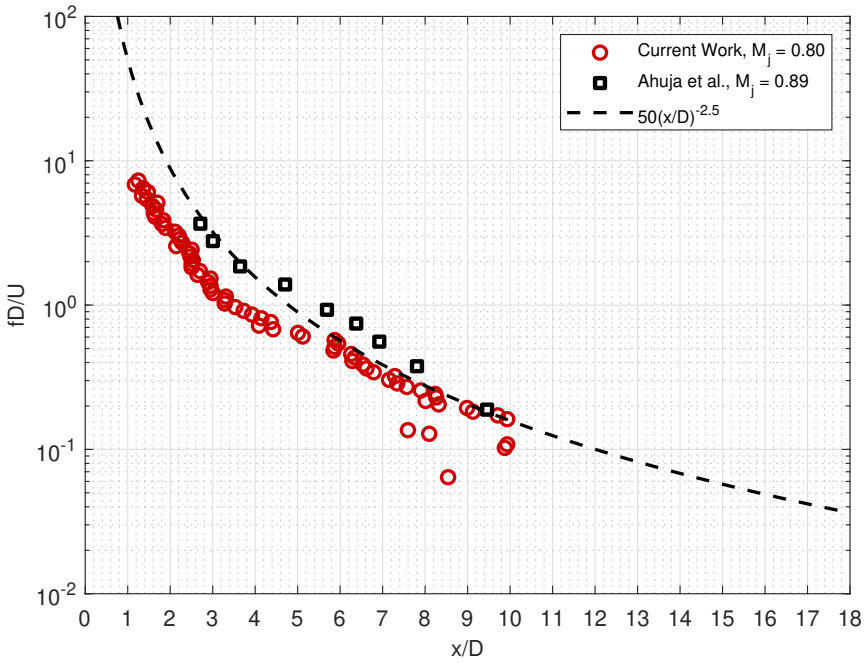

Figure 4.11: Comparison of beamforming peak source location for a 2.44-inch conical jet operated at Mach 0.8 from the current work with similar jet data acquired with the Phase Minimum Technique by Ahuja et al. [15].

from Ahuja et al. is plotted as well. The data from Ahuja et al. approximately lies on top of the best fit curve for this condition, whereas the data for this current study is around a diameter upstream of the curve for Strouhal numbers above 0.5. At Strouhal numbers below 0.5, the peak values from the present study agree well with the best fit curve. The data from the present study and from Ahuja et al. do not agree as well in Figure 4.11 as they do in Figure 4.10; this is most likely due the geometry differences in the conical two-inch nozzle used by Ahuja et al. and the conical 2.44-inch nozzle used in the present study. That being said, in both cases the data from the current study is within one diameter of the best fit curve of other studies, which is no worse than the spread shown by those past studies.

A Comparison of Beamformer Centroid Location with the Polar Correlation Technique

Source location derived from the centroids of the source strength distributions, obtained with acoustic beamforming, is plotted as "Current Work" in Figure 4.12. This data is for the 1.00-inch conical nozzle operated at Mach 0.8. Source location data obtained for a

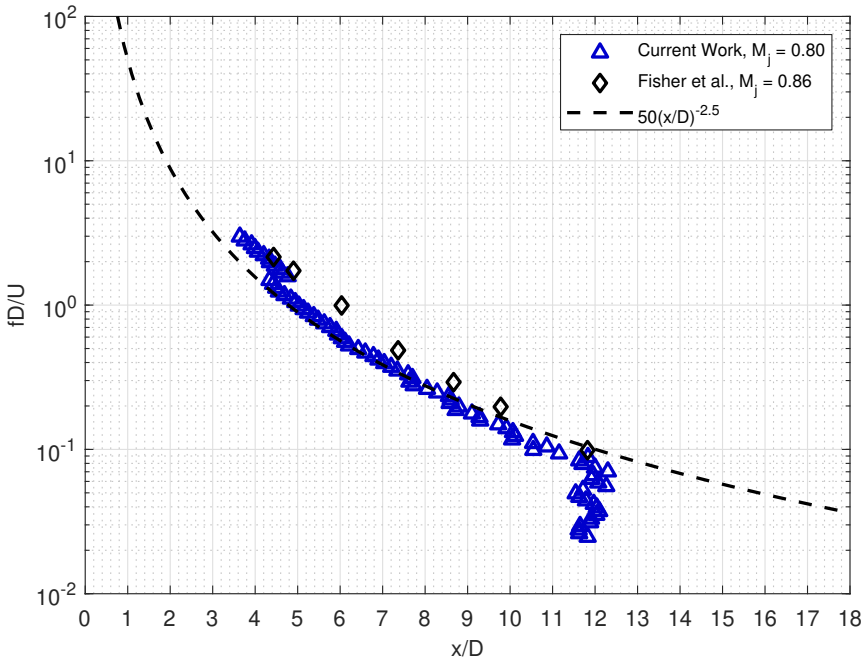

Figure 4.12: Comparison of beamforming centroid source location for a 1.00-inch conical jet operated at Mach 0.8 from the current work with similar jet data acquired with the Polar Correlation Technique by Fisher et al. [27].

1.00-inch jet ran at Mach 0.86 using the Polar Correlation Technique by Fisher et al. [27] is plotted as well. These two methods agree within one diameter of each other, with the locations measured by Fisher et al. being slightly downstream of the locations measured with this present study. For Strouhal numbers between 1.5 and 0.1, the centroid data from the present study matches almost perfectly with the best fit curve of the old studies. At Strouhal numbers above 1.5, side lobes had a slight effect on the centroid calculation, shifting it downstream. At Strouhal numbers below 0.09 the accuracy of the beamformer starts to go down, and as a result the calculated centroid locations are harshly effected.

The beamforming data shown in Figure 4.13 are the peak noise sources for the 2.44-inch nozzle operated at Mach 0.8. Likewise, data for a 2.00-inch jet operated at Mach 0.86 from Fisher et al. is plotted as well. Both sets of data are practically on top of the mean data curve of the old studies. The data from the current study starts to diverge from this curve around $x/D = 8$ due to the measuring limitations of the beamformer described before.

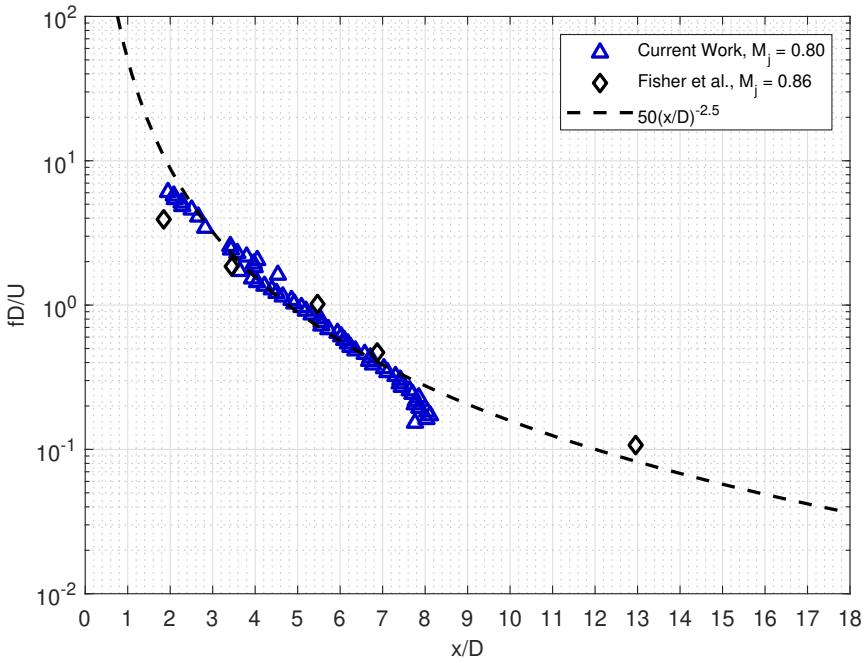

Figure 4.13: Comparison of beamforming centroid source location for a 2.44-inch conical jet operated at Mach 0.8 from the current work with similar jet data acquired with the Polar Correlation Technique by Fisher et al. [27].

4.3.3 Summary of the Comparison of Beamforming Results with Existing Studies

The data from this present work shows very good agreement with those of other studies that use different source location techniques. Both the peak and centroid locations obtained with the acoustic beamformer lie within one nozzle diameter of a best fit curve of selected older studies. This level of agreement is about the same as the spread within the older studies themselves.

4.4 Validation with Nearfield Contour Data

While the results in the previous section show decent agreement between source location obtained with acoustic beamforming in the current work and other methods in prior studies, each method used different nozzles and different facilities from all the rest. It is speculated that these differences may result in vastly different nozzle exit boundary layers, which could affect the jet noise source distributions. To remove this uncertainty, the noz-

zles in the current study were also tested using nearfield noise contours. While different facilities are used in this work for the beamforming and noise contour measurements, the piping in each facility, consisting of the 4-inch diameter supply duct, the plenum chamber, and the attached nozzle, is identical. This results in the most accurate comparison of two source location methods, just short of using the exactly same facility for both.

For the contour tests, a single microphone is traversed (see Figure 3.9 for an illustration of the mount) in an approximately 15 diameters by 15 diameter grid downstream of the jet, acquiring data for one second at each point in the grid. Even though for each test case hundreds of contour plots (one for each frequency) could be generated, doing so would have been excessive and redundant; detailed information about the jet source distribution can be gleaned from just a few contour plots and a plot of all the locations. Additional contour plots are shown in Appendix A.

This section examines the source locations of a conical 1.60-inch jet operated at Mach 0.8 using both an acoustic beamformer and nearfield noise contours. The shapes and source location of a few selected contours are examined and the resulting nearfield contour source locations are compared with those acquired with the acoustic beamformer.

4.4.1 Nearfield Sound Contour Plots

Nearfield sound contours for the conical 1.60-inch jet operated at a Mach number of 0.8 are depicted in Figure 4.14. The shapes of the nearfield contours of this jet change with frequency. If one follows the conventional method of estimating the source location using nearfield contours, the source would be located at the intersection of the dashed line and the x-axis as shown. As one progresses from Figure 4.14a to Figure 4.14f, it is shown that the sources of the normalized frequencies of $fD/U = 1.620$, 2.433, 3.245, 4.058, 4.769, and 5.581 shift from a location of x/D of about 4.0 to about 3.0, 2.5, 2.0, 2.0, and 2.0, respectively. These six contour plots illustrate what many other studies [5, 6, 13, 15, 24, 26, 27, 32] have shown: that higher frequency sources are located closer to the nozzle exit than

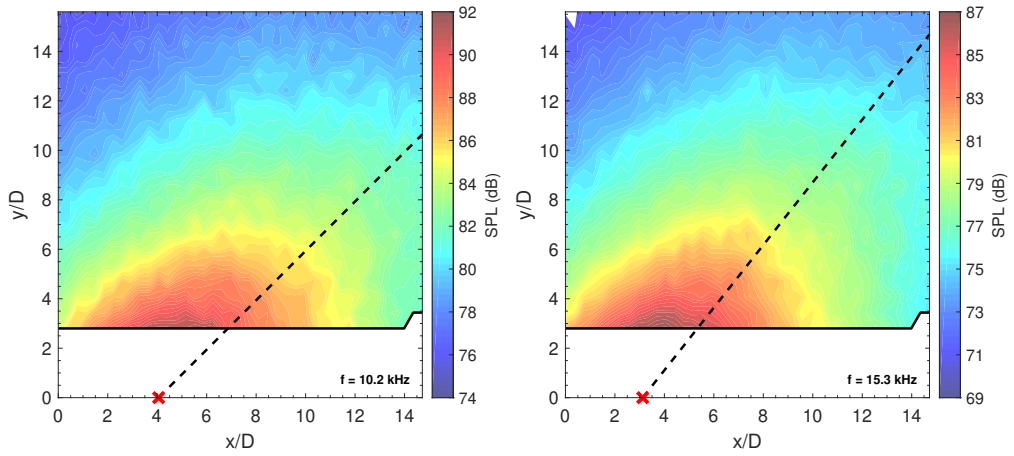

(a) fD/U = 1.620 (b) fD/U = 2.433

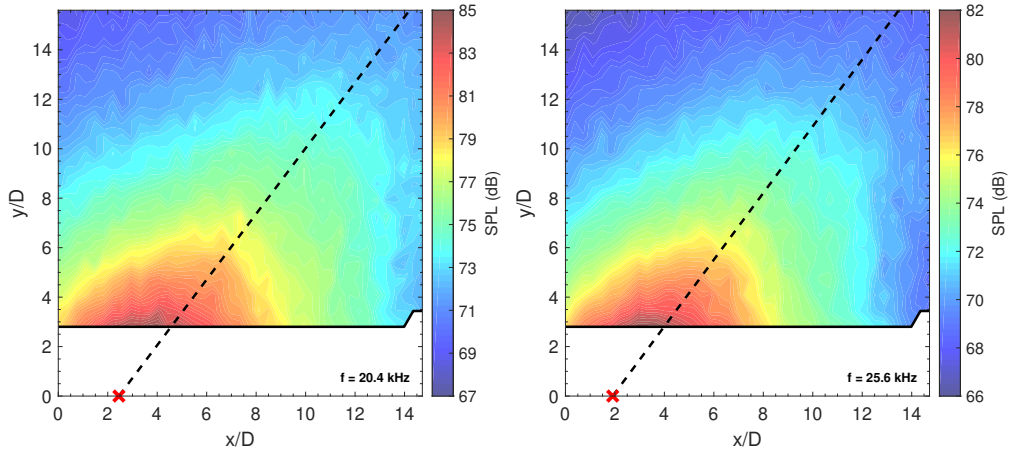

(c) fD/U = 3.245 (d) fD/U = 4.058

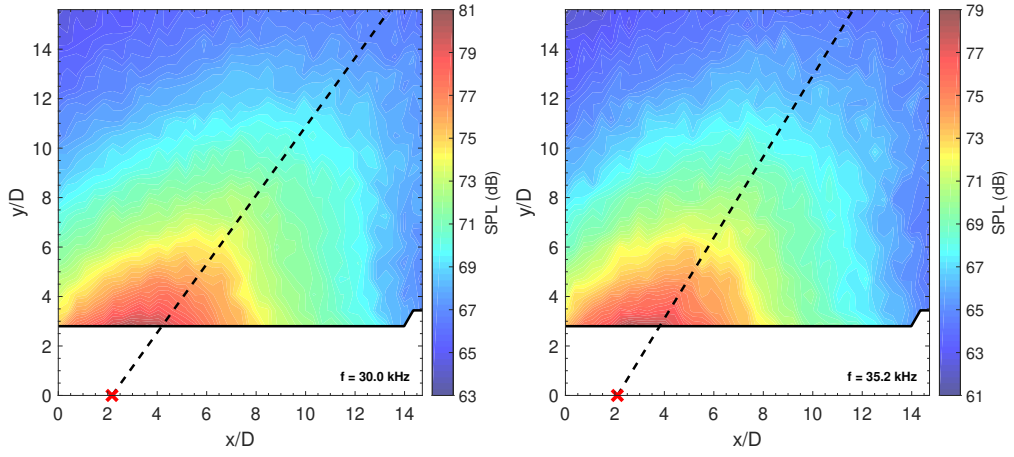

(e) fD/U = 4.769 (f) fD/U = 5.581

Figure 4.14: Selected noise contours for a conical 1.597-inch nozzle with Mach 0.8 flow.

the lower frequency sources.

Before moving on, it is worth noting that the lines drawn through each contour to determine the source location of that frequency are drawn by hand. While efforts have been made (see Section 3.2.3 in Chapter 3) to remove personal bias from this process, there is still some degree of subjectivity in the process. As a result, the source location can vary with this method by as much as ± 2 diameters depending on how the line is drawn.

4.4.2 A Comparison of Beamformer Source Location with that of Nearfield Sound Contours

As was done with the data from previous studies, the source locations obtained from each frequency contour can be seen plotted in the form of Strouhal number (fD/U) versus normalized downstream distance (x/D) in Figure 4.15. Each point of this source location data is obtained using contour plots similar to the ones shown earlier in Figure 4.14. Additional contour plots can be seen in Appendix A. For comparison, the source location of the same condition obtained with the acoustic beamformer is overlaid on top of the noise contour data. Both the peak and centroid location results from the beamformer are shown due to it not being readily apparent from the method as to which (if either) the noise contours points to. While Figure 4.15a displays the full source location range for both source location methods, only data in the range of Strouhal numbers of one to ten are useful for comparison purposes. This is due to the differences in the systems used to acquire the data and process the source locations for each method. For simplicity, Figure 4.15b shows the same data but the axes are set such that only the data relevant for comparing the two methods is shown. A dashed line is drawn through the center of the contour data to be a point of reference.

From examination of the noise source distributions from the two methods shown in Figure 4.15b, it is apparent that the nearfield contour method tends to locate the jet noise source as somewhere between the beamformer peak location and the beamformer centroid location. As the spread of the noise source distribution of the nearfield contours is about one

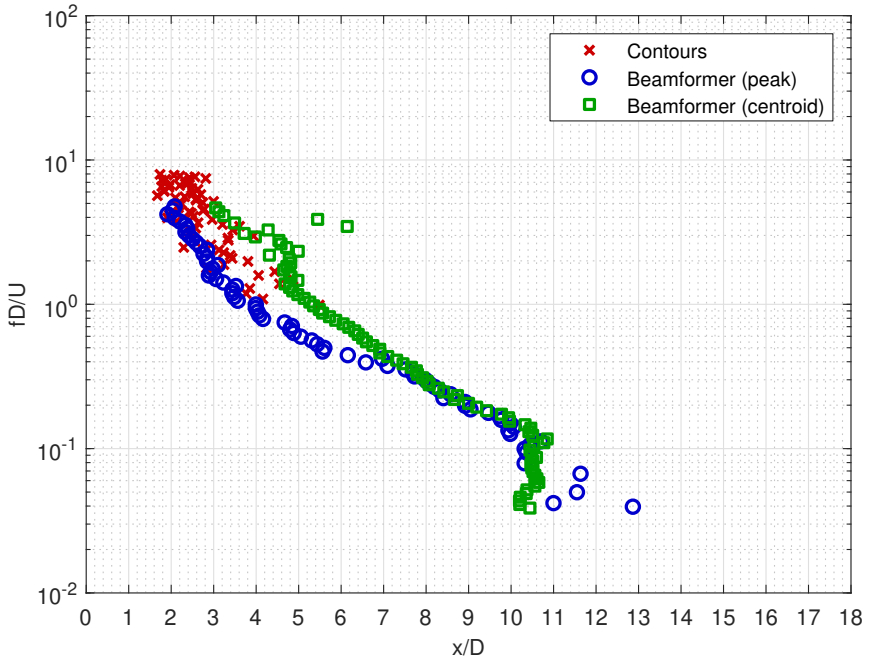

(a) Full plot range

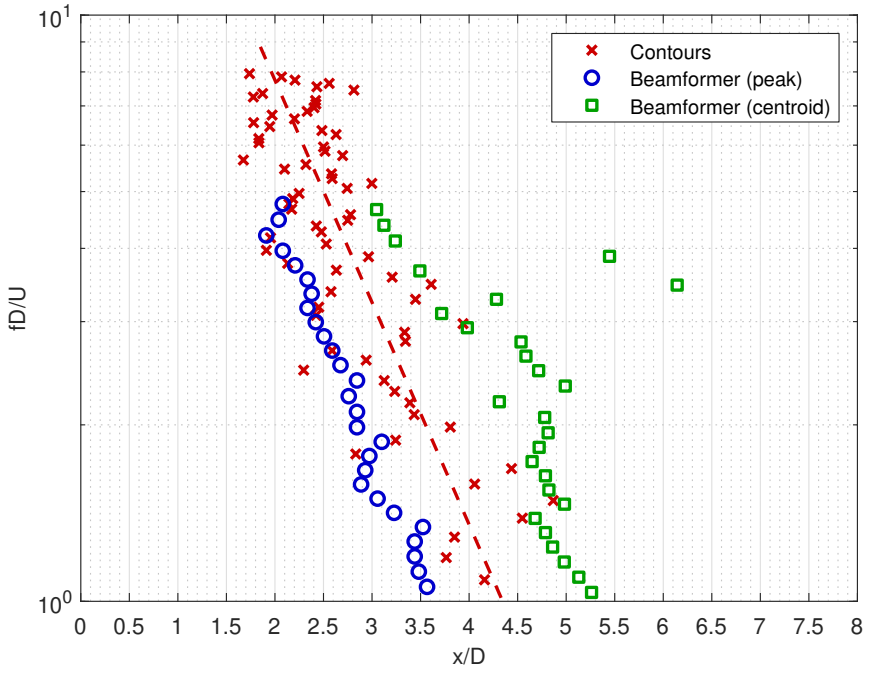

(b) Zoomed in on relevant data

Figure 4.15: Comparison of beamforming and nearfield noise contour source location methods for a 1.60-inch conical jet operated at Mach 0.8. Full data range is shown in (a) and only data relevant for the comparison is shown in (b).

diameter, it can be said to agree with the noise source distributions of the beamformer (both the centroid and peak values) within 0.75 diameters for most Strouhal numbers. This claim is made on the basis of using the dashed mean line of the contour data as reference. Because the source location of the nearfield contours can vary by up to ± 1 diameters depending on how and who draws the lines connecting their peaks, this spread of ± 0.75 diameters between the beamforming method and the contour method may be mainly due to these weaknesses in the nearfield contour method as a source location tool. That being said, an agreement of noise source distributions that is within ± 0.75 diameters is well within the spread shown by past studies in Figure 2.19.

4.4.3 Summary of the Validation of Beamforming with Nearfield Contour Data

On average, the beamforming and noise contour source location methods agreed within 0.5-1 nozzle diameters (on average about 0.75 diameters) for a 1.60-inch conical jet operated at Mach 0.8. Due to the nature of how the source location is measured using noise contours, by drawing a line through the contour peaks and finding the intersections with the jet axis, there is an inherent ± 2 diameter uncertainty in the source location in the results of this method. The data collected shows that the difference between the two methods is on the same order as the difference between methods from past studies listed in Figure 2.19.

4.5 The Ability of Beamforming to Detect Changes in the Noise Source Distribution due to Enhanced Mixing Caused by Tabs

One application of noise source location tools for jet noise, is to examine how certain modifications of nozzle geometry affect the jet noise source distributions. In this section, the beamformer is used to examine how the source location of a one-inch conical jet operated at Mach 0.8 changes due to the addition of tabs to the exit of the nozzle. The tabs are two 5/16-inch, triangular, aluminum protrusions that are attached 180 degrees from each

other in the nozzle exit plane. They can be seen depicted in Figure 3.3 in Section 3.1.

The noise source distributions of the 1.00-inch jet, both with and without (baseline) tabs, are plotted in Figure 4.16. The tabs, very similarly to chevrons in full size jets,

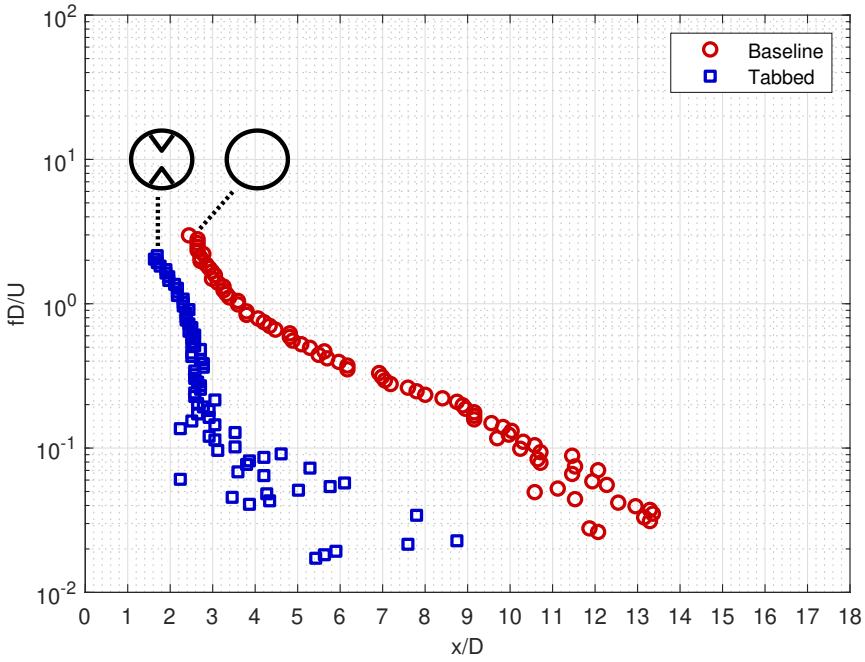

Figure 4.16: Comparison of the noise source distributions of a jet with and without tabs obtained with beamforming. The base nozzle is one inches in diameter and both cases are run at Mach 0.8.

enhance the mixing of the jet and as a result cause the potential core of the jet to shrink. The enhanced mixing in a tabbed jet means that the turbulent mixing layer of the tabbed jet grows much quicker than that of a non-tabbed jet. Because of the quicker growth, a tabbed jet has noise sources of a given frequency located much further upstream than than of a non-tabbed jet. This can be seen in Figure 4.16. The highest frequency noise sources (around and above $fD/U = 1$) are shifted upstream by about one nozzle diameter. The lowest frequency noise sources are shifted by an even greater amount; at a Strouhal number of about 0.1 the tabbed jet has noise sources that are about eight diameters upstream those of the baseline jet.

The trends shown in Figure 4.16 match those shown by Ahuja et al. [15] using the Phase Minimum Technique. A plot comparing a tabbed and non-tabbed one-inch conical nozzle

operated at Mach 0.89 is shown in Figure 2.13 in Chapter 2. This data is not directly plotted against the data from this current study because different types of tabs are used between the two studies, which may impact the comparison.

In summary, the beamformer is able to detect the change is noise source distribution of a jet due to the presence of tabs. Tabs enhance the mixing of a jet, and shift the noise sources of all frequencies upstream. The locations of the lowest frequency noise sources are observed to shift much more than those of the high frequency sources.

4.6 Effect of Observed Source Location Uncertainty on Various Applications of the Technique

In the previous sections it was shown that, depending on the technique, the source location for nozzles of similar size and jet condition can vary by about two diameters for a given Strouhal number. Similarly, it was also shown that the acoustic beamformer obtains source locations within one diameter of other existing methods. The next logical step in this analysis, therefore, is to determine how these differences would affect applications of the noise source distribution. Two of these applications are rendering nearfield data as measured to lossless data and extrapolating nearfield lossless spectra to farfield lossless spectra.

In order to render nearfield data as measured to lossless data, the measured data must be corrected for effects such as humidity, distance between the microphone and the source, and microphone incidence. Other microphone corrections, such as freefield and screen corrections, need to be applied as well; however, only the humidity corrections, the incidence corrections, and distance corrections, when applicable, require the knowledge of the locations of sources of given frequencies to be performed. Source location is required to perform these corrections, because they require both the distance and angle between the source and the microphone to be applied.

When scaling jet noise data to full scale, it is often assumed that the data was measured in the geometric farfield. When measuring in the geometric farfield, jet noise can be scaled by $1/R^2$, where R is the distance between the observation location and the nozzle exit. At a farfield measurement location, even though the jet noise sources are distributed along the jet centerline, the actual difference in distance between each source and the measurement location is very small compared to R. These small differences in distance make very little difference on the sound measured in the farfield. As a result, it is common practice to just use the location of the nozzle exit for all the noise sources, making corrections involving distances and angles to the noise sources very easy. Ahuja et al. [11] has shown that it is reasonably safe to say that data is measured in the farfield as long as the measuring location, R, is at least further away than the size of the largest wavelength of sound being measured. When measuring at distances closer than this, the data is said to be measured in the nearfield. In the nearfield, the distance between the microphone and noise sources of various frequencies are drastically different. Similarly, noise sources of each frequency have sound paths that result in different angles of incidence on the measuring nearfield microphone. As a result, knowledge of the jet's noise source distribution becomes important for correcting the nearfield data. Once lossless data arriving from a given source at a given microphone is available, it is a simple matter to extrapolate the SPL of that frequency to a farfield microphone location. Likewise, measured lossless data at a farfield microphone can be extrapolated in the direction of the source of a given frequency to calculate the nearfield noise.

To determine the effects of source location uncertainty on these applications, both farfield measurements (at 90 diameters) and nearfield measurements (at a sideline distance of 12.5 diameters) are acquired for the 1.60-inch conical jet operated at a Mach number of 0.8. At this condition, the acoustic beamformer is also used to obtain the jet's noise source distribution. A power series was fit through the source distribution with an R-squared value

of 0.968 and can be seen in Equation 4.3 below:

$$x/D = 4.018\left(\frac{fD}{U}\right)^{-0.438} + C. \tag{4.3}$$

The C in the source location fit offsets the source location fit at all frequencies to represent uncertainty in the measured distribution. This curve can be seen plotted through the actual data as well as offsets from -1.0 diameters to 2.0 diameters in Figure 4.17. The offsets

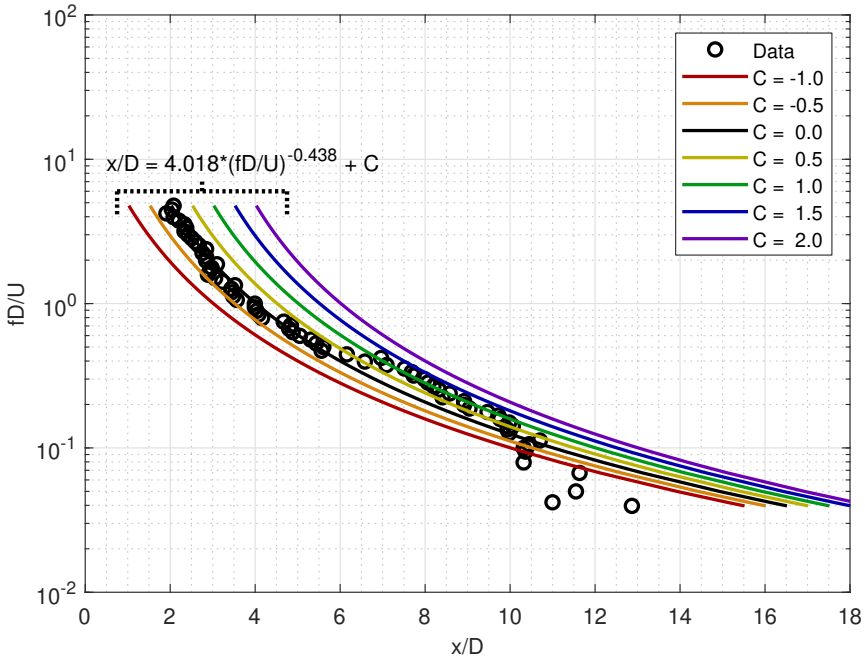

Figure 4.17: Source location for 1.60-inch conical nozzle operated at Mach 0.8. Power fit through the data has an R-squared value of 0.968 and has been offset to represent source location uncertainty.

chosen represent the uncertainties shown in the previous section. Lower offsets than -1.0 were not used because they would result in measured frequencies having source locations upstream of the nozzle exit.

This section contains two main subsections: "Rendering Nearfield Acoustic Data to Lossless Data" and "Extrapolation of Nearfield Acoustic Data to the Farfield". These subsections use the fit offsets described above to observe the effect of source location data on the resulting spectra.

4.6.1 Rendering Nearfield Acoustic Data to Lossless Nearfield Data

When acquiring jet noise data, measures need to be taken so that differences in equipment and environment do not have an effect on the results. These measures are often corrections that are applied to the data that account for any of these differences. For this work, three types of corrections are applied to the recorded data: microphone response corrections, microphone incidence corrections, and humidity corrections. Of the three corrections, only the incidence and humidity corrections rely on noise source location information. While brief descriptions of the incidence and humidity corrections are supplied in this section, a more detailed discussion on rendering microphone data to lossless can be found in Section 3.2.5 of Chapter 3.

Acoustic data needs to be corrected for humidity because sound is attenuated differently at different frequencies when it propagates through the atmosphere. To put it simply, higher frequency noise is attenuated much quicker than lower frequency noise. The amount of attenuation is a function of atmospheric conditions such as humidity, temperature, and pressure. For this work, the attenuation due to humidity is calculated, as a function of given frequency and measured atmospheric conditions, using the method listed in ANSI S1.26-1995 [49]. This calculation results in an attenuation value with units of dB/ft. Using this value and the distance between the microphone and each noise source, the effect of humidity can be removed from the data.

Data measured with a microphone needs to be corrected for microphone incidence. The physical geometry of the microphone has an impact on any sound measured at incidence angles other than zero (in line with the microphone itself). As a result, the sound level measured by a microphone at incidence angles greater than zero is reduced. This reduction effect, as it was with humidity attenuation, increases with frequency of the measured sound. Fortunately, microphone manufacturers provide tables that list incidence losses as a function of frequency and incidence angle, which can be interpolated to correct for the losses.

Using the known position and orientation of each nearfield microphone as well as the calculated source location from Equation 4.3, the distance and incidence angle for each frequency to each microphone are calculated and the corrections described above are applied. When applying the corrections, the source location is purposely offset between -1 diameters and 2 diameters to see how the resulting corrected calculated spectra would differ.

Figure 4.18 illustrates the effect of these offsets on a 30.3 degree microphone and Figure 4.19 illustrates the effects on a 90 degree microphone. For these plots, the spectrum of

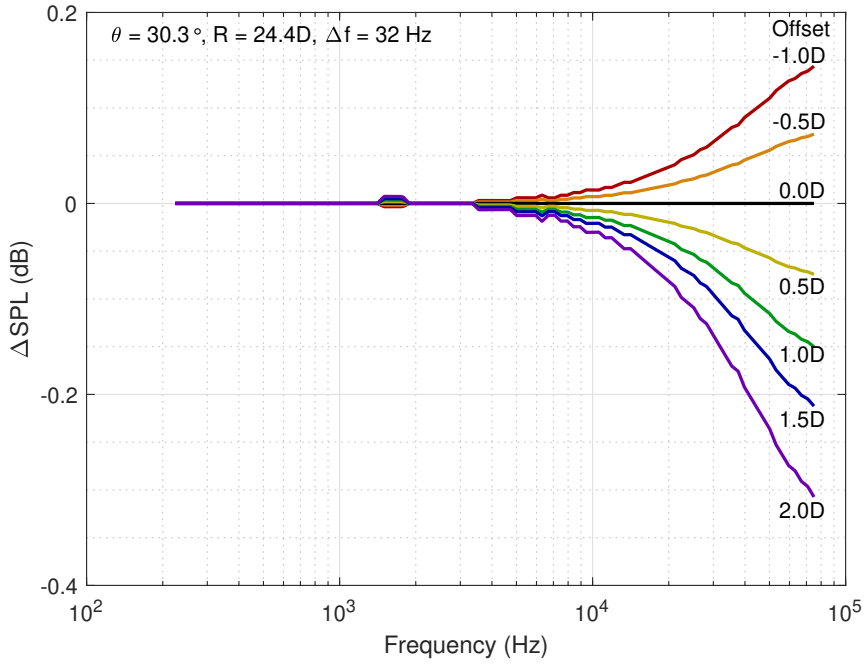

Figure 4.18: Effect of source location offset on microphone corrections for a nearfield microphone at 30 degrees.

the 0.0 diameter offset is subtracted from each data set, so only the difference due to the correction remains. Both figures show that source location error (or offset) has a larger effect as frequency increases, which is expected as both humidity corrections and incidence corrections are larger at higher frequencies. Yet, the corrections are close to 0 dB up to a frequency of 10 kHz and at most 0.3 dB with an offset of two diameters at 75 kHz. Thus, it is safe to say that source location error does not have a significant impact on nearfield microphone correction; for frequencies up to 75 kHz, source location error on

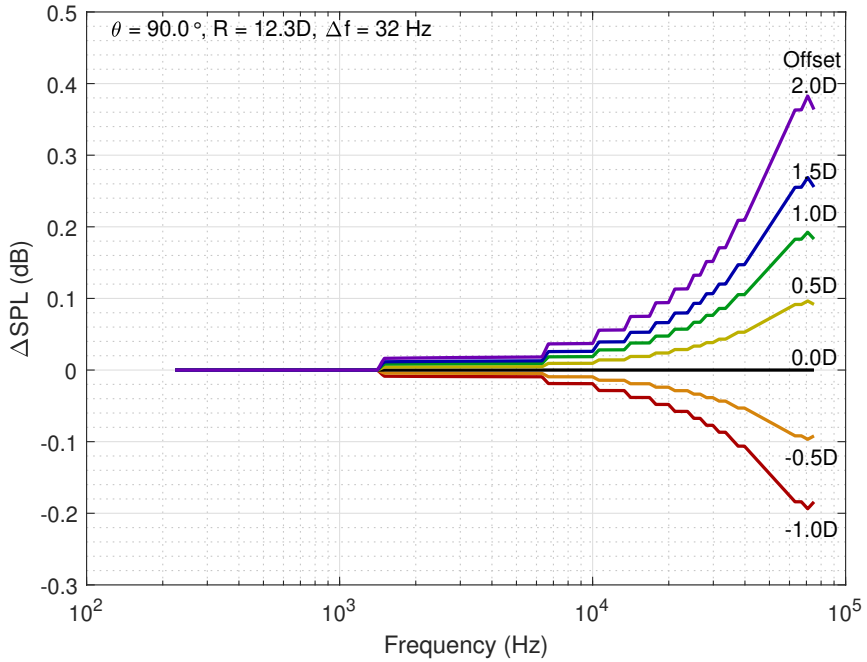

Figure 4.19: Effect of source location offset on microphone corrections for a nearfield microphone at 90 degrees.

the magnitude of two diameters results in less than 0.5 dB of difference in the corrected spectra.

4.6.2 Extrapolation of Nearfield Acoustic Data to the Farfield

In order for corrected nearfield data to be compared to corrected farfield data, one of the two data sets needs to be extrapolated to the same location of the other. Using a method developed by Ahuja et al. [11], the corrected nearfield data is extrapolated to 90 diameters into the farfield. To describe the method simply, a line can be drawn from each frequency source to the location in the farfield where one wants to extrapolate. At some point in space this line intersects with the nearfield arc (most likely between two microphones). The SPL value of that frequency at that location can be calculated by interpolating between the values from the two adjacent microphones. This interpolated value is then assumed to propagate the remainder of the distance to the farfield location, falling off by one over that distance squared. This is repeated for every frequency and eventually constructs the spectra

at the farfield location.

Similar to the nearfield corrections in the previous subsection, the source location listed in Equation 4.3 is used with offsets ranging from -1 diameters to 2 diameters to perform the nearfield to farfield extrapolation. Figures 4.20 and 4.21 contain plots illustrating the differences in extrapolated spectra due to these offsets for a 30 degree and 90 degree farfield location, respectively. As shown in the correction plots in the previous subsection, the

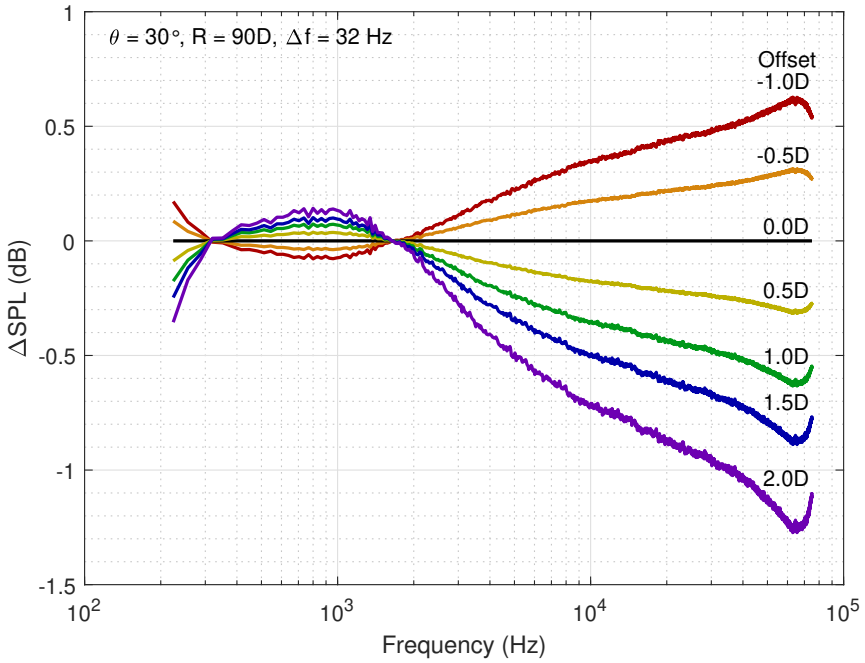

Figure 4.20: Effect of source location offset on nearfield to farfield extrapolation at a polar angle of 30 degrees.

0.0 offset spectra is subtracted from every spectra so only the differences due to the offsets remain. In both cases, higher frequencies are affected more by the offsets than lower frequency sources. For a given offset, extrapolation to 30 degrees is affected less than extrapolation to 90 degrees. Two diameters of source location error result in upwards of 1.25-1.75 dB of difference at high frequencies in extrapolated spectra.

Figures 4.22 and 4.23 show comparisons between the extrapolated data (using no offset) and actual recorded farfield data at the same location. The 30 degree spectra in Figure 4.22 agree slightly better than the 90 degree spectra in Figure 4.23. At most frequencies,

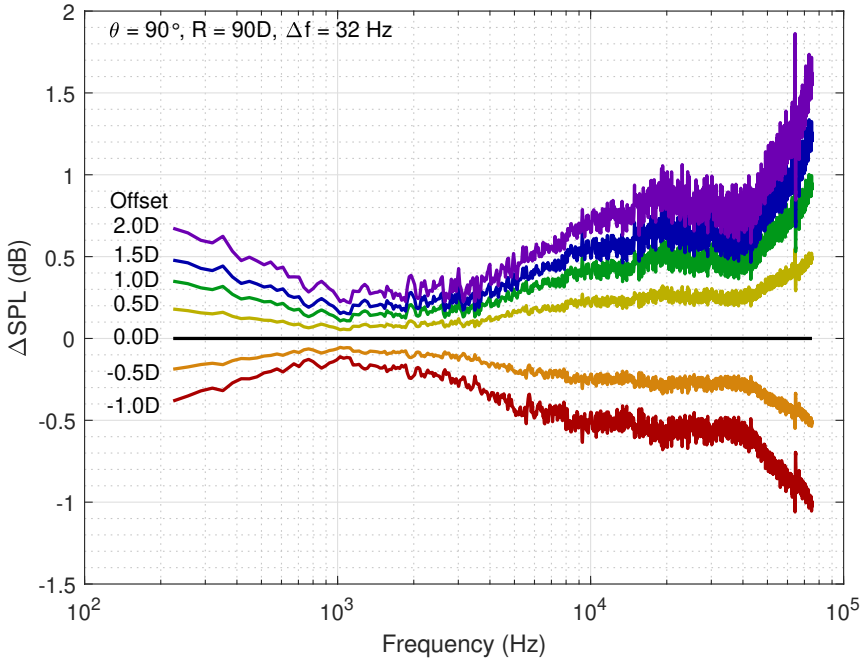

Figure 4.21: Effect of source location offset on nearfield to farfield extrapolation at a polar angle of 90 degrees.

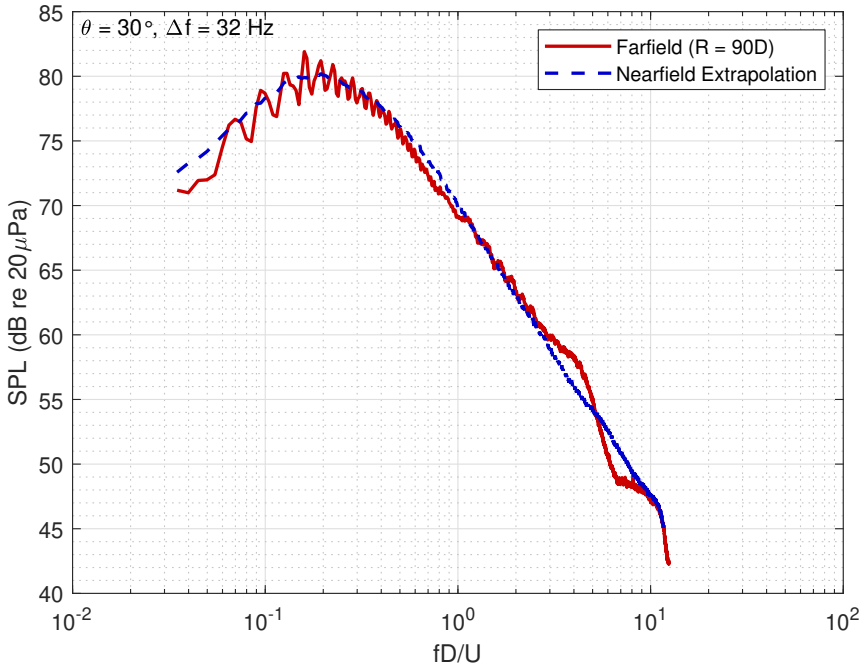

Figure 4.22: Comparison of extrapolated nearfield data with farfield at a polar angle of 30 degrees.

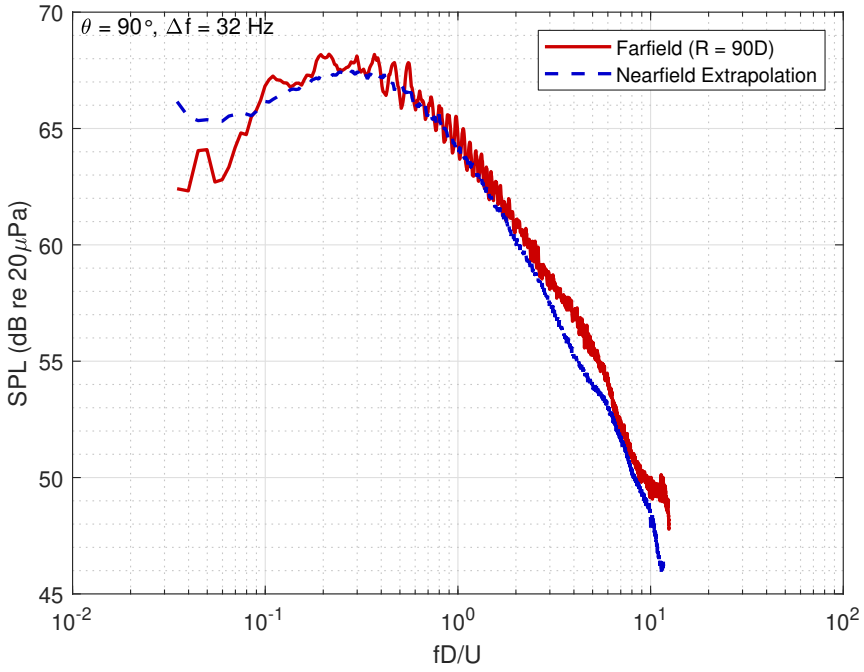

Figure 4.23: Comparison of extrapolated nearfield data with farfield at a polar angle of 90 degrees.

the extrapolated nearfield data at 90 degrees appears to be below the actual spectra; from Figure 4.21 this could be attributed to the actual noise sources being further downstream than what the beamformer shows. This is expected, as the source location used is the peak value location and not the centroid location, which would be further downstream.

4.6.3 Summary of the Effect of Observed Source Location Uncertainty on Various Applications of the Technique

Source location error on the order of two diameters does not have an appreciable effect on nearfield microphone corrections; the effect is on the order of 0.5 dB. This error does have a larger effect when extrapolating nearfield data to farfield data, and can result in almost 2 dB of difference at high frequencies.

4.7 Concluding Remarks

A spread of about two nozzle diameters has been shown when comparing the source location obtained from several different past studies. These differences are due to numerous factors ranging from using different methods, different facilities, and different nozzles/jet conditions. When compared to the most similar conditions from existing studies, the source location obtained with the acoustic beamformer in this thesis matches within 0.5-1.0 diameters; slightly better than the two-diameter agreement shown between all the previous studies.

The source location results of the beamformer and nearfield contours also match within 0.5-1.0 nozzle diameters. This comparison is important, because both methods were run with the exact same nozzles with very similar upstream geometry (up to the plenum); this reduces possible errors associated with having different nozzles and different facilities. From these comparisons it has been concluded that nearfield contours are an imprecise tool for jet noise source location. While the contours do an excellent job illustrating source directionality, the method requires a great degree of subjectiveness when obtaining the actual source location resulting in a variance of about ± 2 diameter in results. As a result, the acoustic beamformer is used to obtain source location for the majority of this work and nearfield contours are reserved as needed for the corroboration of results.

Source location errors on the order of 0.5-1.0 diameters have negligible impacts on microphone corrections and upwards of 1 dB effect on nearfield extrapolation for frequencies below 75 kHz. In both cases, higher frequency noise is affected more by source location error than low frequency noise; this is mitigated, however, by the fact that most source location techniques, including beamforming, have better resolution at higher frequencies. It can thus be concluded that acoustic beamforming is a valid jet noise source location technique and that it being chosen as the primary noise source measurement tool for this work produces results that are either better or comparable with other methods. Which most of

these methods, unlike beamforming, are quite time consuming.

Because all of the tests performed in this chapter are for subsonic jets, it can only be said that the acoustic beamformer is validated as a viable technique for jet-mixing noise source location. Later on in this work, the source locations of supersonic jets are examined with this technique. The subsonic validation performed here also applies to the fine-scale jet-mixing noise component of the supersonic jets. No validation has been performed on locating the noise produced by large scale turbulent structures of the jet. As described by Tam et al. [23] the convecting large scale structures in a supersonic jet radiate sound as Mach waves, predominantly in a downstream direction. For this work, the beamformer array is positioned in the sideline of the jet, around polar angles between 70 and 110 degrees, and as such, most of the noise from these types of sources are not measured by the beamformer. No validation has been performed on the beamformer's ability to detect shock noise in this chapter; however, this validation is performed in Chapter 7 concurrently as supersonic noise source distributions are examined in relation to flow features through flow visualization.

CHAPTER 5
NOZZLE GEOMETRY EFFECTS ON SUBSONIC JET NOISE SOURCE DISTRIBUTIONS

5.1 Introduction

As shown in the previous chapter, noise source distributions acquired by several different studies can vary by as much as two nozzle diameters when plotted as Strouhal number (fD/U) as a function of normalized downstream distance (x/D). Each of these studies use a different method of source location, had completely different jet rigs and nozzles, and operated them at different Mach numbers; all of which can potentially impact the resulting source location. It is fairly common that the differences in the tested nozzles are overlooked when comparing source location between studies. Nozzles that have vastly different internal contours in turn produce different nozzle exit boundary layers. Since the nozzle exit boundary layer defines the starting point of the jet-mixing layer, which is the part of a subsonic jet that produces sound, different nozzle exit boundary layers can result in inconsistent noise source distributions. With this in mind, this chapter focuses on the effect of nozzle geometry on the jet noise source distributions of subsonic jets. To accomplish this, source location measurements of conical and ASME nozzles, which have markedly different nozzle exit boundary layers, are acquired.

In this chapter, the noise source distributions of conical and ASME nozzles are measured for three subsonic Mach numbers: 0.4, 0.6, and 0.8. Conical nozzles linearly converge along their length, while ASME nozzles are contoured to the standard described by Benedict and Wyler [46] and result in thinner nozzle exit boundary layers than their conical counterparts. The effects of nozzle exit diameter and Mach number on the subsonic noise source distributions for these two nozzle types are examined in this chapter. In addition,

any differences in the noise source distributions of the conical and ASME nozzles due to differing nozzle exit boundary layers are explained through the use of nozzle exit velocity profile measurements and schlieren flow visualization.

5.2 Results

As shown in previous studies [5, 6, 13, 15, 24, 26, 27, 32], the noise source distributions of subsonic jets follows the trend of a power series, of the form shown in Equation 5.1, where a and b are placeholder variables for the distribution.

$$\frac{fD}{U} = a\left(\frac{x}{D}\right)^{-b} \tag{5.1}$$

The location of the highest frequency noise produced by a jet is found to be near the nozzle exit ($x/D = 0$) and the frequency of noise produced decreases as one moves downstream along the jet axis. This trend is due to sound being generated in the jet-mixing region of the jet. The jet-mixing region starts infinitesimally small near the nozzle exit and grows with downstream position as the momentum of the jet is reduced by the stagnant air surrounding it. Correspondingly, the size of the turbulent structures in this mixing region responsible for jet-mixing noise is proportional to the size of the mixing region. Higher frequencies of noise are thus produced where these structures are smaller and vice versa. As a result, the noise source distribution follows the trend similar to the one shown in Equation 5.1. It is important to note that an isolated position in the jet-mixing region is not responsible for solely generating noise of a given frequency. Jet noise at a given frequency appears to be generated over a finite length, as shown in Chapter 4 and by other studies [26, 27], and it is their peak or centroid values that follow the power series trend shown in Equation 5.1.

In this work, the source location is plotted as Strouhal number (fD/U) as a function of normalized downstream distance (x/D), as is common practice in jet noise literature. These plots of source location data are referred to as the jet's noise source distribution.

When plotted as such, the noise source distributions should be independent of jet operating conditions such as jet Mach number and nozzle exit diameter. The following subsection examines the validity of this statement. The noise source distributions of nozzles with diameters ranging from one-inch to 2.44-inches are examined at Mach numbers between 0.4 and 0.8. Mach numbers lower than 0.4 are also acquired; however, they contained significant contamination due to upstream valve noise and thus are not used.

5.2.1 Jet Mach Dependence of Subsonic Jet Noise Source Distributions

Figure 5.1 shows jet noise source location as a function of Mach number for nominally 1.56-inch nozzles, where Figure 5.1a is for a 1.60-inch conical nozzle and Figure 5.1b is for a 1.53-inch ASME nozzle. In both figures, Mach numbers of 0.4, 0.6, and 0.8 are tested.

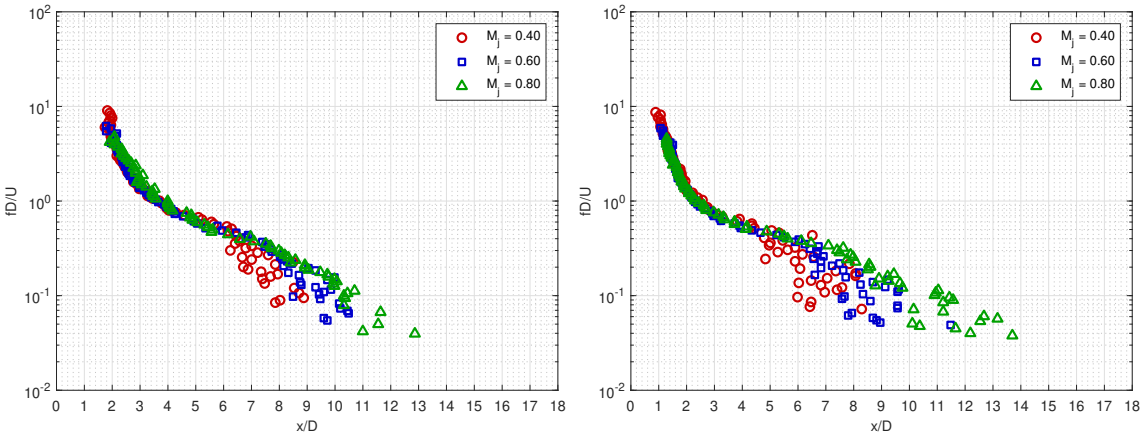

(a) 1.60-inch conical nozzle (b) 1.53-inch ASME nozzle

Figure 5.1: Jet noise source location for nominally 1.56-inch nozzles as a function of jet Mach number.

Comparisons for additional nozzle diameters can be found in Appendix B; they show the same trends as those seen here. Both the ASME and conical nozzles appear to have noise source distributions that are independent of Mach number within the tested range. There are notable differences that appear at lower Strouhal numbers; however, these are mainly due to limitations in beamforming accuracy at low frequencies.

As described in Section 4.2.1 of the previous chapter, the beam width of the beamformer

increases in size as measuring frequency is decreased. Larger beam widths result in less resolution in source location measurements. If the resolution is too low, the beamformer only is able to locate the centroid location for the noise sources of a given frequency. This can still be applied to jet-mixing noise in subsonic jets, as the peak or centroid locations are all that is needed to plot noise source distributions. If the beam width becomes too large, however, even the measured location of the centroid becomes incorrect due to the large area of space being averaged by the beamformer. Because the beam width of the beamformer is a function of frequency, and not Strouhal number, increasing the Mach number makes it appear as if the array becomes less accurate at lower Strouhal number values, as seen in Figure 5.1.

5.2.2 Nozzle Exit Diameter Dependence of Subsonic Jet Noise Source Distributions

Figure 5.2 shows jet noise source location as a function of diameter at Mach 0.8. Com-

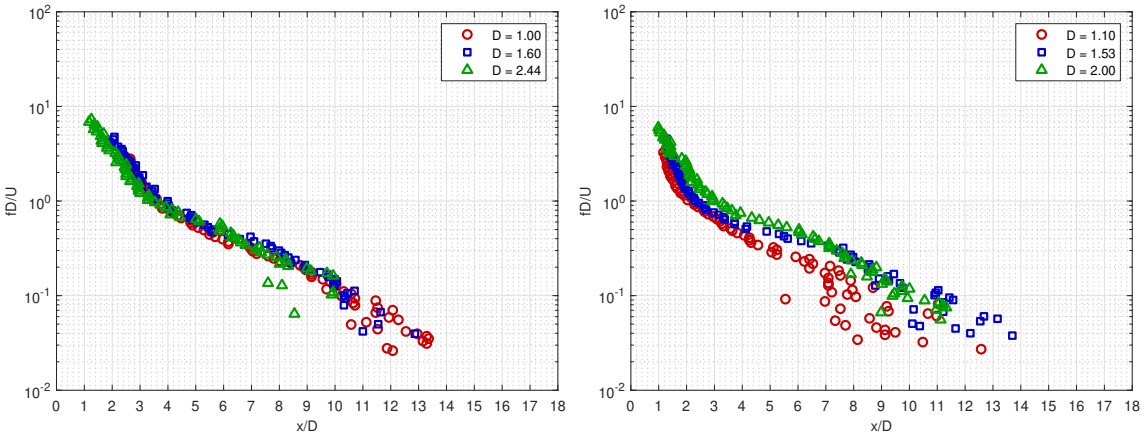

(a) Conical nozzles (b) ASME nozzles

Figure 5.2: Jet noise source location at Mach 0.8 as a function of nozzle exit diameter.

parison plots for other Mach numbers can be found in Appendix B. The conical nozzles in Figure 5.2a have exit diameters of 1.00 inches, 1.60 inches, and 2.44 inches, and the ASME nozzles in Figure 5.2b have exit diameters of 1.10 inches, 1.53 inches, and 2.00 inches. The conical noise source distributions appear to be independent of nozzle exit diameter for the

nozzles tested. The ASME noise source distributions, on the other hand, behave very differently with respect to nozzle exit diameter. As shown in Figure 5.2b, the two-inch ASME nozzle has a noise source distribution that is one-to-two diameters downstream of the 1.1-inch ASME nozzle. The noise source distribution of the 1.53-inch ASME nozzle appears to fall in between the other two nozzle datasets at Strouhal numbers above 0.4 and appears to line up with the two-inch nozzle's at lower Strouhal numbers.

5.2.3 Nozzle Geometry Dependence of Subsonic Jet Noise Source Distributions

The ASME and conical nozzles tested in this work have very different internal geometries from one another, resulting in differences in their noise source distributions. From the comparisons shown in the previous subsections, the ASME and conical noise source distributions are independent of Mach number, within the range tested. While conical nozzle noise source distributions are independent of nozzle exit diameter, the same cannot be said for the ASME nozzles. As the diameter of an ASME nozzle is increased, its noise source distribution appears to be located further downstream than the distributions of the smaller diameter ASME nozzles. In order to explain why the noise source distributions of the ASME nozzles are affected by exit diameter and those of the conical nozzles are not, the two nozzle types need to be directly compared with each other. Furthermore, an analysis and comparison of the velocity profiles of these nozzles is required to fully explain the trends summarized above. This is accomplished in this subsection.

To adequately compare and understand the noise source distributions of the ASME and the conical nozzles, this subsection examines three types of measurements for the two nozzle types: (1) noise source distributions, (2) nozzle-exit boundary layer measurements, and (3) flow visualization.

Noise Source Distributions

Noise source distributions of ASME and conical nozzles of nominally the same exit diameter operated at a Mach number of 0.8 are compared in this subsection. While it would be ideal if the exit diameters were exactly the same for both nozzle types, the slightly different exit diameters used in this work are acceptable because, as shown in the previous subsection, the noise source distributions of the conical nozzles are independent of exit diameter (within the model scales tested in this study). Thus, comparing the noise source distributions of a 1.1-inch ASME nozzle with a 1.0-inch conical should for all intents and purposes provide the same answers as comparing the noise source distributions of the same 1.1-inch ASME nozzle with a 1.1-inch conical nozzle. Any differences in noise source distribution for the two nozzles at nominally the same diameter can thus be attributed to differences in flow development at the exit for the two nozzle types.

In this subsection, data from two different nominal diameters of nozzles are compared with each other: nominally 1.05-inch nozzles and nominally 1.56-inch nozzles. While the actual diameters of the nozzles tested slightly differ from these nominal values, for simplicity the nozzles are referred to as just "1.05-inch" or "1.56-inch" nozzles for the remainder of this chapter. The 1.05-inch nozzles consist of the 1.0-inch conical and the 1.1-inch ASME nozzles. The 1.56-inch nozzles consist of the 1.6-inch conical and the 1.53-inch ASME nozzles. Calculated values that are normalized by nozzle diameter (i.e. x/D and y/D) are normalized using the actual nozzle diameter and not the nominal value.

Figure 5.3a compares the noise source distributions of 1.05-inch conical and ASME nozzles, operated at Mach 0.8. At all Strouhal numbers, the noise sources for the ASME nozzle are one to two nozzle diameters upstream that of the conical nozzle. Figure 5.3b compares the noise source distributions of 1.56-inch conical and ASME nozzles, operated at Mach 0.8. Similar to what was seen for the 1.05-inch nozzles in Figure 5.3a, the noise source distribution curve for the 1.56-inch diameter ASME nozzle is generally shifted upstream of that for the conical nozzle of the same diameter. However, at Strouhal numbers

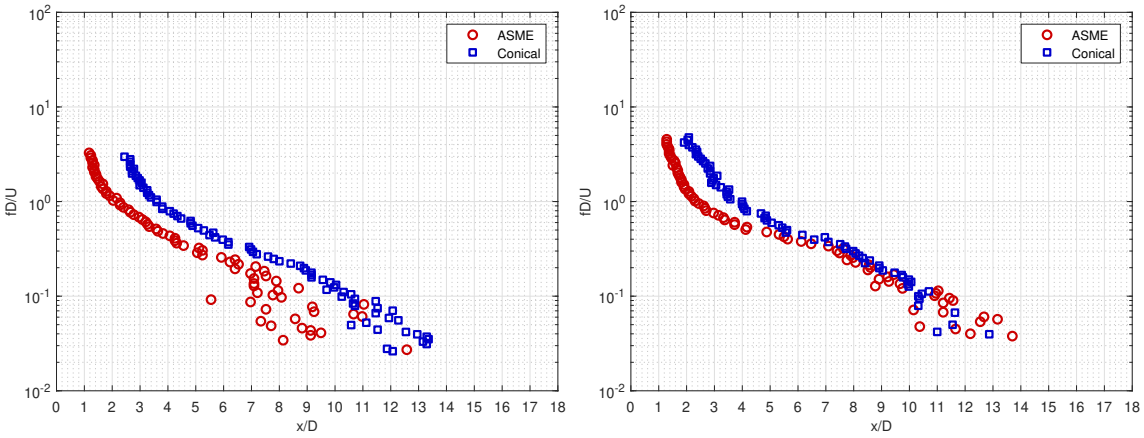

(a) Noise source distributions of 1.05-inch nozzles (b) Noise source distributions of 1.56-inch nozzles

Figure 5.3: Comparison of source location for ASME and conical nozzles at Mach 0.8.

below 0.4 the 1.56-inch ASME nozzle's noise source distribution curve begins to match the conical nozzle's noise source distribution. The same trend can be seen in Figure 5.2b. As the diameter of an ASME nozzle is increased, its noise source distribution curve tends to shift downstream. At large exit diameters, the noise source distribution curve of ASME nozzles has shifted downstream enough that it is almost identical to that of conical nozzles, whose noise source distributions are unaffected by the nozzle exit diameter. In order to understand this trend, one needs to examine the nozzle exit boundary layer and the development of the jet-mixing layer.

Nozzle Exit Boundary Layer Measurements

As shown above in Figure 5.3, the noise source locations at a given Strouhal number for a jet from an ASME nozzle, of a given diameter, are located further upstream compared to a conical jet, at least for the cases involving nozzle exit diameters below two inches. This is in fact due to the flow development upstream of the nozzle exit associated with the internal geometry of ASME nozzles. ASME nozzles are designed to have thinner, more laminar, exit boundary layers than their conical counterparts. As shown by Xu and Antonia [50] as well as by Bogey and Bailly [51], thinner nozzle exit boundary layers initially result

in faster growth of turbulent structures in the jet-mixing layer. Since the frequency of the dominant sound produced by the turbulent structures is inversely proportional to the size of these structures, a nozzle with a smaller exit boundary layer has a noise source distribution that reaches lower frequencies at a much smaller downstream location than a nozzle with a thicker exit boundary layer. To illustrate this point, jet velocity profile measurements are acquired for several downstream locations for the ASME and Conical nozzles.

Before comparing velocity profile plots for the ASME and conical nozzles, the terminology used for these plots is reviewed. In literature, the term δ_{99} is one of the values used to quantify boundary layer thickness. More exactly, this term is defined as the measurement of the distance between locations of zero velocity and 99% of the freestream velocity. This work uses a similar definition except that in addition to being used only for the nozzle exit boundary layer, it is also used to estimate the mixing layer thickness. The mixing layer thickness is defined as the distance, normal to the jet axis, between the potential core of a jet and the outer edge of the mixing layer. Figure 5.4 contains examples of the velocity profile and the mixing layer thickness plots that are shown in this chapter, as well as examples of δ_{99} on each.

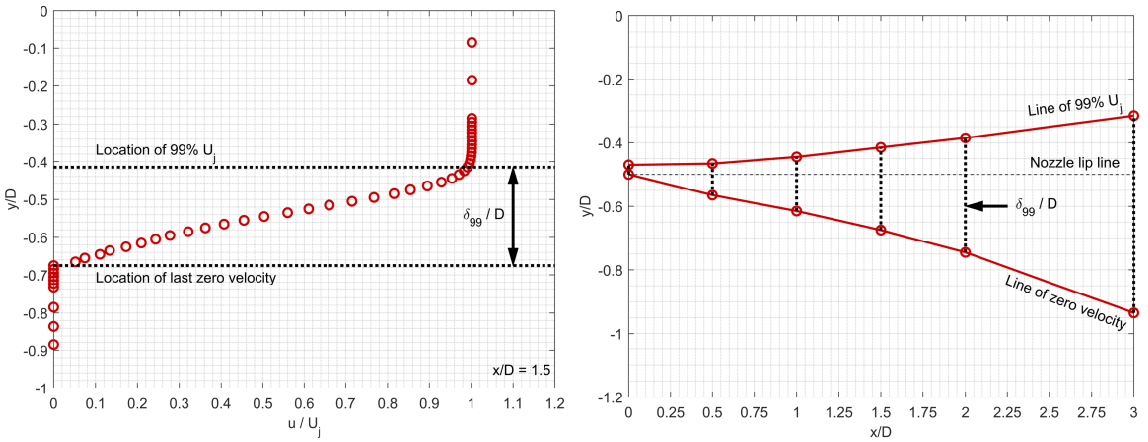

(a) Velocity profile example

(b) Mixing layer example

Figure 5.4: Examples of velocity profile and mixing layer measurements. Locations of 99% U_j and of zero velocity are indicated on each plot as well as an example of the δ_{99} measurement.

In this work, nozzle exit boundary profile measurements are made at an immeasurable distance just downstream of the nozzle exit, instead of exactly at $x/D = 0.0$. As such this location is denoted with an asterisk. While technically not the true nozzle exit boundary layer profile, the velocity profile differences at this location should be negligible.

At downstream locations (x/D) of 0.0*, 0.5, 1.0, 1.5, 2.0, and 3.0, velocity profiles similar to the one shown in Figure 5.4a are obtained. The velocity at each point (u) is normalized by the centerline ($y/D = 0$) jet exit velocity (U_j). The location of $y/D = -0.5$ corresponds the the nozzle lip line, which is located at the edge of the nozzle. Locations of last zero velocity and 99% jet velocity are recorded and are then used to illustrate the width of the mixing layer as seen in Figure 5.4b. Mixing layer plots similar to the one shown in Figure 5.4b give a sense of the size of the jet-mixing layer as a function of downstream location (x/D). The vertical dotted lines are visual representations of the δ_{99} value.

The above definitions are now used for comparing the velocity profiles of the ASME and conical nozzles. Figure 5.5 compares the nozzle exit boundary layers for 1.05-inch nozzles of both geometries. The jet-exit velocity profiles for both nozzles show zero velocity for axial locations past $y/D = -0.5$, as indeed they should. The 1.05-inch ASME nozzle's velocity profile reaches its maximum value in a much shorter distance than the conical nozzle of similar diameter, approximately 0.015 nozzle diameters before the conical nozzle. As a result, it can be said that the 1.05-inch ASME nozzle has a thinner boundary layer at the nozzle exit than the 1.05-inch conical nozzle.

For the 1.56-inch nozzles, the boundary layer profiles can be seen in Figure 5.6. Similar to the 1.05-inch nozzles, the 1.56-inch ASME nozzle appears to have a thinner nozzle exit boundary layer than the 1.56-inch conical nozzle. More exactly, the boundary layer of the ASME nozzle appears to be about 0.012 diameters smaller than that of its conical counterpart. An explanation for the odd shape of the velocity profile of the ASME near the nozzle lip ($y/D = -0.5$) could not be found. This shape is repeatable with multiple measurements and even appears in particle imaging velocimetry measurements. The initial shape

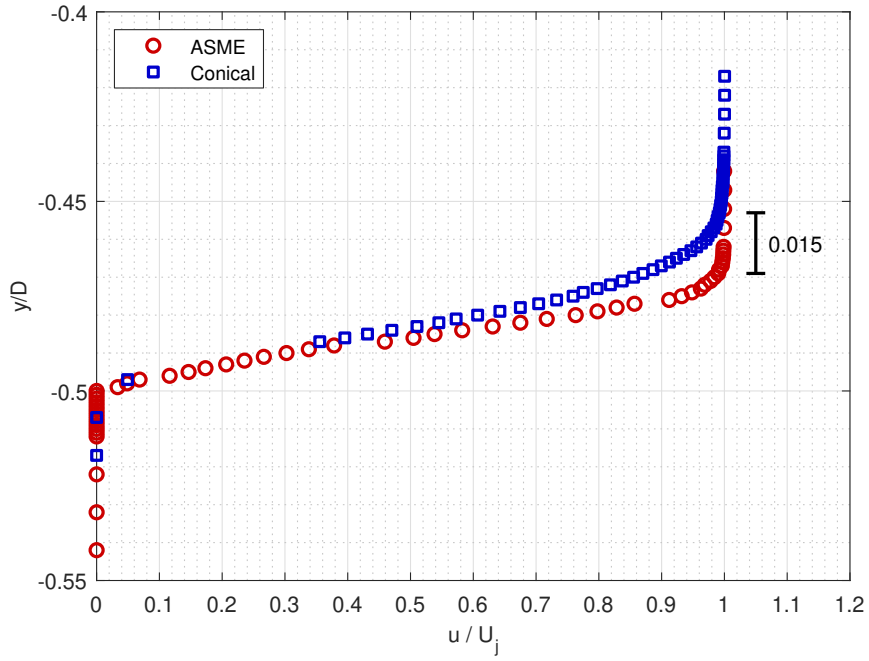

Figure 5.5: Comparison between the exit boundary layer profiles for 1.05-inch diameter nozzles. ($M_j = 0.8$)

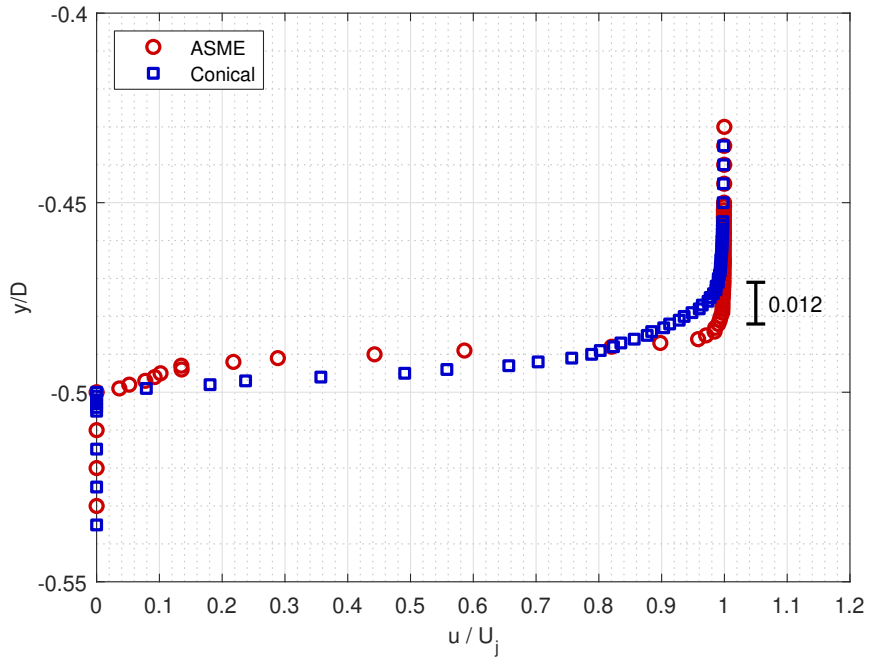

Figure 5.6: Comparison between the exit boundary layer profiles for nominally 1.56-inch diameter nozzles. ($M_j = 0.8$)

(for $u/U_j \leq 0.15$) perfectly matches the shape of the 1.05-inch ASME nozzle's boundary layer profile; afterwards (for $u/U_j > 0.15$), it develops much quicker. Fortunately the odd shape does not impact the boundary layer thickness (δ_{99}) calculations performed in this work.

The calculated nozzle exit boundary layer thickness (δ_{99}) for each nozzle is recorded in Table 5.1 along with the difference in boundary layer thickness between each nozzle type. It is worth noting that the difference in nozzle exit boundary thickness is less for the

Table 5.1: Calculated nozzle exit boundary layer thickness values (δ_{99}) normalized by diameter for each nozzle when operated at Mach 0.8.

Nozzle Diameter (in)	$\delta_{99,\mathrm{Conical}}/\mathrm{D}$	$\delta_{99,\mathrm{ASME}}/\mathrm{D}$	$\delta_{99,\mathrm{Conical}}/\mathrm{D} - \delta_{99,\mathrm{ASME}}/\mathrm{D}$
1.05	0.046	0.031	0.015
1.56	0.030	0.018	0.012

1.56-inch diameter nozzles than the 1.05-inch diameter nozzles. In units not normalized by nozzle diameter, the boundary layer size difference between the larger nozzles is actually greater than the difference between the smaller nozzles; however, when normalized by the larger diameter the final result is smaller. This could potentially explain why the noise source distributions of ASME nozzles start to behave like conical nozzles at larger exit diameters. If this trend continues for larger nozzle diameters, one would expect the difference in boundary layer profile sizes to reduce even further.

Of the nozzles tested, the nozzle exit boundary layer profiles become a smaller percentage of the overall exit velocity profile as nozzle diameter is increased. This can be seen illustrated for the ASME nozzles in Figure 5.7, noting that the conical nozzles follow the same trend. The exit boundary layer of the 1.05-inch ASME nozzle is much thicker in a diameter sense than the 1.56-inch and the 2.00-inch ASME nozzles. In a similar fashion, the 1.05-inch ASME nozzle is the only diameter tested with a noise source distribution curve that is shifted upstream of the noise source distribution curves of the conical nozzles at all Strouhal numbers, as shown in Figure 5.3a. The noise source distribution curve of the 1.56-inch ASME nozzle eventually matches those of conical nozzles at lower Strouhal

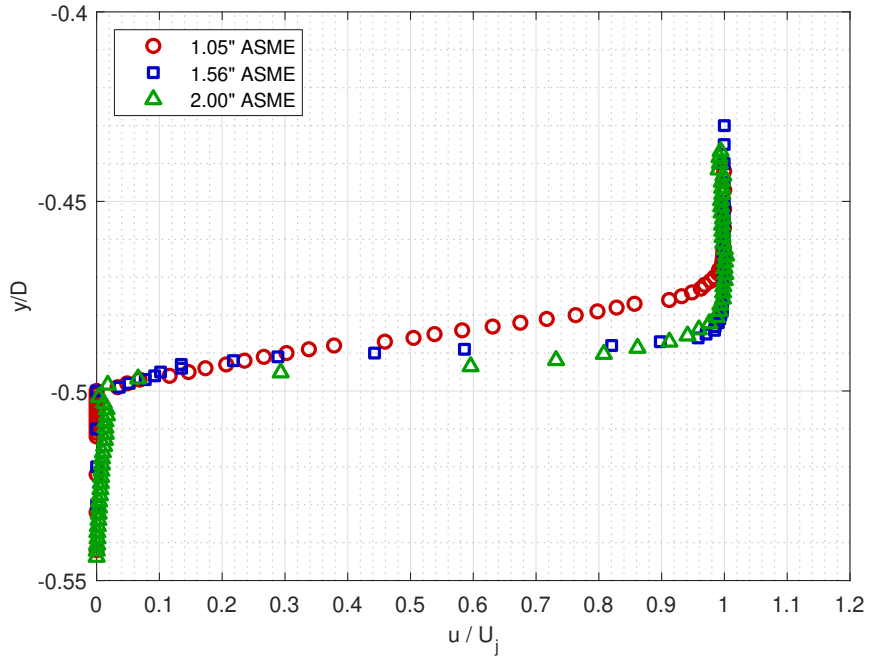

Figure 5.7: Comparison between the exit boundary layer profiles for ASME nozzles. ($M_j = 0.8$)

numbers, and the noise source distribution curve of the 2.00-inch ASME nozzle matches at almost all the Strouhal numbers measured in this work. It is surprising to note that there is not much difference in the exit boundary layer profiles of the 1.56-inch ASME nozzle and the 2.00-inch ASME nozzle, but their noise source distributions curves behave fairly differently near the nozzle exit. To understand why this is so would require performing additional measurements of noise source distributions for ASME nozzles of different exit diameters. This was beyond the scope of the current work (and budget) and is recommended for future work in Section 9.2.

In summary of the data shown so far, both the 1.05-inch and the 1.56-inch nozzle boundary profile results illustrate that the conical nozzle in general has a thicker boundary layer than a corresponding ASME nozzle of similar diameter. This is expected as ASME nozzles are supposed to provide thinner nozzle exit boundary layers. To further investigate how the boundary layer thickness affects the noise source distributions of the jets, the differences in the jet-mixing layer for the two types of nozzles need to be examined.

Velocity profile measurements are acquired at 0.5, 1.0, 1.5, 2.0, and 3.0 diameters downstream of the nozzle exit for the nozzles tested above. At each downstream location, velocity profile measurements similar to the one shown in Figure 5.4a are acquired and are used to obtain mixing layer width plots similar to those shown in Figure 5.4b. Figure 5.8 contains the mixing layer width data for the 1.05-inch diameter nozzles. The data in Figure

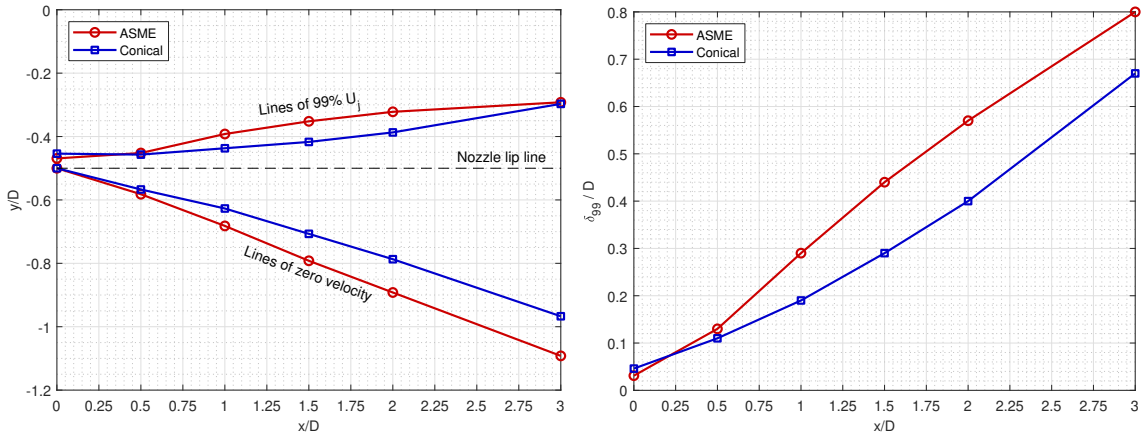

(a) Mixing layer spreading

(b) Mixing layer widths

Figure 5.8: A comparison between the mixing layers of the 1.05-inch nozzles.

5.8a illustrates the spreading of the mixing layer of both the ASME nozzle and the conical nozzle. These plots show that the mixing layer of the ASME nozzle appears to grow faster with downstream distance relative to that of the conical nozzle. The distance between the line of zero velocity and the line of 99% U_j, δ_{99}, is calculated at each downstream location and is used to plot the curves shown in Figure 5.8b. The plots in this figure depict the normalized jet-mixing layer width of each nozzle as a function of normalized downstream distance. Even though the ASME nozzle has a thinner exit boundary layer, and thus an initially smaller mixing layer, by approximately half a diameter downstream, its mixing layer width is already larger compared to that of the conical nozzle. Just as shown experimentally by Xu and Antonia [50] and computationally by Bogey and Bailly [51], the thinner boundary layer results does in fact appear to result in a faster growth rate of the mixing layer.

The same trends can be seen for the 1.56-inch nozzles. Figure 5.9 contains the mixing layer data for the 1.56-inch nozzles. Similar to before, Figure 5.9a shows that the mixing

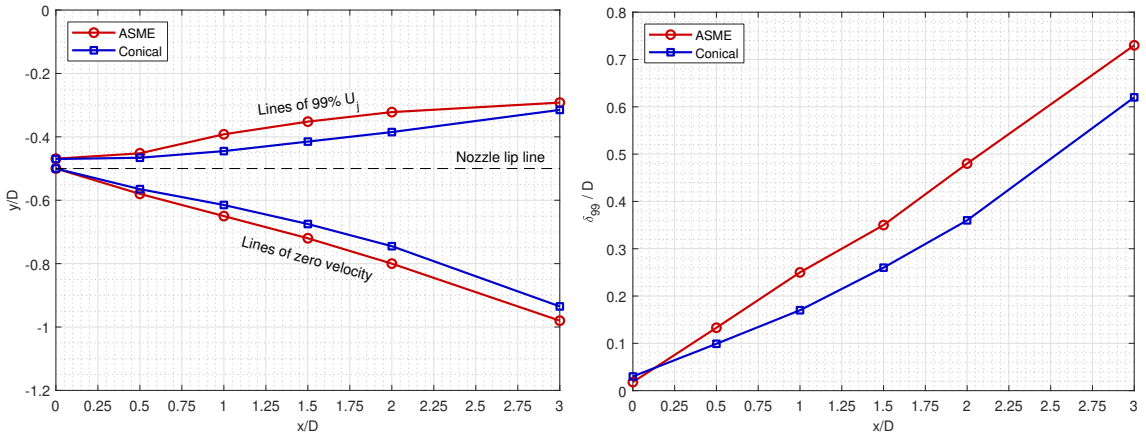

(a) Mixing layer spreading

(b) Mixing layer widths

Figure 5.9: A comparison between the mixing layers of the 1.56-inch nozzles.

layer of the ASME nozzle grows faster as a function of downstream location than that of the conical nozzle.

It is clear from the above discussion that the ASME nozzles, which have thinner nozzle exit boundary layers, have much wider mixing layers than their conical counterparts, at least within the first three diameters of the jet for which the present data was acquired. These results help explain why the source locations plots for these nozzles in Figures 5.3a and 5.3b show that the ASME nozzles have noise sources that are in general located upstream compared to those of the conical nozzles. Because the size of the turbulent structures in the jet-mixing layer are inversely proportional to the frequency of sound produced by that portion of the mixing layer, the larger mixing layers of the ASME nozzles produce lower frequency noise at a given downstream location compared to that of a conical jet. This explains why the noise source distributions of the ASME nozzles appear upstream of the conical noise source distributions in Figure 5.3. To further help illustrate how the ASME jets have mixing layers that initially grow faster than their conical counterparts requires the use of flow visualization techniques.

Flow Visualization

Schlieren flow visualization, obtained simultaneously with the acoustic beamforming data, visually captures the state of the jet with respect to its source location. This visualization method utilizes the refraction of light due to the differing air density in the moving jet to visualize the flow of the jet. A more detailed description of the methodology and setup behind this method can be found in Section 3.1.2 of Chapter 3. The lines of zero velocity from Figures 5.8a and 5.9a are superimposed on the flow visualization images of the corresponding jets to show the outer limits of the jet-mixing layers.

Figures 5.10 and 5.11 contain comparisons of flow visualization for 1.05-inch and 1.56-inch jets, respectively. The ASME jets in Figures 5.10a and 5.11a have turbulent structures that grow at a much faster rate than their conical counterparts, shown in Figures 5.10b and 5.11b. Examining the lower lip ($y/D = -0.5$) of the ASME jet in Figure 5.10a, well defined large-scale turbulent structures become visible just downstream of $x/D = 0$. For the corresponding conical nozzle in Figure 5.10b, on the other hand, well defined turbulent structures become visible at approximately one diameter downstream from the nozzle exit. From this schlieren flow visualization, it is very clear that the mixing of the ASME nozzles is indeed happening quicker than their conical counterparts.

In reference to how the noise source distributions of ASME nozzles at larger diameters begin to resemble those of conical nozzles, Figure 5.12 illustrates how the turbulence of the 1.05-inch, the 1.56-inch, and the 2.00-inch ASME nozzles compares to that of the 1.56-inch conical nozzle. All of these nozzles are operated at a fully-expanded Mach number of 0.8. As the diameter of the ASME nozzle is increased from 1.05 inches in Figure 5.12a to 2.00 inches in Figure 5.12c, the overall turbulence of the jet appears to decrease. In fact, the flow visualization of the 2.00-inch ASME looks very similar to that of the 1.56-inch conical nozzle in Figure 5.12d. This shows that there may be some additional effects, outside of the nozzle exit boundary layer thickness, that impact the noise source distributions of larger diameter ASME nozzles. This is best demonstrated by how the nozzle exit boundary layer

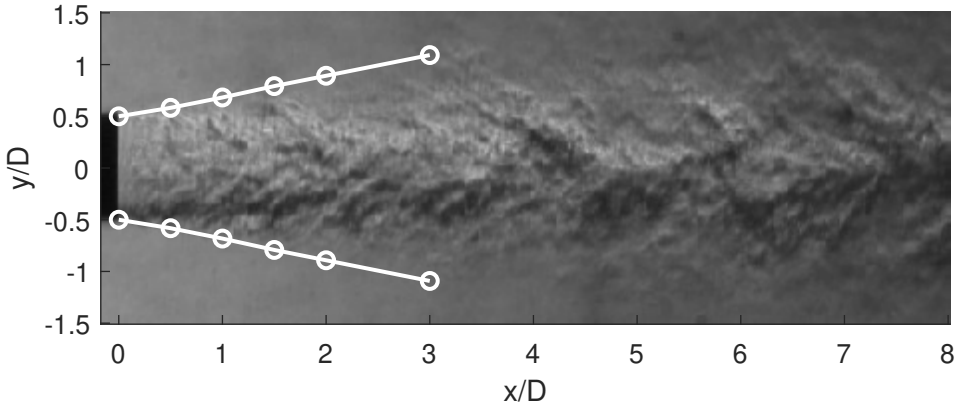

(a) ASME Nozzle

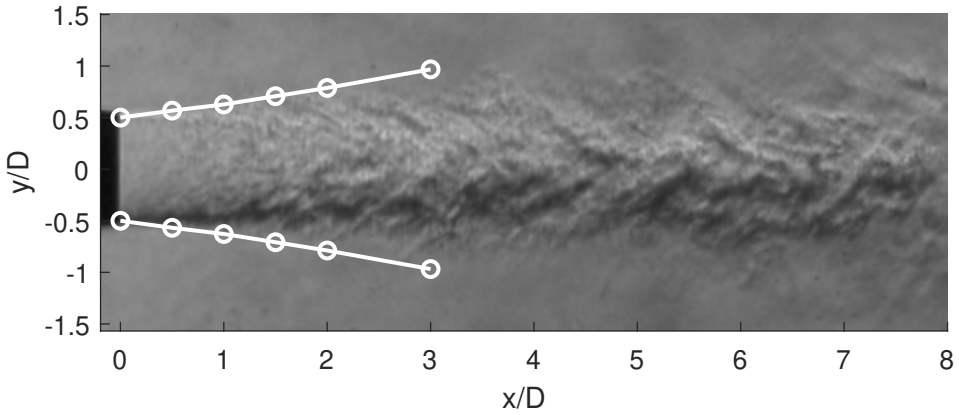

(b) Conical Nozzle

Figure 5.10: A comparison between the schlieren of the 1.05-inch nozzles operated at Mach 0.8.

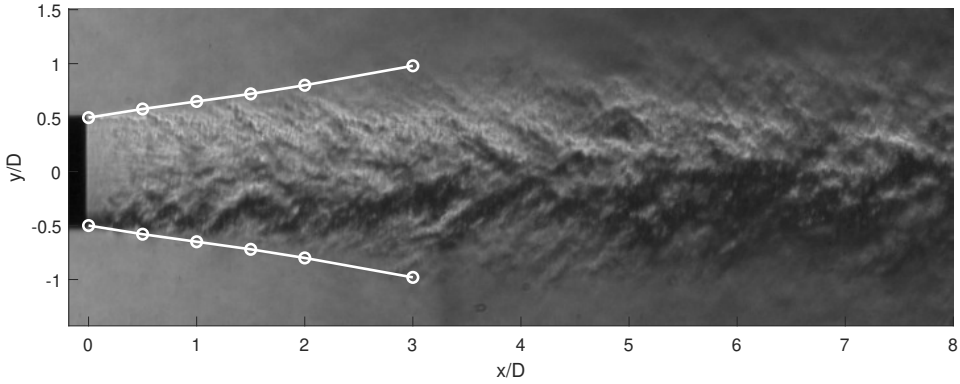

(a) ASME Nozzle

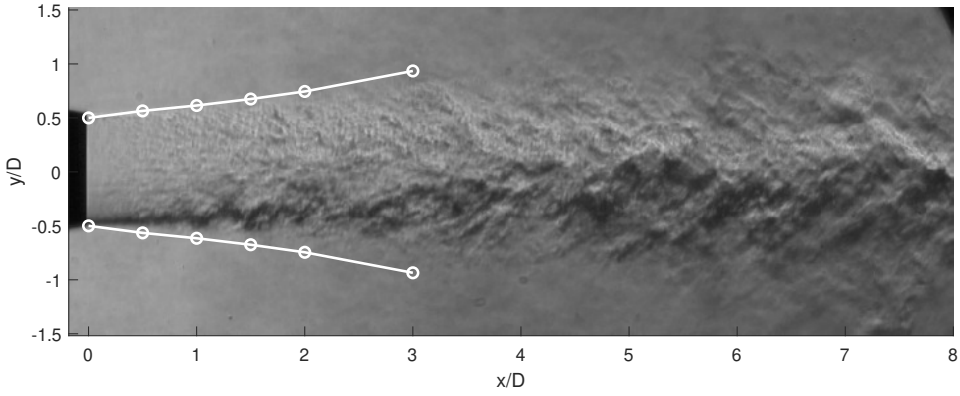

(b) Conical Nozzle

Figure 5.11: A comparison between the schlieren of the 1.56-inch nozzles operated at Mach 0.8.

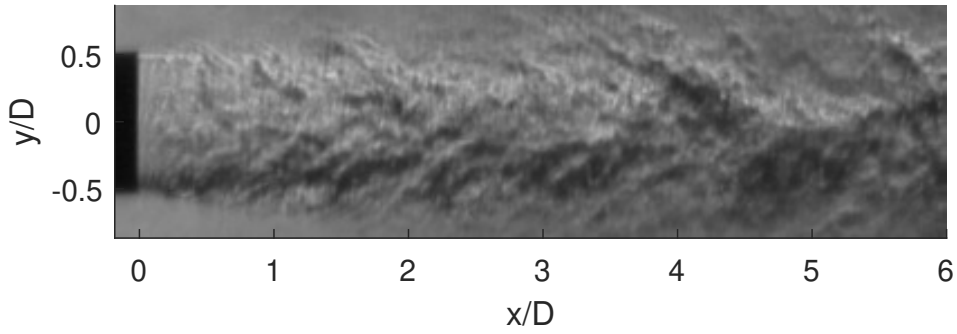

(a) 1.05-inch ASME Nozzle

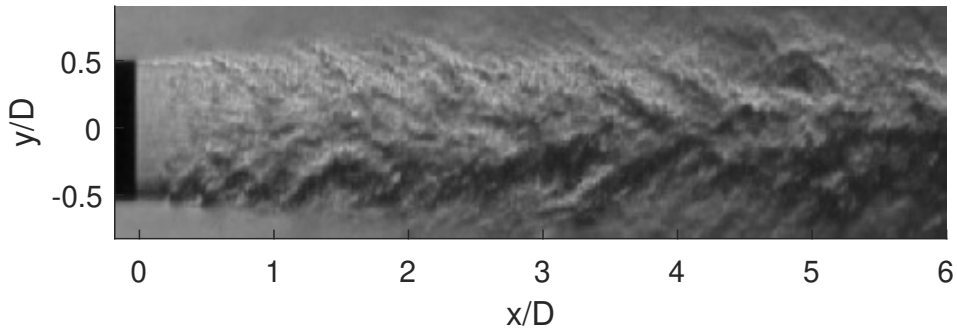

(b) 1.56-inch ASME Nozzle

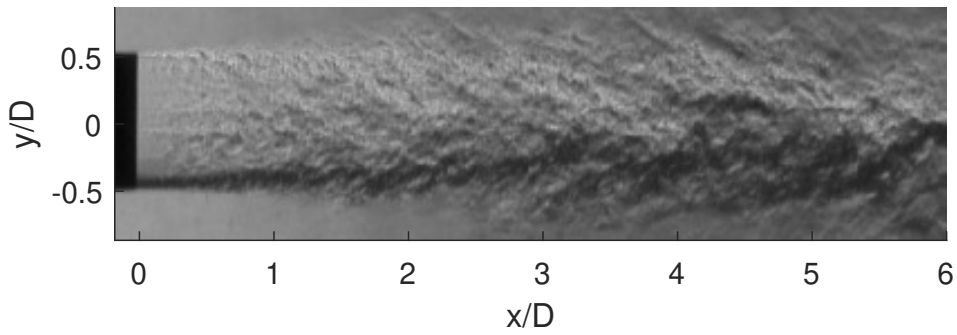

(c) 2.00-inch ASME Nozzle

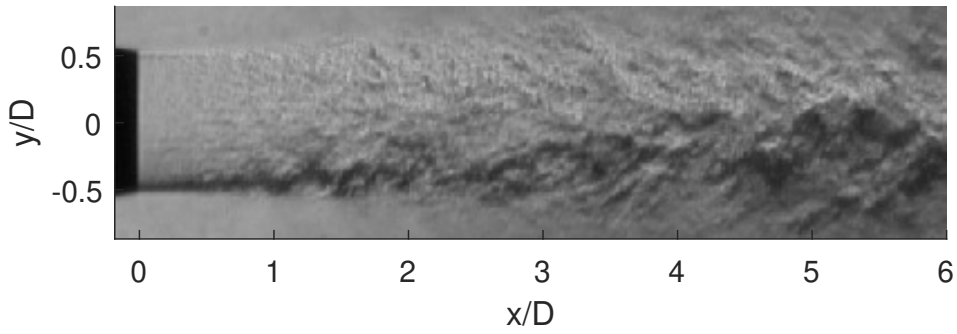

(d) 1.56-inch Conical Nozzle

Figure 5.12: A comparison between the schlieren of the ASME nozzles and the 1.56-inch conical nozzle operated at Mach 0.8.

profiles of the 1.56-inch ASME nozzle and the 2.00-inch ASME nozzle, shown previously in Figure 5.7, are very similar in size and shape, but their mixing layers are very different. The turbulent structures in the 1.56-inch ASME jet grow much quicker than the ones in the 2.00-inch jet.

Summary

The ASME nozzles examined in this section have jet noise source distributions, plotted as Strouhal number (fD/U) versus normalized downstream distance (x/D), that lie upstream of those for similar diameter conical nozzles. These ASME nozzles have thinner nozzle exit boundary layers by design than their conical counterparts, which results in faster growth of turbulent structures in their jet-mixing layer. This has been confirmed with both downstream velocity profile measurements and in schlieren flow visualization. The faster jet-mixing layer growth of the ASME nozzles is what results in the shift of their noise source distributions further upstream relative to the conical nozzles.

5.3 Concluding Remarks

While it is mainly independent of properties such as Mach number or nozzle exit diameter, the subsonic noise source distribution of a jet is very much affected by the internal geometry of a nozzle used to generate it. For subsonic Mach numbers of 0.4, 0.6, and 0.8, it is shown that the subsonic noise source distributions for both ASME and conical nozzles, when examined for each nozzle in isolation, do not change with Mach number when plotted as Strouhal number (fD/U) versus normalized downstream location (x/D). Likewise, the noise source distributions of conical nozzles appear to be independent of nozzle diameter. The noise source distributions of the ASME nozzles tend to shift downstream with increasing nozzle exit diameter.

At subsonic Mach numbers, as shown at Mach 0.8 in Figure 5.3, the 1.05-inch and 1.56-inch diameter ASME nozzles have noise source distribution curves that are shifted

further upstream compared to those for the conical nozzles of similar diameter. The larger diameter 2.00-inch ASME nozzle noise source distribution curve, on the other hand, seems to match with those of the conical nozzles. This is due to the ASME noise source distribution curves shifting further downstream towards the conical noise source distributions as their exit diameter is increased. This shift in source location most likely the result of the difference in nozzle exit boundary layer thickness for the two nozzle types decreasing as diameter is increased (from 0.015 diameters difference for the 1.05-inch nozzles to 0.012 diameters difference for the 1.56-inch nozzles). There may be additional effects outside of the boundary layers that also impact the jet-mixing layer as exit diameter is increased. However, due to the limited number of nozzles used in this work, a detailed explanation of these additional effects cannot currently be made.

The difference in the ASME and conical nozzle noise source distributions is due to different growth rates of each nozzle type's jet-mixing layers. As shown in the nozzle exit boundary layer measurements in Figures 5.5 and 5.6, the ASME nozzles have smaller exit boundary layers compared to their conical counterparts. A thinner exit boundary layer results in faster growth of turbulent structures in the mixing layer of the jet. This claim is not only supported by other existing studies [50, 51] but is apparent in both the mixing layer measurements and schlieren flow visualization previously examined.

CHAPTER 6

NOISE SOURCE DISTRIBUTIONS OF SUBSONIC TWIN JETS

6.1 Introduction

In the previous chapter, the noise source distributions of subsonic single jets were examined. This chapter continues this analysis of jet noise source distributions for twin jets. Two jets operated simultaneously and in close proximity with each other eventually start to interact at some point downstream. This interaction occurs as each jet spreads as the mixing layer of each jet develops with distance, and at a far enough location downstream, the jet-mixing layers of the two jets interact.

Extensive efforts have been made by researchers such as Harper-Bourne [52], Wlezien [53], and Seiner et al. [54, 55] to predict how the nearfield noise changes for twin jets. In their work they note that outside of acoustic coupling between two supersonic jets due to screech, any aerodynamic interaction between the two jets has a minimal impact on the jet noise. This is due to the location at which the jets start interacting being much further downstream than the main noise producing region of the jet. From this finding, it can be hypothesized that the noise source distributions of the twin jets should be minimally affected much until the two jets start interacting.

In this chapter, the noise source distributions of two 0.75-inch circular twin jets are examined for separation distances of 3, 6, and 10 diameters, with both jets operated at Mach 0.8. The noise source distributions for 3 and 6 diameter separations are further analyzed with the used of velocity field measurements obtained using particle imaging velocimetry (PIV).

6.2 Results

6.2.1 Measured Twin Jet Noise Source Distributions

A Note on Source Location Terminology

An illustration of the twin-jet mounting used in this work can be seen in Figure 6.1 with the associated terminology that is used in this chapter. The beamformer views the twin jets

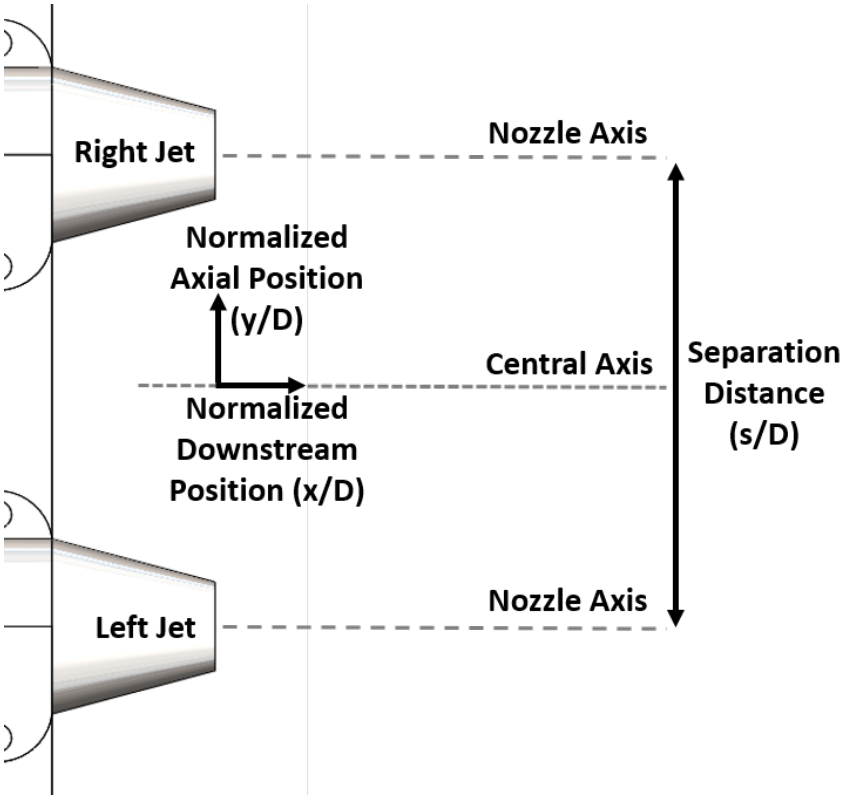

Figure 6.1: Terminology used for twin jet analysis.

as shown in this mounting illustration, side by side. The nozzles are oriented as such so that neither jet shields the other from the beamformer. These two jets are simultaneously operated at the same fully-expanded Mach number of 0.8.

The source location plots in this chapter are plotted with minor differences compared to those seen in previous chapters. An example of typical results for twin jet noise source distributions can be seen in Figure 6.2. The noise source distributions for the twin jets are

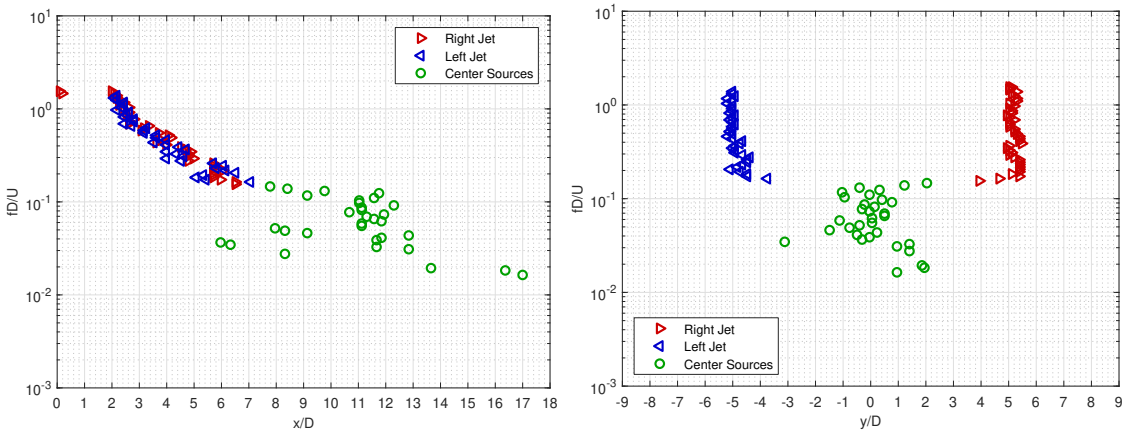

(a) Side View (b) Top View

Figure 6.2: Typical noise source distribution for twin jets. (Nozzle = conical, $D = 0.75$ inches, $M_j = 0.8$, $s/D = 10$)

plotted as both Strouhal number (fD/U) versus normalized downstream position (x/D), identified as the "Side View" shown in Figure 6.2a, and as Strouhal number versus normalized axial position (y/D), identified as the "Top View" shown in Figure 6.2b. The axial position is measured normal to the central axis, as depicted in Figure 6.1, and the central axis is equidistant between both nozzle axes. These two plots are shown side by side for each condition. Additionally, three different symbols are used in each plot. Red right-pointing triangles are for noise sources that emanate from the rightmost jet, and the blue left-pointing triangles are for noise sources that come from the leftmost jet; these are labeled as "Right Jet" and "Left Jet" in each plot, respectively. The green circles represent noise sources that cannot be tied to only one jet; these symbols are labeled as "Center Sources" in the plots.

Source Location Data and Jet-Mixing Location

Figure 6.3 shows that the noise source distribution for the two subsonic jets when separated by ten nozzle diameters and operated at Mach 0.8. The upstream portions, shown in red and blue in the plots in this figure, are nearly identical but still independent of one another. These two independent source location regions end at about seven diameters down-

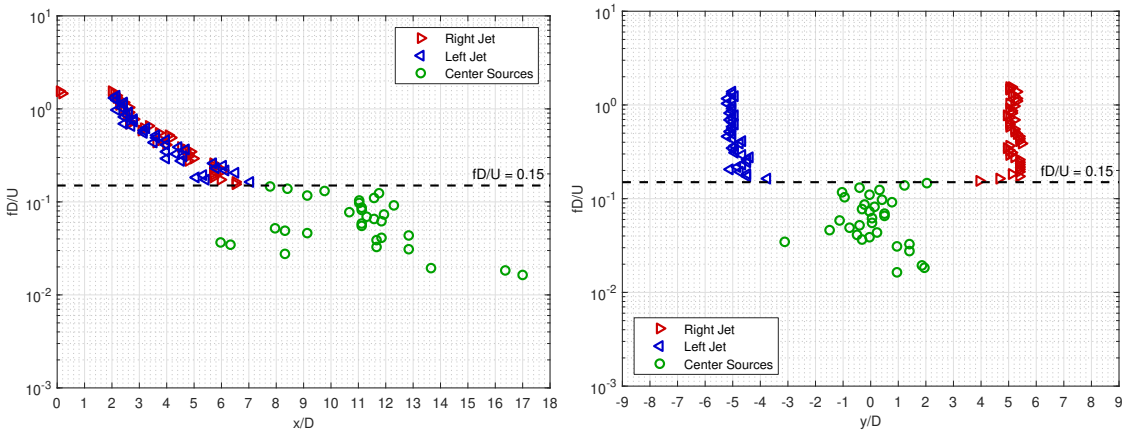

(a) Side View (b) Top View

Figure 6.3: Subsonic noise source distributions of twin jets. (Nozzle = conical, $D = 0.75$ inches, $M_j = 0.8$, $s/D = 10$)

stream. This point corresponds to a Strouhal number of about 0.15 and a frequency of about 2 kHz. At Strouhal numbers below this point, all the noise sources are center sources. It was first thought that the data points called center sources corresponded to a region where the two jets were interacting, but as shown later, the locations of these sources in the top view plot are due to the beamformer not having adequate resolution to separate the two different noise sources from each jet. This problem of resolution makes the noise sources appear to be centered on the central axis ($y/D = 0$) as shown in Figure 6.3b.

The noise source distributions for the subsonic twin jets with a separation distance of six diameters is shown in Figure 6.4. The results for this condition are very similar to those shown for ten diameters of separation. It is shown later in Section 6.2.3 that as separation distance between the two jets is reduced, the minimum Strouhal number at which the two jets can be resolved increases. As the jets are closer together, the independent regions of the jets for $s/D = 6$ end at a higher Strouhal value of 0.25 compared to 0.15 for $s/D = 10$. Similarly, the noise sources after this point again appear to be centered on the central axis of the jet. Slightly above $fD/U = 0.25$, the individual regions of the left and right jets can be seen transitioning towards the center axis.

The trends discussed above continue when the nozzles are placed only three diameters

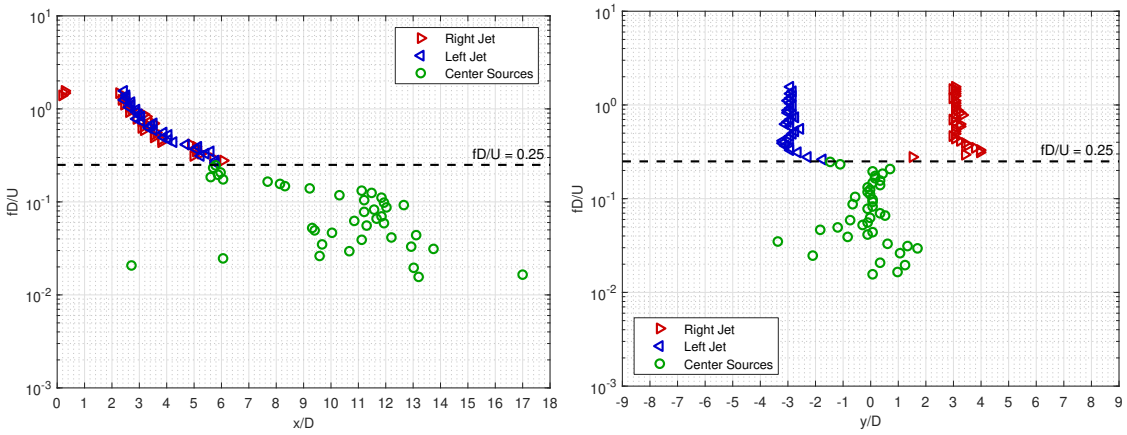

(a) Side View (b) Top View

Figure 6.4: Subsonic noise source distributions of conical twin jets. (Nozzle = conical, $D = 0.75$ inches, $M_j = 0.8$, $s/D = 6$)

apart, as shown in Figure 6.5. At this separation distance the independent jet regions of the

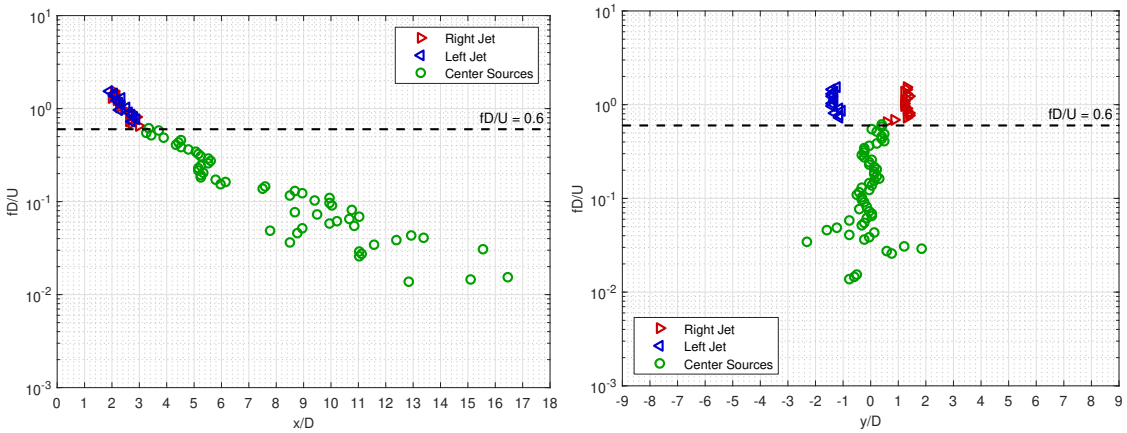

(a) Side View (b) Top View

Figure 6.5: Subsonic noise source distributions of twin jets. (Nozzle = conical, $D = 0.75$ inches, $M_j = 0.8$, $s/D = 3$)

noise source distributions end at $fD/U = 0.6$. As a result, for $s/D = 3$ only the first three diameters of each jet can be separated, the first two diameters of which have frequencies above what the beamformer used in this work can measure. The noise source distribution seen in Figure 6.5b transitions from the right nozzle axis ($y/D = 1.5$) to the central axis ($y/D = 0$).

If one were to look at the twin jet results shown previously without considering effects due to source location resolution, it could be very easy to misattribute the movement of the independent jet source distributions towards the central axis at lower frequencies as a sign of jet mixing. At some point downstream, the two jets mix and combine into one larger jet, and this may actually result in a noise source distribution that looks very similar to the ones shown in this chapter. To prove that this is not the case for the nozzles tested in this work, particle image velocimetry (PIV) measurements have been acquired for the three and six diameter separation conditions shown in this chapter.

Figure 6.6 contains normalized velocity contours for the Mach 0.8 twin jets obtained with PIV. The velocities at each location ($U_{x,y}$) have been normalized by the jet exit velocity

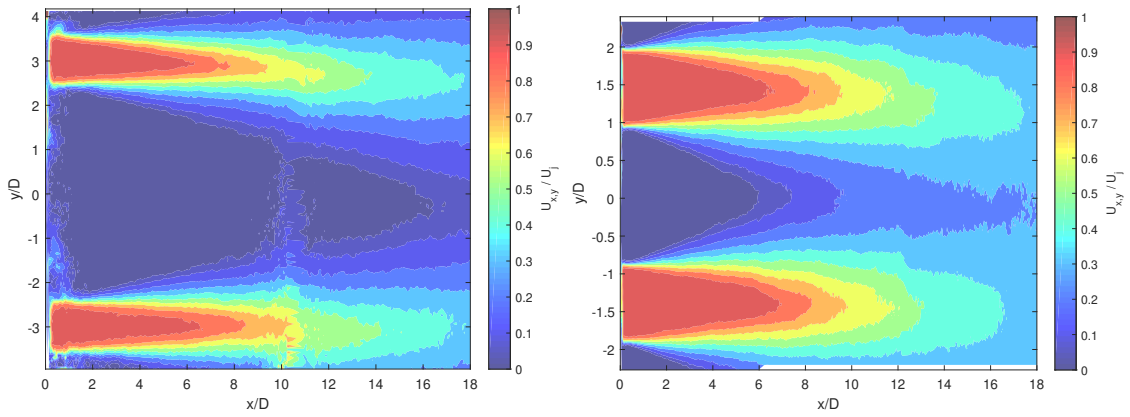

(a) $s/D = 6$ (b) $s/D = 3$

Figure 6.6: PIV measurements for subsonic conical twin jets. (Nozzle = conical, $D = 0.75$ inches, $M_j = 0.8$, $s/D = 3, 6$)

(U_j). To obtain PIV measurements over such a long extent downstream of the nozzle exits, multiple measurements are made at different downstream locations and the results are stitched together. In Figure 6.6a, at around $x/D = 10$ there are some irregularities with the stitching processes due to improper flow seeding; however, this irregularity does not impact the use of the data to determine jet-mixing location, and as such is not a concern for this work.

If one were to use the noise source distributions in Figures 6.4 and 6.5 to determine

the jet-mixing locations for separation distances of six and three diameters, one would reasonably say the jets are mixed when the source locations become centered on the central axis ($y/D = 0$). This location would be about 6-7 diameters for the six-diameter separation condition and about 5 diameters for the three-diameter separation condition. The PIV measurements in Figure 6.6 show that such a statement would be incorrect. The velocity profile plot for six diameters of jet separation, shown in Figure 6.6a, does not show the velocity on the central axis rise above zero until around 16 diameters downstream from the nozzle exits. Assuming both jets spread evenly, the velocity rising above zero on the central axis is a good indication that the jets are starting to interact. The jets themselves do not even come close to mixing in the 18 diameters measured for source location. The velocity profile for three diameters of nozzle separation, shown in Figure 6.6b, shows the velocity on the central axis rise above zero much sooner, at a downstream location of about six diameters; however, the jets are still clearly not mixed by 18 diameters downstream, let alone at the 5 diameters indicated by the source location.

Further proof that the jets are not interacting can be seen in the 90-degree farfield spectra plots shown in Figure 6.7. This figure shows farfield spectra acquired at a polar angle of 90 degrees, with a microphone located in the plane containing the central axis shown in Figure 6.1. Because the two jets are not interacting, the resulting spectra is only 3 dB greater than the spectra of a single jet. This increase is a direct result of the addition of two incoherent sound sources and nothing more. If the jets were interacting, one would expect the twin jet spectrum in Figure 6.1 to look different from the single jet + 3 dB spectrum. This spectra is representative for the other separation distances as well. Because 3 diameters is the smallest separation distance tested and shows no signs of jet interaction, the results for the larger separation distances are expected to show similar results.

As shown below, the resolution of source location measurements obtained with a beamformer is a strong function of the beam width of the beamformer array. The next two subsections describe the calculation of the quantity known as the "beam width" and then show

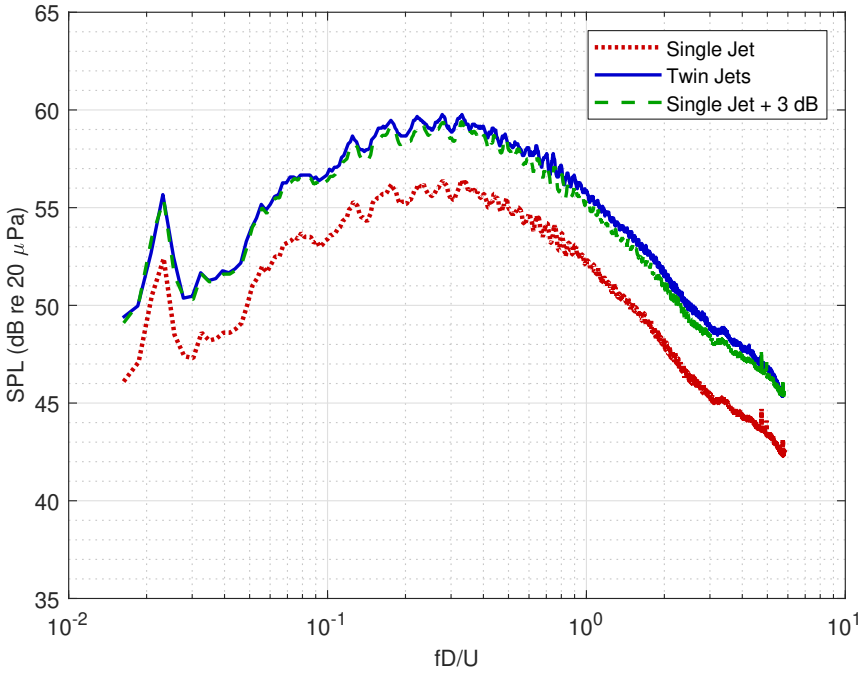

Figure 6.7: 90-degree farfield spectra comparisons for single and twin jets. (Nozzle = conical, $D = 0.75$ inches, $M_j = 0.8$, $s/D = 3$)

how it impacts the twin jet noise source distributions presented above.

6.2.2 Beamformer Beam Pattern Effects on Source Location Accuracy

While an acoustic beamformer can be focused on a specific region in space to measure noise, it still measures noise from all other directions, at a reduced level. The beam pattern of an acoustic beamformer is calculated as the array's response to single frequency plane waves, as shown in Equation 6.1.

$$W(\vec{X}) = \sum_{n=0}^{N-1} w_n \exp\left\{-j2\pi f \frac{\vec{X}}{\left|\vec{X}\right|} \cdot \vec{X_n}\right\} \tag{6.1}$$

The beam pattern (W) of an array with N microphones, for a given frequency (f), is plotted as a function of search location ($\vec{X}$). It is common practice to plot beam pattern as a function of angle with respect to the array center, usually using either the azimuth angle or the elevation angle. The term w_n represents the weights applied to each microphone to

steer the array to a specific location. This calculation is outlined in Array Signal Processing: Concepts and Techniques by Johnson and Dudgeon [56]. Johnson and Dudgeon state that the plane wave response of an array determines the array's output for the general case. As such, the calculated beam patterns give a measure of how well the array attenuates sound from directions other than the focus location. In this work, the beam patterns are calculated using the Phased Array Toolbox in MATLAB.

The beam pattern of an array is comprised of one main lobe and a number of side lobes. The main lobe is the direction in the beam pattern where there are no losses in the received signal, and is the part of the beam pattern that is focused in specific direction to measure the noise source strength. Focusing the array in a specific direction is accomplished by varying the weights for each microphone in the term w_n, shown in Equation 6.1. Side lobes are directions in the beam pattern, outside of the main lobe, at which signals are received with less attenuation. Received signals from directions not containing the main lobe or a side lobe are almost completely attenuated and do not impact source location results. If any side lobes are similar in strength to the main lobe or if they are focused at a noise source that is much louder than the noise source the main lobe is focused, side lobes can result in false positives in source location. Side lobes become more prevalent at higher measuring frequencies.

In this subsection, the beam pattern of the array used in this work is examined for when the beamformer is focused at azimuth angles (α) of 0.0 degrees and -18.24 degrees. Figure 6.8 contains an illustration of the orientation of the beamformer with respect to the exits of the twin nozzles, as used in this work, with these two azimuth angles indicated. While this figure is used to describe the orientation of the twin jets, it is also applicable to all other nozzles examined in this work. In the measurement plane, which is 45.5 inches below the beamformer, azimuth angles of 0.0 degrees and -18.24 degrees correspond to locations directly under the beamformer array center and 15 inches upstream of the array center, respectively. The later location is roughly the location where the nozzle exits are located

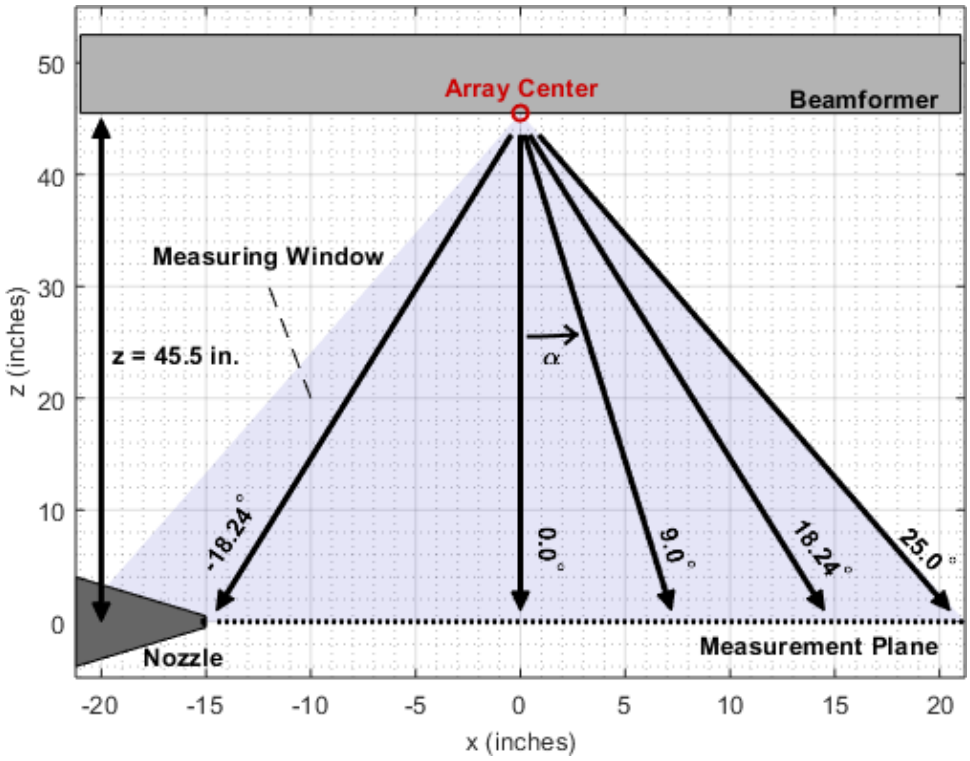

Figure 6.8: Orientation of beamformer with respect to the nozzle exit and definition of azimuth angle, α.

with respect to the beamformer. The measurement plane passes through the twin nozzle exits and along the centerlines of both jets. The size of the measurement plane is determined by the measuring window, as highlighted in blue in Figure 6.8. The measurement window spans from $\alpha = -25°$ to $\alpha = 25°$ and is set by source location processing program, Beamform Interactive.

The azimuth angle (α) can be directly related to the downstream (x) spatial coordinate through Equation 6.2 below, where z is the normal distance between the beamformer and the measurement plane.

$$x = z\tan(\alpha) \tag{6.2}$$

Additional azimuth angles of 9 degrees, 18.24 degrees, and 25 degrees are also included in Figure 6.8. These angles correspond to directions of which beamformer beam width is measured later on in this section.

Figure 6.9 contains waterfall plots of the beam patterns for focus directions of $\alpha = 0^\circ$ and $\alpha = -18.24^\circ$. The frequency and azimuth axes of these plots correspond to the measurement limits of the beamformer used in this work. These plots contain the output of Equation 6.1 for frequencies below 30 kHz and for search directions ($\vec{X}$) in terms of azimuth angle (α). The power values in these plots are normalized with respect to the power of the main lobe and thus can be used to illustrate how sound is attenuated in directions not focused on by the main lobe.

It can easily be confirmed where the array is focused in the waterfall plots in Figure 6.9 using the main lobe, which has a value for normalized power of 0 dB at the focus location. This location is at $\alpha = 0^\circ$ degrees in Figure 6.9a and $\alpha = -18.24^\circ$ in Figure 6.9b. In both cases the main lobe is much more narrow at higher frequencies than at low frequencies. The width of the main lobe is indicative of how quickly the normalized power drops off from the peak value of zero decibels. This width is quantified by the 3 dB beam width, which is how wide the main lobe is in degrees, at -3 dB. Because the width of the main lobe determines the resolution at which noise sources can be detected, narrower beam widths are desired. It is shown in Section 4.2.1 of Chapter 4 that if the beam width encompasses multiple sources of noise when focused in a specific direction, their contributions to the noise field will contaminate the measured value in the focus direction of the main lobe. Narrower beam widths are less likely to be contaminated by contributions from multiple noise sources and result in more accurate noise source distributions.

In order to better visualize the beam patterns and to illustrate the 3 dB beam widths, frequency slices at 1.0 kHz, 5.0 kHz, 10.0 kHz, and 20.0 kHz are obtained from Figure 6.9a and are plotted in Figure 6.10. For these plots, azimuth angle has been converted into the spatial downstream coordinate, x, using Equation 6.2 so that beam pattern effects on the measured source location are easier to discuss. The 3 dB beam width is calculated for each frequency and is converted from azimuth angle to distance as well. The beam width of the main lobe for 1.0 kHz in Figure 6.10a is 14.9 inches. This essentially implies that any

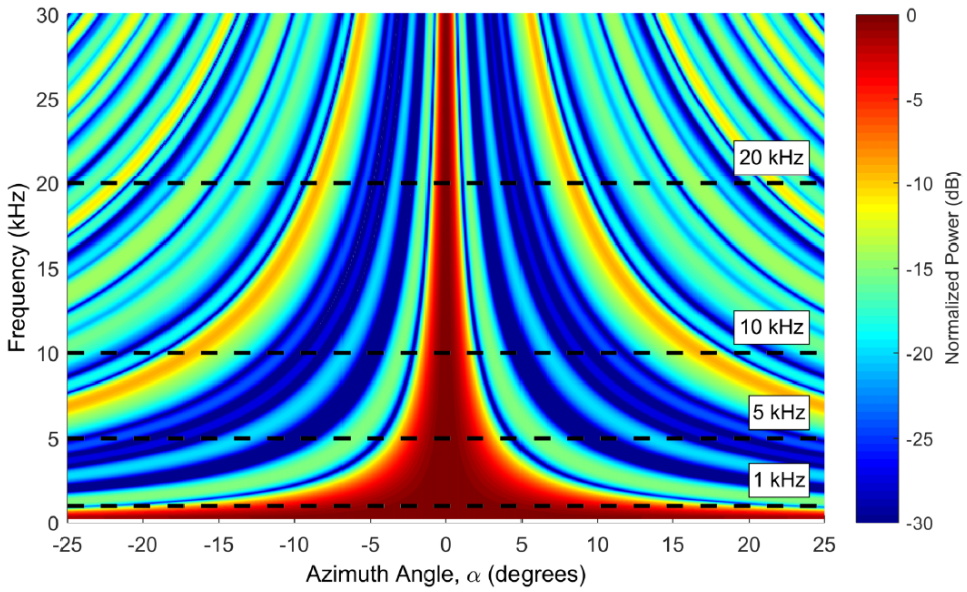

(a) Array focused at $\alpha = 0°$

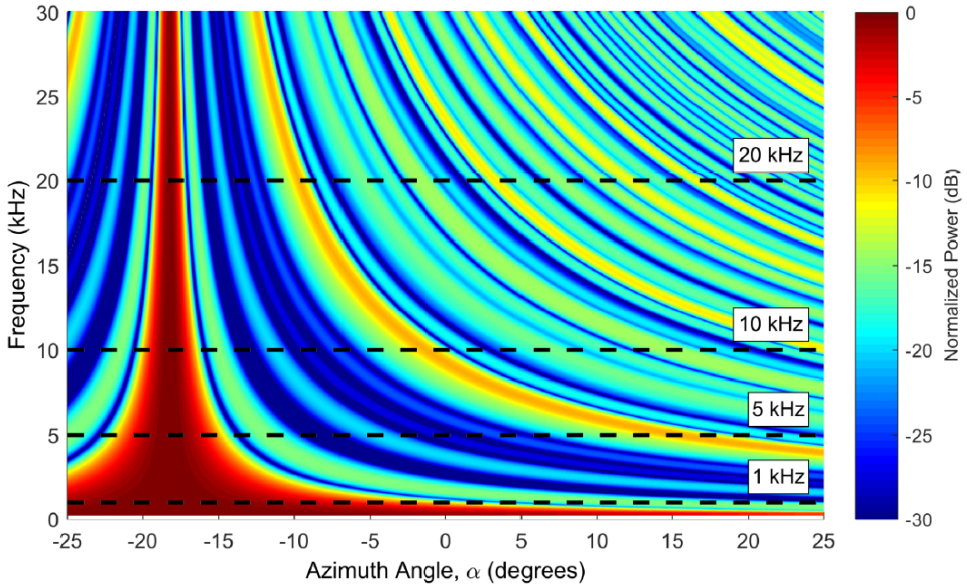

(b) Array focused at $\alpha = -18.24°$

Figure 6.9: Waterfall plots of beamformer array response for when the array is focused at α: (a) $0°$ and (b) $-18.24°$.

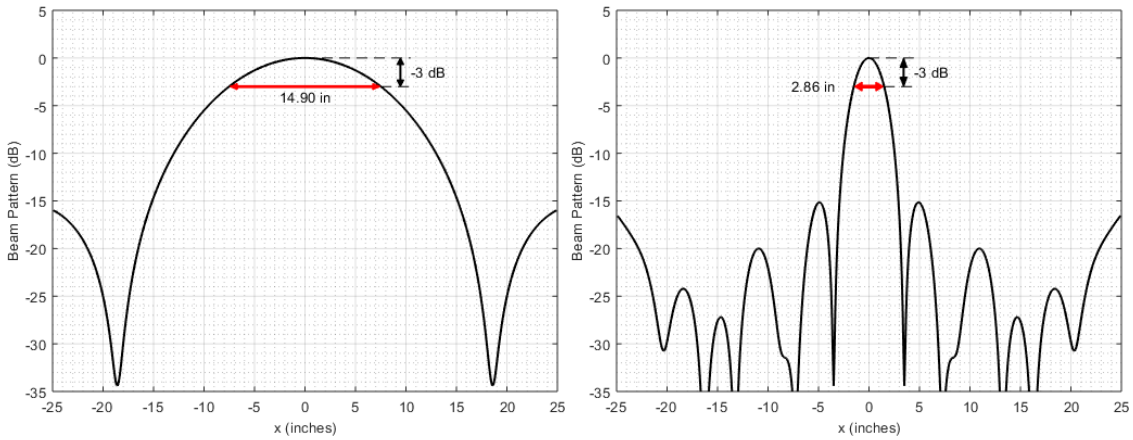

(a) 1.0 kHz beam pattern

(b) 5.0 kHz beam pattern

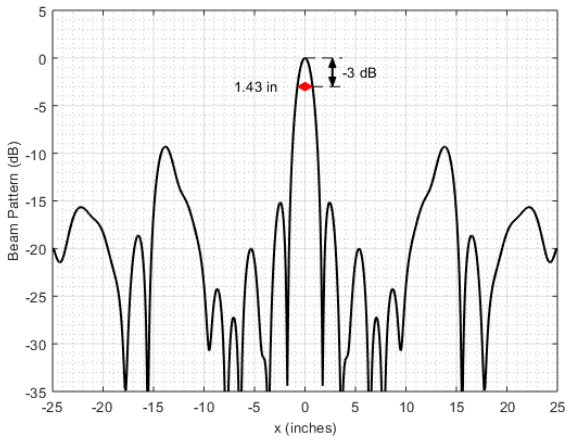

(c) 10.0 kHz beam pattern

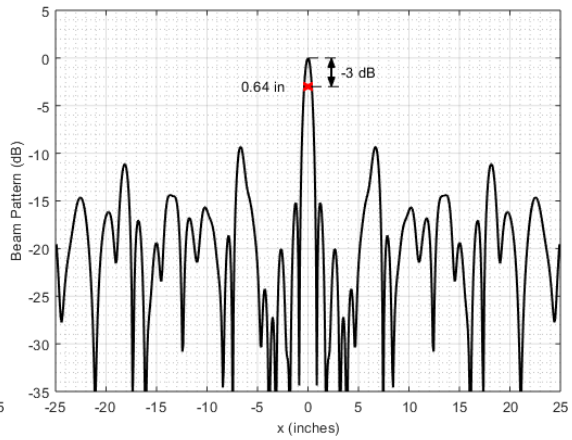

(d) 20.0 kHz beam pattern

Figure 6.10: Beam pattern plots for 1.0 kHz, 5.0 kHz, 10.0 kHz, and 20.0 kHz with the array focused at $\alpha = 0°$.

significant 1 kHz noise source within ± 7.45 inches of $x = 0$ contributes to the measured source strength at $x = 0$. Additionally, multiple 1.0 kHz noise sources must have at least 14.9 inches of space between them to be identifiable as separate sources. If the spacing between noise sources is less than the size of the beam width, the array will locate the centroid of the noise sources instead of individually identifying them.

The beam width of the main lobe for 5.0 kHz shown in Figure 6.10b and is 2.9 inches. The beam width is reduced even further for 10 kHz in Figure 6.10c and for 20.0 kHz in Figure 6.10d to 1.4 inches and 0.6 inches, respectively. The 0.6-inch beam width at 20.0 kHz means that only noise sources within ± 0.3 inches of $x = 0$ contribute significantly to the measured source strength at $x = 0$.

While the smaller beam width for 20.0 kHz is a great improvement over 1.0 kHz, the higher frequency beam patterns have different problems that arise from side lobes. The number of side lobes in the measurement region increase from two in the 1.0 kHz beam pattern, shown in Figure 6.10a, to 28 side lobes in the 20.0 kHz beam pattern, shown in Figure 6.10d. While only two of the 28 side lobes are within 10 dB of the main lobe, care is still needed to be taken at higher frequencies to not mistake side lobe sources as real noise sources. This is mainly accomplished in this work for single jets by excluding measured noise sources that are not located within a few diameters of the jet centerline. The air should be static outside of the jet-mixing layer, and thus there should not be any noise sources in this region. As a result, only erroneous sources due to side lobes should show up more than 1.5 diameters away from the jet centerline. This process becomes more complicated for twin jets due to the presence of more than one significant source at each frequency. As such, there is no simple rule of thumb for eliminating side lobes from twin jet noise source distributions. For the twin jet noise source distributions in this work, only the most obvious side lobe sources are removed. This is done manually on a case-by-case basis.

The same 1.0 kHz, 5.0 kHz, 10.0 kHz, and 20.0 kHz frequency slices are obtained from

the waterfall plot of the array focused on $\alpha = -18.24°$ in Figure 6.9b, and they are plotted in Figure 6.11. For the most part, the beam pattern plots in Figure 6.11 show the same trends

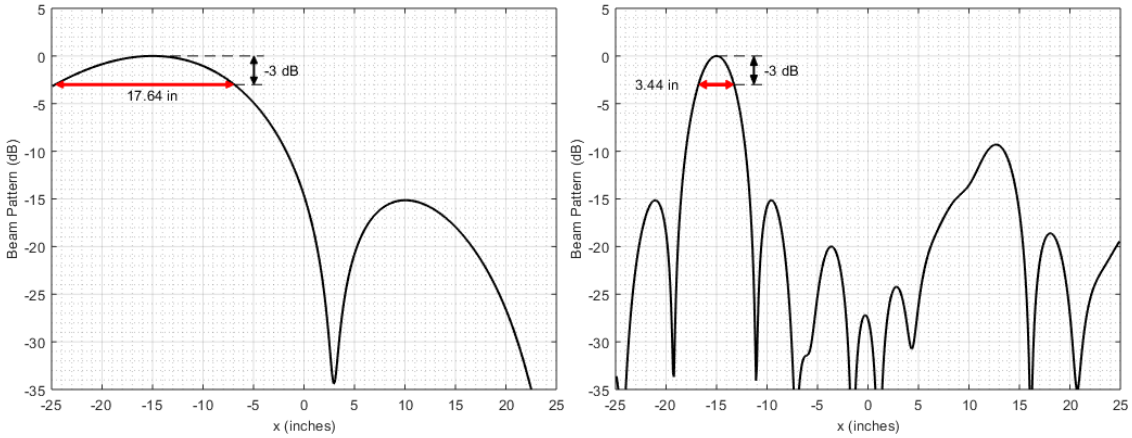

(a) 1.0 kHz beam pattern

(b) 5.0 kHz beam pattern

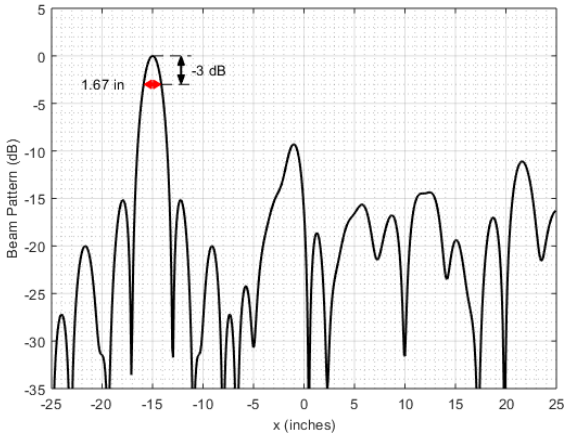

(c) 10.0 kHz beam pattern

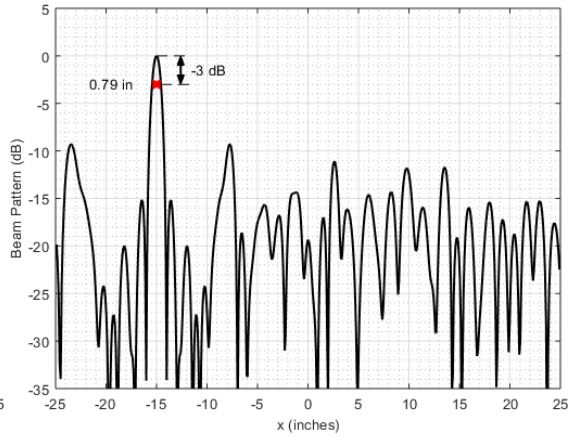

(d) 20.0 kHz beam pattern

Figure 6.11: Beam pattern plots for 1.0 kHz, 5.0 kHz, 10.0 kHz, and 20.0 kHz with the array focused at $\alpha = -18.24°$.

as those in Figure 6.10. The beam widths are slightly larger for the $\alpha = -18.24°$ beam patterns. For 1.0 kHz, 5.0 kHz, 10.0 kHz, and 20.0 kHz, the 3 dB beam widths of the main lobe are 17.6 inches, 3.4 inches, 1.7 inches, and 0.8 inches, respectively. The beam patterns also no longer appear to be symmetrical around the main lobe; the beam pattern to the left of the main lobe appears to be more stretched out, more so at lower frequencies. This is a direct result of the the conversion from azimuth angle to the rectangular x coordinate, in that azimuth angles encompass more x distance on a per degree basis as the azimuth

angle approaches $\pm 90°$ (see Equation 6.2). As a result, when the beamformer is focused at azimuth angles other than zero degrees, the main lobe captures wider space in the x direction.

Figure 6.12 contains plots of the 3 dB beam width for the main lobe, as a function of frequency and focus location in azimuth (α_f), for the beamformer used in this work. The focus locations are at azimuth angles of $0°$, $9°$, $18.24°$, and $25°$ which correspond to

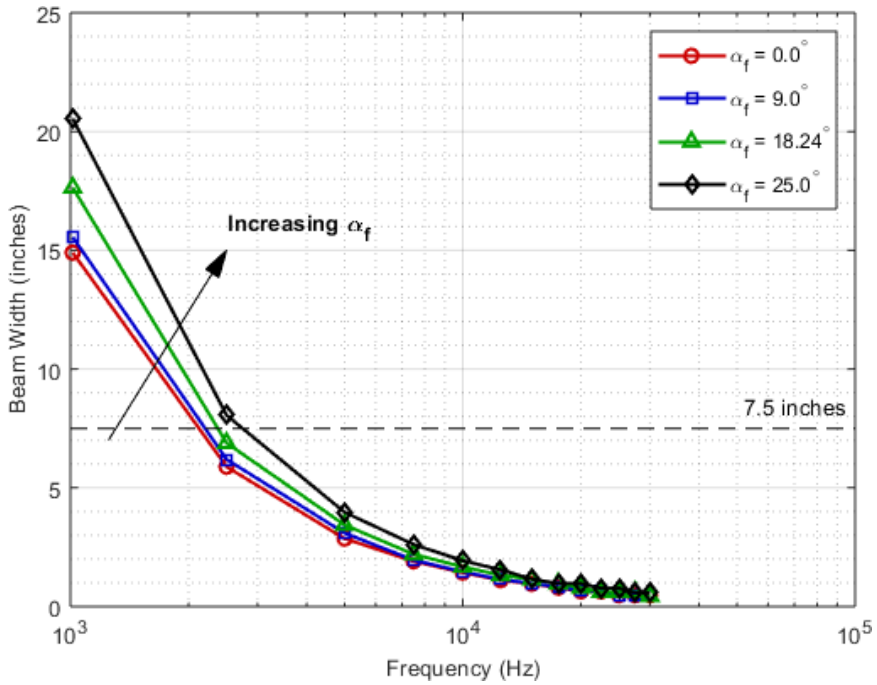

Figure 6.12: Plot of main lobe 3 dB beam widths for when the array is focused at several azimuth angles: $0°$, $9°$, $18.24°$, and $25°$.

x locations of 0, 7.2, 15, and 21.2 inches with respect to the array center, respectively, as shown earlier in Figure 6.8. The azimuth angle of $25°$ corresponds to the farthest x location that is measured by the beamformer in this work. The shape of the beam patterns at positive focus azimuths are mirror images of those at negative focus azimuths, and as a result the beam widths at negative azimuth angles have the same values as the beam widths of the positive azimuth angles. This means that the beam width at $\alpha_f = 18.24°$ has the same value as the beam width at $\alpha_f = -18.24°$, which, as shown in Figure 6.12, roughly coincides with the location of the nozzle exit. The beam width plots in this figure are applicable

not only to the twin jets examined in this chapter, but also to all the other jet noise source location measurements performed in this work.

The data in Figure 6.12 shows that the beam width is much more affected by the focus location at lower frequencies. For example at 1 kHz, the beam width can be as large as 15 to 20 inches, depending on the focus location. At higher frequencies, the effect of focus location becomes less extreme. At frequencies above 10 kHz, the beam width is under two inches for all focus locations, and above 16 kHz, the beam width is under one inch for all focus locations.

The twin jets used in this work are positioned at separation distances of 3, 6, and 10 diameters. The largest separation distance for the 0.75-inch diameter jets is only 7.5 inches. A dashed line is plotted in Figure 6.12 to illustrate this value. Frequencies that result in beam width values larger than this dashed line cannot be resolved between the two jets. In short, frequencies below 2.1 kHz cannot be resolved for any of the separation distances examined in this work. For example at 1 kHz the smallest beam width shown in Figure 6.12 is about 15 inches, twice that of the largest nozzle separation. At smaller separation distances between the two nozzles, the limiting frequency, below which sources of individual frequencies between the two jets cannot be resolved, increases. The next subsection illustrates how this impacts actual jet noise results presented in this chapter.

6.2.3 Impact of Beam Width on Subsonic Twin Jet Noise Source Distributions

The beam widths for 2.0 kHz and 11.0 kHz are plotted in Figure 6.13 on top of the noise source distributions of the twin jets at 10 diameters separation. The frequency of 2.0 kHz roughly corresponds to the frequency at which the beamformer resolution becomes inadequate to resolve the noise sources of the two jets, and the frequency of 11.0 kHz is an example of a frequency where the beam width is small enough to resolve both jets. In each case the beam width is centered on $y/D = 0$; however, this location is just arbitrary for this example and is roughly the same size for a given frequency at every y/D location plotted.

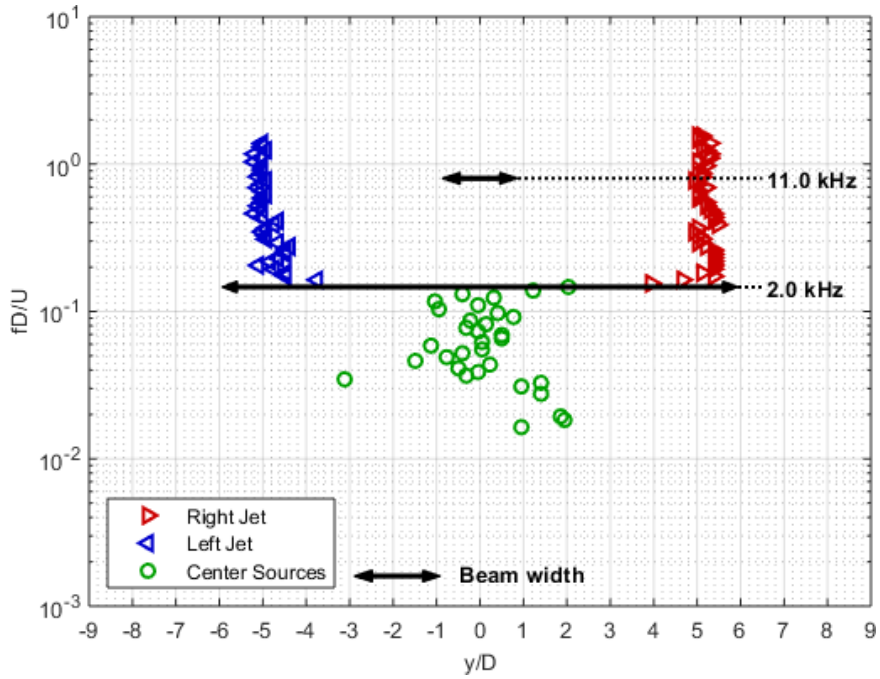

Figure 6.13: Illustration of beam width sizes on the noise source distribution data from Figure 6.3b. (Nozzle = conical, $D = 0.75$ inches, $M_j = 0.8$, $s/D = 10$)

At frequencies higher than 2.0 kHz, using 11.0 kHz for example, the beam width of the beamformer is smaller than the separation distance between the two jets. As a result, the noise sources of both jets can be both identified. At frequencies of 2.0 kHz and below, the beam width is larger than the separation distance between the two jets. As such, the noise sources from each jet cannot be individually separated and the end result is that the array indicates a single noise source at the centroid location between the two jet axes, indicated by the data points represented as "center sources" in Figure 6.13.

The beam widths for 3.3 kHz and 12.0 kHz are plotted in Figure 6.14 on top of the noise source distributions of the twin jets at 6 diameters separation. The value of 3.3 kHz corresponds to the frequency at which the beamformer can no longer differentiate the noise sources of the two jets, and 12.0 kHz is an example of a frequency at which the beamformer can. In this example the beam width at 3.3 kHz is not larger than the jet spacing, but approximately the same size. At frequencies below this value, the beam width is too large for the beamformer to show individual noise sources on the axis of each jet. At

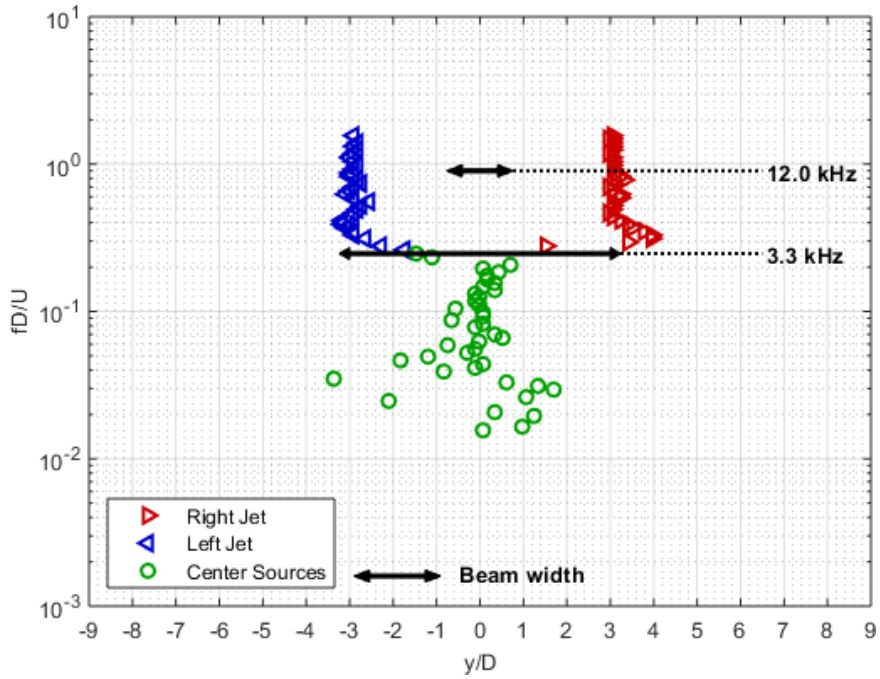

Figure 6.14: Illustration of beam width sizes on the noise source distribution data from Figure 6.4b. (Nozzle = conical, $D = 0.75$ inches, $M_j = 0.8$, $s/D = 6$)

frequencies around this value the noise sources from each jet appear to be approaching the central axis ($y/D = 0$). Because the beam width is still fairly large at these frequencies, the beamformer stills measure contributions from the opposing jet, and as a result, the source location is shifted towards the centroid of the two jets at those frequencies.

The beam widths for 4.8 kHz, 8.5 kHz, and 15.0 kHz are plotted in Figure 6.15 on top of the noise source distributions of the twin jets at 3 diameters separation. In this example, 8.5 kHz represents the frequency at which the resolution of the beamformer starts affecting the source location, and 4.8 kHz represents the frequency at which the beamformer can no longer identify the presence of two separate jets. High frequency noise sources, similar to the ones at 15.0 kHz for example, are easily resolved to be emanating from each of the twin jets due to the small size of the beam width at those frequencies. At frequencies between 4.8 kHz and 8.5 kHz, the source location from the right jet can be seen transitioning towards the central axis as the beam width grows from slightly smaller than the jet separation distance at 8.5 kHz to a slightly larger than the jet separation distance at 4.8 kHz.

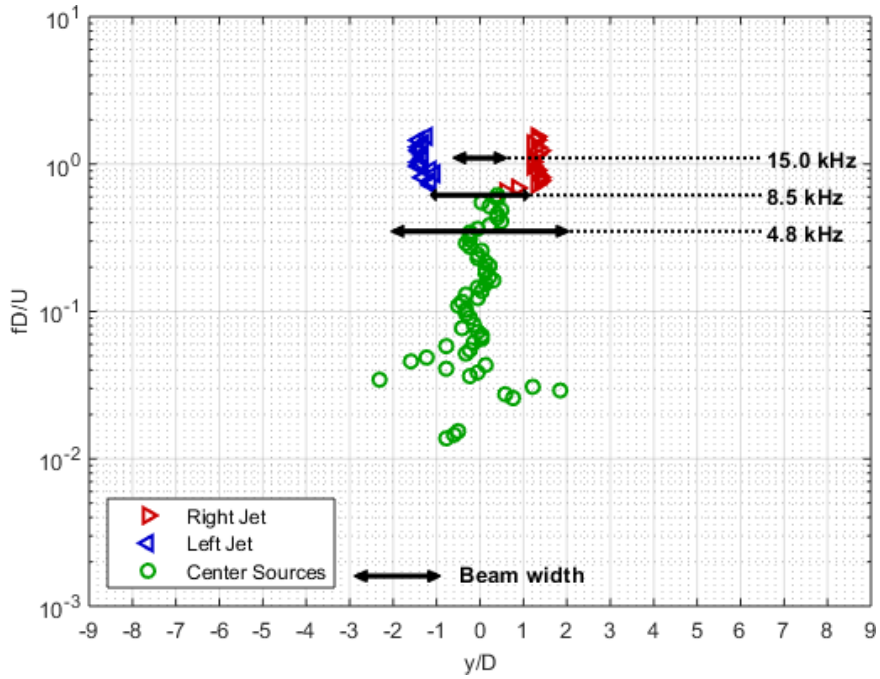

Figure 6.15: Illustration of beam width sizes on the noise source distribution data from Figure 6.5b. (Nozzle = conical, $D = 0.75$ inches, $M_j = 0.8$, $s/D = 3$)

It is worth noting that the noise source distributions plotted as Strouhal number versus normalized downstream distance, shown in Figures 6.3a, 6.4a, and 6.5a, can still be useful even for frequencies below which the beamformer cannot resolve the two jets separately. These noise source distributions can be seen plotted together in Figure 6.16. For Strouhal numbers that correspond to frequencies above about 1 kHz, the noise source distributions for the three nozzle separation distances generally collapse on top of each other. In this frequency range, each separation distance has different starting frequency at which the resolution of the beamformer impacts the source location for plots of Strouhal number versus normalized axial distance. This shows that even though the beam width has a large effect on source location in the axial direction, it does not have as much of an effect in the downstream direction. As a result, large beam widths can still be used to reasonably acquire the source locations of general jet-mixing noise. As shown in this chapter and in Section 4.2 of Chapter 4, low resolution in source location leads to the measurement of the centroid location of the given frequency. Because jet-mixing noise is distributed along the

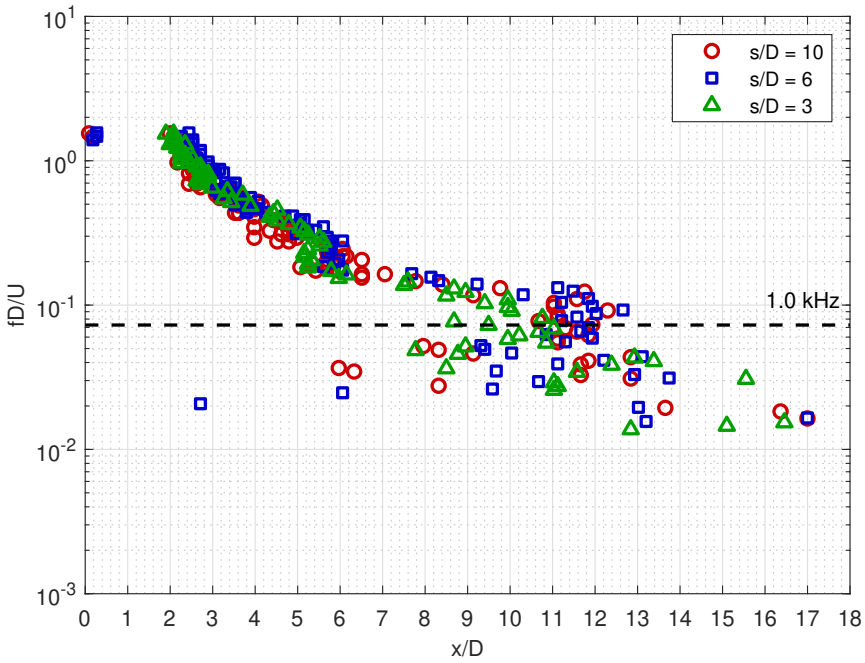

Figure 6.16: Subsonic twin jet noise source distributions compared for various separation distances. (Nozzle = twin conical, $D = 0.75$ inches, $M_j = 0.8$, $s/D = 3$, 6, and 10.)

jet axis, generally only the locations of peak noise or the centroid of the noise distribution are plotted for each frequency. However, at low enough frequencies the source location cannot be used, even for jet-mixing noise of single jets. As the beam width becomes too large for the measurement window, the averaged centroid locations calculated no longer represent the actual centroid location for that given frequency, which in this case appears to be at frequencies below 1.0 kHz.

In summary, the noise source distributions of twin jets cannot be accurately measured below a certain frequency that is a function of the separation distance between the nozzles. This is all related to the size of the beamformer beam width and whether or not the noise sources of the two jets are separated by a distance greater than the size of the beam width. Because the beam pattern, and thus the beam width, of an array is determined by the number of microphones and their locations with respect to the source, source location resolution can only be significantly improved by changing the design of the array or moving the array closer to the source.

6.3 Concluding Remarks

The noise source distributions of twin jets cannot be accurately measured below a certain frequency that is a function of the separation distance between the nozzles. For a given frequency, the beamformer has a resolution determined by the size of the beam width of the main lobe in its beam pattern, which improves with frequency. Lower frequency noise sources need to be located further apart than higher frequency noise sources, otherwise the beamformer ends up averaging their locations to a centroid location. Because the beam pattern, and thus the beam width, of an array is determined by the number of microphones and their locations with respect to the source, source location resolution can only be significantly improved by changing the design of the array or moving the array closer to the source.

For the twin jets tested in this work, the noise source distributions are independent and centered on each jet's nozzle axis at higher frequencies. Below a certain frequency, the noise source distributions give the false impression that they move towards the central axis ($y/D = 0$). This is a result of the beam width of the beamformer being larger than the separation distance between the two nozzles. Eventually, all low frequency noise sources appear centered on $y/D = 0$. In reality, the noise sources should still be centered on each jet's nozzle axis at these frequencies, but the poor resolution of the beamformer caused by large beam widths averages their locations to a single centroid location. Velocity measurements obtained using PIV are used to strengthen the argument that these shifts in source location to the central axis are a result of resolution issues and not due to jet mixing. Over the 18 diameters in which the source location is measured for this work, the velocity measurements show that the jets are barely interacting, let alone mixing.

Even with poor resolution due to a large beam width, the noise source distribution for jet-mixing noise when plotted as Strouhal number (fD/U) versus normalized downstream location (x/D) can still be fairly accurately obtained. The noise source distribution plots of

twin jets at three different separation distances, and thus three different regions where the source location becomes poor, collapse independently of their separation distance. There is a limit to this, however, at extremely low frequencies the beam width of the beamformer is larger than the measuring window and as a result, the measured centroid location may not be the proper centroid location for that frequency.

In summary, to obtain accurate noise source distributions for twin nozzles, measures need to be taken so that the beam width of the array is smaller than the separation distance between the two jets. This can be accomplished with (1) the use of much larger nozzles, (2) specifically designed array geometries, and (3) smaller measuring distances between the jet and the array. All three of these methods have trade offs and it is recommended to always calculate one's array's beam width before proceeding with experimentation.

CHAPTER 7

SUPERSONIC JET NOISE SOURCE DISTRIBUTIONS

7.1 Introduction

The previous chapters have presented jet noise source distributions for subsonic jets. Except at very small angles with respect to the jet axis, where jet noise is dominated by noise produced by large coherent structures (see Tam et al. [23]), much of the subsonic jet noise on the sideline is dominated by that produced by small-scale turbulence. As in the present study, the beamformer is placed in the sideline, parallel to the jet axis, much of the noise captured by it is that associated with small-scale structures. These turbulent structures originate in the mixing layer of the jet, and the frequency of the noise produced by them is inversely proportional to their size. While for shock-free supersonic jets it is expected that the noise source distribution curve is similar to that of subsonic jets, many supersonic jets have additional complications that are introduced by the presence of shock-cells along the length of the jet axis in the potential core. In shock-containing jets, repetitive interactions of the convecting turbulence with the shock cells in the potential core become additional noise sources. These shock cells are a series of shocks and expansions formed in response to the pressure at the nozzle exit not equating to that of the ambient pressure. Depending on the design of the nozzle and jet operating conditions, the pressure at the exit of the nozzle for supersonic jets is either greater than, less than, or equal to ambient pressure. For the converging nozzles used in this work at the supersonic conditions examined in this chapter, the pressure at the nozzle exit is always greater than ambient pressure. Thus, all the jets require further expansion outside of the nozzle to reach ambient conditions, which results in what is called an underexpanded jet.

This chapter presents and discusses supersonic jet noise source distributions. The jet

noise source distributions shown in this chapter are from conical nozzles of diameters 1.0 inch, 1.597 inches, and 2.44 inches. For simplicity, the 1.597-inch nozzle is referred to as the 1.60-inch nozzle in text. The noise source distributions of ASME nozzles are in many ways similar and presented in Appendix C. These noise source distributions are from jets with fully-expanded Mach numbers ranging from 1.0 to 1.6 in increments of 0.2.

7.2 Relationship Between Nozzle Pressure Ratios and Fully-Expanded Mach Number

As mentioned in the introduction, the supersonic jets examined in this work are all underexpanded. When producing a supersonic jet, air must be accelerated (expanded) through a nozzle from subsonic speeds to supersonic speeds. For subsonic flow, air is accelerated by reducing the area of the nozzle; conversely, supersonic flow requires the area of the nozzle to increase in order to accelerate. This means that by only reducing the area of the nozzle, as in the case of the converging nozzles used in this work, air within the nozzle cannot be accelerated past Mach 1.0. As a result, the pressure at the nozzle exit is higher than ambient pressure and, because there cannot be a pressure discontinuity, the air at the exit needs to accelerate outside the nozzle to reach ambient pressure. Because the flow is supersonic, this acceleration is accomplished through a series of expansion waves and oblique shocks, also known as shock cells.

Because this work involves underexpanded jets, the Mach numbers listed for each condition are not quite as useful as they were for subsonic jets. The Mach number in this chapter is identified as the fully-expanded Mach number. The fully-expanded Mach number is the Mach number condition that the jet wants to expand to, for a given nozzle pressure ratio (NPR), in order to reach ambient pressure. The NPR is the ratio of upstream plenum pressure, which is treated as the stagnation pressure, to ambient pressure. Following the convention of earlier researchers in the field of supersonic jet noise, this work uses the

fully-expanded Mach number (M_j) to describe each condition for simplicity. Table 7.1 provides the corresponding NPR for every Mach number discussed in this chapter.

Table 7.1: Reference of fully expanded Mach numbers and the corresponding nozzle pressure ratios.

Mach Number (M_j)	**NPR** $\left(\frac{p_t}{p_a}\right)$
1.0	1.89
1.2	2.42
1.4	3.18
1.6	4.25

7.3 Results

This section is split into four different subsections. First, the terminologies used in this chapter are described. The next two subsections contain an analysis of the source location and flow visualization, respectively, of jets with fully-expanded Mach numbers of 1.0, 1.2, and 1.4. The final subsection details the source location and flow visualization of Mach 1.6 jets.

7.3.1 A Note on Noise Source Terminology with Typical Results

An example of typical results for supersonic noise source distributions and 90-degree farfield spectra measured in this study is given in Figure 7.1. These results are from the 1.60-inch conical jet operated at a fully-expanded Mach number of 1.4.

Figure 7.1a contains a typical supersonic jet noise source distribution plotted as Strouhal number (fD/U) versus normalized downstream distance (x/D). This distribution of noise sources can be divided into three basic regions for this example labeled as A, B, and C in Figure 7.1a: (1) a region, "A," that resembles the subsonic jet-mixing noise distributions as seen in the last two chapters, (2) a region, "B," that appears to contain noise associated with the interaction of turbulence at each shock cell, and (3) a region, "C," that is characterized by having multiple, usually two, different Strouhal number sources at each downstream

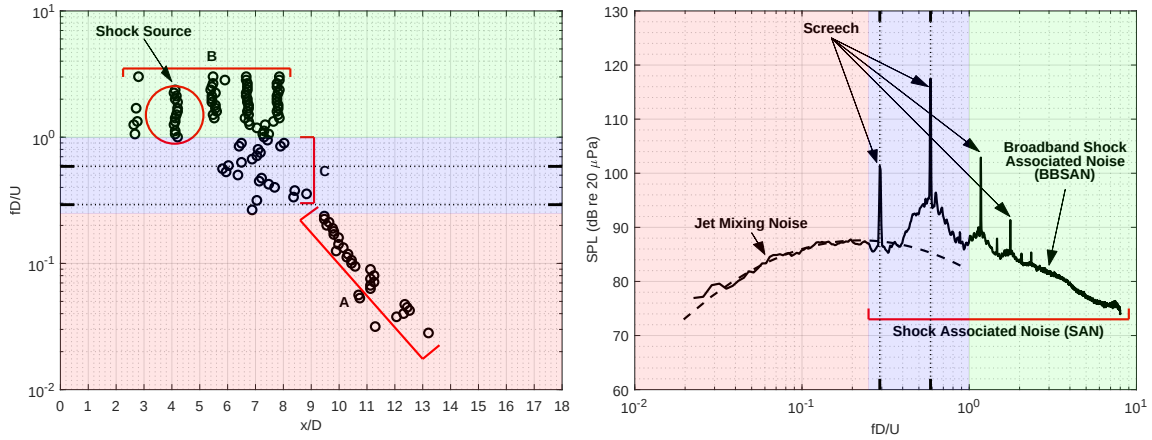

(a) Noise source distribution

(b) $\theta = 90°$, $\Delta f = 32$ Hz

Figure 7.1: Example of typical results for supersonic source location and 90-degree farfield spectra. (Nozzle = conical, $D = 1.60$ inches, $M_j = 1.4$)

location in the region. Regions A, B, and C are referred to as "the jet-mixing region," "the shock source region," and "the multi-source shock noise region," respectively.

The label "Shock Source" is also used in Figure 7.1a. This term that is used to describe the sources associated with the repetitive interaction of convecting turbulence at the end of each shock cell. The repetitive nature of this shock/turbulence interaction manifests itself in the form of sources at a wide range of Strouhal numbers at a single location. In Figure 7.1a, the shock source at $x/D = 4.2$ is circled and labeled; however, there are four additional such sources at x/D values of about 2.75, 5.5, 6.75, and 7.75.

Figure 7.1b shows a typical 90-degree farfield spectrum for a supersonic jet with the same jet-operating conditions for which the noise source distribution of Figure 7.1a is obtained. All spectra in this chapter are rendered lossless and are corrected to a distance 90 diameters. This figure has three labels representing the three well-known components of supersonic jet noise: (1) jet-mixing noise, (2) broadband shock associated noise (BBSAN), and (3) screech. The region of the spectrum marked as "Jet Mixing Noise" corresponds to the noise produced by small-scale turbulence, as seen in the data for subsonic jets discussed earlier. A dashed curve is drawn through this region of the spectra and is extrapolated to

higher Strouhal numbers to show the difference between jet-mixing noise and the shock associated noise (SAN). SAN is made up of BBSAN and screech. The SAN region consists of the spectral region where shock noise is typically dominant. BBSAN is produced by the jet turbulence interacting with the shock cells. Finally, screech is a result of a feedback phenomenon that shows up as a tone (or multiple tones) in the BBSAN region of the spectrum. In order to keep the number of markers on each plot to a minimum, only primary screech tones and their first harmonic (if any) are marked. In Figure 7.1b the screech tone at $fD/U = 0.29$ and its first harmonic at $fD/U = 0.58$ are marked with dashed lines; these same Strouhal numbers are marked in the source location plot in Figure 7.1a for reference.

The backgrounds of the plots in Figures 7.1a and 7.1b are color coded to facilitate analysis of the data between the two very different types of data and plots. A reference for the color scheme used for these backgrounds is shown in Table 7.2. The pink background

Table 7.2: Background color schema used for source location and corresponding spectral plots at $\theta = 90°$.

Background Color	**Source Location Region**	**Spectral Region**
Pink	Jet-mixing noise (A)	Jet-mixing noise
Green	Discrete shock sources (B)	SAN
Blue	Multi-source shock noise region (C)	SAN

in the two plots correspond with the jet-mixing noise region in the source location plot and in the corresponding farfield spectra at $\theta = 90°$. The noise in this region is due to the small-scale turbulence in the jet-mixing layer and the corresponding noise source distribution is very similar in shape as that for subsonic jet noise. In the plots shown in this chapter, this region is defined to end at the Strouhal number at which shock noise starts to dominate jet-mixing noise. The remaining two colored backgrounds, green and blue, comprise the entirety of the SAN region of the jet spectra. The green background encompasses Strouhal numbers associated with source region B of the source location, and the blue background encompasses the remaining Strouhal numbers between the pink and green regions in source

region C.

The Multi-Source Shock Noise Region

Up to this point, there has been little description as to what types of noise sources result in the blue, multi-source shock noise region of the noise source distribution of a supersonic jet. The odd shape of the noise source distribution in this region is attributed to the same beamformer resolution limitations discussed in the previous chapter for twin jets. At high frequencies, the noise sources of the individual twin jets could be separated. This is also why the different shock sources in the green region can be separated. As the source frequency is decreased, the source location resolution of the beamformer decreases and multiple sources within a certain proximity of each other can no longer be resolved. This is reflected in the noise source distributions of the twin jets as the noise sources from the two jets appearing to merge into one source at a centroid location between the two jets, and this occurs because the beam width of the beamformer increases with decrease in frequency. If the beam width is larger than the spacing between noise sources, the beamformer averages the locations of sources of the given frequency like a centroid. Therefore, when the spacing between the individual shock sources, which is constant for all frequencies, is less than the beam width for the given frequency, the beamformer ends up averaging the contributions of the shock sources to a single centroid location.

To further explain how source location resolution impacts the results in the multi-source shock noise region, an example is provided. Figure 7.2 contains the noise source distribution from the typical data shown in Figure 7.1a with the beam widths corresponding to frequencies of 4 kHz, 5.8 kHz, and 10 kHz superimposed on top. From the corresponding spectrum shown in Figure 7.1b, shock noise is the dominant source of noise at Strouhal numbers in the blue and green regions of Figure 7.2. This implies that the shock sources in the green region should extend down into the blue region, as indicated by the green arrows. By $fD/U = 1$ the beamformer cannot separate the shock sources at $x/D = 6.75$ and

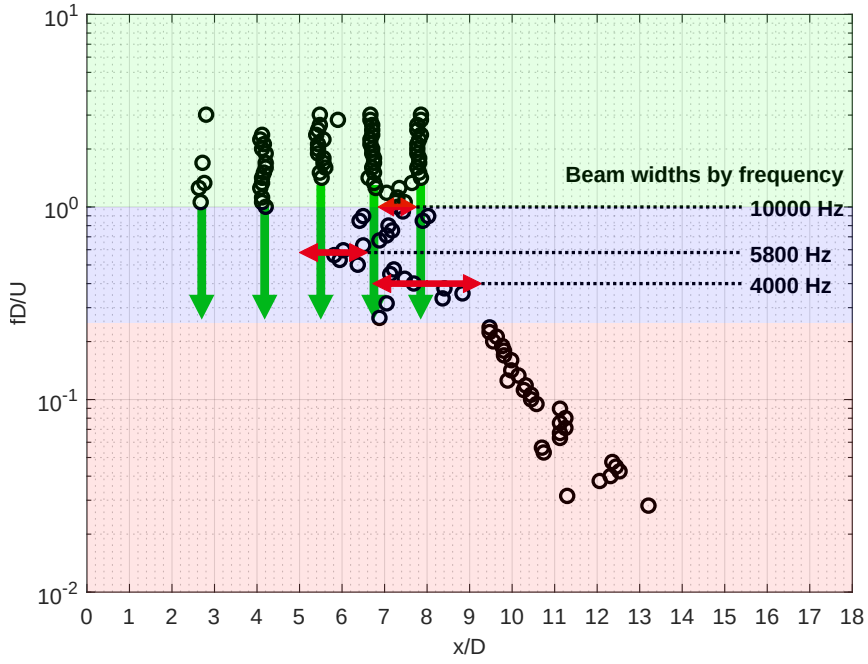

Figure 7.2: Illustration of beam width sizes on the noise source distribution data from Figure 7.1a. (Nozzle = conical, $D = 1.60$ inches, $M_j = 1.4$)

$x/D = 7.75$, and as a result indicates that the source location for that Strouhal number is the averaged, centroid, location between the two shocks, $x/D = 7.4$. The beam width at 10 kHz, corresponding to $fD/U = 1$, is about one diameter. As the measuring frequency gets even lower, the beam width of the beamformer continues to grow. By $fD/U = 0.55$, or 5.8 kHz, the beam width is approximately 1.5 diameters, which is larger than any of the spacings between the shock sources at this condition. At the lower Strouhal range of the multi-source shock noise region, the SPL of the shock noise sources decrease to a point at which the jet-mixing noise sources can start to have an impact on the noise source distribution as well. The effect of this is the shifting the noise source distribution further downstream, towards the jet-mixing noise curve.

The shape of the noise source distribution in this region is highly dependent on the spacing of the noise sources in the region, their frequencies, and their strengths. While the spacing of the shock sources in this region can be reasonably approximated using the shock sources in the green region, the strength variability as a function of frequency for

these individual sources cannot currently be measured with the tools available in this work. Because of this, further analysis cannot be made for noise sources in this region. The data in this region in essence just shows the centroid location for noise sources of a specific Strouhal number. As such, from this point onwards no further attempt is made to attribute the shape of the distribution in this region to the physics of the jet.

On a final note, while the beamformer resolution impacts the source location in the blue region, there is less concern for its impact on the noise source distribution in the pink jet-mixing region. The noise sources in this region are not discrete like the shock noise sources, but instead have some extent along the jet axis. It is common practice to indicate the locations of these types of noise sources in a jet by using either the peak noise location or the centroid noise location. Because low resolution source location locates the centroid of the sources of a given frequency anyways, there is little impact except at the lowest measured frequencies. This has been shown for the subsonic noise source distributions in the three previous chapters.

7.3.2 Supersonic Jet Noise Source Distributions

This subsection focuses on the jet noise source distributions of jets as a function of fully-expanded Mach numbers and nozzle diameter.

Source Location as a Function of Mach Number

Figure 7.3 contains data for the 1.60-inch jet operated at a fully-expanded Mach number of 1.0. The noise source distribution shown in Figure 7.3a matches the subsonic noise source distributions for the same nozzle, as shown in Figure 5.1a in Chapter 5. This shows that, at Mach 1.0, the jet still predominantly produces jet-mixing noise. The spectra shown in Figure 7.3b reinforces this statement, as there does not appear to be any shock noise.

Figure 7.4 contains data for the 1.6-inch conical jet operated at a fully-expanded Mach number of 1.2. This set of plots only has the pink, jet-mixing region highlighted. To help

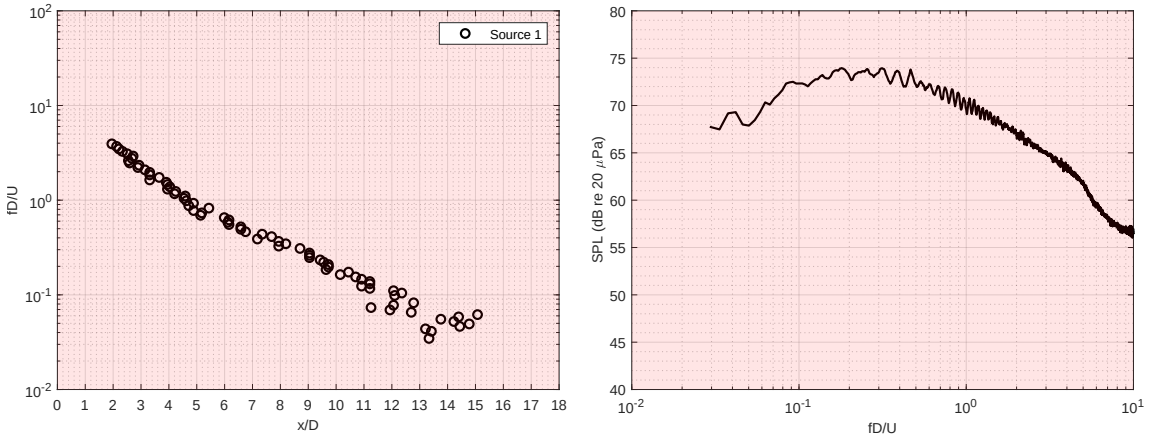

(a) Noise source distribution

(b) $\theta = 90°$, $\Delta f = 32$ Hz

Figure 7.3: Plots of supersonic noise source distribution and 90-degree spectrum. (Nozzle = conical, $D = 1.60$ inches, $M_j = 1.0$)

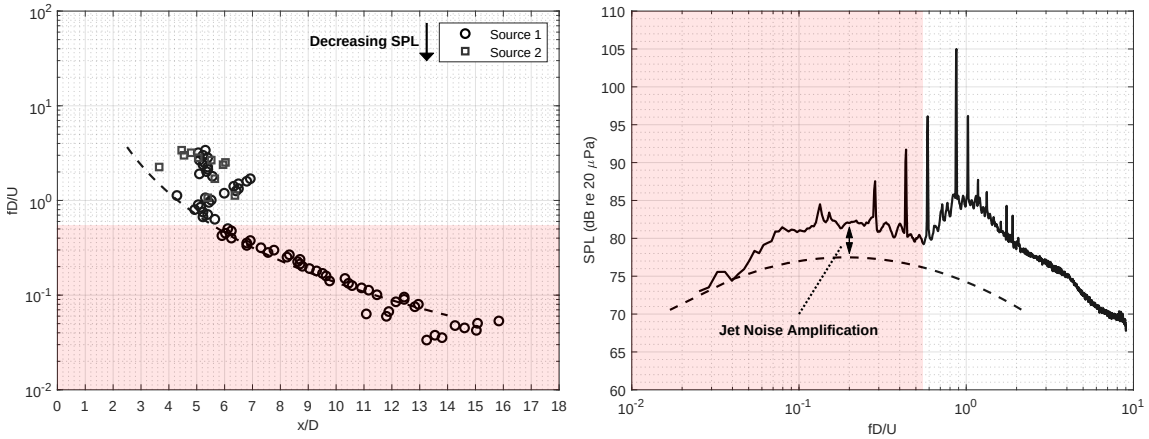

(a) Noise source distribution

(b) $\theta = 90°$ Spectrum, $\Delta f = 32$ Hz

Figure 7.4: Plots of supersonic noise source distribution and 90-degree spectrum, emphasizing jet-mixing noise. (Nozzle = conical, $D = 1.60$ inches, $M_j = 1.2$)

eliminate potential confusion that may arise from plotting all noise sources with the same symbol, as is done in Figure 7.1a, this and the remaining supersonic source location plots in this chapter use up to five symbols to represent different noise sources at the same Strouhal number. Only five symbols are used, because only the five loudest sources at each Strouhal number are identified by the beamformer in this work. These sources are labeled as "Source 1" through "Source 5" in the plots in this chapter. For a given Strouhal number, the louder source is indicated by a lower number (i.e., Source 1 is louder than Source 2). Note that not all Strouhal numbers have all five sources plotted, and likewise not all jet conditions have all five sources plotted either. For example only two sources are plotted in Figure 7.4a. The lack of additional sources means that the beamformer could not detect additional sources beyond those shown.

On the source location plot in Figure 7.4a, there is a dashed line that is a fit of the noise source distribution for the Mach 1.0 jet in Figure 7.3a. This curve matches well with the Mach 1.2 noise source distribution for Strouhal numbers less than 0.8. Likewise, the dashed curve on the spectrum plot for the Mach 1.2 jet in Figure 7.4b is a best fit of the Mach 1.0 spectrum in Figure 7.3b. The fitted curve is corrected for the velocity difference between the two jet conditions by scaling the fit by U_j^7 as suggested by Gaeta and Ahuja [57] for narrowband spectra. Unlike the noise source distributions, the spectra between the two jet conditions do not line up at Strouhal numbers below 0.8. In fact, the spectra for the Mach 1.2 jet is louder at all Strouhal numbers above about 0.04. This jet noise amplification is due to the jet-mixing noise being enhanced by the presence of screech, as shown by Tam et al. [58]. Screech is a feedback phenomena that occurs between the jet-mixing layer and the shock cells of the jet. This phenomena is discussed more in depth later in the chapter. The pink jet-mixing region ends at a Strouhal number of about 0.55. At Strouhal numbers above this value, the spectrum starts to be dominated by broadband shock associated noise.

The same data shown in Figure 7.4 can be seen in Figure 7.5 with the blue and green SAN regions added. In these plots, the green region starts at a Strouhal number of approx-

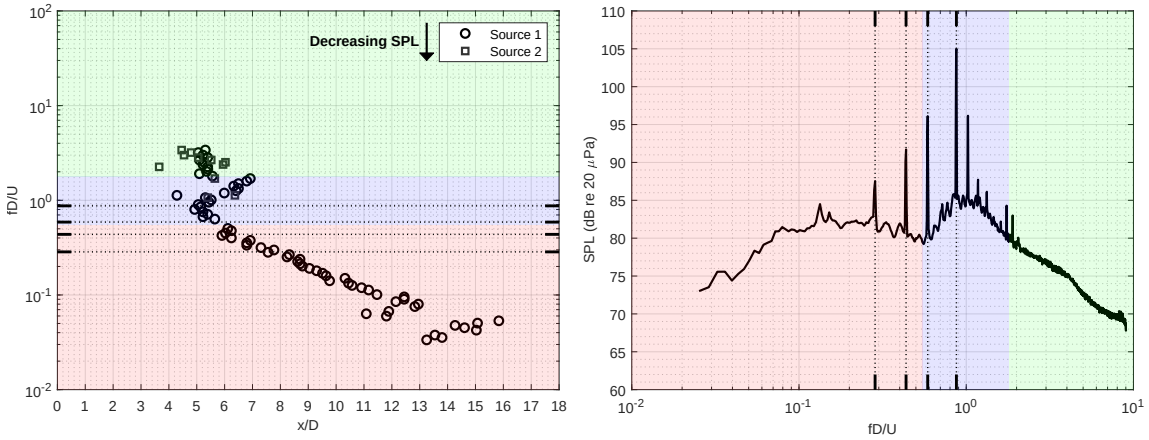

(a) Noise source distribution

(b) $\theta = 90°$, $\Delta f = 32$ Hz

Figure 7.5: Plots of supersonic noise source distribution and 90-degree spectrum. (Nozzle = conical, $D = 1.60$ inches, $M_j = 1.2$)

imately 1.8. There appears to be only one shock source in the noise source distribution in this region, and it is located at a downstream location of about 5.4 diameters, as seen in Figure 7.5a.

The blue region shown in Figure 7.5a, consists of noise sources with Strouhal numbers between 0.55 and 1.8. At Strouhal numbers below $fD/U = 0.8$, the noise source distribution in this region appears to be following the same curve as the jet-mixing noise. This is most likely due to the fact that at these Strouhal numbers jet-mixing noise, while not the dominant source of noise anymore, is similar enough in strength to the SAN that it still contributes to the spectrum shown in Figure 7.5b.

As Mach number is increased, additional trends become apparent in the two SAN regions. Figure 7.6 contains the same data, minus the added terminology, for the jet with a full-expanded Mach number of 1.4 as was shown earlier in Figures 7.1. At this higher Mach number, the noise source distribution in Figure 7.6a contains more than one shock source in the green region of the plot. In particular, there appears to be five shock sources at downstream locations of about 2.75, 4.2, 5.5, 6.75, and 7.75 diameters. The loudest of these sources is the one located at about 7.75 nozzle diameters downstream, as indicated by

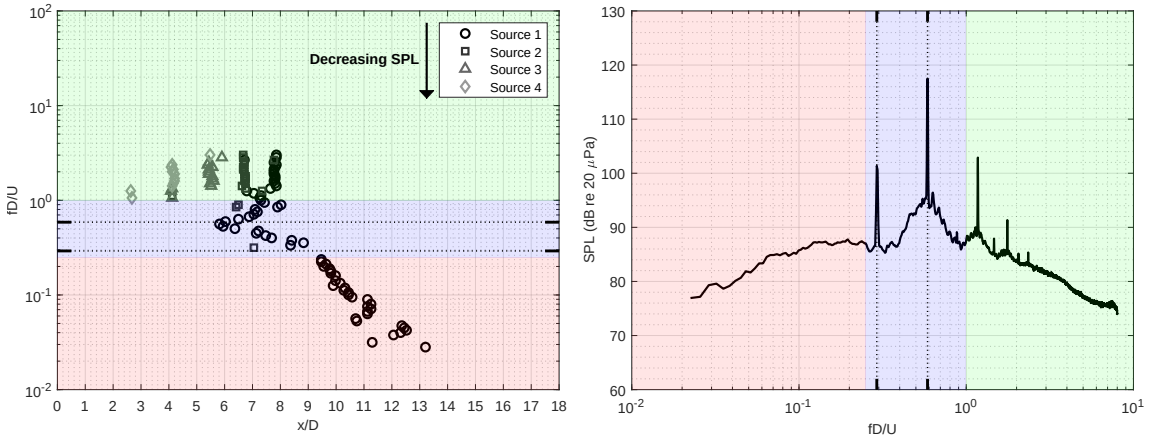

(a) Noise source distribution

(b) $\theta = 90°$, $\Delta f = 32$ Hz

Figure 7.6: Plots of supersonic noise source distribution and 90-degree spectrum. (Nozzle = conical, $D = 1.60$ inches, $M_j = 1.4$)

the circle symbols labeled as "Source 1." The shape of the noise source distribution in the blue region is similar to the one seen for the jet operated at Mach 1.2. The largest difference in the blue region is that at Strouhal numbers below $fD/U = 0.56$, the noise source distribution curve is no longer aligned with the jet-mixing noise curve. This difference may be due increased levels of BBSAN caused by stronger shocks at the higher Mach number condition; however, this cannot be confirmed in this work due to source location resolution limitations in the Strouhal range encompassed by the blue region.

In Figures 7.3 through 7.6, the noise source distributions for the 1.60-inch conical jet operated at Mach numbers ranging from 1.0 to 1.4 have been shown individually. Figure 7.7 contains a plot that compares the noise source distributions for all of these fully expanded Mach number conditions. As done before, several symbols are used for each noise source distribution to show multiple sources at a given Strouhal number; if a condition has less sources plotted, it means the beamformer could not detect as many sources at that jet condition. The normalization method of Strouhal number (fD/U) versus normalized downstream distance (x/D) does not result in the same type of collapse of source location curves for supersonic jets as it did for subsonic jets. At Strouhal numbers below about

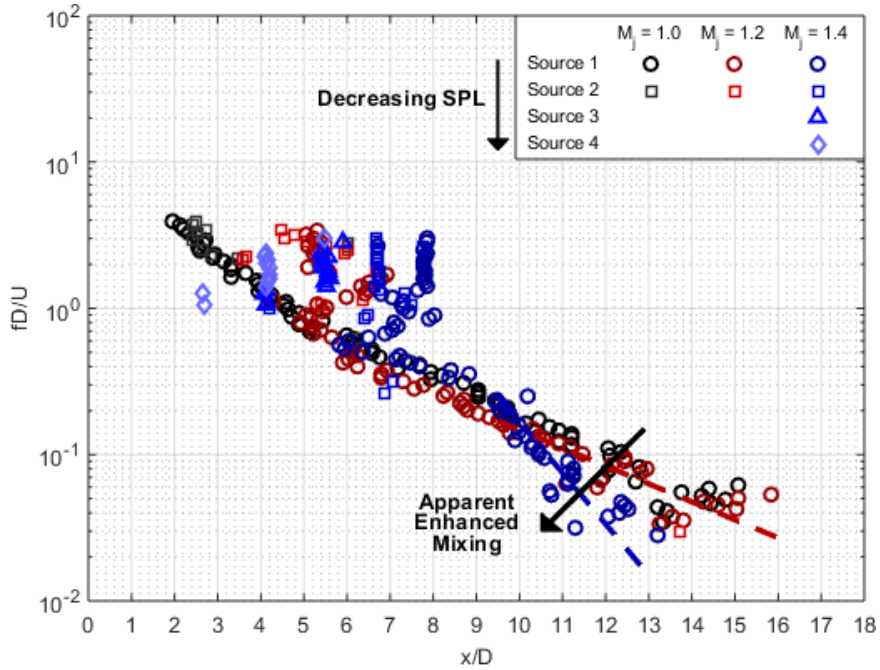

Figure 7.7: Supersonic jet noise source location for the conical 1.60-inch nozzle as a function of jet Mach number.

0.5, the noise source distributions for the Mach 1.2 jet and the Mach 1.4 jet appear to be fairly similar with the noise source distribution of the Mach 1.0 jet, which consists only of jet-mixing noise sources. At Strouhal numbers below about 0.25, the noise source distribution of the Mach 1.4 jet somewhat diverges from the other two, maxing out around two diameters upstream of the other two, as indicated by the dashed lines in Figure 7.7. This is an indication that, after about 9 diameters the Mach 1.4 jet is mixing somewhat faster than the other two jets. This enhanced mixing is most likely due to the high levels of screech at the Mach 1.4 jet condition. As shown in the spectrum for the Mach 1.2 jet in Figure 7.4b, screech has an amplification effect on the jet-mixing noise. At Mach 1.4 the screech tone is much louder than for the Mach 1.2 jet, about 118 dB to 105 dB, and thus the screech of the Mach 1.4 jet has a larger impact on the jet-mixing noise.

At Strouhal numbers above the multi-source shock noise source region, the number of shock sources increase with Mach number. For the Mach 1.0 jet there are no shock sources in the noise source distribution because there should be no shocks in the jet at this

condition. For the Mach 1.2 jet and the Mach 1.4 jet, there is one such source located at about $x/D = 5.4$ and five such sources located at about $x/D = 2.75$, $x/D = 4.2$, $x/D = 5.5$, $x/D = 6.75$, and $x/D = 7.75$, respectively. The difference in number of shock sources at the Mach 1.2 and Mach 1.4 jet condition is due to the shock sources in the Mach 1.2 jet being generally weaker than in the Mach 1.4 jet. There is likely more than one shock source in the Mach 1.2 jet; however, the ones not shown do not produce noise loud enough to be detected by the beamformer. Because there is only one apparent shock source in the noise source distribution of the Mach 1.2 jet, there is not enough information in Figure 7.7 to say whether or not the location of these shock sources are independent of Mach number. It is very unlikely that the locations of these sources are independent of Mach number, however, as these types of noise sources emanate from the shock cells in the jet. As shown by Norum and Seiner [59], the average spacing of shock cells in a supersonic jet increases proportionally to $\sqrt{M_j^2 - 1}$. As such, the spacing between these sources should increase similarly with Mach number.

The locations of the loudest of these shock sources, as marked by symbols of "Source 1" in Figure 7.7, appear to be further downstream with increased Mach number. This agrees with the findings of Norum and Seiner [59], who found that the dominant source of shock noise in underexpanded converging jets is located in the weaker downstream shock cells. The loudest shock source for the Mach 1.2 jet is the only one plotted, located at about $x/D = 5.4$, and the loudest shock source for the Mach 1.4 jet is located at $x/D = 7.75$.

Source Location as a Function of Diameter

Figures 7.8 through 7.10 contain plots that compare the source locations of conical nozzles as a function of exit diameter for a given Mach number. The nozzle diameters tested are 1.00 inch, 1.60 inches, and 2.44 inches.

Figure 7.8 contains the noise source distributions for the conical nozzles run at a fully-expanded Mach number of 1.0. The three curve collapse with each other; in addition, the

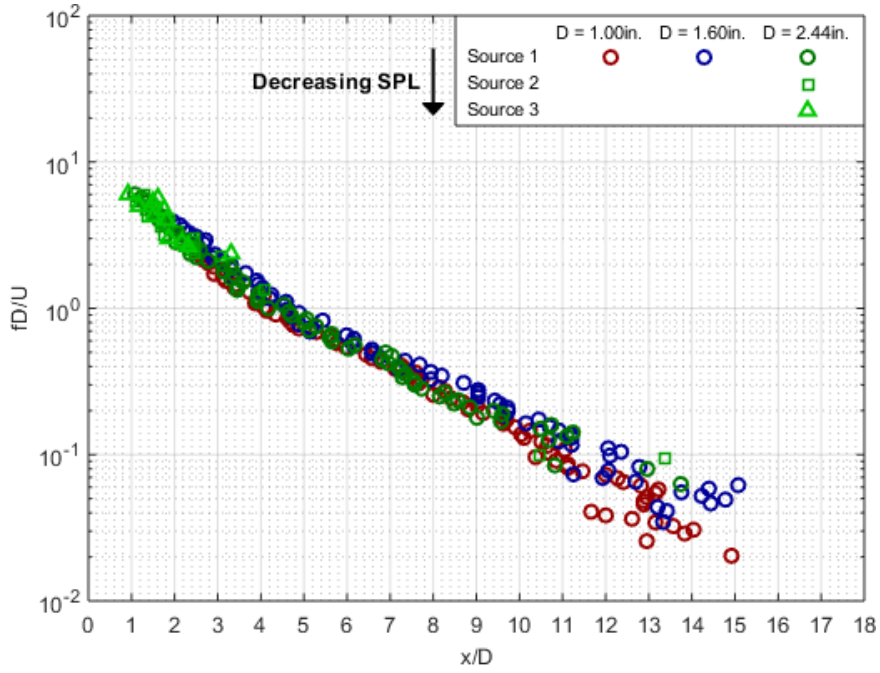

Figure 7.8: Jet noise source location at Mach 1.0 for the conical nozzles at various diameters.

three curves are essentially the same as the noise source distributions of their subsonic counterparts, shown in Chapter 5. For this jet exit condition, there should be no supersonic flow downstream of the nozzle exit, and as a result, only noise sources from jet-mixing noise are present in the sound field of the jet.

Figure 7.9 contains the noise source distributions for the conical nozzles run at a fully-expanded Mach number of 1.2. The noise source distributions of the three different nozzle diameters are fairly similar, though there are a few key differences. The differences are as follows: larger diameter nozzles have more shock sources than smaller ones and the jet-mixing region of the larger diameter nozzles appears to curve slightly more upstream than that of smaller diameter nozzles nozzles. As previously mentioned, the number of shock sources is dependent on the strength of the shock sources themselves. Higher Mach numbers and larger nozzle diameters result in louder shock sources. Due to this, the 2.44-inch jet has six shock sources whereas the 1.60-inch jet only has one. There are no shock sources for the 1.00-inch jet because the noise from these sources are high enough frequency to be

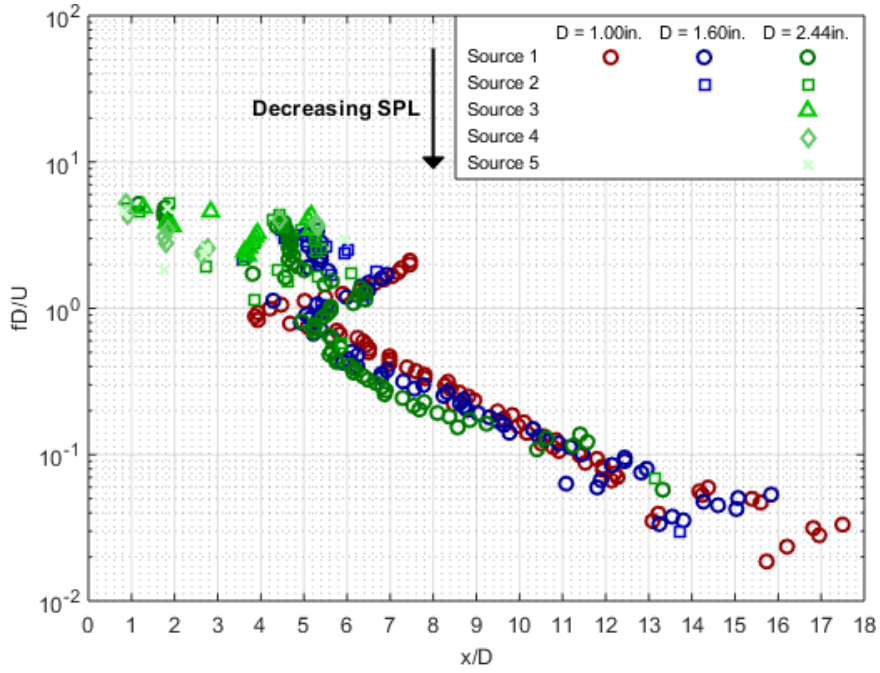

Figure 7.9: Jet noise source location at Mach 1.2 for the conical nozzles at various diameters.

outside of the measuring region of the beamformer used for this work.

The reason why the jet-mixing region of the larger nozzles appears more curved and slightly more upstream than that of the 1.00-inch nozzle, which is relatively flat, is at least partially due to measurement resolution of source location. Smaller nozzles have smaller flow structures, which require finer resolution to accurately resolve the sources at all frequencies. As a result, it is likely that the noise source distributions of the three nozzle diameter jets are very similar in the jet-mixing region at this Mach number condition.

Figure 7.10 contains the noise source distributions for the conical nozzles run at a fully-expanded Mach number of 1.4. The jet-mixing region ($fD/U \leq 0.3$) of all three nozzle diameter jets appear to follow a similar curve. This means that the upstream shift of the jet-mixing curve of the Mach 1.4 jet with respect to those of the lower Mach number conditions, shown in Figure 7.7, is a phenomena that does not just occur for one specific nozzle.

The shock sources of the 1.60-inch jet and the 2.44-inch jet line up almost perfectly at this condition. The shock sources for the 1.00-inch jet at $x/D = 4.2$ and $x/D = 5.5$

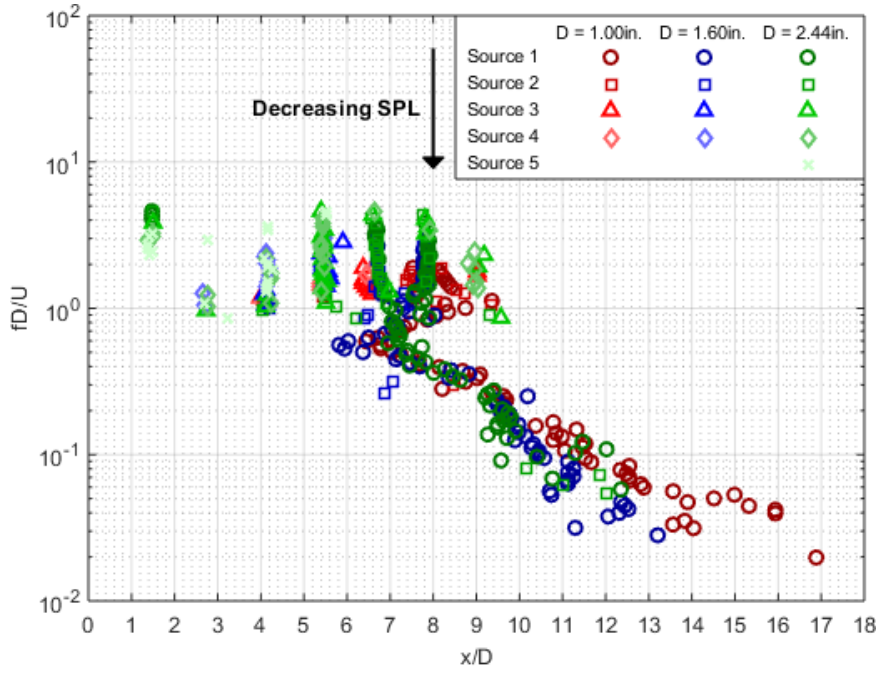

Figure 7.10: Jet noise source location at Mach 1.4 for the conical nozzles at various diameters.

line up as well. However, the discrete shock sources at $x/D = 6.5$ and $x/D = 7.5$ are about 0.25 diameters upstream of the discrete sources of the larger diameter nozzles. For a 1.00-inch diameter nozzle, this difference corresponds to about 0.25 inches, which is well within measurement error range of the beamformer.

The portion of the 1.00-inch jet noise source distribution in Figure 7.10 that is located between eight and nine diameters downstream, at Strouhal numbers above one, appears somewhat similar to a shock source that has been stretched out between the two locations. This specific source is interesting in that it does not match with any of the discrete sources of larger nozzles. The odd shape of this source may yet again be a result of array resolution, as this does not occur for larger diameter nozzles where resolution is less of a problem.

A Note about Screech and Source Location

Figures 7.5 and 7.6 display data for jets that contain screech. Screech is a feedback phenomenon that results from shock-turbulence interaction. This occurs when the thinnest part

of the jet-mixing layer becomes acoustically excited and produces a large scale instability wave that propagates along the mixing layer. The instability wave grows as it propagates downstream and eventually has enough energy to interact with a shock cell and produce high levels of noise. Some of this noise propagates upstream and further excites the mixing layer near the nozzle exit. This cycle keeps repeating and the noise produced keeps getting stronger. As the frequencies of shock noise that propagate upstream in the 180 degree direction are limited to a small band of frequencies, screech appears in the jet noise spectra as one or more tones with extremely high amplitudes.

As there are no shocks in the jet, there is no screech in the spectrum of the Mach 1.0 jet shown in Figure 7.3b. At Mach 1.2, as shown in the spectrum in Figure 7.5b, there are two primary screech tones at Strouhal numbers of 0.285 and 0.437 as well as several harmonics. At Mach 1.4, as shown in the spectrum in Figure 7.6b, there is one primary screech tone at a Strouhal number of 0.292 followed by several harmonics. Tam et al. [58] developed a relationship between fully-expanded Mach number and the frequency of screech in a supersonic jet, which was later refined by Massey and Ahuja [60] taking in account the different mode shapes of the jet instabilities that generate screech. The refined equation for fully-expanded Mach numbers between 1.2 and 1.8 is shown in Equation 7.1.

$$\frac{fD_j}{U_j} = \frac{0.615}{1.1(M_j^2-1)^{1/3}} \left[1 + 0.615M_j \left(1+0.2M_j^2\right)^{-1/2} \sqrt{\frac{T_t}{T_a}}\right]^{-1} \tag{7.1}$$

The term D_j in the above equation is the fully-expanded diameter of the jet and is a function of fully-expanded Mach number (M_j) and design Mach number (M_d), as shown in Equation 7.2.

$$D_j = D \left[\frac{1+0.2M_j^2}{1+0.2M_d^2}\right]^{1.5} \sqrt{\frac{M_d}{M_j}} \tag{7.2}$$

The design Mach number for all the nozzles used in this work is 1.0, because they are all purely converging. Using the above two equations, Strouhal numbers of 0.439 and 0.310 are calculated as the Strouhal numbers for the screech tones in the Mach 1.2 and Mach

1.4 jets, respectively. These two calculated values are very close to the measured values of 0.437 and 0.292, indicating that the tones measured in the spectra for this work are most likely screech.

While there are markers indicating the Strouhal numbers of screech, there is no indication of the source location of the screech tones shown in the noise source distributions in Figures 7.5a and 7.6a.

Discussion and Summary of Source Location Results

The supersonic jet-noise source distributions shown in this work can be broken into three different regions: (1) a region consisting of sources that are caused by the jet's small-scale turbulence, (2) a region consisting of several shock sources caused by the interactions between turbulence and the shock cells in the jet, and (3) an odd region that contains both jet-mixing noise and shock noise, but does not contain discrete shock sources.

The first region, indicated in pink in all plots in this chapter, is comprised of noise sources that emanate from mixing layer of the jet. The noise source distributions in this region are similar in appearance to those of subsonic jets. The small-scale structures in the mixing layer of the jet produce noise with frequency inversely proportional to their size. These structures, and the mixing layer, start near the nozzle exit and grow with distance downstream. As a result, jet-mixing noise is produced at all frequencies. In shock-containing jets, however, shock noise tends to dominate at higher frequencies, thus causing jet-mixing noise to only appear in the source location at lower Strouhal numbers. The additional noise due to shocks can excite the turbulent structures, causing the overall jet-mixing noise to go up due so-called jet noise amplification (see Tam et al. [58] and Ahuja and Blakney [61]). This is often accompanied by the phenomena known as screech, which is a result of feedback between the shock noise propagating towards the nozzle exit and excited turbulent structures. The spectrum in Figure 7.4b clearly shows excited jet-mixing noise. The jet-mixing portion of the Mach 1.2 spectra is about four decibels louder than the refer-

ence spectra of the Mach 1.0 jet (that has been corrected for the velocity difference using U_j^7 scaling), which should be completely unexcited jet-mixing noise.

The second region, indicated in green in the plots presented in this chapter, is comprised of several noise sources that, as shown in the next subsection, correspond with the shock cells in the jet. The shock sources produce noise at a wide range of frequencies in a very small region of space. These are the sources of shock noise described by Harper-Bourne and Fisher [62] and Tam [63]. These sources are responsible for the so-called broadband shock associated noise (BBSAN). This type of noise is generated as turbulent structures pass the tips of the shock cells and cause them to oscillate, producing noise at a wide range of frequencies. Because the strength of these sources are directly related to the Mach number and diameter of the jet, more of these sources are measured at higher Mach numbers and nozzle diameters by the beamformer. When jets are operated at Mach 1.0, there are none of these types of sources, as the jets do not have any shock cells along their lengths.

The third region, indicated in blue in the plots presented in this chapter, contains shock noise sources and is located between the first and second regions in a Strouhal sense. From corresponding spectral plots, it is shown that the noise in this region is dominated by shocks. As such, this region should, at least at higher Strouhal numbers, appear to be a continuation of the multiple shock sources as seen in the green, shock sources region. In actuality, the noise source distribution in this region appears as a continuous curve. The odd shape of the noise source distribution in this region is attributable to resolution limitations of the beamformer used in this work. The beamformer can only isolate noise sources spaced roughly the size of the beam width of its main lobe or larger. At lower frequencies, the size of the beam width is larger than the spacing between the shock cells, and the noise from individual shocks can no longer be isolated. When this occurs, the beamformer ends up plotting the centroid location for a given frequency instead of the various peak locations. At lower Strouhal numbers in this region, the noise source distribution is further modified

by the presence of jet-mixing noise, which is of similar strength to the shock noise at these Strouhal numbers. Because of the measuring limitations in this region, it is very difficult any of the source location at these Strouhal numbers to actual jet properties.

For a given nozzle diameter, the noise source distributions of supersonic jets of various Mach numbers do not collapse to a single curve when plotted as Strouhal number versus normalized downstream location. The jet-mixing region of the noise source distribution, which is very similar to that of a subsonic jet, does not change much with Mach number. The SAN region of the noise source distributions of supersonic jets is in no way independent of Mach number. This is not surprising, as the noise in this region is produced by the shock cells in the jet, the average spacing of which is proportional to $\sqrt{(M_j^2 - 1)}$ as shown by Norum and Seiner [59]. At higher Mach numbers, the average spacing between the shock sources increases, and as a result, the shock sources that are the furthest from the nozzle exit can be found even further downstream (see Figure 7.7).

The locations of the shock sources and generally those for jet-mixing noise are all fairly independent of nozzle diameter when plotted as Strouhal number versus normalized downstream location. Some differences do occur in the jet-mixing region for the largest (2.44-inch) nozzle tested. The noise source distributions in this region for this nozzle tend to be shifted upstream those of the smaller diameter nozzles. This may be associated with the larger diameter jet being more turbulent due to a thicker nozzle exit boundary layer. While the locations of the shock sources are not affected by nozzle diameter, the location of the loudest shock source is. The smaller diameter jets have the loudest shock noise sources farther downstream compared to those of larger diameter nozzles.

This subsection has examined how supersonic source location compares with farfield spectra for a specific conical nozzle at specific Mach numbers. This work seeks to further explore whether the noise source distribution, notably the discrete shock sources, line up with the flow visualization of the jets in the following subsection.

7.3.3 Supersonic Flow Visualization

The purpose of this subsection is to show the schlieren flow visualization for the conditions tested and to link the observed flow features to their corresponding noise source locations. In this subsection, two different types of figures are shown for the schlieren flow visualization data: single frame data and averaged frame data. While turbulent structures show very well in single frames, the turbulence in the jet tends to obscure the shock cells. Because the shock cells are relatively stationary and turbulence is chaotic, the shock diamonds can be brought into focus by averaging a large number of the schlieren video frames together. Both the single frame and the averaged frame data are cropped to show flow features seven diameters downstream of the nozzle exit.

Figure 7.11 contains cropped, but otherwise unmodified, frames of the schlieren video of the 1.60-inch conical jet at various supersonic conditions: Figures 7.11a though 7.11c show the jet at a fully-expanded Mach numbers of 1.0, 1.2, and 1.4, respectively. The first thing to note is that the Mach 1.0 jet, shown in Figure 7.11a, does not have any shock cells while the other conditions do. This lends support to the noise source distribution shown in Figure 7.3, which shows only the jet-mixing noise source distribution. Shock cells are present in the schlieren of the Mach 1.2 jet and the Mach 1.4, however, it is difficult to see them due to the turbulence in the jet.

In order to better view the shock cells themselves, the frames from the schlieren flow visualization data, as shown in Figure 7.11, are averaged over 6.5 milliseconds (200 frames) to create the images shown in Figure 7.12. Figures 7.12a and 7.12b are images of the Mach 1.2 and Mach 1.4 jet, respectively. The Mach 1.0 jet is not included in this figure, as it does not have any shock cells in the jet core. Dashed white lines have been plotted over the images to reference the locations of the shock sources shown in the noise source distributions from Section 7.3.2. As mentioned earlier, the jet is underexpanded at all the conditions tested. This can be well seen in Figure 7.12b where the jet-mixing layer expands outwards right after the nozzle exit, and thus it is known that the depicted shock cells start

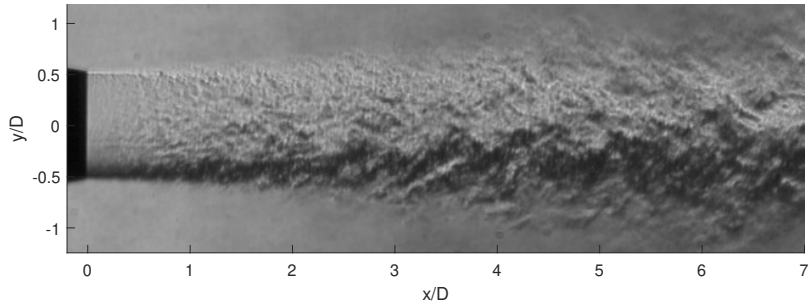

(a) Mach 1.0

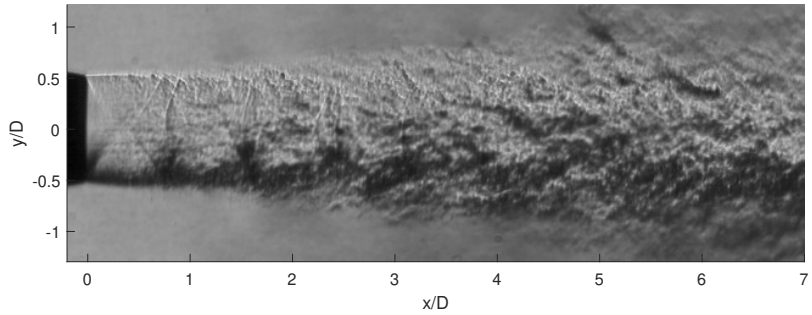

(b) Mach 1.2

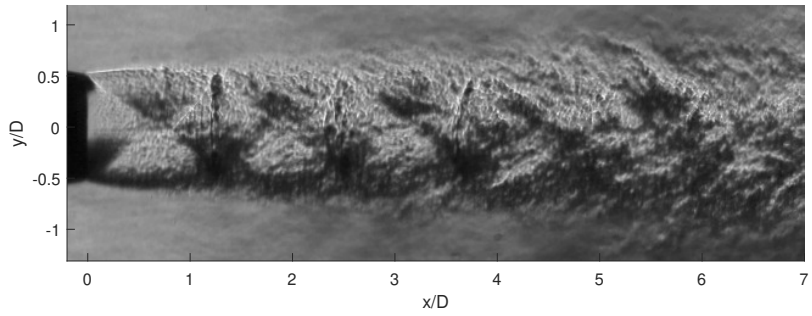

(c) Mach 1.4

Figure 7.11: A comparison of single frames of schlieren flow visualization for a 1.60-inch conical nozzle operated at supersonic Mach numbers.

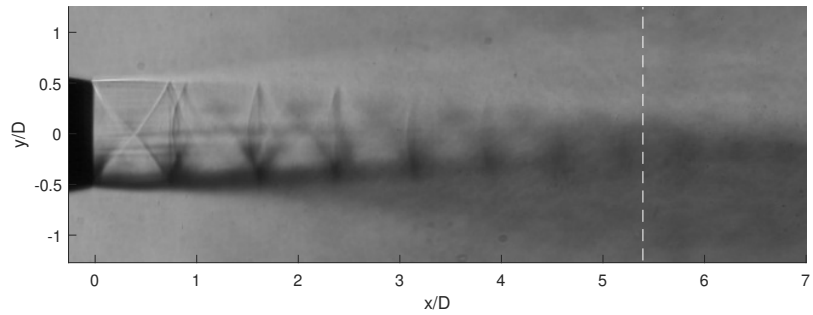

(a) Mach 1.2

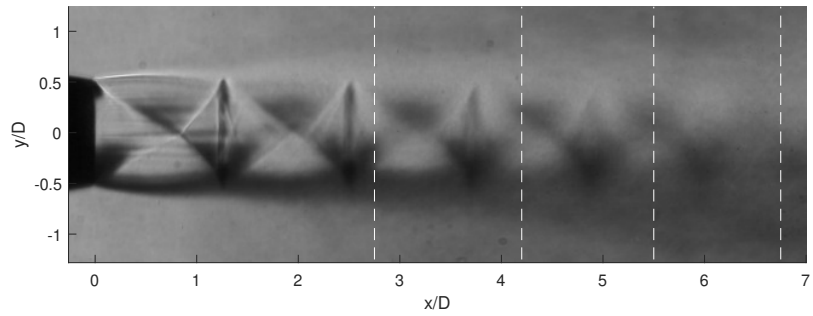

(b) Mach 1.4

Figure 7.12: A comparison of averaged schlieren for a 1.60-inch conical nozzle operated at supersonic Mach numbers. The dashed lines indicate the locations of the shock sources measured by the beamformer (see Figure 7.5a for $M_j = 1.2$ and Figure 7.6a for $M_j = 1.4$).

as expansion waves instead of oblique shocks.

The locations of the shock sources indicated by the beamformer appear to be located downstream of the actual shock cell. For instance, the shock cells are located at x/D of about 1.25, 2.5, 3.75, 4.8, and 6.1 for the Mach 1.4 jet shown in Figure 7.12b and the shock sources that could be measured are located at x/D of about 2.75, 4.2, 5.5, and 6.75, respectively. The noise from the shock cells should be emanating from the points of the shock cells, where the jet-mixing layer interacts with the shock cells. The sound sources appearing to be further downstream than these locations can be explained by jet shear layer refraction effects. The sound from the shock/turbulence interactions has to pass through the mixing layer before it can be measured by the beamformer. The refraction through the shear layer results in the sound curving, making it appear to emanate from further downstream.

Another functionality of the measured shock source locations is that they can be used to fairly accurately measure the spacing of the shock cells in a supersonic jet, assuming enough shock sources are measured by the beamformer to do so. For the Mach 1.4 jet shown in Figure 7.12b, there is an average spacing of about 1.18 diameters between the shock cells in the flow visualization and an average spacing of 1.25 diameters between the shock sources from the source location. Measurements made by Norum and Seiner [59] show the average spacing between shock cells (L) of a converging jet to vary by Equation 7.3.

$$\frac{L}{D} = 1.1\sqrt{M_j^2 - 1} \tag{7.3}$$

Using this equation, the Mach 1.4 jet results in an average shock cell spacing of 1.08 diameters. This is less than the averages of 1.18 diameters (from the schlieren) and 1.25 diameters (from the source location) shown in Figure 7.12b; however, these values are calculated using only the first five shock cells in the jet, later shock cells in the jet core are spaced closer together and would bring the overall average spacing values down.

To fully understand the relationship between the measured source location and schlieren flow visualization, the two sets of data need to be plotted on top of one another. Figure 7.13

shows a typical comparison for the 1.60-inch conical nozzle operated at a fully-expanded Mach number of 1.4. This figure includes five plots, for source locations averages for one-

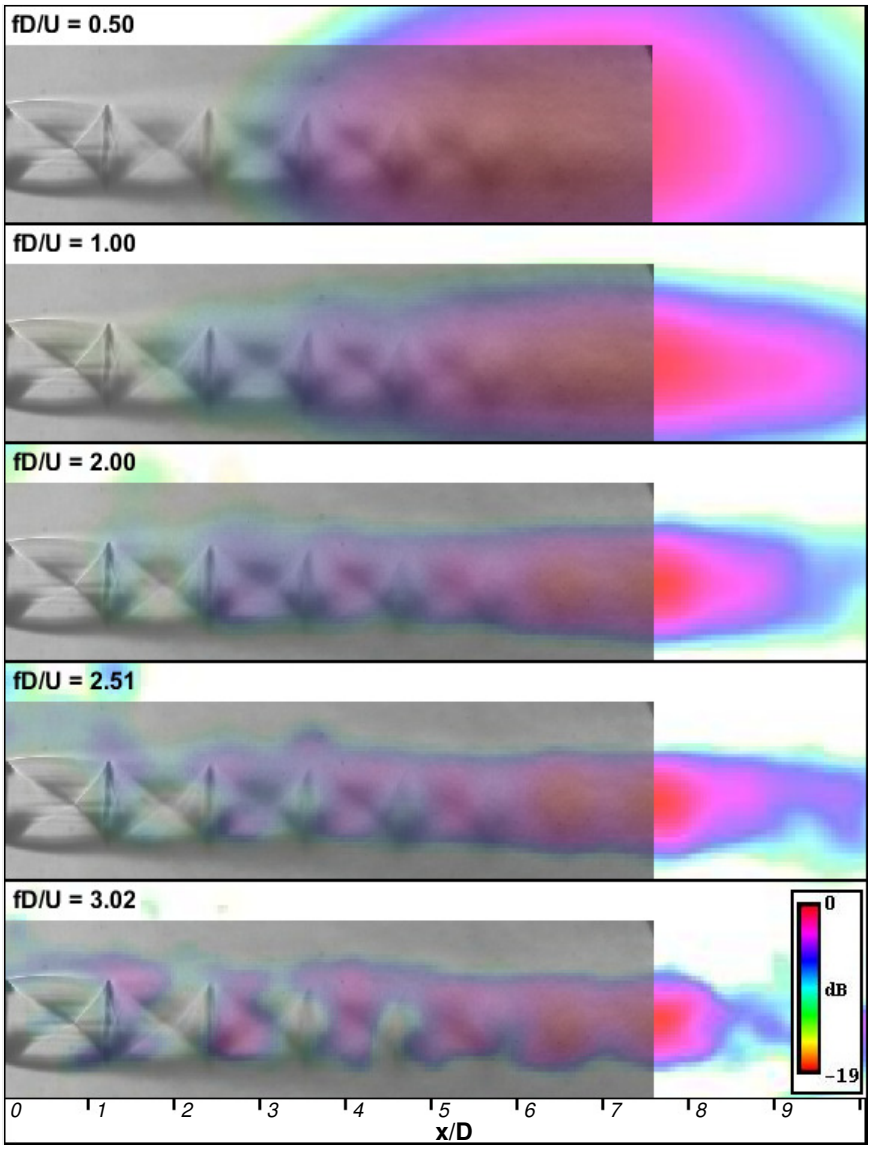

Figure 7.13: Source locations superimposed on the flow visualization. (Nozzle = conical, $D = 1.60$ inches, $M_j = 1.4$)

twelfth octave bands with center frequencies of 5 kHz, 10 kHz, 20 kHz, 25 kHz, and 30 kHz. These frequency values correspond to Strouhal numbers of 0.50, 1.00, 2.00, 2.51, and 3.02, respectively. The colored contours in Figure 7.13 are the two-dimensional source strength distributions that are outputted by the beamformer. The relative maxima of these contours are the values used as the source locations for each frequency.

Using Figure 7.6a as a reference, all of the source location plots in Figure 7.13 correspond with sources in the green source region (i.e. the shock source region), expect for the $fD/U = 0.50$ source plot which is located in the blue source region (i.e. the multi-source shock noise region). These plots illustrate how the measured noise sources appear to be located behind the actual shock cells, and this is especially noticeable in the $fD/U = 3.02$ plot. This figure also shows how the first shock cell, at a location of around 1.25 diameters, produces high frequency noise, approximately between $fD/U = 2.51$ and $fD/U = 3.02$, but does not significantly produce low frequency noise, approximately between $fD/U = 0.50$ and $fD/U = 2.00$. Moving to subsequent shock cells, one can see that they start to produce more lower frequency noise.

At $fD/U = 0.50$, the two dimensional source strength distribution is a single lobe that stretches from about $x/D = 3.5$ to $x/D = 10$. This is another visual representation how the noise emanating from each of the shock cells in this range of downstream positions are averaged together due to to size of the array beam width at 5 kHz, which corresponds to $fD/U = 0.50$ for this jet condition. The peak value of this giant lobe is located approximately at the centroid location of all the $fD/U = 0.50$ noise sources. In comparison, at $fD/U = 3.02$ the beam width is small enough that there are individual peaks in the source strength distribution for each shock cell in the jet.

More comparison plots, such as the one shown in Figure 7.13, for other Mach number conditions can be found in Appendix C. The comparison plot for the jet with a fully expanded Mach number of 1.6 generally shows the same trends as those seen in Figure 7.13. In contrast, the lowest Mach number comparison plots (Mach 1.0 and Mach 1.2) are better examples for source location of jet-mixing noise due to the shock sources being either weak or nonexistent.

Summary of Flow Visualization Results

The locations of the measured discrete shock sources are located slightly downstream of the actual shock cells in a jet, and this is most likely due to shear layer refraction effects. Because this noise is produced by interactions between the shock cells and the jet-mixing layer, the noise must travel through the entirety of the jet-mixing layer before it can be measured, causing the discrepancies shown. The measured shock sources are good points of reference for the spacing of the shock cells in a supersonic jet, as the distance between the measured sources is approximately the same as the actual distances between the shock cells of the jet. The noise produced by the shock cells appears to cover a wider range of frequencies for shock cells that are further downstream.

7.3.4 An Interesting Case in Supersonic Source Location: the Mach 1.6 Jet

Prior to this subsection, only supersonic noise source distributions for fully-expanded Mach numbers of 1.0, 1.2, and 1.4 have been shown. At these Mach numbers the jet-mixing noise portions of the noise source distributions are identical for all Mach numbers. For the jets operated at fully-expanded Mach numbers of 1.6 in this work, the noise source distributions in the jet-mixing region behave somewhat differently. This subsection examines the noise source distributions of Mach 1.6 jets and illustrates how they differ from lower Mach number jets.

The data from the 1.6-inch conical jet operated at a fully-expanded Mach number of 1.6, as shown in Figure 7.14, at first glance appears to follow the same trends as the Mach 1.2 and Mach 1.4 jets. Similar to the increase of discrete sources when the Mach number was increased from Mach 1.2 to Mach 1.4, there are more apparent shock sources at Mach 1.6. There appear to be about seven such sources, and they are located at downstream locations of about 1.75, 3.5, 5.0, 6.75, 8.5, 10, and 11.25. The loudest of these sources (as indicated by symbols of "Source 1" on the plot) for this Mach number appears to be the two sources located at 10 and 11.25 diameters downstream from the nozzle exit. The locations

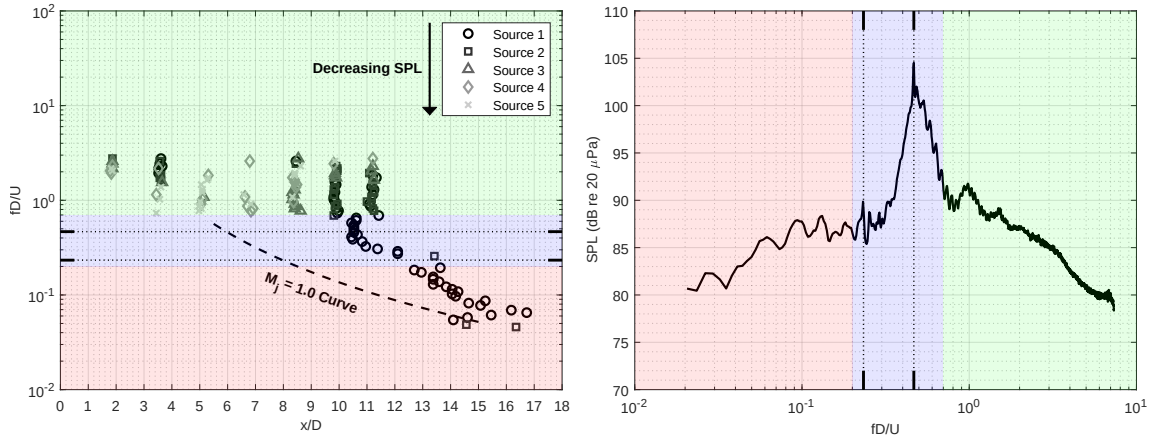

(a) Noise source distribution

(b) $\theta = 90°$, $\Delta f = 32$ Hz

Figure 7.14: Plots of supersonic noise source distribution and 90-degree spectrum (Nozzle = conical, $D = 1.60$ inches, $M_j = 1.6$).

of the first four shock sources are indicated by dashed lines on a frame of averaged flow visualization in Figure 7.15. As shown with the lower Mach number conditions, the shock sources indicate locations just downstream of the shock cells.

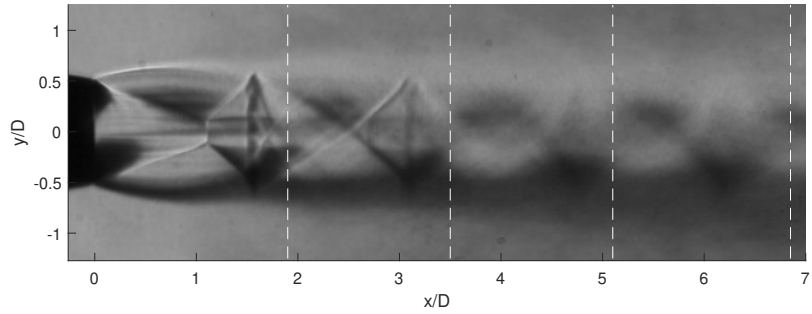

Figure 7.15: Averaged schlieren for a 1.60-inch conical nozzle operated at Mach 1.6. The dashed lines indicate the locations of the discrete sources shown by the beamformer.

The jet-mixing region of the noise source distribution, shown in Figure 7.14a, is no longer in the same location as it was for the lower Mach number conditions, but instead is significantly shifted downstream. This shift can be seen using the Mach 1.0 curve as reference. This curve is the same fit through the Mach 1.0 noise source distribution used earlier in Figure 7.4a. The jet-mixing portion of the noise source distribution for the Mach 1.6 jet is located about two diameters downstream of the reference curve at $fD/U = 0.04$

and increases to about four diameters downstream of the reference curve by $fD/U = 0.2$. This shift may be due to the elongation of the potential core at higher supersonic Mach numbers. While, to the author's best knowledge, there has been no study that models the potential core length for underexpanded supersonic jets, a study by Lau et al. [64] has shown that the length of the potential core for fully-expanded jets increases with M_j^2. Due to the apparent lack of literature, confirming that the shift in jet-mixing source location is due to changes in potential core length thus requires additional PIV measurements to be performed for the Mach 1.2, Mach 1.4, and Mach 1.6 jets. This analysis is recommended for future work in Section 9.2.

The downstream shift in the jet-mixing noise is also seen in the noise source distribution of other nozzle diameters. Figure 7.16 compares the noise source distributions for the 1.0-inch and 1.6-inch conical nozzles at a fully-expanded Mach number of 1.6. The noise

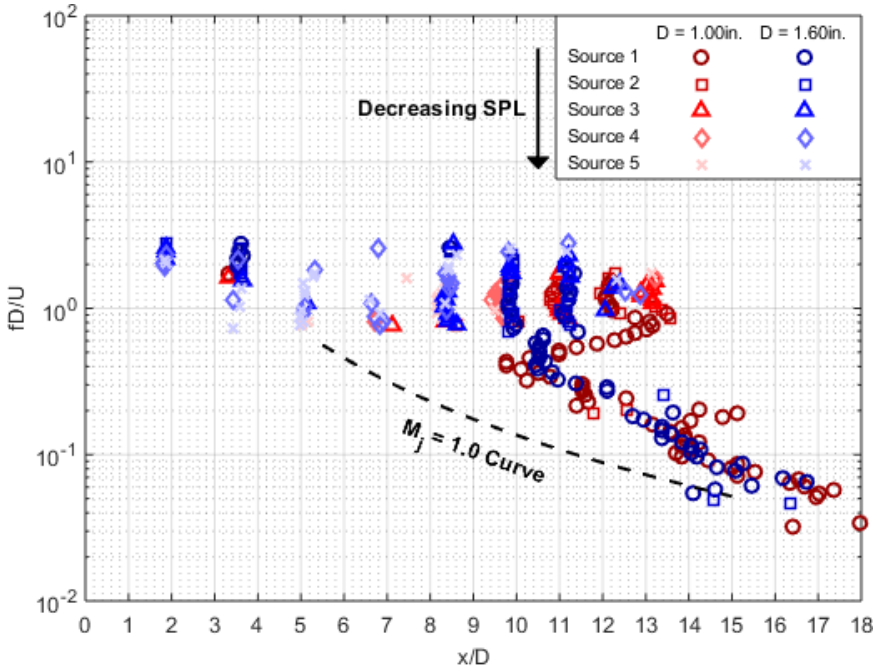

Figure 7.16: Jet noise source location at Mach 1.6 for the conical nozzles of two different diameters.

source distribution for the 2.44-inch nozzle was not acquired as because there was not enough mass flow to achieve a fully-expanded Mach number of 1.6 for that size of nozzle

diameter. Both the shock sources and the jet-mixing noise source distributions line up for both nozzles. Even the multi-source shock noise region appears to have roughly similar source location for both nozzles. The 1.0-inch diameter nozzles appears to have more shock sources downstream of the ones in the 1.6-inch jet. As was the case for lower Mach numbers, the nozzle with the smaller exit diameter has its loudest shock source located further downstream than that of the larger exit diameter nozzle. The loudest shock source for the 1.0-inch nozzle is at a x/D of about 12.1 and for the 1.6-inch nozzle is at a x/D of about 11.

7.4 Concluding Remarks

This chapter primarily focuses on the noise source distributions of a 1.6-inch conical nozzle operated at Mach numbers from 1.0 to 1.4 in steps of 0.2. From these tests, the noise source distributions of these supersonic jets appear to be separated into three different regions: (1) a jet-mixing region, (2) a region containing shock noise sources, and (3) a region that is affected by both jet-mixing noise and discrete shock sources and owes its shape to a lack of resolution in the source location for the frequencies of noise generated in the region.

The jet-mixing region of the noise source distribution, which occurs in the lowest Strouhal numbers measured, is the section of the noise source distribution where the jet-mixing noise associated with the small-scale turbulence is the dominant noise source. The noise source distribution in this region is very similar to that of a subsonic jet. For Mach numbers ranging from 1.0 to 1.4, the source location in this region perfectly collapses with subsonic data when plotted as Strouhal number (fD/U) versus normalized downstream location (x/D). At Mach 1.6, the jet-mixing curve no longer collapses with subsonic data but appears to be shifted further downstream by two to four diameters. For the conical nozzles tested, the noise source location in this region is mostly independent of nozzle exit diameter.

The region that occurs at the highest Strouhal numbers measured in this work is defined by several shock sources that produce a wide range of frequencies. These noise sources are created by the interaction between the tips of shock cells and the jet-mixing layer. The location of these sources is highly dependent on jet Mach number, as they appear further downstream and have more space between them as Mach number increases. In contrast, the location, in x/D, of these sources are independent of diameter. The number of these shock sources that are measured is increased as Mach number and diameter are increased. This is mainly due to the shock sources being stronger, and thus louder, at these conditions, enabling them to be measured.

Finally, the noise source distribution in the Strouhal region between the jet-mixing region and the shock source region is dominated by shock noise sources and attributes its shape to the resolution of the beamformer. The shock sources seen at the highest Strouhal numbers measured also produce noise at the Strouhal numbers that comprise this region. In fact, the noise source distribution of this region should appear as a continuation of the shock sources in the previously described region. However, the beam width of the beamformer becomes larger than the spacings between the shock cells, and thus the shock sources, at these Strouhal numbers. Because larger beam widths result in lower source location resolution, the end result is that the beamformer averages the locations of the shock sources to a centroid location for the given Strouhal number. The odd shape of the distributions in this region are thus affected by the spacing and strength of these shock sources, as well as the Strouhal number of noise being measured. While the spacings can be determined from higher Strouhal number source location measurements (the spacing of the shock sources should not change with Strouhal number), the variance of strengths for these sources as a function of Strouhal number in this region cannot be obtained with the tools available for this work. As such, the results of source location in this region can only be used as general centroid locations for a specific Strouhal number of noise, and no additional information about shock cell structure should be attempted to be pulled from it. The size of this

region should shrink if the resolution of the source location device is improved at lower frequencies.

CHAPTER 8

UNCERTAINTY ANALYSIS

8.1 Introduction

This chapter analyzes the uncertainty in the measurements obtained for the three largest components of this work: (1) the jet operating condition measurements, (2) the acoustic beamforming source location measurements, and (3) the nearfield contour source location measurements.

8.2 Jet Operating Conditions

The source location of various jets are obtained in this work, requiring knowledge of jet conditions such as nozzle exit velocity and Mach number. These values are calculated using Equations 3.20 through 3.22, as shown in Section 3.2.4 in Chapter 3, with measured values of ambient pressure, total pressure, and total temperature. The uncertainties for the devices used for the pressure and temperature measurements in this work are listed in Table 8.1, and they are obtained from the manufacturer of each measuring device. Every facility

Table 8.1: Values of uncertainty for measured jet conditions.

Measurement Type	Uncertainty
Total Pressure (p_t)	± 0.005 psig
Ambient Pressure (p_a)	± 0.0225 psia
Total Temperature (T_t)	$\pm 2.1^{\circ}$R

used in this work use the same models of temperature and pressure devices for recording these values, and thus the uncertainty should be the same for all facilities used in this work.

In order to examine the effects of these uncertainties on the calculations of jet properties like Mach number and jet exit velocity, the method outlined by Coleman and Steele [65]

is used. For a calculated variable, F, that is a function of J other variables, this method states that the total uncertainty, U_F, is a function of the bias limit of that value, B_F, and the precision limit of that value, P_F, as shown in Equation 8.1 below.

$$U_F = \sqrt{B_F^2 + P_F^2} \tag{8.1}$$

The bias limit is a measure of systematic error for a given measurement and can be calculated using Equation 8.2 below.

$$B_F^2 = \sum_{i=1}^{J} \left(\frac{\partial F}{\partial x_i} B_i \right)^2 \tag{8.2}$$

The term x_i represents each variable that is used to calculate F and B_i is that variable's corresponding bias error. The precision limit, on the other hand, is a measure of random error for a given measurement and can be calculated using Equation 8.3 below.

$$P_F^2 = \sum_{i=1}^{J} \left(\frac{\partial F}{\partial x_i} P_i \right)^2 \tag{8.3}$$

Both Equations 8.2 and 8.3 are simplified forms of the equations listed in Coleman and Steele [65], as the terms relating to measuring device correlation are eliminated. In this work there is no correlation in the measuring devices.

The uncertainties listed in Table 8.1 for the measuring devices used in this work are precision uncertainties. The bias uncertainties for these devices are assumed to be zero. The pressure sensors have been calibrated to reduce this type of error, and the temperature sensor, while not usually calibrated, does not have a bias error that will have a meaningful impact on the calculated jet properties. Because all calculations are performed with absolute units for temperature, temperature errors on the order of a few degrees represent less than 0.5% of the measured value. Eliminating bias error, the resulting equation for total

uncertainty of a calculated quantity is shown in Equation 8.4.

$$U_F = \sqrt{\sum_{i=1}^{J} \left(\frac{\partial F}{\partial x_i} P_i \right)^2} \tag{8.4}$$

Using Equation 8.4 with the equations for the various jet conditions in Chapter 3, Equations 3.20 through 3.22, the uncertainties for Mach number, jet exit velocity, and Strouhal number ($St = \frac{fD}{U_j}$) are calculated. The uncertainty equations for these three values, respectively, are listed below in Equations 8.5 through 8.7.

$$U_{M_j} = \sqrt{\left(0.0225 \frac{\partial M_j}{\partial p_a} \right)^2 + \left(0.005 \frac{\partial M_j}{\partial p_t} \right)^2} \tag{8.5}$$

$$U_{U_j} = \sqrt{\left(0.0225 \frac{\partial U_j}{\partial p_a} \right)^2 + \left(0.005 \frac{\partial U_j}{\partial p_t} \right)^2 + \left(2.1 \frac{\partial U_j}{\partial T_t} \right)^2} \tag{8.6}$$

$$U_{St} = \sqrt{\left(0.0225 \frac{\partial St}{\partial p_a} \right)^2 + \left(0.005 \frac{\partial St}{\partial p_t} \right)^2 + \left(2.1 \frac{\partial St}{\partial T_t} \right)^2} \tag{8.7}$$

A more detailed breakdown of these equations can be found in the PhD thesis of Karon [7], where the same uncertainty analysis has been performed for the facilities used in this work.

The uncertainties for Mach number and jet exit velocity calculations for the range of jet conditions used in this work are listed in Table 8.2. These uncertainties are calculated

Table 8.2: Values of uncertainty for jet Mach number and jet exit velocity. All values are calculated using $p_a = 14.18$ psia and $T_t = 519.67$ R.

M_j	U_{M_j}	U_j (ft/s)	U_{U_j} (ft/s)
0.4	± 0.0030	440.0	± 3.3
0.6	± 0.0021	647.6	± 2.4
0.8	± 0.0016	841.8	± 2.3
1.0	± 0.0014	1020.1	± 2.4
1.2	± 0.0012	1181.6	± 2.6
1.4	± 0.0011	1326.0	± 2.8
1.6	± 0.0011	1454.1	± 3.0

using the mean values for atmospheric pressure, 14.18 psia, and total temperature, 519.67 R, obtained from all the tests of this work. These calculated uncertainties show that any random errors associated with the measuring devices used for this work have less than one percent impact on the calculated Mach numbers and jet exit velocities.

As the jet velocity is used to calculate Strouhal number, uncertainty in this quantity also translates into uncertainty in Strouhal number. The data in Table 8.3 illustrates this uncertainty in Strouhal number for a one-inch diameter jet at a range of Mach numbers. Only Strouhal numbers corresponding to frequencies of 1 kHz, 5 kHz, 10 kHz, and 20 kHz

Table 8.3: Values of uncertainty for calculated Strouhal numbers. All values are calculated using $D = 1$ in, $p_a = 14.18$ psia, and $T_t = 519.67$R.

	1000 Hz		5000 Hz		10000 Hz		20000 Hz	
$\mathbf{M_j}$	$\frac{\mathbf{fD}}{\mathbf{U_j}}$	$\mathbf{U_{St}}$	$\frac{\mathbf{fD}}{\mathbf{U_j}}$	$\mathbf{U_{St}}$	$\frac{\mathbf{fD}}{\mathbf{U_j}}$	$\mathbf{U_{St}}$	$\frac{\mathbf{fD}}{\mathbf{U_j}}$	$\mathbf{U_{St}}$
0.4	0.189	± 0.0014	0.947	± 0.0071	1.893	± 0.0142	3.788	± 0.0284
0.6	0.129	± 0.0004	0.643	± 0.0024	1.287	± 0.0049	2.574	± 0.0097
0.8	0.099	± 0.0003	0.495	± 0.0013	0.990	± 0.0027	1.980	± 0.0053
1.0	0.082	± 0.0002	0.408	± 0.0009	0.817	± 0.0019	1.634	± 0.0038
1.2	0.071	± 0.0002	0.352	± 0.0008	0.705	± 0.0015	1.410	± 0.0031
1.4	0.063	± 0.0001	0.314	± 0.0007	0.628	± 0.0013	1.257	± 0.0026
1.6	0.057	± 0.0001	0.287	± 0.0006	0.573	± 0.0012	1.146	± 0.0024

are shown. These conditions should be representative of all other frequencies and all other nozzles. As with the measured jet conditions, the uncertainty in Strouhal number is less than one percent at all frequencies and all conditions.

8.2.1 Summary of Uncertainty in Jet Operating Conditions

Uncertainties due to random error in pressure and temperature measurements has less than one percent effect on the calculations of Mach number, jet exit velocity, and Strouhal number. These types of error should have little to no effect on the results presented in this work.

8.3 Acoustic Beamformer

The majority of the source location results obtained in this work were obtained using an acoustic beamformer. The beamformer used in this work is comprised of 48 Earthworks M30 microphones set in a spiral pattern. A more detailed description of the array geometry is found in Section 3.1.2 of Chapter 3. For a given microphone array geometry, a beamformer has a specific frequency response, called the beam pattern. The beam pattern of an array determines how well the beamformer can detect sources of specific frequencies.

The data acquired by the beamformer is processed and source location data is obtained using the Beamform Interactive software package by OptiNav. A detailed description of this program and the method used for source location analysis is found in Section 3.2.2 of Chapter 3. Due to Beamform Interactive being a closed-box program, the same methods of determining uncertainty for jet conditions used in Section 8.2 cannot be applied here. In the second part of this section, Monte Carlo analysis is used to determine the effects of microphone uncertainties on the source location results obtained with the Beamform Interactive software package.

The one value that all other source location uncertainties are compared against in this chapter is the measurement grid spacing. When processing source location data, Beamform Interactive scans through a two dimensional, x-y plane at a specific offset distance, z, from the array center. In this work, the measuring plane is located 45.5 inches below the beamformer, resulting in a measuring window that is 43.4 inches (x) by 32.6 inches (y) in size. This measuring window contains 307,200 evenly spaced grid points, with spacing of 0.068 inches between each point. The source location cannot have better resolution than this value. As a result, all noise sources have at least ± 0.034 inches of uncertainty in their source location.

8.3.1 Beamformer Beam Pattern Effects on Source Location Accuracy

The beam pattern of a beamformer is a measure of how well the array records sounds from all directions when focused in a specific direction. The main lobe of the beam pattern represents the direction in the beam pattern where there is no loss of received signal. How wide this main lobe is, also called the beam width, affects the beamformer's ability to resolve noise sources. A more detailed description of how this value is calculated can be found in Section 6.2.2 of Chapter 6.

The beam width of the beamformer increases in size as measurement frequency is decreased. If sources of noise for a given frequency are spaced within a beam width apart, the beamformer is not able to identify each source separately and instead ends up only being able to measure the centroid location of that frequency. This effect is shown for twin jet measurements in Chapter 6 and and supersonic jet measurements in Chapter 7. At low frequencies the beamformer is not able to identify either the twin jets or the shock sources in a supersonic jet as individual sources of noise.

A plot of the beam width of the array as a function of frequency and focus angle can be found in Figure 6.12 in Chapter 6. This data is summarized for five frequencies in Table 8.4. An azimuth angle of zero degrees corresponds with the direction directly under the array

Table 8.4: Beam width sizes at selected frequencies and measurement angles.

Azimuth	**1.0 kHz BW (inches)**	**5.0 kHz BW (inches)**	**10.0 kHz BW (inches)**	**20.0 kHz BW (inches)**	**30.0 kHz BW (inches)**
0.00°	14.90	2.86	1.43	0.64	0.48
9.00°	15.55	3.09	1.47	0.65	0.49
18.25°	17.64	3.43	1.67	0.79	0.62
25.00°	20.54	3.97	1.93	0.97	0.58

center and 25 degrees corresponds roughly with the downstream edge of the measurement window of the array used in this work. With a few exceptions at 30 kHz, the beam width generally gets larger as azimuth angle is increased. This means the resolution of the source

location is best directly underneath the array. These calculated values also show that in order to have resolution of ± 1.0 inches at all measuring locations, noise sources must be 10 kHz or above.

8.3.2 Monte Carlo Analysis of the Current Beamforming Method

The source code used to process the beamforming source location data with Beamform Interactive is not accessible to the user, so the exact methods used are unknown. In order to both confirm the accuracy of the source location and determine the affects of microphone errors on source location uncertainty using this program, a Monte Carlo method is used. Monte Carlo analysis is performed for eight source location cases: single point sources of frequencies 1 kHz, 5 kHz, 10 kHz, or 20 kHz located at either $x = 0$ inches or $x = -15$ inches. For all cases the y-coordinate of the point source at zero inches. The sound field from each of these cases are simulated for each of the 48 microphones in the beamforming array using Equation 3.2 shown in Section 3.2.1 of Chapter 3. Random normally distributed errors in the ranges shown in Table 8.5 are included in these simulations. The microphones are treated such that they have $\pm 5\%$ uncertainty in their magnitude measurements and $\pm 2.5^\circ$ uncertainty in their phase measurements. These values could not be acquired for the Earthworks microphones used in this work and are instead approximated from values obtained from similar diameter microphones. The x and y microphone position uncertainties are from manufacturing tolerances and the z position uncertainty is from manual measurement.

Table 8.5: Values of uncertainty for microphones used in Monte Carlo analysis of the Beamform Interactive software package.

Magnitude	**Phase**	**x,y position (inches)**	**z position (inches)**
$\pm 5\%$	$\pm 2.5^\circ$	± 0.0005	± 0.0625

For each case, the sound field is simulated 500 different times and saved as a 48-channel wave file. While Beamform Interactive cannot be directly edited for Monte Carlo analysis,

it does have the capability to batch process the source location of audio files. As such, the 4000 total wave files are processed and the source location for each respective frequency is obtained. Because the wave files generated are fairly large, only the fairly small sample of 500 cases could be generated for each test case before computer space became an issue. While this is not enough to obtain perfect probability distribution functions (PDF) for every condition, it is enough to obtain a decent understanding of the uncertainty of the beamformer.

For a 1000 Hz simulated point source located at $x = 0$ inches and $y = 0$ inches, the resulting probability distribution function of the source location of the 500 repetitions can be seen in Figure 8.1. The x-coordinate of the source location, shown in Figure 8.1a, has a

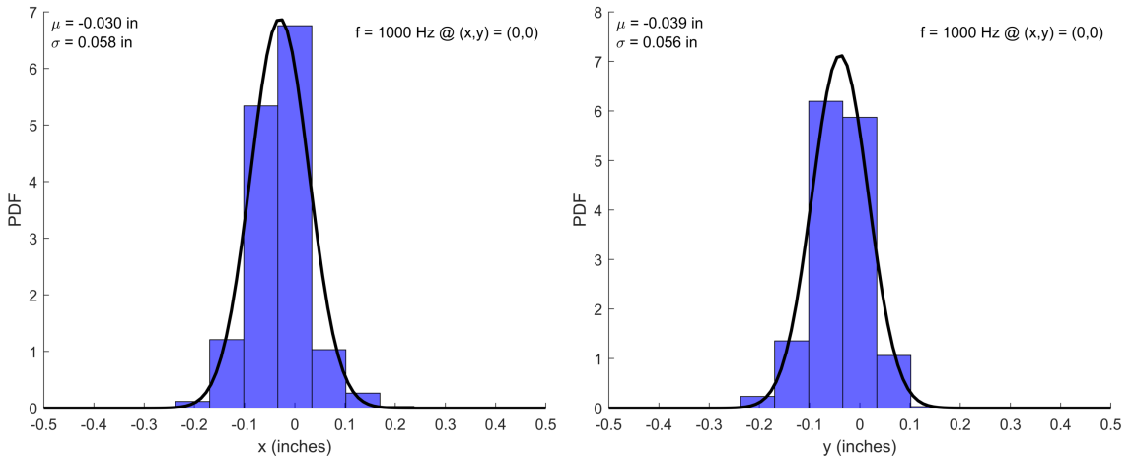

(a) PDF for x

(b) PDF for y

Figure 8.1: Probability distribution functions of the Monte Carlo analysis (N = 500) for the source location of a simulated 1000 Hz point source at $x = 0$ inches and $y = 0$ inches.

mean value of -0.03 inches and 95% confidence interval of $\pm$0.116 inches. Likewise, the y-coordinate of the source location, shown in Figure 8.1b, has a mean value of -0.039 inches and 95% confidence interval of $\pm$0.112 inches. This means that the beamformer can locate the 1000 Hz source within 0.03 inches of its true location give or take 0.112 inches due to microphone uncertainties. Note that the grid spacing limits the source location resolution to at best $\pm$0.034 inches, meaning the 1000 Hz source is only a grid point off with a 95%

confidence range of ± 3 grid points. Each bar on the PDF plots in this chapter represent one grid point.

When the same 1000 Hz noise source is located at $x = -15$ inches and $y = 0$ inches, the new probability distributions appear as shown in Figure 8.2. At this location, the distri-

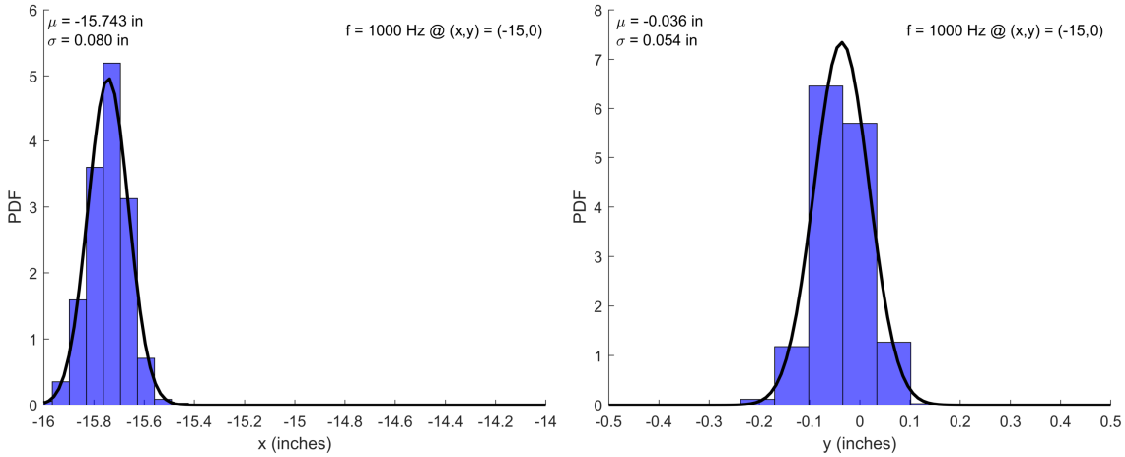

(a) PDF for x

(b) PDF for y

Figure 8.2: Probability distribution functions of the Monte Carlo analysis (N = 500) for the source location of a simulated 1000 Hz point source at $x = -15$ inches and $y = 0$ inches.

bution of the y-coordinate shown Figure 8.2b did not change much from the previous case in Figure 8.1b. The x-coordinate, on the other hand, has a probability distribution function with a mean value of -15.74 inches and a 95% confidence interval of ± 0.16 inches. This results in an error of -0.74 inches or 22 grid points.

By 20000 Hz, the probability distribution functions are comprised of only two boxes, or in other words, two grid points. Figure 8.3 contains the probability distribution function plots for the 20 kHz point source located at $x = 0$ inches and $y = 0$ inches. The mean value for the x-coordinate, shown in Figure 8.3a, is -0.0017 inches with a 95% confidence interval of ± 0.058 inches. This vast improvement over that 1 kHz condition is due to the smaller beam width of the 20 kHz beam pattern, as discussed in Section 6.2.2. The distribution of the y-coordinate has a similar mean value as the 1 kHz condition, -0.036 inches, but a much smaller 95% confidence interval, ± 0.068 inches.

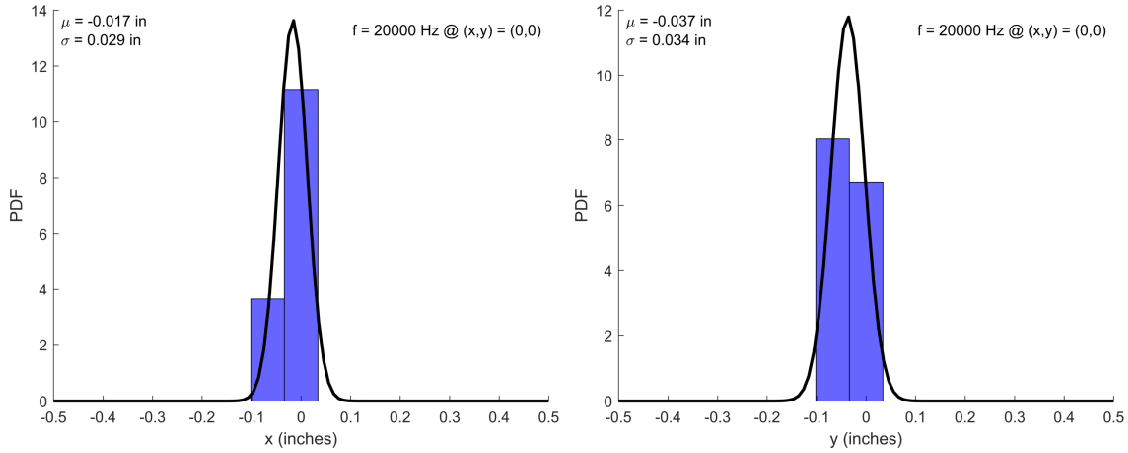

(a) PDF for x (b) PDF for y

Figure 8.3: Probability distribution functions of the Monte Carlo analysis (N = 500) for the source location of a simulated 20000 Hz point source at $x = 0$ inches and $y = 0$ inches.

Figure 8.4 contains the probability distribution function plots for the 20 kHz point source located at $x = -15$ inches and $y = 0$ inches. As was with the 1 kHz conditions,

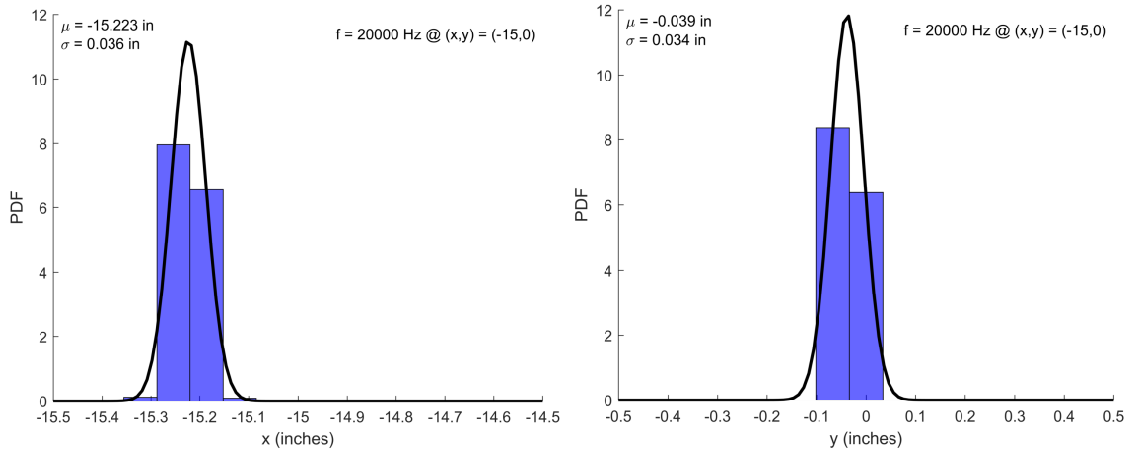

(a) PDF for x (b) PDF for y

Figure 8.4: Probability distribution functions of the Monte Carlo analysis (N = 500) for the source location of a simulated 20000 Hz point source at $x = -15$ inches and $y = 0$ inches.

not much changes with the y-coordinate distribution for this condition. The distribution of the x-coordinate, shown in Figure 8.4a, has a mean value of -15.23 inches with a 95% confidence interval of ± 0.072 inches. This mean value is much closer to the actual location of the noise source than was for the 1 kHz source. The mean value is off by -0.23 inches or

7 grid points.

The mean values and 95% confidence values, $2\sigma_x$, for these distributions as well as for the distributions of the 5000 Hz and 10000 Hz point sources are listed in Table 8.6. In general, when the noise sources are right below the beamformer, at $x = 0$ inches and

Table 8.6: Mean and two sigma values of probability distribution functions of the x and y coordinates obtained for source location of simulated point sources.

frequency (Hz)	$\mathbf{x_{source}}$ **(inches)**	$\mu_\mathbf{x}$ **(inches)**	$\mathbf{2\sigma_x}$ **(inches)**	$\mathbf{y_{source}}$ **(inches)**	$\mu_\mathbf{y}$ **(inches)**	$\mathbf{2\sigma_y}$ **(inches)**
1000	0	-0.030	0.116	0	-0.039	0.112
1000	-15	-15.743	0.160	0	-0.036	0.108
5000	0	-0.030	0.068	0	-0.036	0.068
5000	-15	-15.438	0.086	0	-0.040	0.066
10000	0	-0.021	0.062	0	-0.033	0.068
10000	-15	-15.322	0.000	0	-0.038	0.068
20000	0	-0.017	0.058	0	-0.037	0.068
20000	-15	-15.223	0.072	0	-0.039	0.068

$y = 0$ inches, Beamform Interactive can locate the noise source within one grid point, or 0.034 inches. As the search location moves away from the center of the beamformer, the accuracy decreases. At $x = -15$ inches and $y = 0$ inches, or about where the nozzle exit is located, the source location is off by about three quarters of an inch for a 1000 Hz source and about a quarter of an inch for a 20000 Hz source. This offset appears to approach zero as frequency of the source is increased. The variance of the source location appears to improve with frequency, due to the decrease in beam width, as indicated by smaller values of $2\sigma_x$ and $2\sigma_y$. From this analysis, it is shown that the source location is more affected by the beam width and grid spacing than it is by errors associated with the microphones of the array.

8.3.3 Summary of Uncertainty in Acoustic Beamformer Measurements

There are three main components affecting the accuracy of source location measurements with the acoustic beamformer: the measurement grid spacing, the array beam pat-

tern, and uncertainty associated with microphone position and measurements. The grid spacing used in this work is 0.068 inches, resulting in a maximum possible resolution in source location of ± 0.034 inches. The beam width of the array affects the accuracy of the measurement of individual source strength distributions. In order to have accurate resolution on the order of ± 1 inches or better, the sources of jet have to be at frequencies above 10 kHz. For noise sources at frequencies below this value, the larger size of the beam width limits the ability to detect multiple sources, and at very low frequencies, the beamformer can only be used to locate the centroid location of the sources of the given frequency. Source location errors due to microphone uncertainties are much less than the contributions of the other two components affecting accuracy and as such do not have much impact on the measured data.

8.4 Nearfield Contours

The other method of source location used in this work involves nearfield noise contours. As described in Section 3.2.3 of Chapter 3, the source location is found with contours by drawing a line through the peaks of the contours and noting the intersection location with the jet axis. In this work, this is done by hand and requires significant subjective judgment on the part of the person analyzing the data. Efforts are made to remove personal bias by randomizing the order in which the contours are processed and not letting the user know the corresponding frequencies for the contours they are analyzing.

To get a basic idea on how this method of source location can vary, contours of four frequencies are repeatedly analyzed ten times. These repeat runs are randomly mixed in with the 70 other contours of different frequencies to eliminate additional bias. The mean and 95% confidence ($\pm 2\sigma_x$) values for the source location of these four frequencies can be seen in Table 8.7. These are source location values for the 1.60-inch conical jet operated at Mach 0.8 as discussed in Chapter 4 for comparison with the beamformer. The results in this table show that, while it does improve at higher frequencies, source location measure-

Table 8.7: Mean and two sigma values of selected noise contours when source location is repeated 10 times.

frequency (Hz)	$\mu_{\mathbf{x}}$ **(inches)**	$2\sigma_{\mathbf{x}}$ **(inches)**
10208	4.884	2.249
20448	4.139	1.501
30680	3.151	1.523
40928	3.486	0.859

ments using nearfield contours can vary by as much as $\pm$2.25 inches. This differs from the beamformer in that while the beamformer may have associated uncertainties, every time a specific set of source location data is analyzed by the beamformer, the end result is the same value. Using nearfield contours on the other hand, the source location results may vary by as much as 2.25 inches depending on when the data was analyzed. This can be seen in the 1.5 to 2 diameter spread of nearfield contour data shown in Figure 4.15, the comparison plot of beamforming and nearfield contour source location.

8.5 Concluding Remarks

In this work, uncertainties in measuring devices have less than one percent impact of calculated quantities such as Mach number, jet exit velocity, and Strouhal number. Likewise, uncertainties in microphone measurements and location have little effect on measured source locations. With the acoustic beamformer, measurement grid spacing and array beam width have much larger effects on the accuracy of the source location. Due to 0.068 inch grid spacing, source location resolution obtained with the beamformer cannot exceed $\pm$0.034 inches. This is an acceptable resolution, as it is 4.5% of the diameter of the smallest nozzle tested. The array beam width limits accurate noise source strength distributions to high frequencies, as sources have to be above 10 kHz to be resolved at distances of $\pm$1 inch. While source strength distributions cannot be accurately obtained at low frequencies, source locations can still be obtained by using the peak locations of the measured distributions. In comparison, using nearfield contours to determine source locations is much

less accurate than using an acoustic beamformer. Because source location obtained with nearfield contours is accomplished by hand, there is a variance of ± 2.25 inches or less in the measured source location with this method.

CHAPTER 9
CONCLUSIONS AND SUGGESTIONS FOR FUTURE WORK

9.1 Conclusions

The objectives of this work are as follows:

- to determine how well the acoustic beamforming technique compares with existing methods when measuring the locations of sources of various frequencies in a jet
- to examine how subsonic noise source distributions vary as a function of Mach number and diameter
- to examine how subsonic noise source distributions vary due to differences in nozzle boundary layer thickness caused by differing nozzle geometry
- to explain how subsonic twin jet noise source distributions are affected by source location resolution as a function of separation distance between the jets
- to examine how supersonic noise source distributions vary as a function of nozzle pressure ratio and diameter

This section is divided into four subsections, each one corresponding to a chapter in this work, that detail how these objectives are met and what conclusions are made.

9.1.1 Validation of Acoustic Beamforming as a Viable Technique for Jet-Mixing Noise Source Location

Acoustic beamforming is a relatively new technique for the measurement of jet noise source distributions, and as such its performance is compared against other source location techniques used by others. Previous studies have exhibited a spread of approximately two

nozzle diameters when comparing the jet noise source location among the different studies. These differences are attributed to numerous factors ranging from using different methods, different facilities, and different nozzles/jet conditions. When compared to the most similar conditions from existing studies, the source location obtained with the acoustic beamformer in the present work matches within 0.5-1.0 diameters, which is within the two-diameter variance shown among the previous studies. This comparison is performed at Mach 0.8 with conical nozzles that have exit diameters of one and 2.44 inches.

To reduce the chance of differences in source location being caused by different nozzles and facilities, source location results are likewise compared using the acoustic beamformer and nearfield contours. These tests are performed with the same nozzles and in facilities with similar upstream geometries. The results of these comparisons match within 0.5-1.0 nozzle diameters. From these comparisons as well as the uncertainty analysis performed in Chapter 8, it is shown that nearfield contours are an imprecise tool for jet noise source location. While the contours do an excellent job illustrating source directionality, the method requires a great degree of subjectiveness when obtaining the actual source location resulting in a variance of about ± 2 diameter in results.

Source location errors on the order of 0.5-1.0 diameters have negligible impacts on microphone corrections and upwards of 1 dB effect on the extrapolation of nearfield microphone data to the farfield for frequencies below 75 kHz. In both cases, higher frequency noise is affected more by source location error than low frequency noise; this is mitigated however by the fact that most source location techniques, including beamforming, have better resolution at higher frequencies.

It should be mentioned that the beamforming used in the present work did not measure noise of large-scale structures, so all references to jet-mixing noise refer to noise of small-scale turbulence. Because it produces results that are either better or comparable with other source location methods, and in many case can produce results at a faster rate, it can thus be concluded that acoustic beamforming is a valid and preferable source location technique

for jet noise associated with small-scale turbulence.

9.1.2 Nozzle Geometry Effects on Subsonic Jet Noise Source Location

Subsonic noise source distributions of a subsonic jet are very much affected by the internal geometry of a nozzle used to generate them. This is best illustrated by the difference in noise source distributions of ASME and conical nozzles of similar diameter. At Mach 0.8, the 1.05-inch and 1.56-inch ASME nozzles have noise source distributions that are shifted further upstream at a given Strouhal number compared to those for conical nozzles of similar diameter. This difference in the ASME and conical nozzle noise source distributions is attributed to different growth rates of each nozzle type's jet-mixing layers. Nozzle exit boundary layer profiles show that ASME nozzles have thinner boundary layers than their conical counterparts. The thinner exit boundary layers result in faster downstream growth of turbulent structures in the mixing layer of the jet, resulting in noise source distributions that are shifted further upstream.

It is shown that the subsonic noise source distributions for both ASME and conical nozzles do not change with Mach number when plotted as Strouhal number (fD/U) versus normalized downstream location (x/d). Likewise, the noise source distributions of conical nozzles appear to be independent of nozzle diameter. The noise source distributions of the ASME nozzles however, tend to shift downstream with increasing nozzle exit diameter. This may be due to the difference in nozzle exit boundary layers for the two nozzle types. Unfortunately, nozzle exit boundary layers were only acquired for two nominal diameters in this work, which is not enough data points to confirm a trend.

9.1.3 Noise Source Locations of Twin Circular Jets

The noise source distributions of small-diameter twin jets used in this study cannot be accurately measured below a certain frequency that is a function of the separation distance between the nozzles. For a given frequency, the beamformer has a set resolution determined

by the size of the beam width of the main lobe in its beam pattern and that improves with frequency. Lower frequency noise sources need to be located further apart than higher frequency noise sources, otherwise the beamformer ends up averaging their locations to a centroid location. Because the beam pattern, and thus the beam width, of an array is determined by the number of microphones and their locations with respect to the source, source location resolution can only be significantly changed by changing the design of the array or moving the array closer to the source. The latter solution has limitations, as it is beneficial to stay in the farfield of the noise sources being measured and moving too close to the jets may affect the flow field.

For the twin jets tested in this work, the noise source distributions are independent and centered on each jet's nozzle axis at higher frequencies. Below a certain frequency, the noise source distributions move towards the central axis ($y/D = 0$) as the beam width of the beamformer begins to be larger than the separation distance between the two nozzles. Eventually, all low frequency noise sources appear centered on the central axis. In reality, the noise sources should still be centered on each jet's nozzle axis at these frequencies, but the poor resolution of the beamformer caused by large beam widths averages their locations to a single centroid location in between the two jets. Velocity measurements obtained using PIV are used to support the argument that these shifts in source location to the central axis are a result of resolution issues and not due to jet mixing. Over the 18 diameters in which the source location is measured for this work, the velocity measurements show that the jets are barely interacting, let alone mixing with each other, which is erroneously indicated to be the case by the noise source distribution results.

Even with poor resolution due to a large beam width, the noise source distribution for jet-mixing noise when plotted as Strouhal number (fD/U) versus normalized downstream location (x/D) can still be obtained fairly accurately. The noise source distribution plots of twin jets at three different separation distances, and thus three different regions where the source location becomes poor, collapse independently of their separation distance. There

is a limit to this, however, at extremely low frequencies the beam width of the beamformer is larger than the measuring window and as a result, the measured centroid location may not be the proper centroid location for that frequency.

9.1.4 Supersonic Jet Noise Source Locations

The noise source distributions of supersonic jets in the Mach number range of 1.0 to 1.6 can be separated into three different source location regions: (1) a jet-mixing region, (2) a region containing discrete shock noise sources, and (3) a region that is affected by both jet-mixing noise and shock sources and owes its shape to a lack of resolution in the source location for the frequencies of noise generated in the region.

The jet-mixing region, which occurs in the lowest Strouhal numbers measured, is the section of the noise source distribution where turbulent jet-mixing noise is the dominant noise source. The noise source distribution in this region is very similar to that of a subsonic jet. For Mach numbers ranging from 1.0 to 1.4, the source location in this region perfectly collapses with subsonic data when plotted as Strouhal number (fD/U) versus normalized downstream location (x/D). At Mach 1.6, the jet-mixing curve no longer collapses with subsonic data but appears to be shifted further downstream by two to four diameters. For the conical nozzles tested, the noise source location in this region is mostly independent of nozzle exit diameter.

The region that occurs at the highest Strouhal numbers measured in this work is defined by several discrete shock noise sources that produce a wide range of frequencies. These noise sources are created by the interaction between the tips of shock cells and the jet-mixing layer. The location of these sources is highly dependent on jet Mach number, as they appear further downstream and have more space between them as Mach number increases. In contrast, the location, in x/D, of these sources are independent of diameter. The number of these shock sources that are measured is increased as Mach number and diameter are increased. This is mainly due to the shock sources being stronger, and thus louder, at these

conditions, enabling them to be measured.

Finally, the noise source distribution in the Strouhal region between the jet-mixing region and the discrete shock region is affected by the noise sources in both regions as well as the resolution of the beamformer. This region is called the multi-source shock noise region of the noise source distribution, due to it usually having a shape that results in two or more frequencies being located at the same downstream location in the region. The discrete shock sources discussed in the previous region also produce noise at Strouhal numbers in the multi-source shock noise region. However, the spacings between the discrete shock sources are smaller that the beam width of the beamformer at these Strouhal numbers. The end result is that the beamformer averages the locations of the shock sources to a centroid location for the given Strouhal number. The odd shape of the distributions in this region are thus affected by the spacing and strength of these shock sources, as well as the frequency of noise being measured. As such, the results of source location in this region can only be used as centroid locations for a specific frequency of noise, and no additional information about shock cell structure should be attempted to be pulled from it. The size of this region should shrink if the resolution of the source location device is improved at lower frequencies.

9.2 Suggestions for Future Work

Due to practical limitations, only a handful of nozzles and Mach numbers were tested in this work. In order to better understand phenomena such as how when increasing the diameter of an ASME nozzle from 1.53 inches to 2.00 inches, the noise source distribution of the 2.00-inch ASME nozzle starts to behave similar to a conical nozzle, additional ASME nozzles with diameters between these two values is required. Additional measurements should also be performed by adding straight sections to the ends of the existing ASME nozzles, this will modify the nozzle exit boundary layer, thus allowing one to view how added turbulence affects the noise source distributions. It is the author's belief that the boundary

layer and mixing layers of ASME nozzles become similar to that of conical nozzles when the exit diameter increases past a certain point. Clearly detailed PIV measurements of the jet exit boundary layer and the subsequent flow development will be very beneficial. Also due to monetary and time reasons, PIV measurements could not be made for the supersonic jets examined in this work. As such, detailed PIV measurements should be made of these jets in order to examine how their potential core length varies with their source location.

A major limitation experienced in this work was the hardware of the beamformer. The upper measuring limit of the beamformer is 30 kHz, limiting the range of shock noise that can be measured. This is specifically noticeable in smaller diameter jets where the jet noise spectra is shifted to higher frequencies. Additionally, while the beamformer overall had decent resolution at most of the frequencies measured, there were some cases where it was not sufficient. The twin jets tested in this work could not have their noise source distributions separated below frequencies of 7 kHz and thus it was not possible to visualize how they interact downstream. In the future, repeating these experiments with an array that has better resolution at low frequencies would potentially allow this type of measurement to be possible. Better resolution at lower frequencies would also allow the shock noise sources of smaller diameter jets to be separated and their locations plotted. This will reduce the size of the multi-shock noise source region in supersonic jets and will result in noise source distributions that are more representative of the actual flow features of the jet.

Another interesting case found in this work is the noise source distribution of the 1.00-inch conical nozzle at Mach 0.6, shown in Figure B.1a in Appendix B. The noise source distribution of this jet and the higher Strouhal number noise sources of the Mach 0.4 jet both behave very similar to that of a jet with tabs shown in Figure 4.16 of Chapter 4. Based on other data examined but not presented in this thesis, there are no tones in the jet spectra that would indicate that the jet is excited at these conditions. The spectra of these two conditions do not collapse with those of the other nozzles when jet velocity (U_j^7) and diameter (D^3) scaling is applied but are in fact louder at all frequencies. In the future, further analysis of

this nozzle at Mach numbers around 0.6 should be explored. This analysis would need to include boundary layer profile measurements to see how the state of the jet differs around this Mach number.

Appendices

APPENDIX A

NEARFIELD NOISE CONTOURS

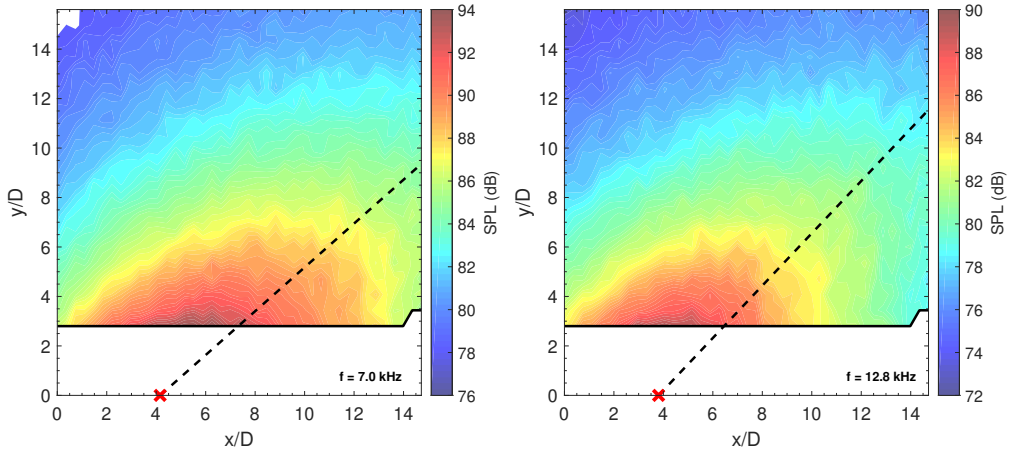

(a) fD/U = 1.110 (b) fD/U = 2.023

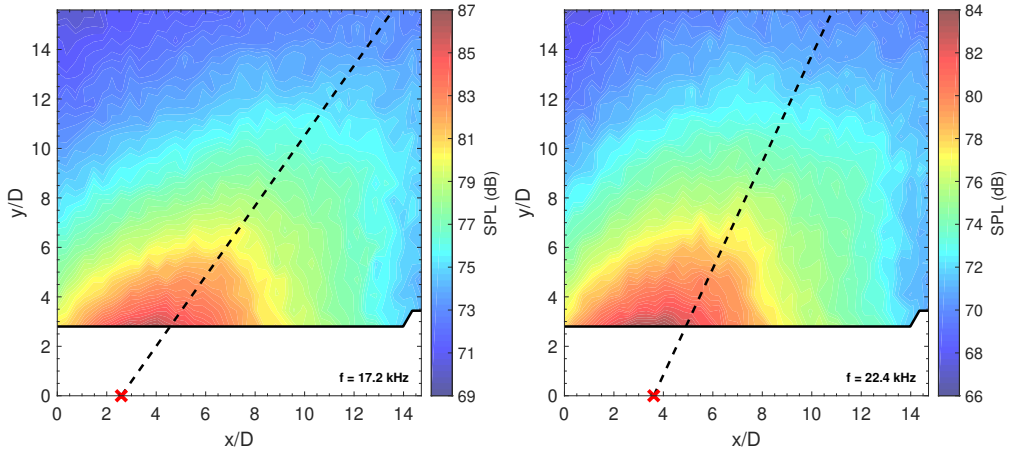

(c) fD/U = 2.733 (d) fD/U = 3.544

Figure A.1: Noise contours for a conical 1.60-inch nozzle with Mach 0.8 flow for Strouhal numbers between 1.110 and 3.544.

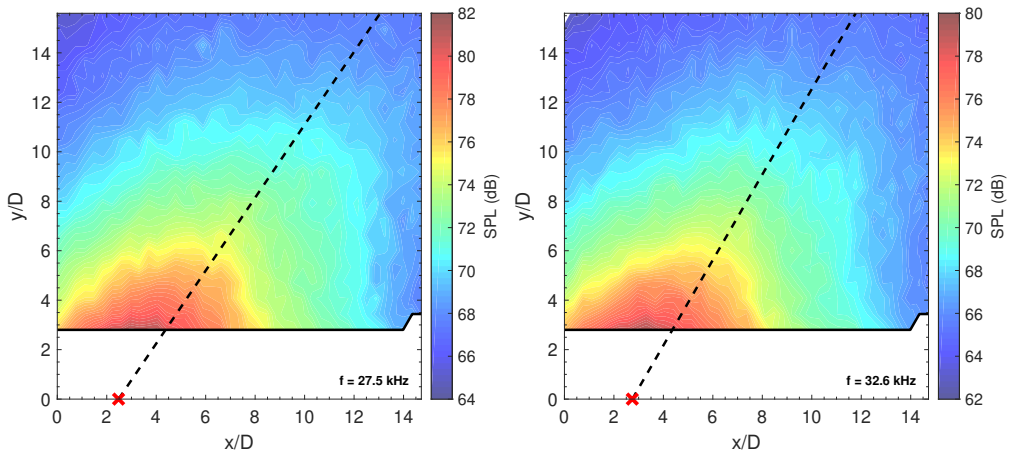

(a) fD/U = 4.355

(b) fD/U = 5.166

(c) fD/U = 5.977

(d) fD/U = 6.383

Figure A.2: Subsonic noise contours for a conical 1.60-inch nozzle with Mach 0.8 flow for Strouhal numbers between 4.355 and 6.383.

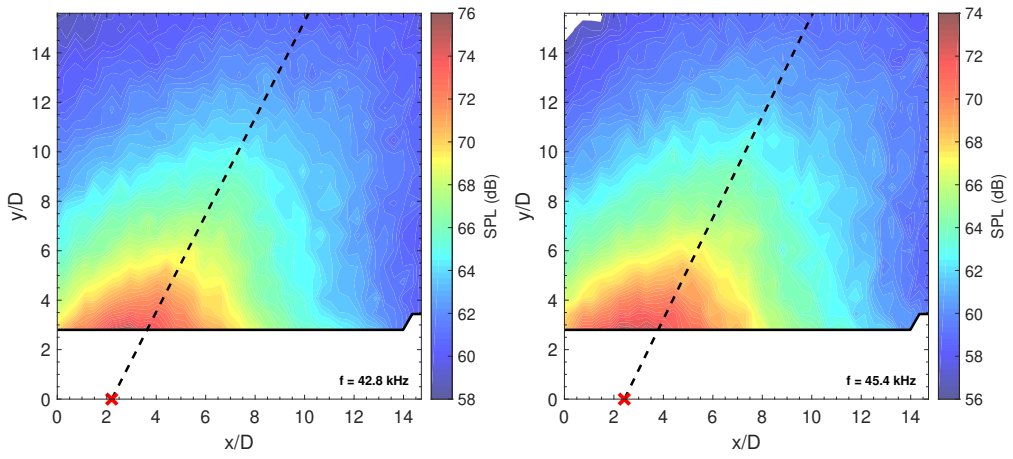

(a) fD/U = 6.789

(b) fD/U = 7.194

(c) fD/U = 7.498

(d) fD/U = 8.005

Figure A.3: Subsonic noise contours for a conical 1.60-inch nozzle with Mach 0.8 flow for Strouhal numbers between 6.789 and 8.005.

APPENDIX B

SUBSONIC SOURCE LOCATION PLOTS

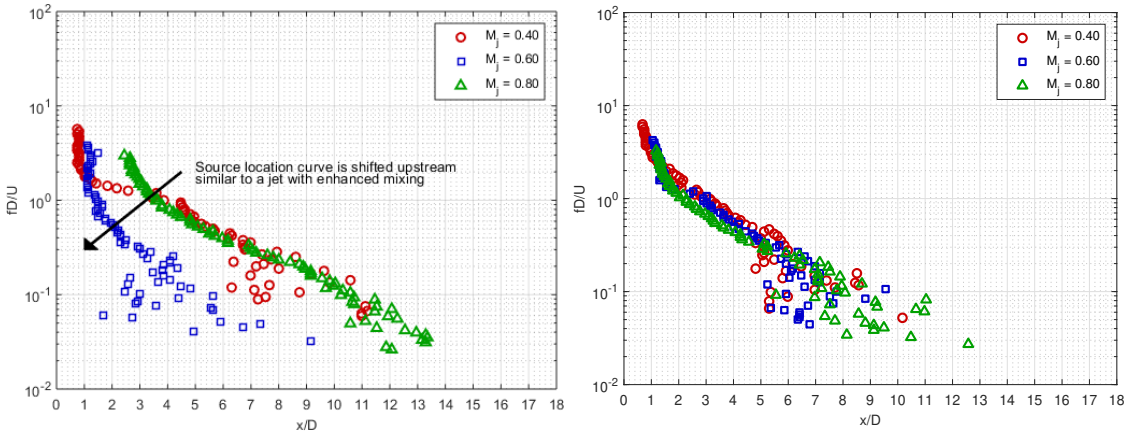

(a) 1.00-inch conical nozzle (b) 1.10-inch ASME nozzle

Figure B.1: Jet noise source location for nominally one-inch nozzles as a function of jet Mach number.

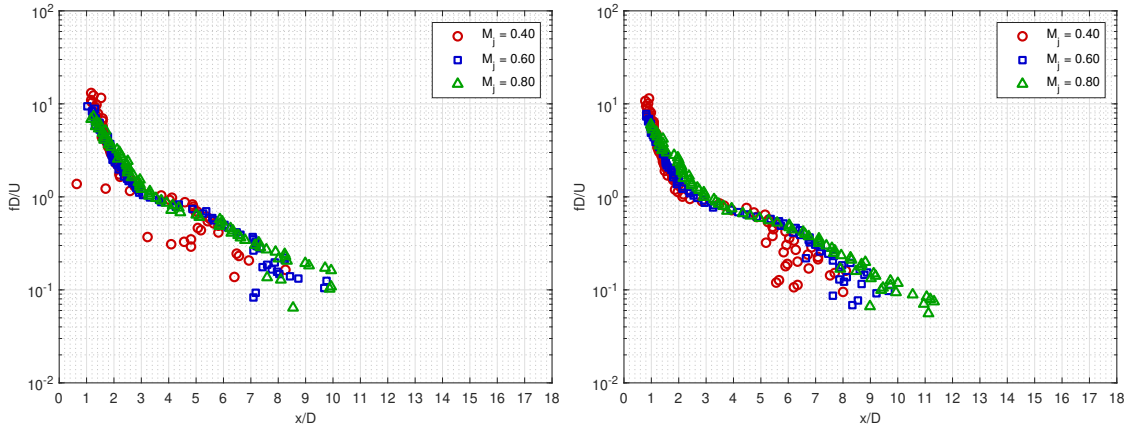

(a) 2.44-inch conical nozzle (b) 2.00-inch ASME nozzle

Figure B.2: Jet noise source location for nominally two-inch nozzles as a function of jet Mach number.

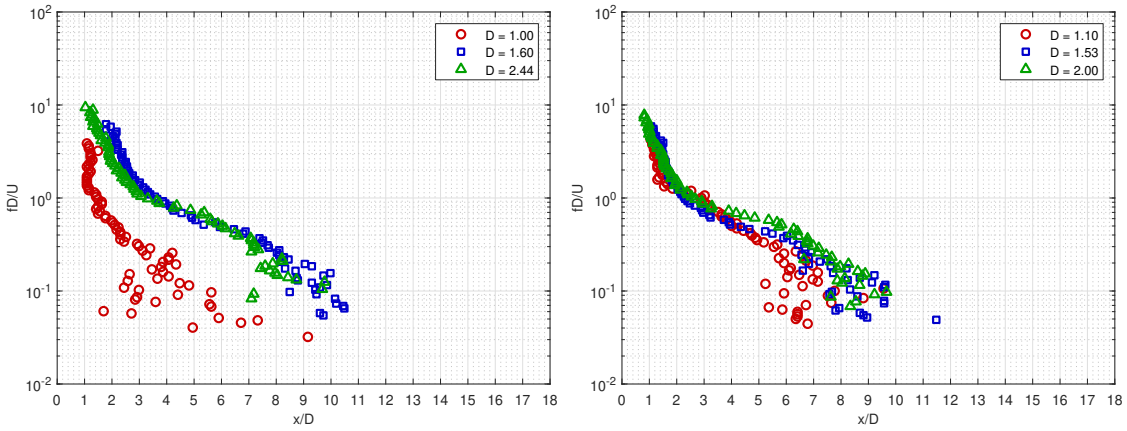

(a) Conical nozzles

(b) ASME nozzles

Figure B.3: Jet noise source location at Mach 0.6 as a function of nozzle exit diameter.

APPENDIX C

SUPERSONIC SOURCE LOCATION PLOTS

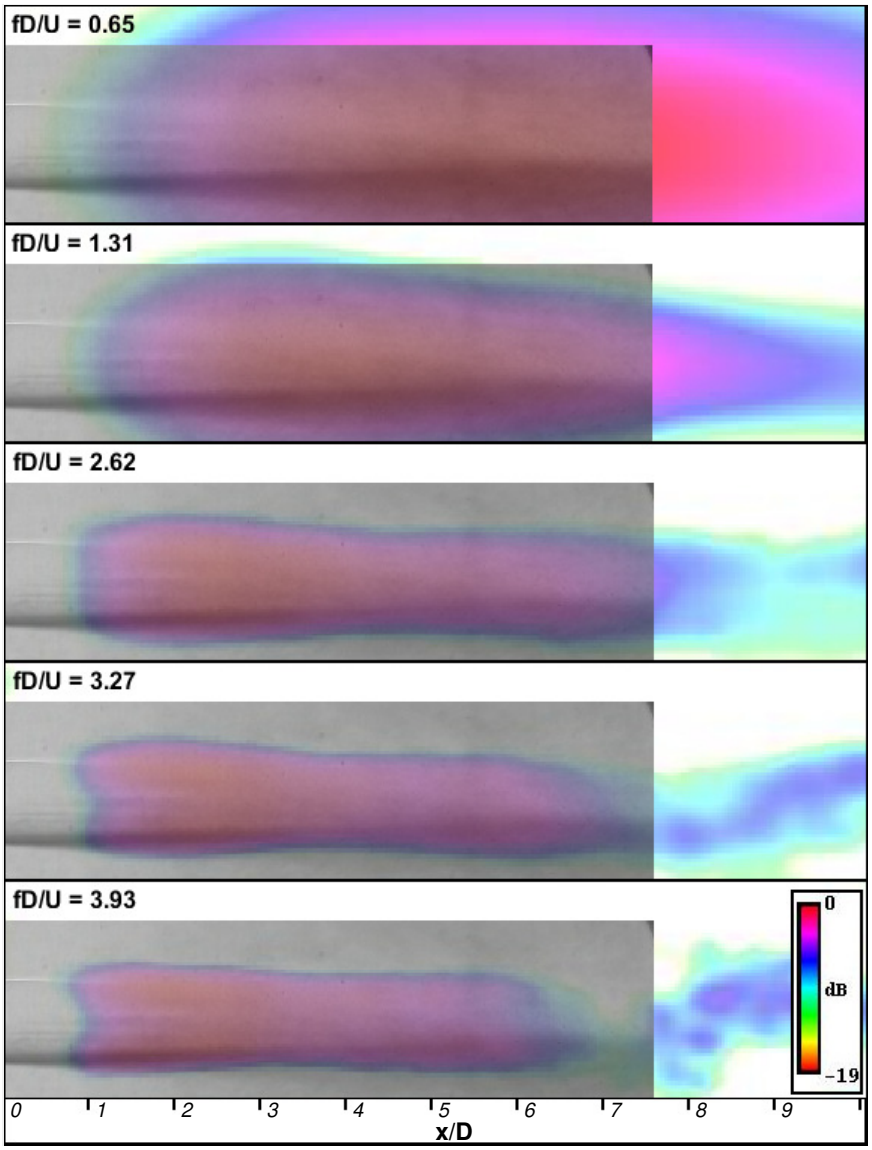

Figure C.1: Source locations superimposed on the flow visualization of a 1.60-inch conical nozzle operated at Mach 1.0. The symbol "x" marks the location determined by the beamformer as the source location for that frequency.

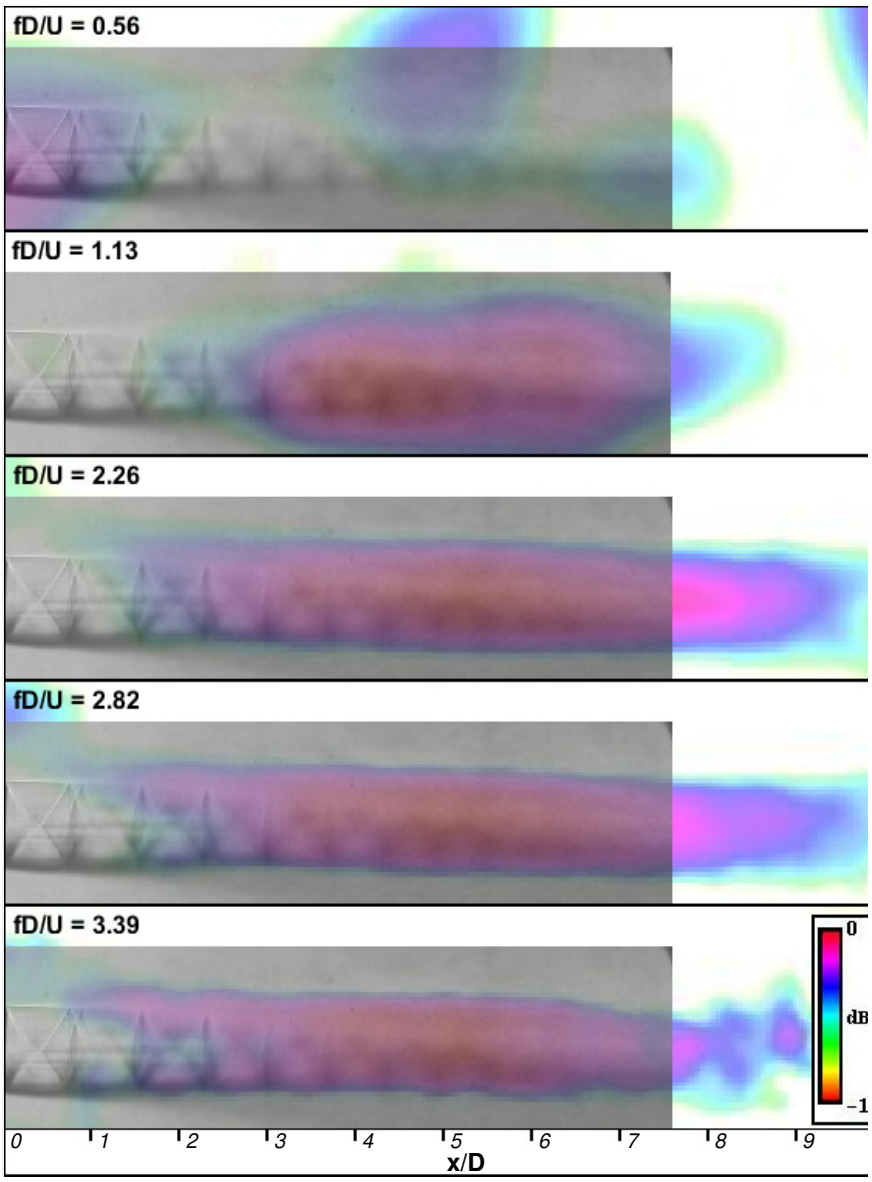

Figure C.2: Source locations superimposed on the flow visualization of a 1.60-inch conical nozzle operated at Mach 1.2. The symbol "x" marks the location determined by the beamformer as the source location for that frequency.

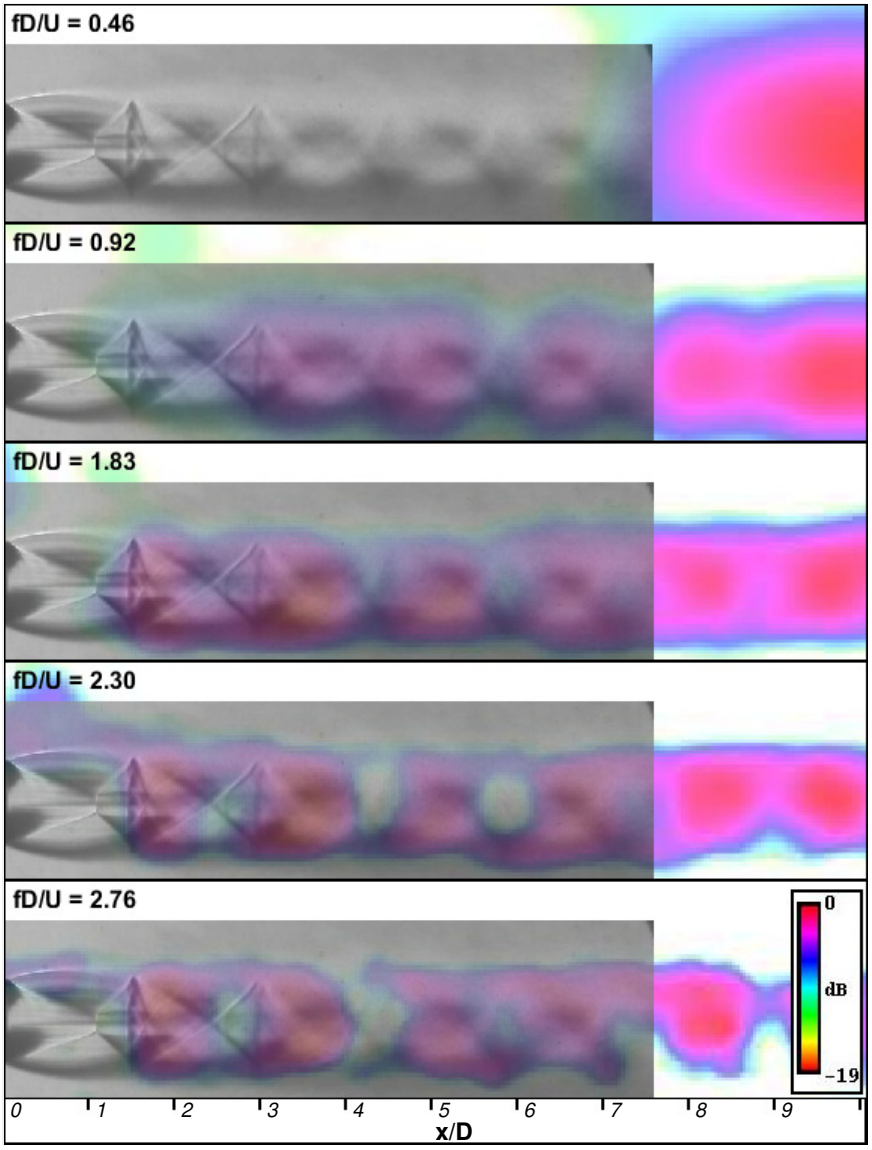

Figure C.3: Source locations superimposed on the flow visualization of a 1.60-inch conical nozzle operated at Mach 1.4. The symbol "x" marks the location determined by the beamformer as the source location for that frequency.

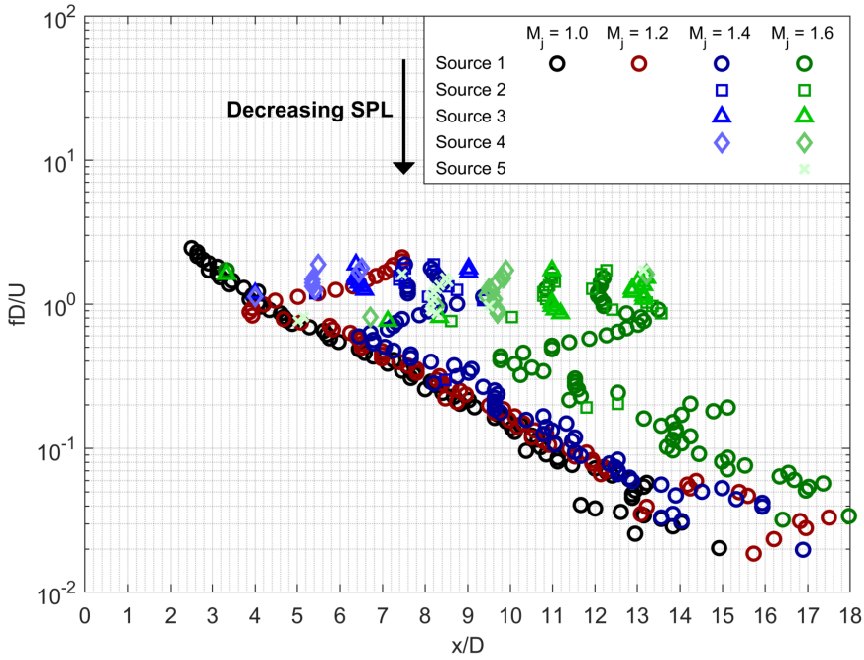

Figure C.4: Supersonic jet noise source location for the conical 1.00-inch nozzle as a function of jet Mach number.

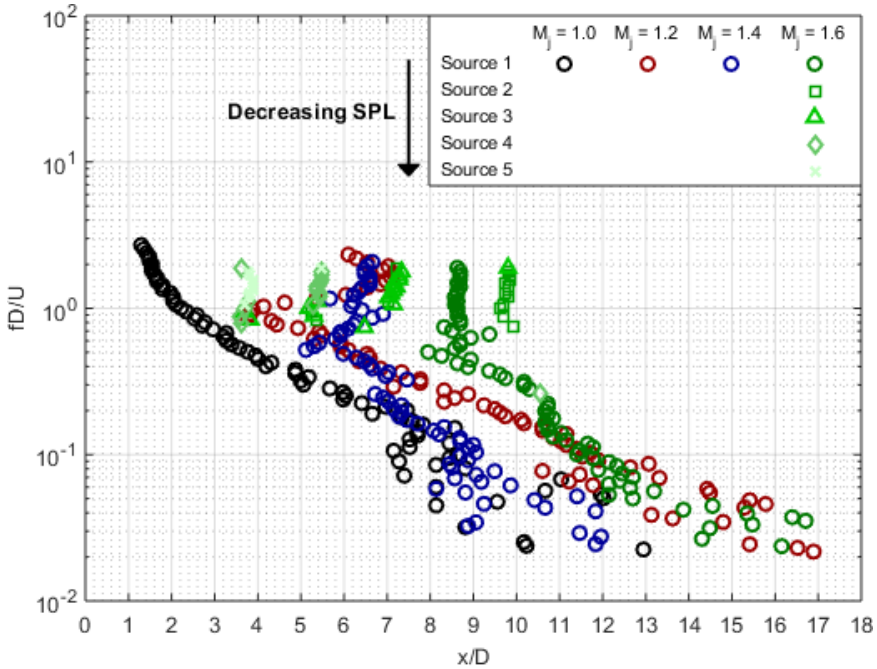

Figure C.5: Supersonic jet noise source location for the ASME 1.10-inch nozzle as a function of jet Mach number.

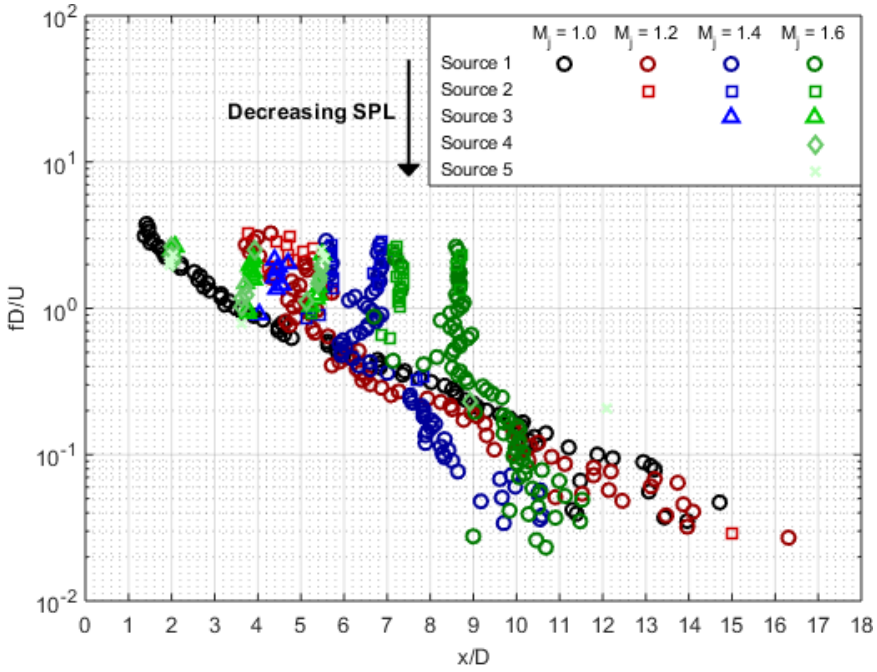

Figure C.6: Supersonic jet noise source location for the ASME 1.53-inch nozzle as a function of jet Mach number.

BIBLIOGRAPHY

[1] Soderman, P. and Noble, S., "A four-element end-fire microphone array for acoustic measurements in wind tunnels," Tech. Rep. NASA-TM-X-62331, National Aeronautics and Space Administration, January 1974.

[2] Sijtsma, P. and Stoker, R., "Determination of absolute contributions of aircraft noise components using fly-over array measurements," *AIAA journal*, Vol. 2958, No. 2004, 2004, pp. 10.

[3] Elkoby, R., Brusniak, L., Stoker, R., Khorrami, M. R., Abeysinghe, A., and Moe, J. W., "Airframe noise results from the QTD II flight test program," *AIAA journal*, Vol. 3457, 2007.

[4] Venkatesh, S. R., Polak, D. R., and Narayanan, S., "Beamforming algorithm for distributed source localization and its application to jet noise," *AIAA journal*, Vol. 41, No. 7, 2003, pp. 1238–1246.

[5] Lee, S. S. and Bridges, J., "Phased-array measurements of single flow hot jets," *11th AIAA/CEAS Aeroacoustics Conference*, 2005, AIAA-2005-2842.

[6] Venkatesh, S., Polak, D., and Narayanan, S., *Phased array design, validation, and application to jet noise source localization*, Aeroacoustics Conferences, American Institute of Aeronautics and Astronautics, 2000.

[7] Karon, A., *Potential Factors Responsible for Discrepancies in Jet Noise Measurements of Different Studies*, Ph.D. thesis, Georgia Institute of Technology, 2016.

[8] Tanna, H. and Morris, P., "In-flight simulation experiments on turbulent jet mixing noise," *Journal of Sound and Vibration*, Vol. 53, No. 3, 1977, pp. 389–405.

[9] Ahuja, K., Tester, B., and Tanna, H., "The free jet as a simulator of forward velocity effects on jet noise," Tech. Rep. NASA-CR-3056, National Aeronautics and Space Administration, October 1978.

[10] Lord, W., Jones, C., Stern, A., Head, V., and Krejsa, E., "Mixer-ejector nozzle for jet noise suppression," *26th Joint Propulsion Conference*, 1990, AIAA-90-1909.

[11] Ahuja, K., Tester, B., and Tanna, H., "Calculation of far-field jet noise spectra from near-field measurements using true source location," *11th Fluid and Plasma Dynamics Conference*, 1978, AIAA-78-1153.

[12] Brooks, T., Humphreys, W., and Plassman, G., *DAMAS Processing for a Phased Array Study in the NASA Langley Jet Noise Laboratory*, Aeroacoustics Conferences, American Institute of Aeronautics and Astronautics, 2010.

[13] Podboy, G. G., Bridges, J. E., and Henderson, B. S., "Phased array noise source localization measurements of an F404 nozzle plume at both full and model scale," *ASME Turbo Expo 2010: Power for Land, Sea, and Air*, American Society of Mechanical Engineers, 2010, pp. 179–208.

[14] Podboy, G. G., "Jet-Surface interaction test: phased array noise source localization results," *ASME Turbo Expo 2012: Turbine Technical Conference and Exposition*, American Society of Mechanical Engineers, 2012, pp. 381–414.

[15] Ahuja, K., Massey, K., and D'Agostino, M., "A simple technique of locating noise sources of a jet under simulated forward motion," *4th AIAA/CEAS aeroacoustics Conference*, 1998, AIAA-98-2359.

[16] Lighthill, M. J., "On sound generated aerodynamically. I. General theory," *Proceedings of the Royal Society of London A: Mathematical, Physical and Engineering Sciences*, Vol. 211, The Royal Society, 1952, pp. 564–587.

[17] Lighthill, M. J., "On sound generated aerodynamically. II. Turbulence as a source of sound," *Proceedings of the Royal Society of London A: Mathematical, Physical and Engineering Sciences*, Vol. 222, The Royal Society, 1953, pp. 1–32.

[18] Lighthill, M. J., "Jet noise," *AIAA Journal*, Vol. 1, No. 7, 1963, pp. 1507–1517.

[19] Laufer, J., Schlinker, R., and Kaplan, R., "Experiments on supersonic jet noise," *AIAA Journal*, Vol. 14, No. 4, 1976, pp. 489–497.

[20] Schlinker, R. H., *Supersonic jet noise experiments*, Ph.D. thesis, University of Southern California, 1975.

[21] Tam, C. K., Golebiowski, M., and Seiner, J. M., "On the two components of turbulent mixing noise from supersonic jets," *2nd AIAA/CEAS Aeroacoustics Conference*, 1996, AIAA-96-1716.

[22] Tam, C. K., Pastouchenko, N. N., and Schlinker, R. H., "Noise source distribution in supersonic jets," *Journal of Sound and Vibration*, Vol. 291, No. 1, 2006, pp. 192–201.

[23] Tam, C. K., Viswanathan, K., Ahuja, K., and Panda, J., "The sources of jet noise: experimental evidence," *Journal of Fluid Mechanics*, Vol. 615, No. 1, 2008, pp. 253–292.

[24] Westley, R. and Lilley, G. M., "An investigation of the noise field from a small jet and methods for its reduction," Tech. rep., College of Aeronautics Cranfield, 1952.

[25] Yu, C. J. and Dosanjh, D. S., "Noise field of a supersonic Mach 1.5 cold model jet," *The Journal of the Acoustical Society of America*, Vol. 51, No. 5A, 1972, pp. 1400–1410.

[26] Chu, W., Laufer, J., and Kao, K., "Noise source distribution in subsonic jets," *Internoise 72*, 1972, pp. 472–476.

[27] Fisher, M., Harper-Bourne, M., and Glegg, S., "Jet engine noise source location: The polar correlation technique," *Journal of Sound and Vibration*, Vol. 51, No. 1, 1977, pp. 23–54.

[28] Tester, B. and Fisher, M., "Engine noise source breakdown - Theory, simulation and results," *7th Aeroacoustics Conference and Exhibit*, 1981, AIAA-81-2040.

[29] Battaner, J. P., "New automated source breakdown algorithm for jet noise," *9th AIAA/CEAS Aeroacoustics Conference and Exhibit*, 2003, AIAA-2003-3324.

[30] Soderman, P. T. and Noble, S. C., "Directional microphone array for acoustic studies of wind tunnel models," *Journal of Aircraft*, Vol. 12, No. 3, 1975, pp. 168–173.

[31] Billingsley, J. and Kinns, R., "The acoustic telescope," *Journal of Sound and Vibration*, Vol. 48, No. 4, 1976, pp. 485–510.

[32] Narayanan, S., Barber, T., and Polak, D., "High subsonic jet experiments: turbulence and noise generation studies," *AIAA journal*, Vol. 40, No. 3, 2002, pp. 430–575.

[33] Breen, N. P. and Ahuja, K. K., "Measuring Jet Noise Source Locations with Acoustic Beamforming," *53rd AIAA Aerospace Sciences Meeting*, 2015, AIAA-2015-0735.

[34] Dougherty, R. P. and Stoker, R. W., "Sidelobe suppression for phased array aeroacoustic measurements," *AIAA paper*, Vol. 2242, 1998, pp. 1998.

[35] Dougherty, R. P., "Advanced time-domain beamforming techniques," *10th AIAA/CEAS Aeroacoustics Conference*, 2004, AIAA-2004-2955.

[36] Dougherty, R., *Extensions of DAMAS and Benefits and Limitations of Deconvolution in Beamforming*, Aeroacoustics Conferences, American Institute of Aeronautics and Astronautics, 2005.

[37] Dougherty, R., "Improved generalized inverse beamforming for jet noise," *International Journal of Aeroacoustics*, Vol. 11, No. 3-4, 2012, pp. 259–290.

[38] Dougherty, R. P., *Functional Beamforming for Aeroacoustic Source Distributions*, AIAA Aviation, American Institute of Aeronautics and Astronautics, 2014.

[39] Dougherty, R. and Podboy, G., *Improved Phased Array Imaging of a Model Jet*, Aeroacoustics Conferences, American Institute of Aeronautics and Astronautics, 2009.

[40] Ahuja, K. and Brown, W., "Shear flow control by mechanical tabs," *2nd Shear Flow Conference*, 1989, AIAA-89-0994.

[41] Papamoschou, D., "Wavepacket modeling of the jet noise source," *International Journal of Aeroacoustics*, Vol. 17, No. 1-2, 2018, pp. 52–69.

[42] Harker, B. M., Neilsen, T. B., Gee, K. L., Wall, A. T., and James, M. M., "Wavepacket modeling and full-scale military jet noise beamforming analyses," *54th AIAA Aerospace Sciences Meeting*, 2016, AIAA-2016-2129.

[43] Stout, T. A., Gee, K. L., Neilsen, T. B., Wall, A. T., and James, M. M., "Source characterization of full-scale jet noise using acoustic intensity," *Noise Control Engineering Journal*, Vol. 63, No. 6, 2015, pp. 522–536.

[44] Wall, A. T., Leete, K. M., Gee, K. L., Neilsen, T. B., James, M. M., and McKinley, R. L., "Preliminary Investigation of Multilobe Fighter Jet Noise Sources Using Acoustical Holography," *23rd AIAA/CEAS Aeroacoustics Conference*, 2017, AIAA-2017-3520.

[45] Merino-Martinez, R., Sijtsma, P., Snellen, M., Ahlefeldt, T., Antoni, J., Bahr, C., Blacodon, D., Ernst, D., Finez, A., Funke, S., Geyer, T., Haxter, S., Herold, G., Huang, X., Humphreys, W. M., Lec, Q., Malgoezar, A., Michel, U., Padois, T., and Spehr, C., "A Review of Acoustic Imaging Methods Using Phased Microphone Arrays," 03 2017.

[46] Benedict, R. and Wyler, J., "Analytical and experimental studies of ASME flow nozzles," *Journal of Fluids Engineering*, Vol. 100, No. 3, 1978, pp. 265–274.

[47] Arnold, D. P., *A MEMS-based directional acoustic array for aeroacoustic measurements*, 2001.

[48] Ahuja, K., "Designing clean jet-noise facilities and making accurate jet-noise measurements," *International Journal of Aeroacoustics*, Vol. 2, No. 3, 2003, pp. 371–412.

[49] Acoustical Society of America. Standards Secretariat, *American National Standard Method for the Calculation of the Absorption of Sound by the Atmosphere*, American Institute of Physics, 1978.

[50] Xu, G. and Antonia, R., "Effect of different initial conditions on a turbulent round free jet," *Experiments in Fluids*, Vol. 33, No. 5, 2002, pp. 677–683.

[51] Bogey, C. and Bailly, C., "Influence of nozzle-exit boundary-layer conditions on the flow and acoustic fields of initially laminar jets," *Journal of Fluid Mechanics*, Vol. 663, 2010, pp. 507–538.

[52] Harper-Bourne, M., "Twin-jet near-field noise prediction," *6th Aeroacoustics Conference and Exhibit*, 2000, AIAA-2000-2084.

[53] Wlezien, R., "Nozzle geometry effects on supersonic jet interaction," *AIAA journal*, Vol. 27, No. 10, 1989, pp. 1361–1367.

[54] Seiner, J., Manning, J., and Ponton, M., "Model and full scale study of twin supersonic plume resonance," *25th AIAA Aerospace Sciences Meeting*, 1987, AIAA-87-0244.

[55] Seiner, J. M., Manning, J. C., and Ponton, M. K., "Dynamic pressure loads associated with twin supersonic plume resonance," *AIAA Journal*, Vol. 26, No. 8, 1988, pp. 954–960.

[56] Johnson, D. H. and Dudgeon, D. E., *Array signal processing: concepts and techniques*, PTR Prentice Hall Englewood Cliffs, 1993.

[57] Gaeta, R. and Ahuja, K., "Subtle Differences in Jet Noise Scaling with Narrow Band Spectra Compared to 1/3-Octave Band," *9th AIAA/CEAS Aeroacoustics Conference and Exhibit*, 2003, AIAA-97-3124.

[58] Tam, C. K., Seiner, J. M., and Yu, J., "Proposed relationship between broadband shock associated noise and screech tones," *Journal of sound and vibration*, Vol. 110, No. 2, 1986, pp. 309–321.

[59] Norum, T. and Seiner, J., "Broadband shock noise from supersonic jets," *AIAA journal*, Vol. 20, No. 1, 1982, pp. 68–73.

[60] Massey, K., Ahuja, K., Massey, K., and Ahuja, K., "Screech frequency prediction in light of mode detection and convection speed measurements for heated jets," *3rd AIAA/CEAS Aeroacoustics Conference*, 1997, AIAA-97-1625.

[61] Ahuja, K. and Blakney, D., "Tone excited jets, part IV: acoustic measurements," *Journal of Sound and Vibration*, Vol. 102, No. 1, 1985, pp. 93–117.

[62] Harper-Bourne, M. and Fisher, M. J., "The noise from shock waves in supersonic jets," *Proceedings of the AGARD Conference on Noise Mechanisms*, No. 131, 1973.

[63] Tam, C. K., "Supersonic jet noise," *Annual Review of Fluid Mechanics*, Vol. 27, No. 1, 1995, pp. 17–43.

[64] Lau, J. C., Morris, P. J., and Fisher, M. J., "Measurements in subsonic and supersonic free jets using a laser velocimeter," *Journal of Fluid Mechanics*, Vol. 93, No. 1, 1979, pp. 1–27.

[65] Coleman, H. W. and Steele, W. G., "Engineering application of experimental uncertainty analysis," *AIAA journal*, Vol. 33, No. 10, 1995, pp. 1888–1896.

VITA

Nicholas Breen was born in Rockford, Illinois on November 13, 1990, and his family moved to Acworth, Georgia in 1998. His interest in science and engineering matured throughout his school years, especially during his time at Kennesaw Mountain High School in the magnet program for math and science. Through the magnet program, Nicholas was able to obtain hands on experience in geology in a class that took place in five different western states. It was an engineering internship at the Georgia Tech Research Institute (GTRI) that set his sight on the skies. By the end of his high school career he knew that he wanted to be an aerospace engineer, and that Georgia Tech would propel him towards this goal.

Nicholas graduated with his Bachelor of Science in Aerospace Engineering from Georgia Tech in May 2014, and he continued on at Georgia Tech to obtain his Master of Science degree in December 2017. While at Georgia Tech, Nicholas had the pleasure of being a teaching assistant for a MATLAB class and a co-op at the Aerospace, Transportation, and Advanced Systems Laboratory of GTRI. Also durring his time at Georgia Tech, Nicholas met and fell in love with his wife, Nicole Breen. Nicholas has since continued to work at GTRI as a graduate research assistant under the guidance of Professor Krish Ahuja.